université PARIS-SACLAY

Studying the nucleon structure via Double Deeply Virtual Compton Scattering at the Jefferson Laboratory

Thèse de doctorat de l'université Paris-Saclay

École doctorale n° 576 Particules hadrons énergie et noyau : instrumentation, image, cosmos et simulation (Pheniics)
Spécialité de doctorat: physique hadronique
Unité de recherche : Université Paris-Saclay, CNRS, IJCLab, 91405, Orsay, France
Référent : Faculté des sciences d'Orsay

Thèse présentée et soutenue à Orsay, le 28/07/2020, par

Shengying ZHAO

Composition du Jury

Michel GUIDAL Docteur, Université Paris-Saclay	Président
Jian-Ping CHEN Docteur, Jefferson Laboratory	Rapporteur
Marc VANDERHAEGHEN Professeur, Johannes Gutenberg-Universität Mainz	Rapporteur
Nicole d'HOSE Docteur, CEA Saclay	Examinatrice
Haiyan GAO Professeur, Duke University	Examinatrice
Eric VOUTIER Docteur, Université Paris-Saclay	Directeur de thèse

Thèse de doctorat

NNT : 2020UPASS147

Acknowledgments

First of all, I am deeply appreciative of the financial support of the China Scholarship Council (CSC) and the French Centre National de la Recherche Scientifique (CNRS).

I would like to express my most sincere gratitude and appreciation to my thesis supervisor, Eric Voutier, for his guidance, patience and encouragement over the last few years. His dedication, enthusiasm and insights into physics have been a great source of inspiration for me. He has been always available and helpful whenever I met difficulties or challenges in my study, and his careful reading of my thesis and his suggestions have significantly improved the quality of this document. Without him, none of this work would have been possible. It is my fortune and honor to be able to work under his supervision.

I carried out my thesis in the JLab/EIC team of the Physique des Hautes Energies (PHE) group at the Laboratoire de Physique des 2 Infinis Irène Joliot-Curie (IJCLab). I wish to address my heartfelt gratitude to my colleagues, who provided me with a professional academic atmosphere and a friendly working environment to pursue my research. Special thanks go to Raphaël Dupré, Mostafa Hoballah, Dominique Marchand, Carlos Muñoz Camacho, and Silvia Niccolai for their appreciated help and valuable discussions. I would also like to acknowledge all my PhD and post-doc colleagues for the wonderful time spent together.

Most of my study involves the VGG model, and I am grateful to its excellent creators. Especially, I would like to thank Michel Guidal, who gave me the valuable guidance of using and developing the VGG code and spent his precious time to answer all my questions. I would also like to thank Marc Vanderhaeghen for the priceless explanation of the theoretical knowledge of the DDVCS process and the warm welcome during my visit in Mainz.

Further gratitude goes to Alexandre Camsonne, who provided me with the opportunity to visit JLab. The valued discussion with him improved my understanding of the experimental aspects of this work. I would also like to extend my appreciation to Zhiwen Zhao for offering the acceptance parameters of the SoLID spectrometer and sharing his great ideas about the DDVCS experimental projection with SoLID.

My thanks are due to Jian-Ping Chen and Marc Vanderhaeghen for the careful reading of the manuscript. Besides, I thank Nicole d'Hose, Haiyan Gao, and Michel Guidal for accepting being part of the examination committee and showing their interest in my work.

Finally, I would like to thank my family for their wise counsel and endless support. I also thank my friends for providing a happy distraction to rest my mind outside of my research.

Contents

Introduction

Negatively charged electrons and a positively charged nucleus constitute an atom being the basic building brick of normal matter. The nucleus consists of protons and neutrons, together known as nucleons, which were considered to be elementary particles until the 1950s. For all we know today, nucleons are composed of more basic constituents called quarks, bound together by the exchange of gluons.

Electrons are elementary particles and interact with others mostly through electromagnetic interaction which is described by an extremely precise theory, Quantum Electrodynamics (QED). Meanwhile, quarks and gluons are also elementary particles governed by the theory of strong interactions, Quantum Chromodynamics (QCD). The understanding of how QCD works in detail remains an outstanding problem in physics.

QED describes the interaction of charged particles in terms of the exchange of photons, which are electrically neutral. In contrast, QCD attributes the strong forces among quarks and gluons to their color charge. The fact that gluons carry color charge causes the gluons to interact with each other. QCD exhibits two main characteristics: color confinement and asymptotic freedom.

Color confinement is the phenomenon that color charged quarks and gluons cannot be isolated from their bound state, namely hadron. As the distance increases, the strong coupling constant becomes extremely large and the strong force binds them within the hadron. Even if high enough external energy is given to be able to separate a single quark or gluon, it would be bound with new quarks and gluons created by the external energy and produce a new hadron. This hadronization process also occurred shortly after the Big Bang when quarks and gluons cooled into hadrons with several simple structural properties.

Asymptotic freedom is the phenomenon that quarks behave as free particles at extremely short distances. In other word, the strong coupling constant is very small at high energy. In this case, accurate perturbative calculations are allowed as in QED.

In the non-perturbative regime of QCD, the most well established and promising theory at present is the lattice QCD, opening an exciting field and being progressing fast. By evaluating QCD numerically on a discretized space–time Euclidean lattice, it provides predictions for some category of non-perturbative objects. Practically, the complex quark and gluon structure of the nucleon in its non-perturbative regime is parametrized by the structure functions. They are mainly measured through lepton scattering due to the structureless nature of leptons and accurate description of QED. For instance, Form Factors (FFs) have been measured by elastic scattering and Parton Distribution Functions (PDFs) through Deep Inelastic Scattering (DIS).

Unifying Form Factors and Parton Distribution Functions, a new type of structure functions named Generalized Parton Distributions (GPDs) have emerged over the 1990s. With richer information about the partons (*i.e.* quarks and gluons) within the nucleon embedded in GPDs, they become one of the most powerful tools to study nucleon struc-

ture.

The GPDs are accessed mainly in Deep Exclusive Scattering (DES), *i.e.* the exclusive leptoproduction of a photon or a meson on the nucleon. The simplest and the theoretically cleanest process is Deeply Virtual Compton Scattering (DVCS). Since the beam spin asymmetry measurements at HERMES and CLAS at the beginning of the 2000s, a series of DVCS experiments have been followed and impressive progress has been made, gradually providing a deeper understanding of the nucleon structure.

However, the DVCS process has a restriction by its nature for the direct measurement of GPDs. Further GPDs information requires other processes, particularly the Double Deeply Virtual Compton Scattering (DDVCS), subject of the present studies. This thesis presents the DDVCS theoretical framework, the model-predicted experimental projections including an ideal configuration and the large acceptance detector SoLID (Solenoidal Large Intensity Device), and develops a scheme to extract GPDs information from simulated pseudo data. The text is organized as follows:

- Chapter 1 briefly reviews the theoretical and experimental aspects of nucleon structure functions. In particular, the theoretical framework of GPDs and the VGG model based on double distributions are introduced, as well as the golden DVCS channel accessing GPDs. The DDVCS process is concisely described in terms of its benefits and difficulties by the end of this chapter.

- Chapter 2 introduces the theoretical framework for the DDVCS process, including kinematics and cross section. The formalism of the 7-fold differential cross section is then introduced, followed by two kinds of 5-fold differential cross section integrated over the angles. By the end of the chapter, the experimental observables in terms of the 5-fold cross section are presented.

- Chapter 3 presents the model-predicted observables in some specific kinematical scenarios, including the azimuthal dependence of the cross section and their azimuthal moments. The sensitivities to GPDs are discussed by the end of the chapter.

- Chapter 4 presents the approach for the DDVCS events generation, the binning based on the distribution of the events and the expected observables in an ideal situation.

- Chapter 5 presents the realistic projections with specific experimental setups. The feasibility of the experiments with the small acceptance detector SHMS (Super High Momentum Spectrometers) is firstly discussed, followed by the expected observables with the large acceptance detector SoLID (Solenoidal Large Intensity Device).

- Chapter 6 introduces two different methods for the extraction of GPDs information from DDVCS data. The performances of the methods applied to the simulated pseudo-data are also presented.

Chapter 1

Accessing nucleon structure via DDVCS

1.1 Nucleon structure functions

Nucleons have been thought to be elementary particles, namely point-like, fundamental particles that do not consist of any other particles. In the period from 1953 to 1956, the first explicit evidence of the extented nature of the proton was obtained through elastic electron proton scattering at Stanford [1]. Nucleon Form Factors, which can be related to the spatial distribution of charges in the nucleon, have been introduced for interpreting elastic *ep* cross section ever since. The project leader, Robert Hofstadter, was awarded the Nobel Prize in 1961 "for his pioneering studies of electron scattering in atomic nuclei and for his thereby achieved discoveries concerning the structure of the nucleons".

With the development of accelerator technology, the beam energy has significantly improved. It has been observed that as the momentum transfer increases, the cross section rapidly decreases compared to elastic elctron scattering. At sufficiently large momentum transfer, Deep Inelastic Scattering where nucleons break up becomes dominant. From the beginning of 1967 at SLAC, experiments with GeV electron beam energy was conducted on a target consisting either of liquid hydrogen or of deuterium. In contrast to elastic scattering, a scaling behavior was observed, which is the phenomenon that the cross section at large momentum transfer is almost independent on the momentum transfer [2]. This so-called Bjorken scaling demonstrated the presence of point-like charged constituent within the nucleons, which were named "partons" by Feynman before quarks and gluons were generally accepted. Parton Distribution Functions describing the momentum distribution of the quarks within the nucleon have been introduced. The 1990 Nobel prize was awarded to Friedman, Kendall and Taylor "for their pioneering investigations concerning deep inelastic scattering of electrons on protons and bound neutrons, which have been of essential importance for the development of the quark model in particle physics".

FFs and PDFs have been measured for around half a century but are still an intense subject of investigation. Despite these extraordinary achievements, a complete understanding of the nucleon internal structure was still inaccessible. For example, FFs integrate over the information related to the dynamics of partons inside nucleons and PDFs do not provide information about their spatial distributions. In order to have a stronger theoretical tool revealing the mystery of nucleon structure, especially the spin structure, the formalism of Generalized Parton Distributions has been introduced in the mid-1990s [3, 4, 5, 6, 7]. Encoding the correlations between transverse spatial distribu-

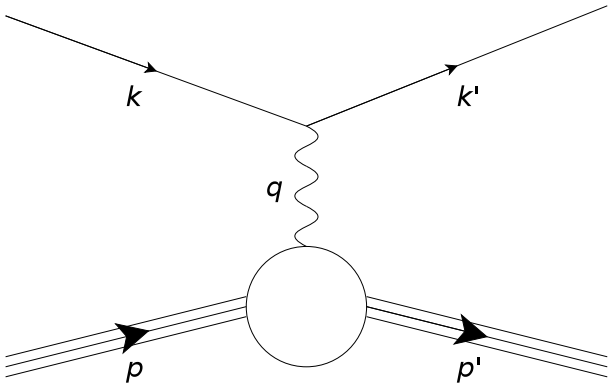

Figure 1.1: Feynman diagram relative to the one photon exchange approximation of the electron nucleon elastic scattering.

tions and longitudinal momentum distributions of partons inside the nucleon, GPDs allow a 3-dimensional imaging of the nucleon. As a result of these position-momentum correlations, GPDs provide a way to measure the unknown orbital momentum contribution of quarks to the total spin of the nucleon through Ji's sum rule [4]. They also enable indirect access to one of the gravitational form factors encoding the shear forces and pressure distribution on the quarks in the proton [8, 9, 10].

1.1.1 Form Factors and Parton Distribution Functions

Elastic scattering and Form Factors

The electron nucleon elastic scattering $eN \to eN$, where N represents either a proton or a neutron, can be described in terms of a single virtual photon exchange process (Born term) in the lowest-order approximation, as shown in Fig. 1.1. This approximation is expected to offer an accurate description due to the small coupling constant of the electromagnetic interaction. In this case, the elastic scattering is characterized by the squared four-momentum transferred to the nucleon $q^2 = (k - k')^2 = (p' - p)^2$, where $k(E, \boldsymbol{k})$, $k'(E', \boldsymbol{k'})$, p, p' are the four-momenta of the incident and scattered, electron and nucleon, respectively. The virtuality of the exchanged photon defined as $Q^2 = -q^2$ can be thought as the resolution or the scale with which one probes the internal structure of the nucleon. With larger Q^2, smaller structure can be observed.

The laboratory frame differential cross section for the detection of the electron in elastic scattering writes

$$\frac{d\sigma}{d\Omega} = \left(\frac{d\sigma}{d\Omega}\right)_{\text{Mott}} \left\{ F_1^2(Q^2) + \tau \left[F_2^2(Q^2) + 2\left[F_1(Q^2) + F_2(Q^2)\right]^2 \tan^2\frac{\theta_e}{2} \right] \right\} \tag{1.1}$$

where $\tau = Q^2/4M^2$ with M being the nucleon mass, and θ_e is the polar angle between the beam and the scattered electron. The Mott cross section for elastic scattering from a point-like nucleon reads

$$\left(\frac{d\sigma}{d\Omega}\right)_{\text{Mott}} = \frac{\alpha^2 \cos^2(\theta_e/2)}{4E^2 \sin^4(\theta_e/2)} \frac{E'}{E}, \tag{1.2}$$

where the fraction E'/E is the energy correction from the recoil nucleon. $F_1(Q^2)$ and $F_2(Q^2)$ are the Dirac and Pauli Form Factors, which are the only structure functions allowed in the Born term by relativistic invariance.

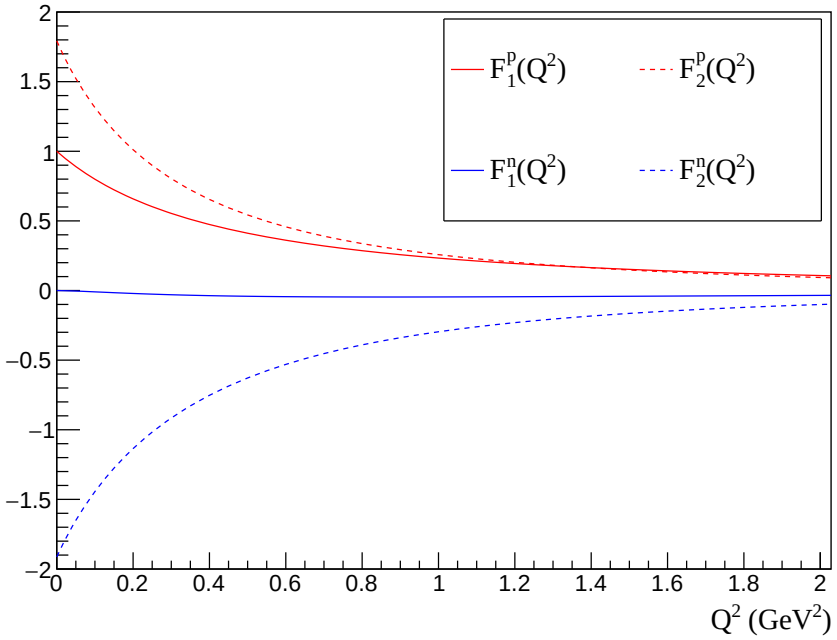

Figure 1.2: Dirac and Pauli Form Factors. The red curves correspond to the proton and the blue ones to the neutron; the solid curves stand for $F_1(Q^2)$ and the dashed ones for $F_2(Q^2)$.

In the static limit, $Q^2 = 0$, Dirac Form Factor represents the proton (p) or neutron (n) electric charge: $F_1^p = 1$, $F_1^n = 0$, while Pauli Form Factor equals to the anomalous magnetic moment: $F_2^p = 1.79$, $F_2^n = -1.91$. Fig. 1.2 shows the Form Factors as functions of Q^2 evaluated by adopting the extended Gari-Krüpelmann model (GKex02S) [11].

Experimental cross section data are most easily analysed in terms of another set of Form Factors, the Sachs Form Factors $G_E(Q^2)$ and $G_M(Q^2)$, also named electric and magnetic form factor, respectively. They are related with $F_1(Q^2)$ and $F_2(Q^2)$ following

$$\begin{aligned} G_E^i(Q^2) &= F_1^i(Q^2) - \tau F_2^i(Q^2), \\ G_M^i(Q^2) &= F_1^i(Q^2) + F_2^i(Q^2), \end{aligned} \tag{1.3}$$

where i is the index referring to the the nucleon type ($i = p, n$). The cross section can be rewritten in terms of the Sachs Form Factors in a simpler form, without an interference term, serving the separation method of $G_E^2(Q^2)$ and $G_M^2(Q^2)$ known as the Rosenbluth technique:

$$\frac{d\sigma}{d\Omega} = \left(\frac{d\sigma}{d\Omega}\right)_{\text{Mott}} \frac{1}{1+\tau}\left[G_E^2(Q^2) + \frac{\tau}{\epsilon}G_M^2(Q^2)\right], \tag{1.4}$$

where ϵ is the longitudinal polarization degree of the virtual photon defined as

$$\epsilon = \frac{1}{1 + 2(1+\tau)\tan^2(\theta_e/2)}. \tag{1.5}$$

Taking advantage of the linear dependence on ϵ in the reduced cross section, which reads

$$\sigma_{\text{red}} = \frac{\epsilon(1+\tau)}{\tau}\left(\frac{d\sigma}{d\Omega}\right) \Big/ \left(\frac{d\sigma}{d\Omega}\right)_{\text{Mott}} = \frac{\epsilon}{\tau}G_E^2(Q^2) + G_M^2(Q^2), \tag{1.6}$$

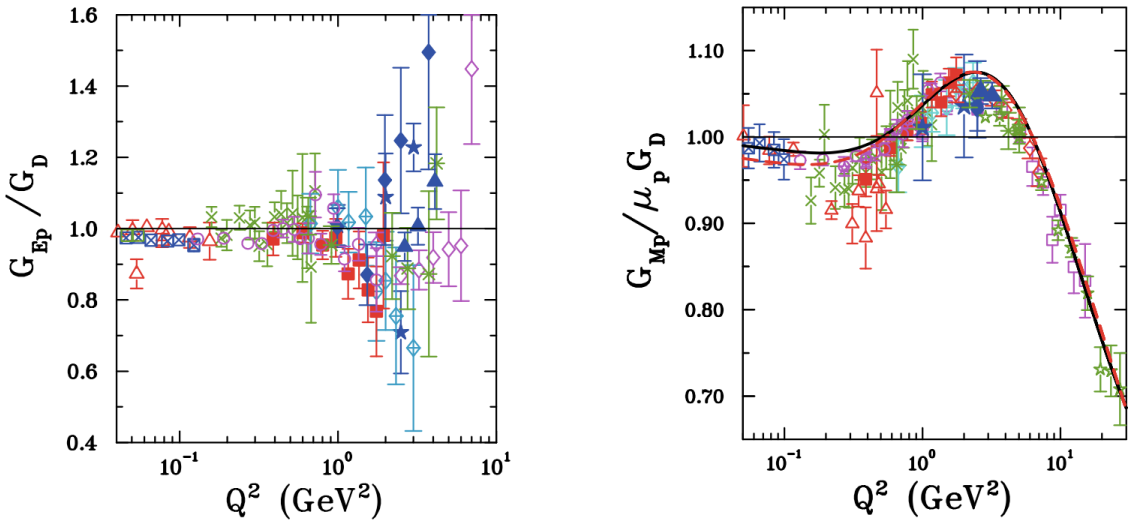

Figure 1.3: The proton Form Factors extracted from worldwide cross section measurements as functions of Q^2. The figure is extracted from [13].

the Rosenbluth separation technique indicates that the slope of the linear relation is proportional to $G_E^2(Q^2)$ and the intercept equals to $G_M^2(Q^2)$.

The two Sachs Form Factors, $G_E(Q^2)$ and $G_M(Q^2)$, required to describe the nucleon charge and magnetization distribution have been traditionally obtained by cross section measurements and more recently from polarization observables. In the static limit, the proton and neutron magnetic Form Factors $G_M^p(0)$ and $G_M^n(0)$, are equal to their magnetic moments, μ_p and μ_n, while the proton and neutron electric Form Factors $G_E^p(0)$ and $G_E^n(0)$, are equal to their electric charge. The earliest experiments at low Q^2 found

$$G_E^p(Q^2) \approx \frac{G_M^p(Q^2)}{\mu_p} \approx \frac{G_M^n(Q^2)}{\mu_n} \approx G_D(Q^2),$$

where $G_D(Q^2)$ is the dipole parameterization approximately characterizing the Q^2-dependence of these Form Factors:

$$G_D(Q^2) = \left(1 + \frac{Q^2}{0.71}\right)^{-2}, \quad Q^2 \text{ in GeV}^2. \tag{1.7}$$

$G_E^n(Q^2)$ can also be roughly described by the dipole model at low Q^2 following

$$G_E^n(Q^2) = -\frac{\mu_n \tau}{1 + 5.6\tau} G_D(Q^2), \tag{1.8}$$

which was deduced from fits of low Q^2 experimental data [12].

The data for $G_M^p(Q^2)$ have good consistency between different experiments up to 30 GeV^2, however, the determination of $G_E^p(Q^2)$ at Q^2 larger than 2 GeV^2 has suffered from large error bars, as shown in Fig. 1.3. The neutron electric form factor, $G_E^n(Q^2)$, is small and difficult to extract from cross section experiments. All these difficulties originated from the theoretical direction of cross section experiments, the Rosenbluth separation technique. New experimental methods using spin observables were needed which pushed the development of polarized targets and new accelerators with high duty factor and polarized electron beams. Let me introduce a recent review [13] with respect to the elastic scattering and electromagnetic Form Factors.

Proton charge radius

The determination of the proton charge radius R_E from the proton electric Form Factor measured experimentally through the elastic scattering of electrons off protons is the subject of an intense scientific activity. According to the definition

$$R_E = \sqrt{-6\frac{dG_E^p(Q^2)}{dQ^2}\bigg|_{Q^2=0}}, \tag{1.9}$$

the experimental method to determine R_E consists in the evaluation of the derivative of the electric Form Factor of the proton $G_E(Q^2)$ at zero-momentum transfer.

Within a non-relativistic ($Q^2 \ll 4M^2$) description of the internal structure of the proton, one can interpret the Form Factors in terms of the Fourier transforms of the nucleon charge and magnetization distributions:

$$G_{E,M}(Q^2) \approx G_{E,M}(\boldsymbol{q}^2) = \int_0^\infty e^{i\boldsymbol{q}\cdot\boldsymbol{r}}\rho(\boldsymbol{r})d^3\boldsymbol{r}, \tag{1.10}$$

where $\rho(\boldsymbol{r})$ is either the electric or the magnetic spatial distribution function. At $Q^2 = 0$, $G_{E,M}(0) = \int \rho(\boldsymbol{r})d^3\boldsymbol{r}$ represents the nucleon charge or magnetic moments as mentioned previously. Particularly, let us focus on the proton charge distribution. The MacLaurin expansion of the electric Form Factor $G_E^p(Q^2)$ writes

$$G_E^p(Q^2) = \sum_{n=0}^{\infty}\frac{(-1)^n}{(2n+1)!}\langle r^{2n}\rangle_E\, Q^{2n} = 1 - \frac{1}{6}\langle r^2\rangle_E\, Q^2 + \frac{1}{120}\langle r^4\rangle_E\, Q^4 + \cdots, \tag{1.11}$$

where

$$\langle r^{2n}\rangle_E = (-1)^n\frac{(2n+1)!}{n!}\frac{d^nG_E^p(Q^2)}{d(Q^2)^n}\bigg|_{Q^2=0} \tag{1.12}$$

relates the electric Form Factor to the even moments $\langle r^{2n}\rangle_E$ of the charge density $\rho_E(\boldsymbol{r})$

$$\langle r^{2n}\rangle_E \equiv 4\pi\int_0^\infty \boldsymbol{r}^2\boldsymbol{r}^{2n}\rho_E(\boldsymbol{r})d\boldsymbol{r}. \tag{1.13}$$

Consequently, the non-relativistic charge radius of the proton, namely the root-mean-square (rms) radius, can be expressed as

$$R_E = \sqrt{\langle r^2\rangle_E}. \tag{1.14}$$

Experimentally, R_E can be extracted by fitting the first few terms of the above MacLaurin expansion of the Form Factor to the world experimental data at low Q^2. However, the proton charge radius has been suffered from a substantial discrepancy between two different measurements: the elastic electron proton scattering and the spectroscopy of muonic hydrogen atoms. The first measurement using muonic hydrogen atoms [14] found a 5-σ discrepancy compared with previous results [15], which became known as the proton radius puzzle. The most recent R_E obtained from the high-precision elastic scattering experiment (PRad) at Hall B of Jefferson Laboratory [16] supported the highly accurate results from muonic hydrogen experiments. Because no convincing explanation for the discrepancy has been proposed, further efforts will be pursued to validate the latest results and to critically assess the different measurement techniques.

Similar relations hold for the magnetic form factor $G_M^p(Q^2)$ and the proton magnetic radius R_M. However, the determination of the magnetic radius is more challenging because the contribution of $G_M^p(Q^2)$ to the cross section is, at low Q^2, suppressed by the factor τ as shown in Eq. (1.4).

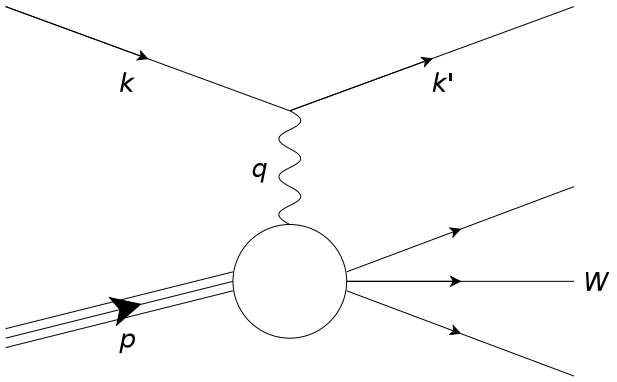

Figure 1.4: Feynman diagram relative to the one photon exchange approximation of DIS.

Deep Inelastic Scattering and Parton Distribution Functions

The electron nucleon inclusive scattering, also called Deep Inelastic Scattering, can be expressed by $eN \to eX$ where X stands for an undefined final state. Fig. 1.4 shows the process in the one photon exchange approximation, where W is the invariant mass of the recoiling target system X. W is defined as

$$W^2 = (p+q)^2 = M^2 + 2M\nu - Q^2, \tag{1.15}$$

where $\nu = E - E'$ is the electron energy loss.

On the assumption of one photon exchange, the differential cross section for Deep ($Q^2 \gg M^2$) Inelastic ($W^2 \gg M^2$) Scattering in which only the electron is detected is given by

$$\frac{d^2\sigma}{d\Omega dE'} = \left(\frac{d\sigma}{d\Omega}\right)_{\text{Mott}} \left[W_2(\nu, Q^2) + 2W_1(\nu, Q^2)\tan^2\frac{\theta_e}{2}\right]. \tag{1.16}$$

This expression is analogous to the Rosenbluth cross section given by Eq. (1.4) but the energy correction E'/E in Eq. (1.2) shall be removed for the Mott cross section in Eq. (1.16). The two structure functions W_1 and W_2 are functions of ν and Q^2 summarizing all the information about the structure of the nucleons obtained by scattering unpolarized electrons from an unpolarized nucleon target.

A scaling behavior had been predicted by Bjorken [17] for the DIS process before it was verified by the subsequent experiments. In the Bjorken limit ($Q^2 \to \infty$, $\nu \to \infty$ and fixed Q^2/ν), the DIS cross section has the signature of the Q^2-independence, namely the absence of a scale in the process, which is know as "scaling". The structure functions W_1 and W_2 become functions of a Bjorken variable only:

$$MW_1(\nu, Q^2) = F_1(x_{\text{B}}), \tag{1.17}$$

$$\nu W_2(\nu, Q^2) = F_2(x_{\text{B}}), \tag{1.18}$$

where the Bjorken variable writes

$$x_{\text{B}} = \frac{Q^2}{2p\cdot q} = \frac{Q^2}{2M\nu}. \tag{1.19}$$

$x_{\text{B}} = 1$ ($Q^2 = 2M\nu$) corresponds to the elastic scattering. The accumulation of DIS data for more than 50 years shows that the scaling begins to be valid already at $Q^2 \approx 1$ GeV^2.

As we have already seen in the process of elastic scattering, an object with a finite size should have Q^2-dependent Form Factors describing its structure. Thus, the Bjorken

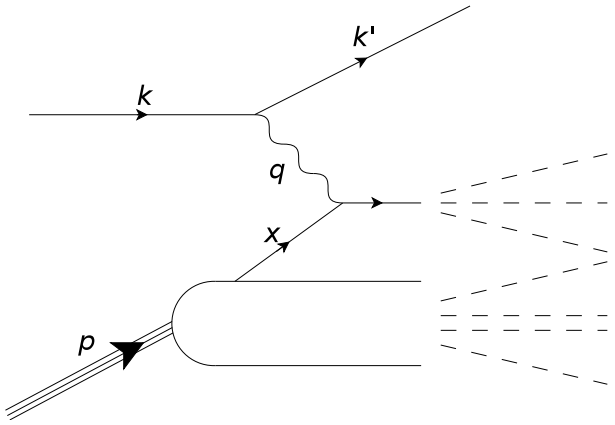

Figure 1.5: The DIS process in the Bjorken limit: the photon interacts with a single quark of the nucleon. The struck quark escapes the nucleon and hadronizes in an undetermined final state.

scaling in the DIS gives evidence on the behavior of point-like, charged particles within the nucleon, which are called "partons" in Feynman's parton model [18]. The model assumes an infinite momentum frame of reference and no interaction among the partons while the virtual photon is exchanged. Therefore, electrons scattered from "free" partons and the scattering reflects the properties and motions of the partons. This assumption was subsequently shown to be a consequence of QCD known as asymptotic freedom [19, 20]. Moreover, the Callan-Gross relation,

$$F_2(x_{\mathrm{B}}) = 2x_{\mathrm{B}}F_1(x_{\mathrm{B}}), \tag{1.20}$$

was verified experimentally, proving that the partons are particles with a spin of 1/2, *i.e.* the well-known "quarks" inside nucleon.

In the Bjorken limit, the nucleon can be thought as a collection of non-interacting point-like quarks, one of which carries a fraction x of the total longitudinal momentum of the nucleon and interacts with the photon exchanged between the electron and the nucleon in the DIS process, as shown in Fig. 1.5. Since the mass of the scattered quark is negligible compared with Q^2 and ν, one has

$$(xp + q)^2 = 2xp \cdot q - Q^2 \simeq 0. \tag{1.21}$$

Thus, the momentum fraction x simply equals to the Bjorken variable x_{B} in the DIS case:

$$x = \frac{Q^2}{2p \cdot q} = x_{\mathrm{B}}. \tag{1.22}$$

We can define a function $q(x)$ representing the probability that the nucleon contains a quark of the flavor q inside a fast-moving nucleon, and carries a fraction x of its longitudinal momentum. The DIS cross section can be calculated by combining probabilities and the structure function F_2 therefore can be expressed by

$$F_2(x) = x\sum_q e_q^2 q(x), \tag{1.23}$$

where e_q is the electric charge of the quark q. The functions $q(x)$ are so-called Parton Distribution Functions (PDFs) and can be accessed by measuring $F_1(x)$ and $F_2(x)$ in DIS experiments.

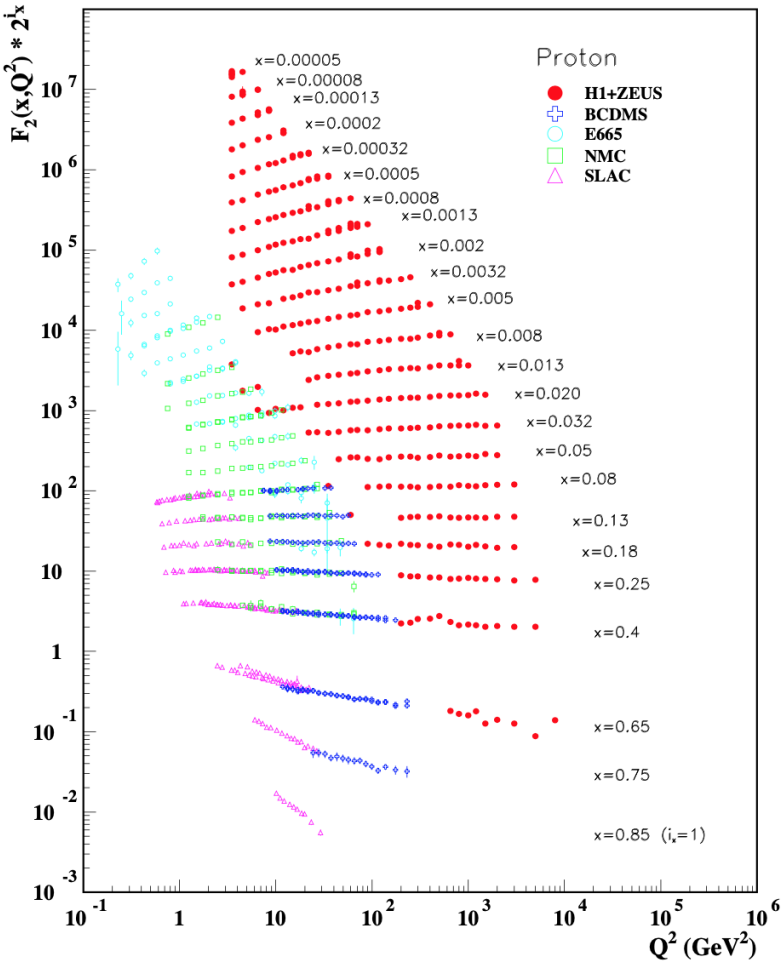

Figure 1.6: The proton structure function F_2 as a function of Q^2 in bins of fixed x. The figure is extracted from [21].

PDFs are still an intense subject of investigation. The scaling property is related to the assumption that the transverse momentum of the partons in the infinite momentum frame of the proton is small. In QCD, however, the radiation of gluons from the quarks violates this assumption, leading to logarithmic scaling violations, which are particularly large at small x, as shown in Fig. 1.6. The radiation of gluons produces the evolution of the structure functions, *i.e.* the variation with Q^2. As Q^2 increases, more and more gluons are radiated, which in turn split into quark-antiquark ($q\bar{q}$) pairs. This process leads both to the softening of the initial quark momentum distributions and to the growth of the gluon density and the $q\bar{q}$ sea as x decreases. The behavior of PDFs at large x is still a mystery and needs understanding.

Factorization

The complex quark and gluon structure of the nucleon, governed by QCD, in its non-perturbative regime is not applicable to the powerful method of perturbative QCD (only just starting to be extracted in lattice QCD in a phenomenologically relevant way), nor is any other cross section that involves initial-state hadrons. The structure functions (FFs or PDFs) are determined from experimental data. One uses a procedure known as QCD factorization where one separates a point-like, short-distance, "hard" subprocess, from the

complex, long-distance, "soft" structure of the nucleon. Thus, the hard subprocess is then perturbatively computable and the soft long-distance physics is encoded into structure functions. As in the DIS process (Fig. 1.5), the hard subprocess of the photon-quark interaction implies short distances (large Q^2) and short time (large energy ν), occupying a very small space-time volume. On the other hand, the scales involved in the formation of the hadron non-perturbative wave function are much larger, of the order of a typical hadronic scale (1 GeV). Hence, the two scales are uncorrelated and will not interfere. Thus, although the process depends on the hadronic state from which a given constituent has come, this is basically irrelevant for the hard interactions. All information about long-distance physics is encoded into PDFs reflecting the soft internal structure of the nucleon.

Since the number of quarks carrying the bulk of the nucleon momentum is small, the photon is usually absorbed by one quark per collision. The probability for coherent scattering on an n-quark configuration is suppressed by n^{th} power of the photon virtuality [22],

$$\mathcal{P}_n \sim \left(\frac{|\delta \boldsymbol{z}_\perp|^2}{\pi R_N^2}\right)^n \sim \frac{1}{(Q^2 \pi R_N^2)^n} \ . \tag{1.24}$$

The transverse distance probed by the virtual photon in the nucleon is of order $\delta \boldsymbol{z}_\perp \sim 1/Q$, and πR_N^2 is the transverse area of the nucleon. These power-suppressed corrections are named higher twists. Thus, in "leading twist" approximation at high Q^2, one can restrict all considerations to the photon scattering on a single quark, as shown in Fig. 1.5 for the DIS process. Conventionally, the leading twist is also called twist-2 and higher twist-$(m+2)$ corrections are suppressed in powers of $(1/Q)^m$ with respect to the twist-2. In addition, the QCD strong coupling constant α_s decreases when Q^2 increases. When $\alpha_s \ll 1$ allowing perturbation theory techniques to be applied, the amplitude of a "hard" process can be expressed as a series in powers of α_s. In principle to calculate the amplitude, one is supposed to draw and calculate all of the infinite number of possible Feynman diagrams and add them up to get the total amplitude. The leading order (LO) term is described by a single tree-level Feynman diagram, such as Fig. 1.1 for the elastic scattering and Fig. 1.5 for the DIS process. Higher order corrections are suppressed by powers of α_s with respect to the leading order, which are called next-to-leading order (NLO) corrections, next-to-next-to-leading order (NNLO) corrections, etc. The leading order and the leading twist approximation will be kept in the bulk of this document.

In summary, in the electron nucleon scattering the nature of the interaction of the virtual photon with the nucleon depends strongly on wavelength. At very low electron energies, the scattering is equivalent to that from a "point-like" object. At low electron energies, the scattering is equivalent to that from an extended charged object. At high electron energies, the wavelength is sufficiently short to resolve sub-structure, *i.e.* constituent quarks. At very high electron energies the nucleon appears to be a sea of quarks and gluons.

1.1.2 Generalized Parton Distributions

Although FFs and PDFs have been precisely measured and have allowed remarkable progress for the understanding the nucleon structure, there are still questions that cannot be answered by these quantities. A new avenue in the study of nucleon structure opened up in the last decade of 20th century with the investigation of exclusive electroproduction

processes. One significant concept called Generalized Parton Distributions (GPDs) was introduced, in which the three-dimensional structure of nucleons is embedded.

GPDs are four universal factorizing structure functions H^q, E^q, $\widetilde{H}^q$ and $\widetilde{E}^q$, describing, at leading twist level, the non-perturbative quark structure of the nucleon [3, 4, 5, 6, 7]. Each GPD is defined for a given quark flavor $q = u, d, s, \cdots$. Omitting the Q^2-dependence associated with QCD evolution equation, GPDs depend on three parameters: x, ξ and t. x is the average longitudinal momentum fraction of the quark, ξ is the transferred longitudinal momentum fraction or skewness parameter, and t is the squared momentum transfer between the final nucleon and the intial one, namely $t = \Delta^2 = (p' - p)^2$. x varies between -1 and 1 and ξ in principle also between with -1 and 1 but, due to time reversal invariance, the range of ξ is reduced between 0 and 1. If $x > \xi$, GPDs correspond to the probability amplitude of picking a quark (or an antiquark if $x < -\xi$) of momentum fraction $x + \xi$ from the nucleon and inserting it back with a different momentum fraction $x - \xi$ plus some transverse momentum represented by t, as illustrated in Fig. 1.7. The remaining region $-\xi < x < \xi$ implies finding a quark (positive momentum fraction) and putting back an antiquark (negative momentum fraction). In this region, the GPDs behave like a meson distribution amplitude and can be interpreted as the probability amplitude of finding a quark-antiquark pair in the nucleon. This kind of information on $q\bar{q}$ configurations in the nucleon and, more generally, the correlations between quarks (or antiquarks) of different momenta are relatively unknown and reveal the richness and novelty of the GPDs.

The GPDs H and E correspond to averages over the quark helicity. They are therefore called unpolarized GPDs. The GPDs $\widetilde{H}$ and $\widetilde{E}$ involve differences of quark helicities and are called polarized GPDs. At the nucleon level, E and $\widetilde{E}$ are associated with a flip of the nucleon spin while H and $\widetilde{H}$ leave it unchanged. The four GPDs therefore reflect the four independent helicity-spin combinations of the quark-nucleon system. These are illustrated in Fig. 1.8.

Fig. 1.8 shows only the quark helicity conserving GPDs. When the quark helicity is flipped, one defines "transversity" GPDs H_T, E_T, $\widetilde{H}_T$ and $\widetilde{E}_T$. However, they are not in the discussion of this document. In addition, the gluon GPDs (can be simply represented by finding a gluon instead of a quark and putting it back in Fig. 1.8) in principle have a small impact in the valence region at moderate energy. Although recent research [23, 24] indicates that gluon contributions may not be negligible, gluon GPDs do not come within the scope of the present study.

The present studies concern the Double Deeply Virtual Compton Scattering (DDVCS) process within the context of 12 GeV upgrades of the Continuous Electron Beam Accelerator Facility at the Jefferson Laboratory (JLab12). I therefore concentrate only on the valence region and GPDs in the following text refer to the four quark helicity conserv-

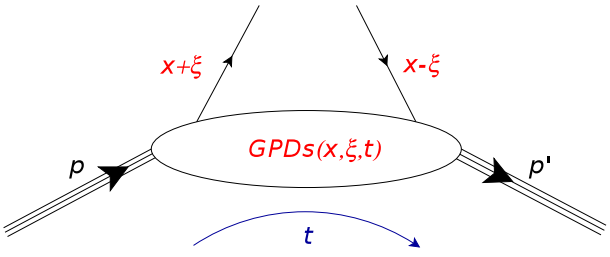

Figure 1.7: Symbolic representation of GPDs.

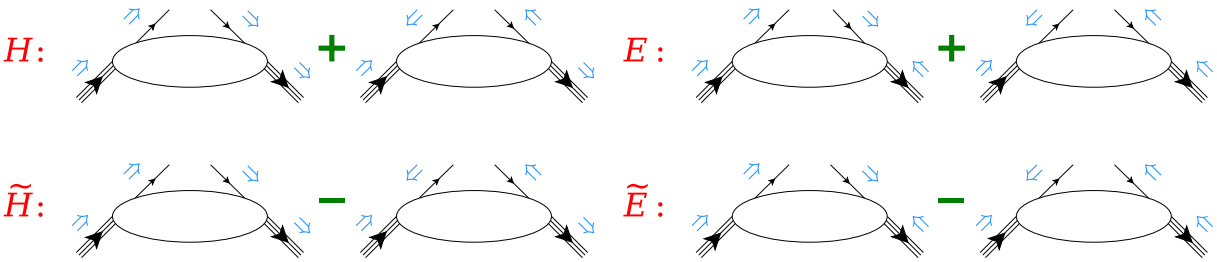

Figure 1.8: The various quarks helicity and nucleon spin orientations with respect to the four GPDs.

ing GPDs. For more details, see a recent review [25] about GPDs in the valence region. To study the matter dominated by gluons and sea quarks originating from gluons will require the higher energy and beam polarization of the future Electron Ion Collider (EIC) at Brookhaven National Laboratory (BNL), see the EIC White Paper [26] for more details.

Properties of GPDs

GPDs depend on two additional variables compared with PDFs and FFs. They are therefore a much richer source of nucleon structure information and have the characters of both PDFs and FFs.

In the forward limit (*i.e.* $\xi = 0$ and $t = 0$), corresponding to zero momentum transfer, some GPDs reduce to one-dimensional PDFs:

$$H^q(x, \xi = 0, t = 0) = q(x), \tag{1.25}$$
$$\widetilde{H}^q(x, \xi = 0, t = 0) = \Delta q(x), \tag{1.26}$$

where $q(x)$ and $\Delta q(x)$ are the unpolarized and polarized PDFs, respectively, obtained from DIS. The origin of these relations is the optical theorem and the symmetry of the forward Compton process (see Fig. 1.9), corresponding to zero four-momentum transfer, *i.e.* $\xi = 0$ and $t = 0$.

On the other hand, at finite momentum transfer, there are model-independent sum rules which relate the first moments of GPDs to the FFs:

$$\int_{-1}^{1} dx H^q(x, \xi, t) = F_1^q(t), \tag{1.27}$$
$$\int_{-1}^{1} dx E^q(x, \xi, t) = F_2^q(t), \tag{1.28}$$
$$\int_{-1}^{1} dx \widetilde{H}^q(x, \xi, t) = G_A^q(t), \tag{1.29}$$
$$\int_{-1}^{1} dx \widetilde{E}^q(x, \xi, t) = G_P^q(t), \tag{1.30}$$

where $F_1^q(t)$, $F_2^q(t)$, $G_A^q(t)$ and $G_P^q(t)$ are the contribution of the quark flavor q to the Dirac, Pauli, axial-vector and pseudo-scalar FFs, respectively. When referring to the quark FFs in the following, they are considered in the notation to be for the proton, e.g. $F_1^u(t) = F_1^{u/p}(t)$. In this notation, the proton (p) and nucleon (n) Dirac FFs are related

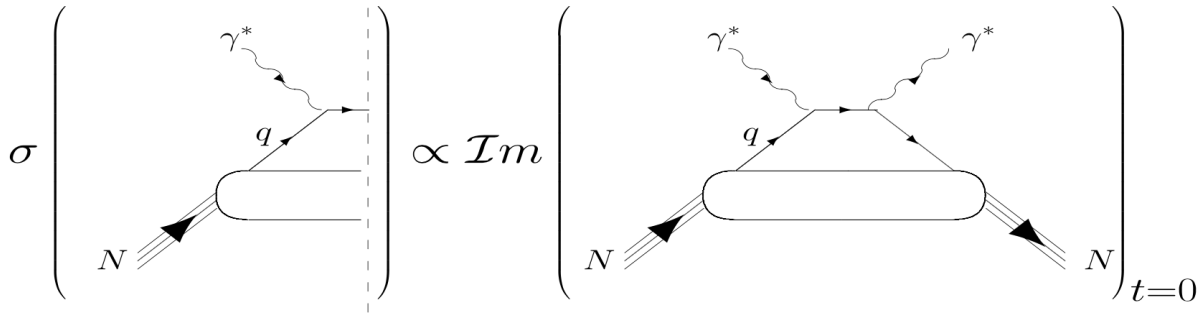

Figure 1.9: The optical theorem: the cross section of the DIS process is equal to the imaginary part of the forward double virtual Compton amplitude. The figure is extracted from [25].

to the quark FFs, neglecting strange quarks, as

$$\begin{aligned} F_1^p(t) &= \frac{2}{3}F_1^u(t) - \frac{1}{3}F_1^d(t), \\ F_1^n(t) &= \frac{2}{3}F_1^d(t) - \frac{1}{3}F_1^u(t). \end{aligned} \tag{1.31}$$

Similar relations hold for the Pauli FFs F_2^q.

It can be seen that the PDFs and the FFs appear as simple limits or moments of the GPDs. The correspondence of GPDs to PDFs and FFs presages a possibility of studying a spatial distribution of partons inside the nucleon. Actually, GPDs provide nucleon tomography allowing one to extract the density of partons carrying a given fraction x of the nucleon longitudinal momentum as a function of the position $\boldsymbol{b}_\perp$ in the plane perpendicular to the nucleon motion. For $\xi = 0$ (where $t = -\Delta_\perp^2$), meaning no change of the longitudinal momentum of the active parton, the density for unpolarized partons inside an unpolarized nucleon is expressed by:

$$q(x, \boldsymbol{b}_\perp) = \int \frac{d^2\boldsymbol{\Delta}_\perp}{4\pi^2} e^{-i\boldsymbol{b}_\perp \cdot \boldsymbol{\Delta}_\perp} H^q(x, 0, t). \tag{1.32}$$

Therefore, the zero-skewness GPDs can be interpreted as the probability of finding a parton with longitudinal momentum fraction x at a given transverse distance in the nucleon. In this way, the information contained in PDFs, as measured in DIS, and the information contained within FFs, as measured in elastic scattering, are combined and correlated in the GPDs description. This density gets distorted when the nucleon is polarized. This effect is described by adding extra expressions related to the GPDs $\widetilde{H}^q$ and E^q. For instance, the longitudinal polarization of partons distributed in a longitudinally polarized nucleon according to $q(x, \boldsymbol{b}_\perp)$ can be studied with the Fourier transform of GPD $\widetilde{H}^q$:

$$\Delta q(x, \boldsymbol{b}_\perp) = \int \frac{d^2\boldsymbol{\Delta}_\perp}{4\pi^2} e^{-i\boldsymbol{b}_\perp \cdot \boldsymbol{\Delta}_\perp} \widetilde{H}^q(x, 0, t). \tag{1.33}$$

Similar expression holds for the GPD E^q:

$$e^q(x, \boldsymbol{b}_\perp) = \int \frac{d^2\boldsymbol{\Delta}_\perp}{4\pi^2} e^{-i\boldsymbol{b}_\perp \cdot \boldsymbol{\Delta}_\perp} E^q(x, 0, t). \tag{1.34}$$

In this case, $e^q(x, \boldsymbol{b}_\perp)$ can be related to a shift of parton density generated in a transversely polarized nucleon [27].

As shown in Eqs. (1.27)-(1.30), GPDs are linked to FFs through the 0^{th} order Mellin moment, which is actually a particular case of a major property of GPDs known as polynomiality. The property expresses that the n^{th} order Mellin moment of a given GPD is always an even polynomial in ξ of order n (for even n) or $n+1$ (for odd n), e.g. for the GPD H:

$$\int_{-1}^{1} dx\ x^n H^q(x,\xi,t) = \begin{cases} h_0^{q(n)}(t) + \xi^2 h_2^{q(n)}(t) + \cdots + \xi^n h_n^{q(n)}(t) & \text{if } n \text{ is even,} \\ h_0^{q(n)}(t) + \xi^2 h_2^{q(n)}(t) + \cdots + \xi^n h_{n+1}^{q(n)}(t) & \text{if } n \text{ is odd.} \end{cases} \tag{1.35}$$

There are similar rules for the GPDs E^q, $\widetilde{H}^q$ and $\widetilde{E}^q$. The GPD E^q has the same coefficient $h_{n+1}^{q(n)}(t)$ as H but with the opposite sign. For the GPDs $\widetilde{H}^q$ and $\widetilde{E}^q$, the maximal ξ power is $n-1$ instead of $n+1$ when n is odd. The fact that only even powers of ξ appear is a consequence of the time reversal invariance which states that $H(x,-\xi,t) = H(x,\xi,t)$.

In particular, the 1^{th} order Mellin moments of the GPDs H and E:

$$\int_{-1}^{1} dx\ xH^q(x,\xi,t) = h_0^{q(1)}(t) + \xi^2 h_2^{q(1)}(t), \tag{1.36}$$

$$\int_{-1}^{1} dx\ xE^q(x,\xi,t) = e_0^{q(1)}(t) - \xi^2 h_2^{q(1)}(t), \tag{1.37}$$

lead to Ji's sum rule [4, 5], allowing for the evaluation of total angular momentum carried by quarks J_q:

$$\int_{-1}^{1} dx\ x\left[H^q(x,\xi,t=0) + E^q(x,\xi,t=0)\right] = h_0^{q(1)}(0) + e_0^{q(1)}(0) = 2J_q. \tag{1.38}$$

The ξ dependence drops out from the sum rule. As we know, nucleons have a spin of 1/2. However, we do not fully understand how the spin of nucleons is made up from its constituents, namely the so-called nucleon "spin puzzle" [28]. It was shown in [4] that there exists a gauge-invariant decomposition of the nucleon spin: $1/2 = J_q + J_g$, where J_g is the total gluon contributions to the nucleon total angular momentum. On one hand, the total quark spin contribution J_q decomposes into the quark spin ($\Delta\Sigma/2$) and quark orbital contributions (L_q) to the nucleon spin. $\Delta\Sigma$ has been measured through polarized DIS experiments, and its different determinations point to a value in the range 20-30%. On the other hand, for the gluons it is still an open question how to decompose the total angular momentum J_g into orbital angular momentum and gluon spin parts, in such a way that both can be related to observables. Nevertheless, GPDs provides a model-independent way for the determination of the quark orbital contribution to the nucleon spin through the sum rule and therefore completes the quark sector of the spin puzzle.

In addition, it is remarkable fact that the GPDs also enable indirect access to the basic mechanical properties of the nucleon encoded in the gravitational form factors (GFFs) of the energy-momentum tensor. In particular, the GPD H has the access to one of the GFFs through its 1^{th} order Mellin moment, which can be recast

$$\int_{-1}^{1} xH(x,\xi,t)dx = M_2(t) + \frac{4}{5}\xi^2 d_1(t). \tag{1.39}$$

The GFF $d_1(t)$ encodes the shear forces and pressure distribution on the quarks in the proton [8, 9, 10].

1.1.3 GPDs parameterization

There are a few parameterizations of GPDs such as models based on Double Distributions (DDs), the dual parameterization, etc. Here I introduce the VGG model. It is a model based on DDs, was firstly proposed by M. Vanderhaeghen, P. A. M. Guichon and M. Guidal [29], and developed as the field of GPDs grew and improved [30, 31, 32, 33].

Double Distributions

Double Distributions were originally introduced in [34, 35] and they provide an elegant guideline to parameterize the (x, ξ)-dependence of the GPDs. The idea of the DDs is to decorrelate the transferred momentum Δ from the initial nucleon momentum p (see Fig. 1.7). The link between a GPD and a DD,

$$\mathrm{GPD}^q_{\mathrm{DD}}(x,\xi) = \int_{-1}^{1} d\beta \int_{-1+|\beta|}^{1-|\beta|} d\alpha \; \delta(x-\beta-\xi\alpha)\mathrm{DD}^q(\beta,\alpha), \tag{1.40}$$

is only a change of variables through a linear relation $x = \beta + \xi\alpha$. The $\mathrm{DD}^q(\beta,\alpha)$ can be thought as the probability amplitude of finding a quark carrying a longitudinal momentum fraction β of the average nucleon momentum and a fraction $(1+\alpha)/2$ of the transferred momentum Δ. Because of the linear relation between x and ξ imposed by the δ function, the n^{th} order Mellin moment of Eq. (1.40) will always produce a ξ^n power, which automatically satisfies the polynomiality relation in Eq. (1.35). The DDs should fulfill the requirements at two limiting cases. Firstly, when $\Delta = 0$, namely $\xi = 0$, the β-dependence must contain the standard inclusive PDF $q(\beta)$, the forward limit of GPDs. Secondly, when the final nucleon momentum equals zero, the $\mathrm{DD}^q(\beta,\alpha)$ must take the shape of a distribution amplitude of mesons. A form which fulfills these requirements is

$$\mathrm{DD}^q(\beta,\alpha) = h(\beta,\alpha)q(\beta), \tag{1.41}$$

$$h(\beta,\alpha) = \frac{\Gamma(2b+2)}{2^{2b+1}\Gamma(2b+1)} \frac{[(1-|\beta|)^2-\alpha^2]^b}{(1-|\beta|)^{2b+1}}, \tag{1.42}$$

where $h(\beta,\alpha)$ is a profile function depending on one free parameter b. The higher the b value, the weaker the ξ-dependence for the GPD. For example, when $b \to \infty$, $h(\beta,\alpha) \to 1$ and the DD becomes a ξ-independent PDF. In principle, one can define a value for the valence, b_{val}, and another one for the sea, b_{sea}.

The the n^{th} order moment of GPDs built on DDs by Eq. (1.40) does not satisfy the polynomiality relation when n is odd. The so-called D-term $D(x/\xi, t)$ has been introduced in [36] to complete the parameterization for the missing power ξ^{n+1}. It can be decomposed in a Gegenbauer series as

$$D(z) = (1-z^2)\sum_{n=1}^{\infty} d_n C_n^{3/2}(z), \tag{1.43}$$

where only odd n appears in the sum. $z = x/\xi$ and varies from -1 to 1. The D-term receives the same contribution from each quark flavor. One can then define a D-term contribution for each quark flavor by the factor $N_f = 3$, denoting the number of light quark flavors (u, d, s), as

$$D^q(z) = \frac{1}{N_f} D(z). \tag{1.44}$$

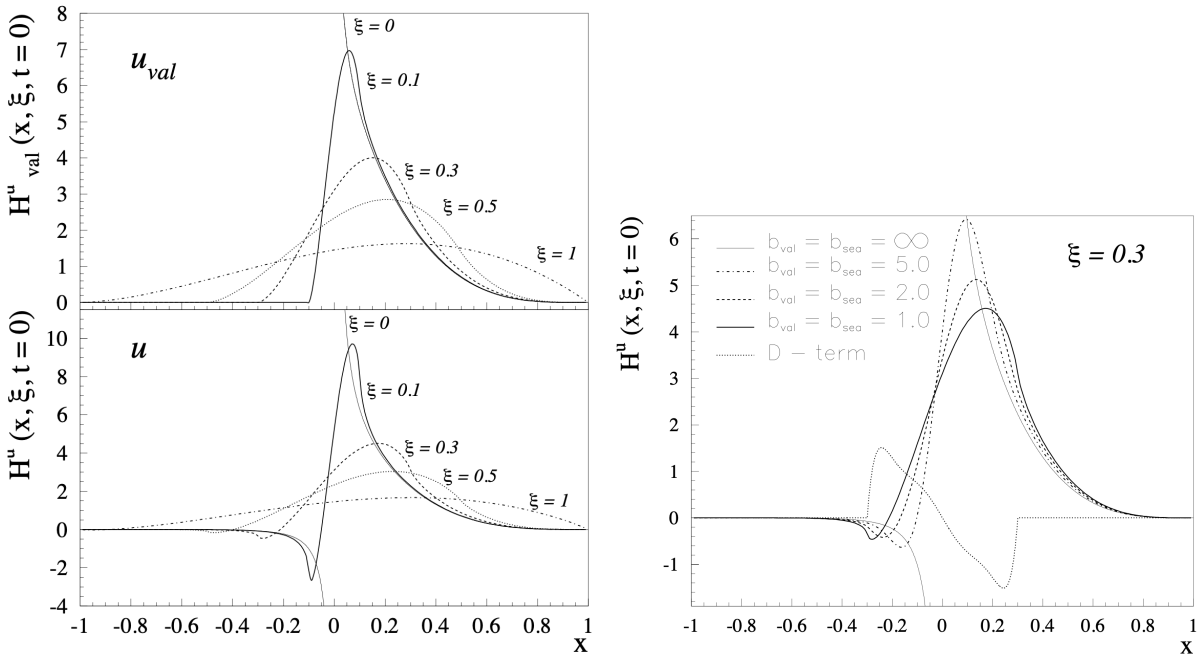

Figure 1.10: Left panels: Double Distribution part to the valence (top panel) and total (bottom panel) u-quark GPD H^u at $t = 0$ for different ξ and $b_{\rm val} = b_{\rm sea} = 1$. Right panel: Double Distribution part to the u-quark GPD H^u at $t = 0$ and $\xi = 0.3$ for different values of the parameters $b_{\rm val}$ and $b_{\rm sea}$. The figures are extracted from [31].

The left panels of Fig. 1.10 show the parameterization of Eqs. (1.40)-(1.42) for the DD part to the u-quark GPD H^u, for the parameter value $b_{\rm val} = b_{\rm sea} = 1$. It can be seen how the GPD approach the forward u-quark distribution as $\xi \to 0$. The right panel of Fig. 1.10 shows the dependence of the DD part to the u-quark GPD H^u on the parameters $b_{\rm val}$ and $b_{\rm sea}$. In the limit $b_{\rm val} = b_{\rm sea} = \infty$, one finds back the foward u-quark distribution.

VGG model and factorized t-dependence

VGG model is based on the DDs (+ D-term) ansatz for the (x, ξ)-dependence of the GPDs and offers the parameterization of the t-dependence. The main constraint on the t-dependence of GPDs comes from the sum rules of Eqs. (1.27)-(1.30), where the first moment of the GPDs is given by the FFs. The simplest factorization ansatz in the form of $H(x, \xi, t) = H(x, \xi)F_1(t)$ can be adopted in the small $-t$ region to parameterize the t-dependence of GPDs, which fulfills the sum rules at small $-t$. As for the hard exclusive reactions (DVCS and DDVCS) t should be a small scale compared to the hard scale Q^2 of the reaction, only the small $-t < 1$ GeV^2 region will be concerned by the present study.

(a) For the GPD H:

The complete t-independent part $H^q(x, \xi) = H^q(x, \xi, t = 0)$ is parameterized by a DD + D-term form as mentioned above:

$$H^q(x,\xi) = H^q_{\rm DD}(x,\xi) + \theta(\xi - |x|)\frac{1}{N_f}D(\frac{x}{\xi}), \tag{1.45}$$

where $H^q_{\rm DD}$ is given by the DD ansatz of Eqs. (1.40)-(1.42).

For the GPD H^q and for a quark of flavor q, the first moment is determined in terms of the Dirac Form Factor F_1^q for a quark of flavor q in the proton. In the

small $-t < 1$ GeV^2 region, the simplest parameterization of the t-dependence of $H^q(x,\xi,t)$ consists of a t-factorized ansatz:

$$\begin{aligned} H^u(x,\xi,t) &= H^u(x,\xi)F_1^u(t)/2, \\ H^d(x,\xi,t) &= H^d(x,\xi)F_1^d(t), \end{aligned} \tag{1.46}$$

where $F_1^u(t)$ and $F_1^d(t)$ are given by Eq. (1.31). Due to $F_1^p(0) = 1$ and $F_1^n(0) = 0$ as shown in Fig. 1.2, the u quark Form Factor at $t = 0$ is normalized as $F_1^u(0) = 2$ so as to yield the normalization of 2 for the PDF $u(x)$ in the proton, while the d quark Form Factor at $t = 0$ is normalized as $F_1^d(0) = 1$ so as to yield the normalization of 1 for the PDF $d(x)$ in the proton. The ansatz not only satisfies the sum rule constraint of Eq. (1.27), but also yields the correct forward limit for the PDFs:

$$H^u(x,0,0) = H^u(x,0) = u(x), \quad H^d(x,0,0) = H^d(x,0) = d(x). \tag{1.47}$$

Note that the sum rule of Eq. (1.27) only gives a constraint for the valence part of the GPD, as the sea contribution drops out of this sum rule. The t-dependence for the valence quark holds for the sea quark part in the VGG model. Moreover, the D-term is not at all constrained by this sum rule as it is odd in x. The t-dependence for the D-term is assumed to be the same as for the DD contribution to the GPD H^q in the VGG model.

(b) For the GPD E:

In order to guarantee that the D-term contribution is cancelled in the combination $H + E$. The D-term contributes with opposite sign to H and E. Therefore, the t-independent $E^q(x,\xi)$ is parameterized as

$$E^q(x,\xi) = E^q_{\rm DD}(x,\xi) - \theta(\xi - |x|)\frac{1}{N_f}D(\frac{x}{\xi}). \tag{1.48}$$

The parameterization of the DD part $E^q_{\rm DD}(x,\xi)$ is more difficult since no DIS constraint exists for the x-dependence. In the forward limit, $e^q(x) = E^q_{\rm DD}(x,0,0)$ is unknown except its first moment is given by the sum rule of Eq. (1.28) in terms of the Pauli Form Factor $F_2^q(0)$ for a quark of flavor q. The quark Form Factors $F_2^u(0)$ and $F_2^d(0)$ are normalized through the nucleon anomalous magnetic moments, *i.e.* $F_2^p(0) = \kappa^p = 1.79$ and $F_2^n(0) = \kappa^n = -1.91$. One can define $\kappa^u = F_2^u(0)$ and $\kappa^d = F_2^d(0)$ for the quarks and find

$$\kappa^u = 2\kappa^p + \kappa^n = 1.67, \quad \kappa^d = 2\kappa^n + \kappa^p = -2.03. \tag{1.49}$$

The sum rule of Eq. (1.28) then writes in the forward limit:

$$\int_{-1}^{1} dx\ e^q(x) = \kappa^q. \tag{1.50}$$

For the x-dependence of the forward distribution $e_q(x)$, a sum of valence and sea quark parameterization is implemented in the VGG model as

$$\begin{aligned} e^u(x) &= A^u u_{\rm val}(x) + B^u\delta(x), \\ e^d(x) &= A^d d_{\rm val}(x) + B^d\delta(x), \end{aligned} \tag{1.51}$$

where the parameter A^q is related to J^q by the Ji's sum rule as

$$A^q = \frac{2J^q - M_2^q}{M_2^{q_{\rm val}}}, \tag{1.52}$$

and the parameter B^q is given by the sum rule of Eq. (1.50). M_2^q ($M_2^{q_{\rm val}}$) is the total fraction of the proton momentum carried by the (valence) quarks and anti-quarks of flavor q. The total angular momenta carried by u and d quarks, J_u and J_d, enter now directly as free parameters in the parameterization.

For the ξ-dependence, the DD part $E^q_{\rm DD}(x,\xi)$ is generated also through the DD ansatz with the replacement of the unpolarized PDF $q(\beta)$ in Eq. (1.41) by the forward distribution $e^q(\beta)$.

The t-dependence of $E^q(x,\xi,t)$ is constrained through the first sum rule of Eq. (1.28) in terms of the Pauli Form Factor $F_2^q(t)$. In the small $-t$ region, the simplest parameterization satisfying this sum rule consists of a factorized ansatz

$$E^q(x,\xi,t) = E^q(x,\xi) G_D(t), \tag{1.53}$$

where $G_D(t)$ given by Eq. (1.7) is the dipole model of elastic Form Factors representing the t-dependence of E^q.

(c) For the GPD $\widetilde{H}$:

Based on the polynomiality of the polarized GPD $\widetilde{H}$ and $\widetilde{E}$, D-term does not necessarily enter in the parameterization of the (x,ξ)-dependence. Therefore, the DD part $\widetilde{H}^q(x,\xi)$ is directly parameterized through the DD ansatz with the replacement of the unpolarized PDF $q(\beta)$ in Eq. (1.41) by the polarized PDF $\Delta q(\beta)$.

Similarly, the t-dependence parameterization of $\widetilde{H}^q(x,\xi,t)$ which fulfills the sum rule of Eq. (1.29) is

$$\widetilde{H}^q(x,\xi,t) = \widetilde{H}^q(x,\xi) \frac{G_A^q(t)}{G_A^q(0)}, \tag{1.54}$$

(d) For the GPD $\widetilde{E}$:

As for the GPD E, no DIS constraint exists for the x-dependence of $\widetilde{E}$. However, in the chiral quark-soliton model calculation, $\widetilde{E}$ reduces to a pion pole contribution at small t and the pion pole part to $\widetilde{E}$ dominates over a wide range of t and ξ values [31]. The t-dependence is constrained by the sum rule of Eq. (1.30) in terms of the pseudo-scalar Form Factor $G_P^q(t)$. Therefore, the GPD $\widetilde{E}^q(x,\xi,t)$ is entirely parameterized through a pion pole contribution and a t-factorized ansatz as

$$\widetilde{E}^u(x,\xi,t) = -\widetilde{E}^d(x,\xi,t) = \frac{1}{2}\theta(\xi - |x|)\frac{1}{\xi}\phi_{\rm as}\left(\frac{x}{\xi}\right) G_P(t), \tag{1.55}$$

where the asymptotic distribution amplitude $\phi_{\rm as}(z) = 3/4\ (1-z^2)$ and $G_P(t)$ is the induced pseudo-scalar Form Factor of the nucleon. The contribution corresponds to a meson exchange and lives only in the $|x| \leqslant \xi$ region.

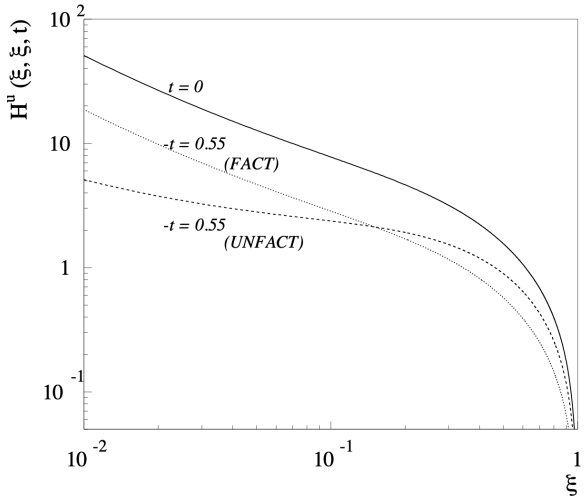

Figure 1.11: The ξ-dependence of $H^u(\xi,\xi,t)$ at $-t = 0$ and 0.55 GeV^2 for factorized (FACT) and unfactorized (UNFACT) models. The figures are extracted from [31].

Unfactorized t-dependence: Regge phenomenology

It remains to be investigated how realistic the factorized parameterizations are if one goes away from the $t = 0$ region. In particular, the cross sections for ρ^0 electroproduction on the proton, in which the GPDs H enter, measured at HERMES [37], shows an exponential fall-off in the region of $-t < 0.5$ GeV^2. A factorized ansatz deviates over this t region already noticeably from an exponential fall-off [31]. The VGG model then provides a more sophisticated estimate of the t-dependence of GPDs based on Regge theory. The Regge picture suggests a $x^{\alpha(t)}$ behavior at small x. Assuming a linear Regge trajectory with the slope α', the parameterization of GPD H^q at $\xi = 0$ consists of the unfactorized ansatz:

$$H^q(x,0,t) = q(x)x^{-\alpha' t}. \tag{1.56}$$

α' is a free parameter which can be constrained by the sum rules of Eq. (1.27) linking the GPD H^q to the Dirac Form Factor F_1^q. For the proton, a rather narrow range of values around $\alpha' = 1.0$-1.1 GeV^{-2} are favored [33]. The full dependence of $H^q(x,\xi,t)$ can be obtained through Eq. (1.40) by replacing the DD ansatz given by Eq. (1.41) with a Regge-type Double Distribution

$$\mathrm{DD}_R^q(\beta,\alpha,t) = h(\beta,\alpha)q(\beta)\beta^{-\alpha' t}. \tag{1.57}$$

Fig. 1.11 shows the comparison of the factorized model of Eq. 1.46 for $H^u(\xi,\xi,t)$ with the unfactorized model of Eq. 1.57. One sees that the unfactorized model leads to an increasingly larger reduction when going to smaller ξ (typical for a Regge type ansatz) and to an enhancement at larger ξ.

The ansatz is only valid for the small $-t$ region, because at larger values of $-t$ the first moment of Eq. (1.56) is dominated by the large x region, for which a Regge ansatz does not hold. The modification of Regge ansatz is introduced in the VGG model in order to satisfy the FF counting rule at large $-t$. For example, the GPD $H^q(x,0,t)$ is parameterized as

$$H^q(x,0,t) = q(x)x^{-\alpha'(1-x)t}. \tag{1.58}$$

Similarly, the modified Regge-type (R2) Double Distribution writes

$$\mathrm{DD}_{R2}^q(\beta,\alpha,t) = h(\beta,\alpha)q(\beta)\beta^{-\alpha'(1-\beta)t}. \tag{1.59}$$

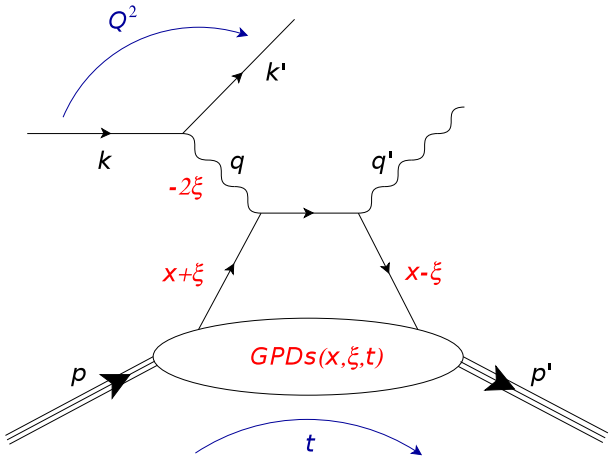

Figure 1.12: Handband diagram of the DVCS process: at leading order and leading twist, DVCS can be seen as the absorption of a virtual photon by a quark of the nucleon, followed by the quasi-instantaneous emission of a real photon by the same quark.

In summary, the VGG model is based on very few free parameters. The parameters b_{val} and b_{sea} drive the (x, ξ)-dependence, which are set to 1 by default. The recent fit to the DVCS data indicates the VGG model with small skewness effects of sea quark ($b_{\text{sea}} = 5$) is in good agreement with the data [38]. The parameter α' drives the t-dependence. The fit to the nucleon FFs data yielded $\alpha' = 1.105$ GeV^{-2} [33]. The parameters J_u and J_d control the normalization of the GPD E and are unknown. The constraint of J_u and J_d can be extracted from proton and neutron DVCS data [39] and provides a better understanding of the nucleon spin. The VGG model has been adopted for the estimate of DDVCS observables shown in the following chapters.

1.2 Deeply Virtual Compton Scattering

Among the hard exclusive electroproduction processes, Deeply Virtual Compton Scattering (DVCS) is one of the cleanest channels and bears the best promises to extract the GPDs from experimental data. It refers to the subprocess $\gamma^* N \to N\gamma$ of the exclusive electroproduction of real photons $eN \to eN\gamma$.

In the Bjorken limit and for small enough momentum transfer to the nucleon with respect to the photon virtuality ($-t \ll Q^2$), the factorization theorem allows one to express the DVCS amplitude as a convolution of the hard scattering part, being calculable within the perturbative QCD approach, and soft structure functions GPDs, describing an emission of quark from the nucleon and its subsequent reabsorption, as shown by the so-called "handband diagram" in Fig. 1.12.

1.2.1 Kinematics

Four independent variables are needed to describe the 3-body final state reaction $eN \to eN\gamma$ at a fixed beam energy E. They are usually chosen as Q^2, x_{B}, t and ϕ. Q^2 is the virtuality of the photon $Q^2 = -q^2 = -(k - k')^2$, where $q(\nu, \boldsymbol{q})$, $k(E, \boldsymbol{k})$ and $k'(E', \boldsymbol{k'})$ are the four-momenta of the virtual photon, incident and scattered electron, respectively. x_{B} is the Bjorken variable defined in Eq. (1.19). Unlike for the DIS process, it is not equal

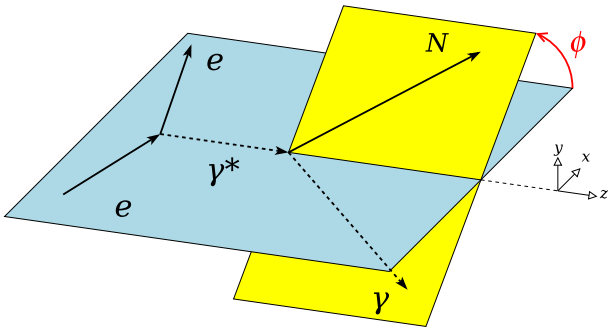

Figure 1.13: DVCS in the target rest frame.

to the average longitudinal momentum fraction x in the DVCS process. t is the squared momentum transfer to the nucleon. The skewness ξ is related to x_{B} as

$$\xi = x_{\mathrm{B}} \frac{1 + t/2Q^2}{2 - x_{\mathrm{B}} + x_{\mathrm{B}}(t/Q^2)} \simeq \frac{x_{\mathrm{B}}}{2 - x_{\mathrm{B}}} \tag{1.60}$$

Finally, ϕ is the azimuthal angle between the electron scattering plane ($e \to e\gamma^*$) and the hadronic production plane ($\gamma^* N \to \gamma N$), as illustrated in Fig. 1.13. Its explicit definition within the Trento convention is in [40].

In the DVCS experiments, at a fixed beam energy E, measurements of the final electron (E', θ_e) with the real photon (ν', θ_γ) are enough to get all information with respect to the final state, where θ_e is the polar angle between the beam and the scattered electron, θ_γ is the polar angle between the incident virtual photon and the outgoing real photon, and ν' is the energy of the real photon. For example, the JLab Hall A experiments [41] detected only two particles of the final state, the scattered electron and the real photon, and a cut on the missing mass of the proton was used to identify the exclusive process. The detection of all three particles of the final state is an over-constrained situation which can be used to experimentally reject possible background contamination and ensure the exclusivity of the process as done with the large acceptance detector CLAS [42]. The Lorentz invariant variables can be expressed by the experimental variables through

$$Q^2 = 4EE' \sin^2(\theta_e/2), \tag{1.61}$$

$$x_{\mathrm{B}} = \frac{2EE' \sin^2(\theta_e/2)}{M(E - E')}, \tag{1.62}$$

$$t = -\frac{Q^2 M + \dfrac{Q^2}{x_{\mathrm{B}}} \left[\dfrac{Q^2}{2Mx_{\mathrm{B}}} - \cos\theta_\gamma \sqrt{Q^2 + \left(\dfrac{Q^2}{2Mx_{\mathrm{B}}} \right)^2} \right]}{M + \dfrac{Q^2}{2Mx_{\mathrm{B}}} - \cos\theta_\gamma \sqrt{Q^2 + \left(\dfrac{Q^2}{2Mx_{\mathrm{B}}} \right)^2}}. \tag{1.63}$$

Phase space

Although the Lorentz invariant variables describing DVCS are independent on each other, their ranges are inter-dependent. The total center-of-mass energy for DVCS can be expressed as

$$W = \sqrt{(q+p)^2} = \left(M^2 + \frac{Q^2}{x_{\mathrm{B}}} - Q^2 \right)^{\frac{1}{2}}. \tag{1.64}$$

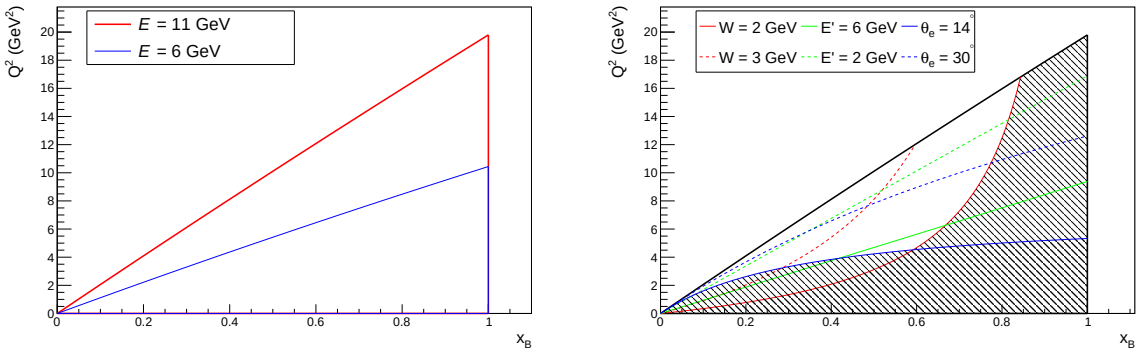

Figure 1.14: Left panel: DVCS (Q^2, x_{B}) phase space at 6 GeV (blue) and 11 GeV (red) beam energy. Right panel: DVCS (Q^2, x_{B}) phase space at 11 GeV with specific kinematic conditions represented by the colored curves. The shaded area corresponds to the region rejected by the physics ($W \geqslant 2$ GeV) constraints and the geometrical constraints ($\theta_e \geqslant 14°$) of the Hall A spectrometers. The remaining open area shows the available region one can possibly access.

In order to allow at minima a proton in the final state, the center-of-mass energy must be larger than or at least equal to the nucleon mass M, resulting in

$$x_{\mathrm{B}} \leqslant 1 \tag{1.65}$$

where the equality represents elastic scattering, kinematically similar to a DVCS reaction with emission of a photon at rest. At a fixed x_{B}, we can infer the DVCS minimum and maximum Q^2:

$$Q^2{}_{\min} = 0, \quad Q^2{}_{\max} = \frac{4E^2 M x_{\mathrm{B}}}{M x_{\mathrm{B}} + 2E}. \tag{1.66}$$

These relations can be applied to infer the (Q^2, x_{B}) phase space, as shown in Fig. 1.14 (left panel). The vertical lines at $x_{\mathrm{B}} = 1$ represent the elastic scattering limit; the horizontal lines at $Q^2 = 0$ represent $Q^2{}_{\min}$ for any possible x_{B}; the diagonals represent $Q^2{}_{\max}$ for any possible x_{B}. Consequently, any combination of (Q^2, x_{B}) for the DVCS reaction must be within the triangle-form phase space. One clearly sees the benefit of higher beam energies accessing a broader phase space, and reaching at fixed x_{B} a larger range in Q^2. This is one of the motivations of the JLab 12 GeV energy upgrade. More importantly, the flux of generated virtual photons increases with beam energy, and JLab12 benefits the measurements with increasing cross section. I stress that this study is based on JLab12 and all the calculations and simulations in the following chapters are performed with the fixed beam energy $E = 11$ GeV. Fig. 1.14 (right panel) shows some specific kinematic conditions within the (Q^2, x_{B}) phase space.

Conditions are required for the applicability of GPDs formalism and the validity of the handbag approximation. Precisely, the virtuality Q^2 must be sufficiently large for the reaction to happen at the parton level ($Q^2 \gg M^2$) and much larger than the squared momentum transfer to the nucleon ($-t/Q^2 \ll 1$). To ensure that the experimental data are from the deep inelastic scattering regime (with nuclear excitation well above the main nucleon resonances) the squared hadronic center-of-mass energy W must be large. Specifically, we require

$$W \geqslant 2 \text{ GeV}. \tag{1.67}$$

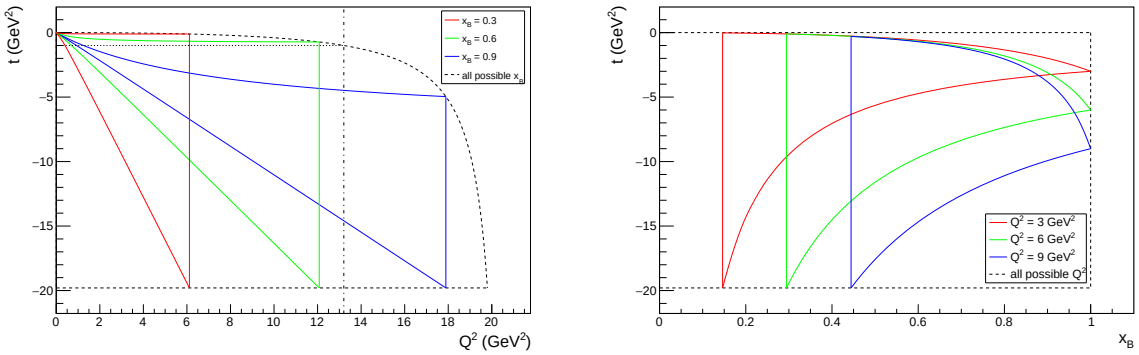

Figure 1.15: DVCS (t, Q^2) and (t, x_{B}) phase space.

Moreover, several kinds of constraints can also originate from a detector. In the first dedicated DVCS experiment in JLab Hall A [43], for instance, the electromagnetic calorimeter was centered along the direction of the virtual photon. Geometrical constraints for the positions of detectors imply $\theta_e \geqslant 14°$. These constraints are represented as shaded zones in Fig. 1.14 (right panel). One can search available kinematical setting only in the allowed area, corresponding to the open area in Fig. 1.14.

At fixed Q^2 and x_{B}, the boundary of t is given by

$$t_{\mathrm{max,min}} = -\frac{Q^2 M + \dfrac{Q^2}{x_{\mathrm{B}}}\left[\dfrac{Q^2}{2Mx_{\mathrm{B}}} \pm \sqrt{Q^2 + \left(\dfrac{Q^2}{2Mx_{\mathrm{B}}}\right)^2}\right]}{M + \dfrac{Q^2}{2Mx_{\mathrm{B}}} \pm \sqrt{Q^2 + \left(\dfrac{Q^2}{2Mx_{\mathrm{B}}}\right)^2}}, \tag{1.68}$$

where the $+$ $(-)$ sign stands for t_{max} (t_{min}). Note that the minimum and maximum definitions for t correspond to $|t|$.

In Fig. 1.15 (left panel), the areas enclosed by the colored solid curves represent the (t, Q^2) phase space at fixed x_{B} (0.3, 0.6 and 0.9). At a fixed Q^2, a smaller x_{B} has a wider range in t and the t-range of small x_{B} contains the one of large x_{B}. At $Q^2 = 0$, the phase space collapses in one single point at $t = 0$, independently of x_{B}. The area

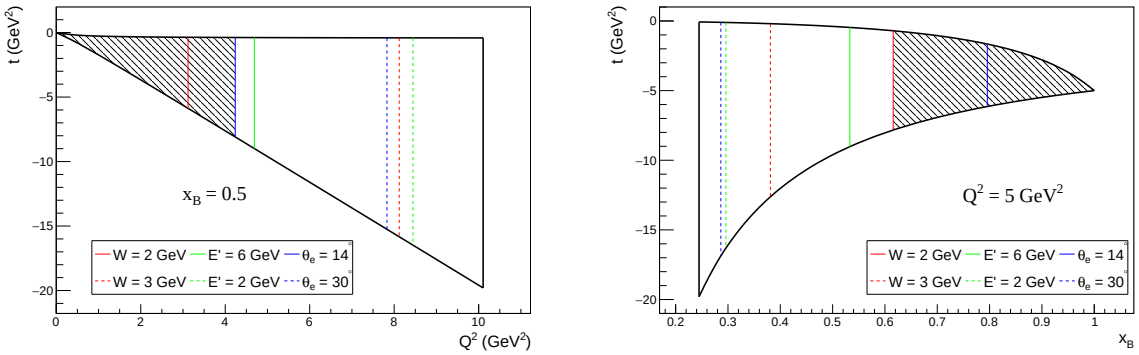

Figure 1.16: Left panel: DVCS (t, Q^2) phase space at fixed $x_{\mathrm{B}} = 0.5$. Right panel: DVCS (t, x_{B}) phase space at fixed $Q^2 = 5$ GeV^2. The specific kinematic conditions are represented by the colored curves.

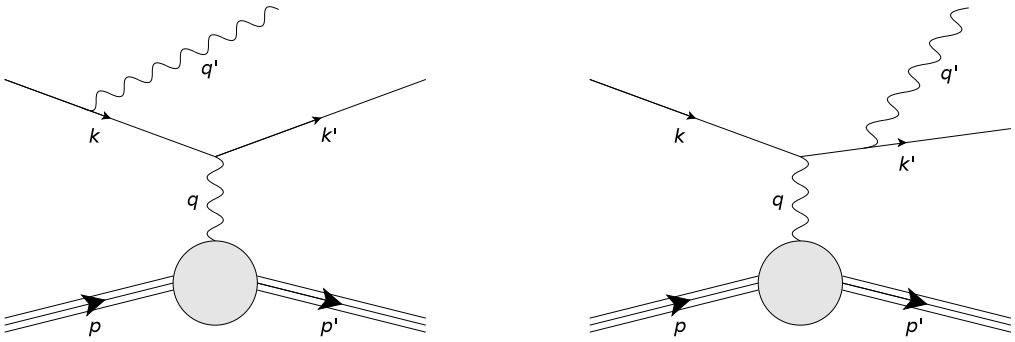

Figure 1.17: BH diagrams for the emission of a real photon by the incoming and the outgoing electrons.

delimited by the black dashed curves represents the envelope of each single (t, Q^2) phase space that is the (t, Q^2) phase space for all possible $x_{\rm B}$. This envelope indicates that there exists a maximum Q^2 under the condition that $-t$ shall be smaller than a certain value. For example, the maximum $Q^2 = 13.2$ GeV^2 (the dashed-dotted line) is given by the condition of $-t < 1$ GeV^2 (the dotted line stands for $-t = 1$ GeV^2), and $x_{\rm B}$ can not be larger than 0.657. In Fig. 1.15 (right panel), the areas enclosed by the colored solid curves represent the $(t, x_{\rm B})$ phase space at fixed Q^2 (3, 6, 9 GeV^2). At a fixed $x_{\rm B}$, a larger Q^2 has a wider range in t. The t-ranges of small and of large Q^2 overlap over the small $x_{\rm B}$ region and separate in the vicinity of $x_{\rm B} = 1$. Each area at $x_{\rm B} = 1$ turns into a point which represents elastic scattering condition where $t = Q^2$. The area delimited by the black dashed curves represents the $(t, x_{\rm B})$ envelope that is the $(t, x_{\rm B})$ phase space of all possible Q^2. Fig. 1.16 shows some special kinematic conditions within the (t, Q^2) and $(t, x_{\rm B})$ phase space. Similarly to the right panel of Fig. 1.14, the shaded zones represent the region refused by the physics constraint $W \leqslant 2$ GeV and the experimental inspired one $\theta_e \geqslant 14^\circ$.

1.2.2 The amplitude of the electroproduction of real photons

In the electroproduction of real photons, DVCS amplitude interferes with a so-called Bethe-Heitler (BH) process [44], which has the same initial and final states as DVCS and is experimentally indistinguishable from the DVCS process. The BH process is a basic process for the production of real photons, where the real photons are produced from the interaction of an incoming or outgoing electron with the Coulomb field of an atom or a nucleus, as shown in Fig. 1.17. The total amplitude for the reaction is then expressed by a sum of amplitudes for two processes as

$$\mathcal{T}^2 = |\mathcal{T}_{\rm BH} + \mathcal{T}_{\rm DVCS}|^2 = |\mathcal{T}_{\rm BH}|^2 + |\mathcal{T}_{\rm DVCS}|^2 + \mathcal{I} \tag{1.69}$$

where

$$\mathcal{I} = \mathcal{T}_{\rm DVCS}\mathcal{T}^*_{\rm BH} + \mathcal{T}^*_{\rm DVCS}\mathcal{T}_{\rm BH} \tag{1.70}$$

represents the interference term. Given the knowledge of the elastic FFs, the BH contribution is calculable in QED.

The importance of the BH relative to the DVCS strongly depends on the kinematic domain. It can largely dominate or be negligible compared with DVCS. The presence of BH can be seen as an amplifier of the DVCS process when one measures observables sensitive to the BH-DVCS interference.

1.2.3 Compton Form Factors

The GPDs enter the DVCS cross section through Compton Form Factors (CFFs), which are convolution integrals over the quark loops of the diagram of Fig. 1.12 and the corresponding crossed diagram. At leading order and leading twist, the CFFs $\mathcal{F} \in \{\mathcal{H}, \mathcal{E}, \widetilde{\mathcal{H}}, \widetilde{\mathcal{E}}\}$ are of the form

$$\mathcal{F} = \int_{-1}^{1} dx\ F(x,\xi,t) \left(\frac{1}{x-\xi+i\epsilon} \pm \frac{1}{x+\xi-i\epsilon} \right), \tag{1.71}$$

where $F \in \{H, E, \widetilde{H}, \widetilde{E}\}$ stands for a generic nucleon GPD and the + and − signs apply to the unpolarized GPDs (H, E) and to the polarized GPDs $(\widetilde{H}, \widetilde{E})$, respectively. One easily notices that the variable x is integrated over, which is a "mute" variable not accessible for DVCS experiments. In the integrals, GPDs are weighted by the factors originated from the propagator of the quark in the diagrams. At leading order and leading twist, the CFF can be decomposed into its real and imaginary part as

$$\mathcal{F}(\xi,\xi,t) = \sum_q e_q^2 \left\{ \mathcal{P} \int_0^1 dx\ F_+^q(x,\xi,t) \left(\frac{1}{x-\xi} \pm \frac{1}{x+\xi} \right) - i\pi F_+^q(\xi,\xi,t) \right\}. \tag{1.72}$$

Here, the sum runs over all quark flavors, $\mathcal{P}$ denotes the principal value integral, the x-range of integration is reduced from $\{-1, 1\}$ to $\{0, 1\}$ and F_+^q is the singlet GPD combination of the quark flavor q defined as

$$F_+^q(x,\xi,t) = F^q(x,\xi,t) \mp F^q(-x,\xi,t), \tag{1.73}$$

where the − sign applies to $F^q \in \{H^q, E^q\}$ and + sign to $F^q \in \{\widetilde{H}^q, \widetilde{E}^q\}$, acting contrarily to the signs in Eqs. (1.71) and (1.72). Therefore, the maximum information that can be extracted from DVCS experiment data at a given (ξ, t) point is $F(\pm\xi, \xi, t)$, when the measured observables are sensitive to the imaginary part of the DVCS amplitude, and $\int_{-1}^{1} dx[F(\mp x, \xi, t)/(x \pm \xi)]$, when one measures the observables sensitive to the real part of the DVCS amplitude. I introduce theoretical work [45] for the analytical relations between the DVCS observables and the CFFs.

The quark flavor decomposition of a nucleon GPD F accessed through DVCS is written for a proton (p) and a neutron (n)

$$\begin{aligned} F^p(\xi,\xi,t) &= \frac{4}{9}F^u(\xi,\xi,t) + \frac{1}{9}F^d(\xi,\xi,t), \\ F^n(\xi,\xi,t) &= \frac{4}{9}F^d(\xi,\xi,t) + \frac{1}{9}F^u(\xi,\xi,t). \end{aligned} \tag{1.74}$$

Note that the flavor-dependent GPDs in the notation always refer to the corresponding quark flavor in the proton, e.g. $F^u = F^{u/p}$ as mentioned for Eq. (1.31).

Here, I stress that the CFFs extracted from DVCS observables only depend on ξ and t and the x-dependence of the GPDs is totally absent, which is certainly an important gain of information but not sufficient to map out the full dependence of GPDs. In addition, I remind that the notation of CFFs in Eqs. (1.71) and (1.72) is slightly different from [45], where the authors include a minus sign for both real and imaginary part of the CFFs.

1.2.4 Experimental observables

The four GPDs correspond to the four independent quark helicity and nucleon spin combinations in the handbag diagram, as shown in Fig. 1.8. In order to separate them, one

uses the spin degrees of freedom of the beam and of the target and measures various polarization observables. I present here only the beam polarization observables. For all possible beam and target polarization observables, one finds their theoretical description in [45] and their experimental measurements in [46]. I remind that the definition of the azimuthal angle of Belitsky [45] differs from the Trento convention and one has the relation $\phi_{\text{[Belitsky]}} = \pi - \phi$.

Cross section

The total cross section for the exclusive electroproduction of a real photon $d^4\sigma$, representing the 4-fold differential cross section $d^4\sigma/dx_{\rm B}dQ^2dtd\phi$, can be expressed as the combinations of beam charge and polarization following

$$d^4\sigma \sim d^4\sigma^{\rm BH}_{\rm UU} + d^4\sigma^{\rm DVCS}_{\rm UU} + (-e_l)d^4\sigma^{\rm I}_{\rm UU} + P_l\left[d^4\sigma^{\rm DVCS}_{\rm LU} + (-e_l)d^4\sigma^{\rm I}_{\rm LU}\right], \tag{1.75}$$

where e_l and P_l are the charge and the helicity of the lepton beam, respectively. In Eq. (1.75), the first subscript refers to the beam polarization state ("U" stands for unpolarized and "L" for longitudinal polarization) while the second refers to the target polarization (only for unpolarized target here), and the superscripts refer to the contributions of BH, DVCS and their interference (I) amplitudes. In general, the interference contributions are of great interest since they give accesses to CFFs in a linear fashion while the CFFs enter the DVCS contributions in a bilinear one. Moreover, the beam spin contributions are sensitive to the imaginary parts of CFFs and the unpolarized contributions to both the real and imaginary. Specifically for all the terms in Eq. (1.75), the Fourier expansions in ϕ up to twist-3 are given in [45] by

$$d^4\sigma^{\rm BH}_{\rm UU} \propto \frac{1}{\mathcal{P}_1(\phi)\mathcal{P}_2(\phi)}\left[c_0^{\rm BH} + c_1^{\rm BH}\cos(\phi) + c_2^{\rm BH}\cos(2\phi)\right], \tag{1.76}$$

$$d^4\sigma^{\rm DVCS}_{\rm UU} \propto c_0^{\rm DVCS} + c_1^{\rm DVCS}\cos(\phi) + c_2^{\rm DVCS}\cos(2\phi), \tag{1.77}$$

$$d^4\sigma^{\rm I}_{\rm UU} \propto \frac{1}{\mathcal{P}_1(\phi)\mathcal{P}_2(\phi)}\left[c_0^{\rm I} + c_1^{\rm I}\cos(\phi) + c_2^{\rm I}\cos(2\phi) + c_3^{\rm I}\cos(3\phi)\right], \tag{1.78}$$

$$d^4\sigma^{\rm I}_{\rm LU} \propto \frac{1}{\mathcal{P}_1(\phi)\mathcal{P}_2(\phi)}\left[s_1^{\rm I}\sin(\phi) + s_2^{\rm I}\sin(2\phi)\right], \tag{1.79}$$

$$d^4\sigma^{\rm DVCS}_{\rm LU} \propto s_1^{\rm DVCS}\sin(\phi). \tag{1.80}$$

The lepton propagators $\mathcal{P}_1(\phi), \mathcal{P}_2(\phi)$ can be calculated within the framework of QED from the kinematic variables. The Fourier coefficients $c^{\rm BH}$ in pure BH cross section contain the Dirac and Pauli FFs. Since F_1 and F_2 can be considered as well known at small $-t$, the BH process is precisely calculable theoretically.

The coefficients $c_1^{\rm I}$ and $s_1^{\rm I}$ arise at the twist-2 level, which are expected to dominate the cross sections and to provide the main access to the CFFs. The coefficient $c_1^{\rm I}$ is proportional to a linear combination of the real parts of CFFs,

$$c_1^{\rm I} \propto \text{Re}\left\{F_1\mathcal{H} + \xi(F_1+F_2)\widetilde{\mathcal{H}} - \frac{t}{4M^2}F_2\mathcal{E}\right\}, \tag{1.81}$$

and the coefficient $s_1^{\rm I}$ is proportional to the same linear combination of the imaginary parts of the CFFs,

$$s_1^{\rm I} \propto {\rm Im}\ \left\{ F_1\mathcal{H} + \xi(F_1+F_2)\widetilde{\mathcal{H}} - \frac{t}{4M^2}F_2\mathcal{E} \right\}. \tag{1.82}$$

The coefficients $c_0^{\rm DVCS}$ and $c_0^{\rm I}$ are also related to twist-2 CFFs. For the kinematically suppressed coefficient $c_0^{\rm I}$, the dominant part of it is approximately proportional to $c_1^{\rm I}$,

$$c_0^{\rm I} \propto -\frac{\sqrt{-t}}{Q}c_1^{\rm I}. \tag{1.83}$$

Finally, the DVCS coefficient $c_0^{\rm DVCS}$ is related to a bilinear combination of the CFFs as

$$c_0^{\rm DVCS} \propto 4\,(1-x_{\rm B})\left(\mathcal{H}\mathcal{H}^* + \widetilde{\mathcal{H}}\widetilde{\mathcal{H}}^*\right) - x_{\rm B}^2\left(\mathcal{E}\mathcal{E}^* + \mathcal{H}\mathcal{E}^* + \mathcal{E}\mathcal{H}^* + \widetilde{\mathcal{H}}\widetilde{\mathcal{E}}^* + \widetilde{\mathcal{E}}\widetilde{\mathcal{H}}^*\right), \tag{1.84}$$

where the CFFs suppressed by the $-t/Q^2$ factor are not shown in this expression. These relations for the twist-2 coefficients do not cover the target mass effects and finite-t corrections to DVCS [47, 48]. The other coefficients are related to combinations of CFFs of either higher twist or helicity flip GPDs. I only present here the coefficients sensitive to the quark helicity conserving GPDs at leading twist. For DVCS data analyses, higher twist and higher order QCD corrections may need to be included, as recent results suggest that their contributions might not be negligible [24].

Cross sections with polarized electron beam

With polarized electron beam, unpolarized cross section $\sigma_{\rm UU}^-$ and beam spin cross section difference $\Delta\sigma_{\rm LU}^-$ are built as

$$\sigma_{\rm UU}^- = \frac{1}{2}\left(d^4\sigma_{\rightarrow}^- + d^4\sigma_{\leftarrow}^-\right) = d^4\sigma_{\rm UU}^{\rm BH} + d^4\sigma_{\rm UU}^{\rm DVCS} + d^4\sigma_{\rm UU}^{\rm I}, \tag{1.85}$$

$$\Delta\sigma_{\rm LU}^- = \frac{1}{2}\left(d^4\sigma_{\rightarrow}^- - d^4\sigma_{\leftarrow}^-\right) = d^4\sigma_{\rm LU}^{\rm DVCS} + d^4\sigma_{\rm LU}^{\rm I}, \tag{1.86}$$

where the $-$ sign in the superscripts denotes the beam charge and the arrow $\rightarrow$ (or $\leftarrow$) in the subscripts refers to the beam polarization $P_l = 1$ (or -1).

Neglecting non-dominant DVCS terms and the coefficients suppressed by kinematics and higher twist, both the real and imaginary parts of the linear combination of CFFs in Eqs. (1.81) and (1.82) can be quantitatively obtained from $c_1^{\rm I}$ and $s_1^{\rm I}$, respectively. The kinematic factors ξ and t being small, the measurements of unpolarized cross section and beam spin cross section difference on a proton target are mainly sensitive to, respectively, ${\rm Re}\mathcal{H}^p$ and ${\rm Im}\mathcal{H}^p$. In the neutron case, following the small value of F_1^n ($F_1^n \approx 0$ at small t, as shown in Fig. 1.2) and the cancellation between u and d polarized parton distributions in $\widetilde{\mathcal{H}}^n$ [31], the approximation of $s_1^{\rm I}$ for a neutron target writes

$$s_1^{\rm I} \propto -\frac{t}{4M^2}F_2\ {\rm Im}\mathcal{E}^n \tag{1.87}$$

and similar relation hold for $c_1^{\rm I}$ and ${\rm Re}\mathcal{E}^n$. Therefore, the measurements on a neutron target offer the sensitivity to the GPD E and become then of direct relevance in the determination of the quark angular momentum of Eq. (1.38). See [39, 49] for more about DVCS off neutron.

Cross sections with polarized electron and positron beams

With only polarized electron beam, the quantitative access to the Fourier coefficients of the interference terms is complicated by the presence of DVCS terms. This entanglement can be resolved by taking into account the explicit dependence of the interference terms on the lepton beam charge.

Using polarized electron and polarized positron beams, one can measure four experimental observables built as

$$\sigma_{\rm UU} = \frac{1}{4}\left[\left(d^4\sigma^-_{\rightarrow} + d^4\sigma^-_{\leftarrow}\right) + \left(d^4\sigma^+_{\rightarrow} + d^4\sigma^+_{\leftarrow}\right)\right] = d^4\sigma^{\rm BH}_{\rm UU} + d^4\sigma^{\rm DVCS}_{\rm UU}, \quad (1.88)$$

$$\Delta\sigma^{\rm C}_{\rm UU} = \frac{1}{4}\left[\left(d^4\sigma^-_{\rightarrow} + d^4\sigma^-_{\leftarrow}\right) - \left(d^4\sigma^+_{\rightarrow} + d^4\sigma^+_{\leftarrow}\right)\right] = d^4\sigma^{\rm I}_{\rm UU}, \quad (1.89)$$

$$\Delta\sigma_{\rm LU} = \frac{1}{4}\left[\left(d^4\sigma^-_{\rightarrow} - d^4\sigma^-_{\leftarrow}\right) + \left(d^4\sigma^+_{\rightarrow} - d^4\sigma^+_{\leftarrow}\right)\right] = d^4\sigma^{\rm DVCS}_{\rm LU}, \quad (1.90)$$

$$\Delta\sigma^{\rm C}_{\rm LU} = \frac{1}{4}\left[\left(d^4\sigma^-_{\rightarrow} - d^4\sigma^-_{\leftarrow}\right) - \left(d^4\sigma^+_{\rightarrow} - d^4\sigma^+_{\leftarrow}\right)\right] = d^4\sigma^{\rm I}_{\rm LU}, \quad (1.91)$$

where the two observables with "C" in the superscripts denote beam charge cross section differences and the others without it symbolize charge-averaged cross sections. One readily sees that interference terms as well as the DVCS terms are singled out.

Positron beams have been promoted at JLab. The PEPPo (Polarized Electrons for Polarized Positrons) concept is potentially capable of operating at low beam energies (a few MeV) with high polarization transfer from incident electrons to created positrons [50]. This technique was demonstrated at the injector of the Continuous Electron Beam Accelerator Facility (CEBAF) [51], extends polarized positron capabilities from GeV to MeV electron beams, and opens access to the development of a polarized positron beam at JLab.

Asymmetries

Asymmetries are observables which are relatively straightforward to extract experimentally due to the cancellation of normalization factors (such as detector acceptance and efficiency) and many sources of systematic errors in the ratio.

With polarized electron beam, one measures the Beam Spin Asymmetry (BSA) defined as

$$A^-_{\rm LU} = \frac{\Delta\sigma^-_{\rm LU}}{\sigma^-_{\rm UU}} = \frac{d^4\sigma^{\rm DVCS}_{\rm LU} + d^4\sigma^{\rm I}_{\rm LU}}{d^4\sigma^{\rm BH}_{\rm UU} + d^4\sigma^{\rm DVCS}_{\rm UU} + d^4\sigma^{\rm I}_{\rm UU}}. \quad (1.92)$$

The BSA has a shape close to a $\sin\phi$ and its leading twist expansion can be parameterized as a form of $(a\sin\phi)/(1+c\cos\phi+d\cos 2\phi)$ where higher twist terms are neglected and only dominant terms are kept. The access to $s^{\rm I}_1$ via the BSA is complicated by the presence of $c^{\rm I}_1$ in the denominator. Again, this entanglement can be cancelled by using beams of opposite charges.

Using polarized electron and polarized positron beams, one can measure three asym-

metries built as

$$A_{\rm UU}^{\rm C} = \frac{\Delta\sigma_{\rm UU}^{\rm C}}{\sigma_{\rm UU}} = \frac{d^4\sigma_{\rm UU}^{\rm I}}{d^4\sigma_{\rm UU}^{\rm BH} + d^4\sigma_{\rm UU}^{\rm DVCS}}, \tag{1.93}$$

$$A_{\rm LU} = \frac{\Delta\sigma_{\rm LU}}{\sigma_{\rm UU}} = \frac{d^4\sigma_{\rm LU}^{\rm DVCS}}{d^4\sigma_{\rm UU}^{\rm BH} + d^4\sigma_{\rm UU}^{\rm DVCS}}, \tag{1.94}$$

$$A_{\rm LU}^{\rm C} = \frac{\Delta\sigma_{\rm LU}^{\rm C}}{\sigma_{\rm UU}} = \frac{d^4\sigma_{\rm LU}^{\rm I}}{d^4\sigma_{\rm UU}^{\rm BH} + d^4\sigma_{\rm UU}^{\rm DVCS}}, \tag{1.95}$$

and the asymmetry azimuthal moments. For example, the cos(0) and cos(ϕ) moments of $A_{\rm UU}^{\rm C}$, and the sin(ϕ) moment of $A_{\rm LU}^{\rm C}$ write

$$A_{\rm UU}^{\rm C,cos(0)} = \frac{1}{2\pi}\int_0^{2\pi} d\phi\ A_{\rm UU}^{\rm C}(\phi), \tag{1.96}$$

$$A_{\rm UU}^{\rm C,cos(\phi)} = \frac{1}{\pi}\int_0^{2\pi} d\phi\ A_{\rm UU}^{\rm C}(\phi)\cos\phi, \tag{1.97}$$

$$A_{\rm LU}^{\rm C,sin(\phi)} = \frac{1}{\pi}\int_0^{2\pi} d\phi\ A_{\rm LU}^{\rm C}(\phi)\sin\phi. \tag{1.98}$$

At some kinematics, the contribution of the BH term in the denominator is strongly dominated by the constant coefficient $c_0^{\rm BH}$, to the degree that one can neglect the other BH coefficients, the unpolarized DVCS contribution and the effect of the ϕ-dependence of the BH propagators. In this case, the moments give direct access to the Fourier coefficients. Specifically, the three moments above are related to twist-2 GPDs via the Fourier coefficients $c_0^{\rm I}$, $c_1^{\rm I}$ and $s_0^{\rm I}$ in Eqs. (1.81)-(1.83).

In summary, it is obviously a very complex task to actually measure the GPDs. Given the convolution over x in the amplitudes, the number of CFFs to extract, the quark flavor decomposition, not to mention the Q^2 evolution and higher-twist corrections, it calls for a broad experimental program comprising the measurements of different DVCS observables on proton and neutron over large kinematics coverages. Since the beginning of this century, various measurements of DVCS have been conducted worldwide. The measurements by HERMES [52] at DESY and by CLAS [42] at JLab have proved the existence of a DVCS asymmetry signal and have launched a global experimental campaign for GPDs. The DVCS experiment in Hall A [41] at JLab has proved, via a Q^2-scaling test, that the factorization and the hypothesis of leading-twist dominance can already be valid at relatively low Q^2 ($\sim$ 1 GeV^2). Beam Spin Asymmetries measured with CLAS [53] have provided important constraints for the study of the GPD H in a wide kinematic range. Nowadays, the new generation of experiments is running, such as Hall A, NPS (Neutral Particle Spectrometer) in Hall C, and CLAS12 at the upgraded CEBAF and COMPASS-II at CERN. In particular, the data analysis for 12 GeV DVCS in Hall A have been completed [54]. In the future, the Electron Ion Collider (EIC) at BNL will continue this long-term mapping of GPDs..

1.3 Double Deeply Virtual Compton Scattering

The CFFs extracted from DVCS experimental data provide precious constraints on the (ξ, t)-dependence of GPDs. However, GPDs depend on three variables x, ξ and t. In

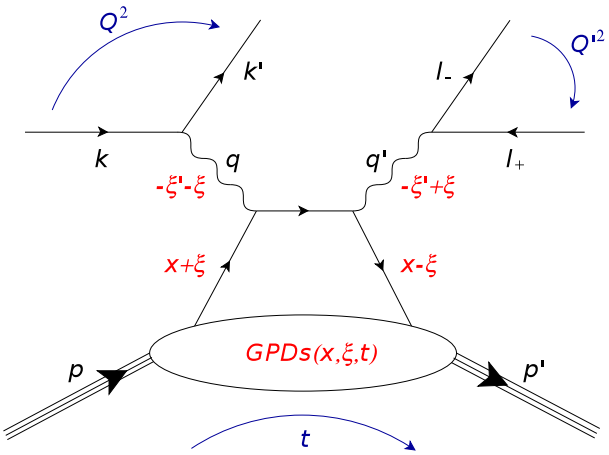

Figure 1.18: Handband diagram of the DDVCS process for leading order and leading twist (there is also a crossed diagram where the final photon is emitted from the initial quark).

order to map them ultimately, x-dependence still need to be uncovered, in principle with the help of a model-dependent deconvolution with adjustable parameters. It was first proposed by M. Guidal and M. Vanderhaeghen [55], at the same time by A. V. Belitsky and D. Müller [56, 57], that the x-dependence of GPDs can be indepedently accessed via measuring the so-called Double Deeply Virtual Compton Scattering (DDVCS) process. It corresponds to the intermediate process $\gamma^* N \to N l^- l^+$ of the exclusive electroproduction of a lepton pair $eN \to eNl^-l^+$.

At sufficiently high virtuality of the incident space-like photon ($Q^2 \gg M^2$) and small enough momentum transfer to the nucleon with respect to the photon virtuality ($-t \ll Q^2$), DDVCS can be seen as the absorption of a space-like photon by a quark of the nucleon, followed by the quasi-instantaneous emission of a time-like virtual photon by the same quark, which finally decays into a muon pair, as shown on the handbag diagram of Fig. 1.18.

In the handbag diagram, the virtuality of the time-like photon is defined by

$$Q'^2 = q'^2, \tag{1.99}$$

which is different from the definition of the incident virtual photon $Q^2 = -q^2$. I introduce the average photon momentum $\bar{q}$, the average nucleon momentum P and nucleon momentum transfer Δ:

$$\bar{q} = \frac{1}{2}(q + q'), \quad P = \frac{1}{2}(p + p'), \quad \Delta = p' - p = q - q'. \tag{1.100}$$

Neglecting the target mass effects and t corrections, the Lorentz invariants are built as

$$\xi' = -\frac{\bar{q}^2}{2P \cdot \bar{q}} = \frac{Q^2 - Q'^2 + t/2}{2Q^2/x_{\mathrm{B}} - Q^2 - Q'^2 + t} \tag{1.101}$$

$$\xi = -\frac{\Delta \cdot \bar{q}}{2P \cdot \bar{q}} = \frac{Q^2 + Q'^2}{2Q^2/x_{\mathrm{B}} - Q^2 - Q'^2 + t} \tag{1.102}$$

where ξ' is the generalized Bjorken variable and ξ is the skewness. If $Q'^2 = 0$, the final photon becomes real, corresponding to the DVCS process, which leads to the restriction $\xi' = \xi$ in the Bjorken limit. If $Q^2 = 0$, the initial photon is a real photon, referring to the Timelike Compton Scattering (TCS) [58, 59], which leads to the restriction $\xi' = -\xi$ in the Bjorken limit. Thus, DDVCS process is the generalized case of DVCS and TCS processes.

1.3.1 Benefits for GPDs program

The CFFs entering the DDVCS amplitude at leading order and leading twist are given by

$$\mathcal{F} = \int_{-1}^{1} dx\ F(x,\xi,t)\left(\frac{1}{x-\xi'+i\epsilon} \pm \frac{1}{x+\xi'-i\epsilon}\right). \tag{1.103}$$

In comparison with the DVCS case, the GPDs $F \in \{H, E, \widetilde{H}, \widetilde{E}\}$ in Eq. (1.103) (and the application of $\pm$ signs) is the same as in Eq. (1.71) but the weighted factors $\frac{1}{x\mp\xi'\pm i\epsilon}$ are different since the DVCS restriction $\xi' = \xi$ no longer holds for quark propagators in the DDVCS diagrams. The CFFs of DDVCS then consist of the real and imaginary parts following

$$\mathcal{F}(\xi',\xi,t) = \sum_q e_q^2 \left\{\mathcal{P}\int_0^1 dx\ F_+^q(x,\xi,t)\left(\frac{1}{x-\xi'} \pm \frac{1}{x+\xi'}\right) - i\pi F_+^q(\xi',\xi,t)\right\}. \tag{1.104}$$

where the singlet GPD combination F_+^q is given by Eq. (1.73). It is obvious that imaginary part $\mathrm{Im}\mathcal{F}(\xi',\xi,t)$ directly accesses the information of GPDs at $x = \pm\xi'$. By varying the virtualities of both incoming and outgoing photons, one can vary independently the scaling variables ξ' and ξ and eventually map out the GPDs as function of its three arguments independently. The x-dependence of GPDs is particularly important for the access to the strong force distribution via the 1^{th} oder Mellin moment of GPD H of Eq. (1.39) and for nucleon imaging strictly defined at zero skewness [27]. The x-dependence at non-zero ξ also provides a deeper investigation of the ξ-independence of the Ji sum rule of Eq. (1.38).

It can be easily inferred from Eq. (1.73) that the singlet GPD combination $F_+^q(x,\xi,t)$ is an antisymmetric function of x for $F^q \in \{H^q, E^q\}$,

$$H_+^q(-x,\xi,t) = -H_+^q(x,\xi,t), \quad E_+^q(-x,\xi,t) = -E_+^q(x,\xi,t), \tag{1.105}$$

and an symmetric function for $F^q \in \{\widetilde{H}^q, \widetilde{E}^q\}$,

$$\widetilde{H}_+^q(-x,\xi,t) = \widetilde{H}_+^q(x,\xi,t), \quad \widetilde{E}_+^q(-x,\xi,t) = \widetilde{E}_+^q(x,\xi,t), \tag{1.106}$$

Moreover, from the definition of ξ' and ξ in Eqs. (1.101)-(1.102) one obtains

$$\xi' = \xi\frac{Q^2 - Q'^2}{Q^2 + Q'^2} \tag{1.107}$$

in the Bjorken limit. This relation indicates that ξ', and consequently the imaginary part of the CFFs $\mathrm{Im}\mathcal{H}(\xi',\xi,t)$ and $\mathrm{Im}\mathcal{E}(\xi',\xi,t)$, changes sign about $Q^2 = Q'^2$ ($\xi' = 0$), which procures a strong testing ground of the universality of the GPD formalism [60].

The DDVCS process has the restriction $|\xi'| < \xi$, which is a simple consequence of the time-like nature of the final state photon. In other words, one can access only the $|x| < \xi$ region of the GPDs, as shown in Fig. 1.19. Although one does not access the whole range in x, the gain of information on the GPDs is tremendous as no deconvolution is involved to access this region of the GPDs. However, to construct sum rules, one also needs information in the region $|x| > \xi$. To access that range one would need two space-like virtual photons, which arises in two-photon exchange events in elastic electron nucleon scattering [55, 57].

I stress here that I use the notation of Ji [4, 5] for GPDs. The notations of ξ' and ξ are the same as in [59]. They related to the notation of Guidal [55] by $\xi' \equiv (2\xi' - \xi)_{[\text{Guidal}]}$ and

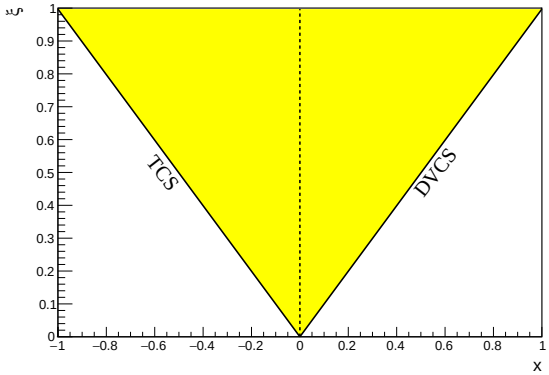

Figure 1.19: The Coverage of the singlet GPDs $F_+(x,\xi,0)$ accessed by the imaginary parts of the CFFs entering the DDVCS (the yellow area), DVCS (the diagonal $x=\xi$) and TCS (the diagonal $x=-\xi$) processes. The x-axis ($\xi=0$) represents the coverage of forward PDFs accessed by the DIS process. $H_+(x,\xi,0)$ and $E_+(x,\xi,0)$ change sign at the dashed line ($x=0$).

to the notation of Belitsky [56, 57] by $\xi' \equiv \xi_{\text{[Belitsky]}}$ and $\xi \equiv -\eta_{\text{[Belitsky]}}$. In the following, I also use the notation for the eight CFFs that can be extracted from the DDVCS process:

$$\text{Re}\mathcal{H}(\xi',\xi,t) = \mathcal{P}\int_0^1 dx\,[H(x,\xi,t) - H(-x,\xi,t)]\,C^+(x,\xi'), \tag{1.108}$$

$$\text{Re}\mathcal{E}(\xi',\xi,t) = \mathcal{P}\int_0^1 dx\,[E(x,\xi,t) - E(-x,\xi,t)]\,C^+(x,\xi'), \tag{1.109}$$

$$\text{Re}\widetilde{\mathcal{H}}(\xi',\xi,t) = \mathcal{P}\int_0^1 dx\,\left[\widetilde{H}(x,\xi,t) + \widetilde{H}(-x,\xi,t)\right]C^-(x,\xi'), \tag{1.110}$$

$$\text{Re}\widetilde{\mathcal{E}}(\xi',\xi,t) = \mathcal{P}\int_0^1 dx\,\left[\widetilde{E}(x,\xi,t) + \widetilde{E}(-x,\xi,t)\right]C^-(x,\xi'), \tag{1.111}$$

$$\text{Im}\mathcal{H}(\xi',\xi,t) = H(\xi',\xi,t) - H(-\xi',\xi,t), \tag{1.112}$$

$$\text{Im}\mathcal{E}(\xi',\xi,t) = E(\xi',\xi,t) - E(-\xi',\xi,t), \tag{1.113}$$

$$\text{Im}\widetilde{\mathcal{H}}(\xi',\xi,t) = \widetilde{H}(\xi',\xi,t) + \widetilde{H}(-\xi',\xi,t), \tag{1.114}$$

$$\text{Im}\widetilde{\mathcal{E}}(\xi',\xi,t) = \widetilde{E}(\xi',\xi,t) + \widetilde{E}(-\xi',\xi,t), \tag{1.115}$$

where the coefficient functions $C^\pm$ are functions of x and ξ' given by

$$C^\pm(x,\xi'), = \frac{1}{x-\xi'} \pm \frac{1}{x+\xi'}. \tag{1.116}$$

One clearly sees that they are (anti)symmetric function in ξ',

$$\text{Re}\{\mathcal{H},\mathcal{E}\}(-\xi',\xi,t) = \text{Re}\{\mathcal{H},\mathcal{E}\}(\xi',\xi,t), \tag{1.117}$$

$$\text{Re}\{\widetilde{\mathcal{H}},\widetilde{\mathcal{E}}\}(-\xi',\xi,t) = -\text{Re}\{\widetilde{\mathcal{H}},\widetilde{\mathcal{E}}\}(\xi',\xi,t), \tag{1.118}$$

$$\text{Im}\{\mathcal{H},\mathcal{E}\}(-\xi',\xi,t) = -\text{Im}\{\mathcal{H},\mathcal{E}\}(\xi',\xi,t), \tag{1.119}$$

$$\text{Im}\{\widetilde{\mathcal{H}},\widetilde{\mathcal{E}}\}(-\xi',\xi,t) = \text{Im}\{\widetilde{\mathcal{E}},\widetilde{\mathcal{E}}\}(\xi',\xi,t). \tag{1.120}$$

Finally, the complex functions of the CFFs write

$$\mathcal{F}(\xi',\xi,t) = \text{Re}\mathcal{F}(\xi',\xi,t) - i\pi\text{Im}\mathcal{F}(\xi',\xi,t), \tag{1.121}$$

where $\mathcal{F} \in \{\mathcal{H}, \mathcal{E}, \widetilde{\mathcal{H}}, \widetilde{\mathcal{E}}\}$, and the singlet GPDs directly write $F_+(x,\xi,t)$ for nucleons, where $F_+ \in \{H_+, E_+, \widetilde{H}_+, \widetilde{E}_+\}$. The current notation of the eight CFFs in Eqs. (1.108)-(1.115) follows the notation of VGG for DVCS [29, 30, 31, 32, 33] and for TCS [59], and differs from the notation of Belitsky [57], where Belitsky includes a minus sign for the real parts of CFFs and include $-\pi$ factors for the imaginary parts.

1.3.2 Challenge of DDVCS experiments

Not taking target polarization into account, the fully differential cross section of the exclusive electroproduction of a lepton pair is a 7-fold differential cross section, which is denoted, for simplicity, by

$$d^7\sigma = \frac{d^7\sigma}{dx_{\rm B} dQ^2 dt dQ'^2 d\phi d\Omega_l}. \tag{1.122}$$

When integrating $d^7\sigma$ over the solid angle Ω_l of the produced lepton pair, the resulting 5-fold DDVCS cross section $d^5\sigma$ reduces in the limit $Q'^2 \to 0$ to [55]

$$d^5\sigma = \frac{d^5\sigma}{dx_{\rm B} dQ^2 dt dQ'^2 d\phi} \to \frac{d^4\sigma}{dx_{\rm B} dQ^2 dt d\phi} \left(\frac{N}{Q'^2}\right), \tag{1.123}$$

where the 4-fold DVCS cross section $d^4\sigma$ appears on the right. The factor N is given by

$$N = \frac{4}{3}\left(\frac{\alpha_{\rm em}}{4\pi}\right) \tag{1.124}$$

where $\alpha_{\rm em} \approx 1/137$ is the fine structure constant, which is introduced by the decay of the time-like photon into the lepton pair. At $Q'^2 = 1$ GeV^2, the DDVCS cross section is reduced by at least a factor N of order 10^{-3}. At lower values of Q'^2, the DDVCS cross section rises, however, as $1/Q'^2$. In DDVCS, the value of Q'^2 cannot reach zero and the minimal is limited by the final lepton mass. It was demonstrated in [55] that Eq. (1.123) starts to be valid around $Q'^2 = 10^{-1}$ GeV at typical JLab kinematics. Thus, the DDVCS process is most challenging from the experimental point of view due to the small magnitude of the cross section. The measurements of DDVCS observables require high luminosity and large acceptance detectors for reasonable statistics.

Furthermore, the consideration of the electroproduction of e^+e^- pairs requires the addition of antisymmetrization due to the identity of the electrons in the final state. This complex antisymmetrization issue hampers any reliable experimental study. The production of muon pairs is the only feasible and promising channel for DDVCS with electron beam, necessitating a muon detector. The alternative approach is to investigate the production of electron pairs with a muon beam possibly at COMPASS [61] if luminosity allows.

Finally, the muon pair signal in the $eN \to eN\mu^-\mu^+$ reaction is contaminated by the muons resulting from the decay of vector mesons. In order to minimize contamination from meson decay, the measurements might be performed by avoiding the regions of Q'^2 close to meson thresholds. However, this certainly restricts the phase space in the measurements of GPDs and calls for even higher luminosity since the DDVCS cross section decreases as $1/Q'^2$ in Eq. (1.123).

Due to the challenges above, DDVCS data have never been extracted. Thanks to the 12 GeV upgrade of the CEBAF accelerator, it has been proposed as Letter-of-Intent to

investigate the electroproduction of muon pairs with CLAS12 [62] and with SoLID [63] respectively. In Hall B, the muon pair final state is employed to avoid antisymmetrization issue for DDVCS, as well as reducing combinatorial background in a simultaneous measurment of J/Ψ electroproduction. The standard CLAS12 forward detectors is shielded by a 30 cm thick Tungsten absorber to allow operation as a muon detector and run at luminosity around 10^{37} cm^{-2}·s^{-1} after various modification of the CLAS12 detector. In Hall A, the SoLID spectrometer is a large acceptance solenoidal detector designed to run a high luminosity, which could be used for DDVCS by adding an end-cap muon detector. A parasitic measurement during the J/Ψ experiment at a luminosity of order 10^{37} cm^{-2}·s^{-1} would open the investigation of the DDVCS process and would guide a dedicated experiment at 10 times larger luminosity. An muon detector R&D program is ongoing to meet the requirements for DDVCS with SoLID [60].

Considering the experimental challenges associated to DDVCS in terms of luminosity and detector acceptance, it appears necessary to establish the pertinence of this process at reachable kinematics at existing facilities. Thus, I focus my study on the investigation of DDVCS for a 11 GeV beam and a proton target within the context of JLab. Polarized targets cannot sustain the required luminosity and therefore falls beyond the scope of this study. The discussion of a small-acceptance experiment at a high luminosity, measuring the sign change behavior of the beam spin observables by varying Q'^2 at fixed $(Q^2, x_{\rm B}, t)$ points, is the starting point of this investigation. From an extended data set covering a large kinematic domain, the dependence of GPDs on the three physics variable would eventually be extracted. Before all of these, I present the theoretical formalism of the DDVCS process in the following chapter.

Chapter 2

Theoretical framework

2.1 Kinematics and phase space

2.1.1 Kinematics

Seven independent variables are required to describe the 4-body final state reaction $eN \to eNl^+l^+$ at a fixed beam energy E. They are usually chosen as Q^2, $x_{\rm B}$, t, Q'^2, ϕ and Ω_l. The former four Lorentz invariants are defined by the four-momenta of particles as

$$\begin{aligned} Q^2 = -q^2 = -(k-k')^2, \quad x_{\rm B} = \frac{Q^2}{2p\cdot q}, \\ Q'^2 = q'^2 = (l_- + l_+)^2, \quad t = \Delta^2 = (p'-p)^2 = (q-q')^2, \end{aligned} \tag{2.1}$$

where the particle momenta are indicated in Fig. 1.18. The azimuthal angle ϕ between the electron scattering plane ($e \to e\gamma^*$) and the hadronic production plane ($\gamma^* N \to \gamma^{*\prime} N$) is defined within the Trento convention [40]. The solid angle of a final-state lepton Ω_l is usually chosen in the l^-l^+ center-of-mass frame, whose differential element is given by

$$d\Omega_l = \sin\theta_l d\theta_l d\varphi_l. \tag{2.2}$$

Angles are graphically defined in Fig. 2.1.

In DDVCS experiments, at a fixed beam energy E, the invariant Q^2 and the Bjorken variable $x_{\rm B}$ can be determined by the measurements of the final electron (E', θ_e) by the relation Eqs. (1.61)-(1.62). The invariants Q'^2, t and the angles can be obtained by the measurements of the three-momenta of the final muon pair. Similarly to DVCS experiments, the measurements of the recoiled nucleon provide kinematic redundancy and overconstraint, which is the best way to ensure exclusivity of the process.

Reference frames

Various reference frames are applied in the computations for DDVCS. The intermediate process $\gamma^* N \to \gamma^{*\prime} N$ of the DDVCS process is an analog of the DVCS process and one can choose a similar frame (Fig. 1.13) to describe the subprocess. The calculation for the time-photon decay is usually performed in a center-of-frame frame, as well as with respect to kinematics boundaries. The reference frames and the corresponding computations are listed in the following:

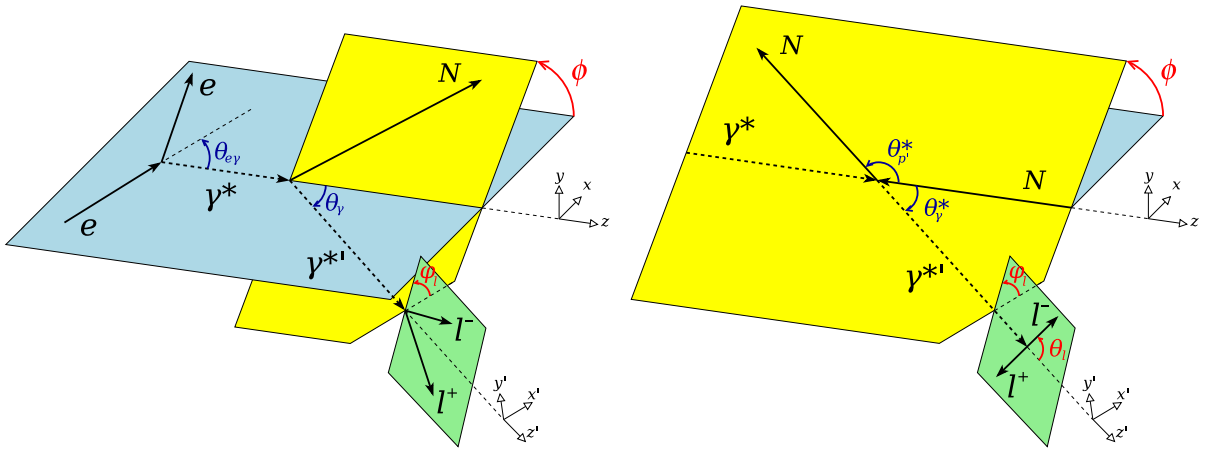

Figure 2.1: Left panel: DDVCS in the target rest frame. The coordinate system (x, y, z) with the z-axis being aligned to the spacelike virtual photon is named TRF-I, while the one (x', y', z') with z' along the timelike photon is named TRF-II. Right panel: DDVCS in the center-of-mass frames. The $\gamma^* N$ CM frame is related to TRF-I by the boost of the space-like photon along z-axis, while the $l^- l^+$ CM frame is related to TRF-II by the boost of the time-like photon along z'-axis. φ_l and θ_l are respectively the azimuthal and polar angles between the l^- and the time-like photon in the $l^- l^+$ CM frame.

(a) Firstly, I introduce the first target rest frame (TRF-I) in which the z-axis is directed in the direction of the three-momentum of the space-like photon and the x-axis is chosen on the electron scattering plane and for positive x-component of the incoming lepton momentum (Fig. 2.1 left panel). In TRF-I, the momenta of the particles are given as follows:

(i) For the initial nucleon and the space-like photon, one has

$$p = (M, 0, 0, 0), \quad q = (\nu, 0, 0, q^z) \tag{2.3}$$

where the photon components can be given by the invariants as

$$\nu = \frac{Q^2}{2Mx_{\rm B}}, \quad q^z = \sqrt{Q^2 + \left(\frac{Q^2}{2Mx_{\rm B}}\right)^2}. \tag{2.4}$$

(ii) For the incident electron, the momentum writes

$$k = (E, k^x, 0, k^z) = E(1, \sin\theta_{e\gamma}, 0, \cos\theta_{e\gamma}), \tag{2.5}$$

where $\theta_{e\gamma}$ is the polar angle between the incident electron and the space-like photon. One has

$$\sin\theta_{e\gamma} = \frac{Q\sqrt{E(E-\nu) - Q^2/4}}{Eq^z}, \quad \cos\theta_{e\gamma} = \frac{E\nu + Q^2/2}{Eq^z}. \tag{2.6}$$

(iii) For the time-like photon, the momentum writes

$$q' = (\omega, \omega\boldsymbol{v}), \tag{2.7}$$

where its energy and velocity can be described by the invariants following

$$\omega = \nu + \frac{t}{2M}, \quad v = |\boldsymbol{v}| = \sqrt{1 - \frac{Q'^2}{\omega^2}}. \tag{2.8}$$

(b) Secondly, I introduce the $\gamma^* N$ CM frame (Fig. 2.1 right panel), in which the variables are denoted by an asterisk superscript, in order to derive the boundary of the invariant t. The center-of-mass total energy W is given by Eq. (1.64), and the momenta of the particles in the $\gamma^* N$ CM frame write as follows:

(i) For the initial nucleon $p^*(E_p^*, \boldsymbol{p}^*)$ and the space-like photon $q^*(\nu^*, \boldsymbol{q}^*)$, one has

$$E_p^* = \frac{M\nu + M^2}{W}, \quad \nu^* = \frac{M\nu - Q^2}{W}, \quad |\boldsymbol{p}^*| = |\boldsymbol{q}^*| = \frac{q^z M}{W}. \tag{2.9}$$

(ii) For the final nucleon $p'^*(E_{p'}^*, \boldsymbol{p'}^*)$ and the time-like photon $q'^*(\omega^*, \boldsymbol{q'}^*)$, there are

$$\begin{aligned} E_{p'}^* &= \frac{W^2 - Q'^2 + M^2}{2W}, \quad \omega^* = \frac{W^2 + Q'^2 - M^2}{2W}, \\ |\boldsymbol{p'}^*| = |\boldsymbol{q'}^*| &= \frac{1}{2W}\sqrt{\left[(W-M)^2 - Q'^2\right]\left[(W+M)^2 - Q'^2\right]}. \end{aligned} \tag{2.10}$$

Consequently, the final nucleon energy in TFR-I can be obtained by using Lorentz transformation as

$$\begin{aligned} E_{p'} &= \frac{1}{2W^2}\Big\{(\nu + M)(W^2 - Q'^2 + M^2) \\ &\quad + q^z \cos\theta_{p'}^* \sqrt{\left[(W-M)^2 - Q'^2\right]\left[(W+M)^2 - Q'^2\right]}\Big\}, \end{aligned} \tag{2.11}$$

and the components of the time-like photon momentum $q'(\omega, q'^x, q'^y, q'^z)$ are give by

$$\begin{aligned} \omega &= \frac{1}{2W^2}\Big\{(\nu + M)(W^2 + Q'^2 - M^2) \\ &\quad + q^z \cos\theta_\gamma^* \sqrt{\left[(W-M)^2 - Q'^2\right]\left[(W+M)^2 - Q'^2\right]}\Big\}, \end{aligned} \tag{2.12}$$

$$q'^x = -\frac{\cos\phi \sin\theta_\gamma^*}{2W}\sqrt{\left[(W-M)^2 - Q'^2\right]\left[(W+M)^2 - Q'^2\right]}, \tag{2.13}$$

$$q'^y = -\frac{\sin\phi \sin\theta_\gamma^*}{2W}\sqrt{\left[(W-M)^2 - Q'^2\right]\left[(W+M)^2 - Q'^2\right]}, \tag{2.14}$$

$$\begin{aligned} q'^z &= \frac{1}{2W^2}\Big\{q^z(W^2 + Q'^2 - M^2) \\ &\quad + \cos\theta_\gamma^*(\nu + M)\sqrt{\left[(W-M)^2 - Q'^2\right]\left[(W+M)^2 - Q'^2\right]}\Big\}, \end{aligned} \tag{2.15}$$

where θ^* is the scattering angle of the time-like photon and scattered nucleon in the $\gamma^* N$ CM frame with the relationship $\theta_{p'}^* = \pi - \theta_\gamma^*$ ranging from 0 to π. The square of the momentum transfer to the nucleon $t = (p - p')^2$ then writes

$$\begin{aligned} t &= -\frac{M}{W^2}\Big\{(\nu + M)(W^2 - Q'^2 + M^2) - 2MW^2 \\ &\quad + q^z \cos\theta_{p'}^* \sqrt{\left[(W-M)^2 - Q'^2\right]\left[(W+M)^2 - Q'^2\right]}\Big\}. \end{aligned} \tag{2.16}$$

The definitions of $t_{\rm min}$ and $t_{\rm max}$ in DDVCS are similar to DVCS, and write

$$\begin{aligned} t_{\rm min,max} &= -\frac{M}{W^2}\Big\{(\nu+M)(W^2-Q'^2+M^2)-2MW^2 \\ &\quad \pm q^z\sqrt{\left[(W-M)^2-Q'^2\right]\left[(W+M)^2-Q'^2\right]}\Big\}, \end{aligned} \tag{2.17}$$

with the + (−) sign standing for $t_{\rm max}$ ($t_{\rm min}$).

(c) Thirdly, it is very suitable for evaluation of scalar products of four-momenta at intermediate stages in the second target rest frame (TRF-II), in which the z'-axis is directed along the velocity vector $\boldsymbol{v}$ of the time-like photon and the x'-axis lies in the hadron scattering plane (Fig. 2.1 left panel). In TRF-II, the particle momenta read as follows:

(i) For the initial nucleon and the two photons, one obvious has

$$p=(M,0,0,0), \quad q=(\nu,q^z\sin\theta_\gamma,0,q^z\cos\theta_\gamma), \quad q'=(\omega,0,0,\omega v), \tag{2.18}$$

with

$$\cos\theta_\gamma=\frac{Q^2-Q'^2+t+2\nu\omega}{2q^z\omega v}. \tag{2.19}$$

(ii) For the incoming electron, the momentum reads

$$\begin{aligned} k &= E(1,\ -\sin\theta_{e\gamma}\cos\theta_\gamma\cos\phi+\cos\theta_{e\gamma}\sin\theta_\gamma, \\ &\quad \sin\theta_{e\gamma}\sin\phi,\ \sin\theta_{e\gamma}\sin\theta_\gamma\cos\phi+\cos\theta_{e\gamma}\cos\theta_\gamma). \end{aligned} \tag{2.20}$$

(d) Finally, I introduce the l^-l^+ CM frame (Fig. 2.1 right panel), in which the variables are denoted by an asterisk superscript except the angles θ_l and φ_l of the final lepton l^-. Since the lepton angles defined in the l^-l^+ CM frame are chosen to describe the differential cross section (see Sec. 2.2), their asterisk superscript is removed for neat expressions for the cross section. In this frame, the momentum of the final lepton l^- writes

$$l^*_-=\left(\frac{Q'}{2},\frac{Q'}{2}\boldsymbol{\beta}\right), \tag{2.21}$$

where velocity $\boldsymbol{\beta}$ is given by

$$\beta=|\boldsymbol{\beta}|=\sqrt{1-\frac{4m_\mu^2}{Q'^2}} \tag{2.22}$$

with the lepton (muon) mass m_μ. Consequently, the momentum of l^- viewed from TRF-II moving with the velocity $-\boldsymbol{v}$ is given by

$$\begin{aligned} l_- &= \Big(\frac{1}{2}\omega(1+v\beta\cos\theta_l),\ \frac{1}{2}Q'\beta\sin\theta_l\cos\varphi_l, \\ &\quad \frac{1}{2}Q'\beta\sin\theta_l\sin\varphi_l,\ \frac{1}{2}\omega(v+\beta\cos\theta_l)\Big), \end{aligned} \tag{2.23}$$

form which the momentum l_+ of the other lepton is simply deduced by the substitution of

$$\left\{\begin{array}{lcl}\varphi_l & \to & \varphi_l+\pi \\ \theta_l & \to & \pi-\theta_l\end{array}\right. \quad \text{or} \quad \beta\to-\beta. \tag{2.24}$$

Using the particle momenta in TRF-II and introducing the energy loss fraction y of the electron and the nucleon mass correction factor ϵ,

$$y = \frac{p\cdot q}{p\cdot k} = \frac{\nu}{E}, \quad \epsilon = \frac{2Mx_{\rm B}}{Q}, \tag{2.25}$$

the invariant form of the scalar products entering the cross section can be derived as

$$\begin{aligned} k\cdot\Delta &= -\frac{1}{2y(1+\epsilon^2)}\Bigg\{(Q^2+Q'^2)\left(1-2K\cos\phi+\frac{y\epsilon^2}{2}\right) \\ &\quad -t\left(1-x_{\rm B}(2-y)+\frac{y\epsilon^2}{2}\right)\Bigg\}, \end{aligned} \tag{2.26}$$

$$\begin{aligned} l_-\cdot\Delta &= -\frac{\beta}{4v}\Bigg\{(Q^2+Q'^2)\left(\frac{v}{\beta}+\cos\theta_l+2\frac{QQ'}{Q^2+x_{\rm B}t}\frac{K\sin\theta_l\cos\varphi_l}{\sqrt{1-y-y^2\epsilon^2/4}}\right) \\ &\quad +t\left(\frac{v}{\beta}+\frac{Q^2-2x_{\rm B}Q'^2+x_{\rm B}t}{Q^2+x_{\rm B}t}\cos\theta_l\right)\Bigg\}, \end{aligned} \tag{2.27}$$

where

$$K = \frac{1}{2(Q^2+Q'^2)}\sqrt{\left(1-y-\frac{y^2\epsilon^2}{4}\right)\left[4x_{\rm B}(1-x_{\rm B})+\epsilon^2\right](t_{\rm min}-t)(t-t_{\rm max})}. \tag{2.28}$$

Symmetric variables

The Fourier expansions of DDVCS cross section in azimuthal angles has been only published by A. V. Belitsky and D. Müller in [57], where the results are presented in terms of the symmetric variables. These are introduced to describe approximate forms of scalar products entering the cross section, considered to be accurate enough for a leading twist evaluation of the cross section.

A few symmetric variables have been introduced in Eqs (1.100)-(1.102) in Section 1.3. Besides, an addition variable $\tilde{y}$ is introduced in [57] to make the results look symmetric and is given by

$$\frac{1}{\tilde{y}} = \frac{p\cdot l_-}{p\cdot q'} = \frac{1+v\beta\cos\theta_l}{2} \simeq \frac{1+\cos\theta_l}{2}. \tag{2.29}$$

$\tilde{y}$ ranges in the interval $[1,+\infty)$ and $1/\tilde{y}$ can be interpreted as the lepton energy fraction of the decay.

Neglecting the nucleon mass corrections $\sim M^2/Q^2$ and keeping only the leading and sub-leading terms in the $1/(2P\cdot\bar{q})$ expansion, the scalar products of Eqs.(2.26) and (2.27) recast

$$k\cdot\Delta \approx \frac{\bar{q}^2}{y}\frac{\xi}{\xi'}(1-2K\cos\phi), \quad l_-\cdot\Delta \approx \frac{\bar{q}^2}{\tilde{y}}\frac{\xi}{\xi'}(1+2\widetilde{K}\cos\varphi_l), \tag{2.30}$$

with

$$\bar{q}^2 = -\frac{1}{2}\left(Q^2-Q'^2+t/2\right), \tag{2.31}$$

and

$$K \approx \frac{1}{2\xi}\sqrt{\left(-\frac{\xi'}{\bar{q}^2}\right)\left(\frac{1-\xi}{1+\xi}\right)(\xi+\xi')(1-y)(t_{\rm min}-t)}. \tag{2.32}$$

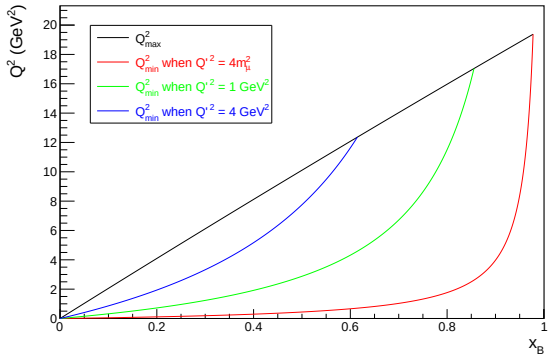

Figure 2.2: DDVCS $(Q^2, x_{\rm B})$ phase space.

The symmetric variable $\widetilde{K}$ can be derived through the substitution $\xi' \to -\xi'$ and $y \to \tilde{y}$,

$$\widetilde{K} \approx \frac{1}{2\xi}\sqrt{\left(-\frac{\xi'}{\bar{q}^2}\right)\left(\frac{1-\xi}{1+\xi}\right)(\xi-\xi')(\tilde{y}-1)(t_{\rm min}-t)}. \tag{2.33}$$

The scalar products and symmetric variables are used for the Fourier expansions of cross section (see Sec. 2.2).

2.1.2 Phase space

Electron view: $(Q^2, x_{\rm B})$ phase space

If the DDVCS process happens in the eN reaction, $E_{p'}$ shall be at least larger than M. Taking into account this condition in the $\gamma^* N$ CM frame, namely $E^*_{p'} \geqslant M$, one obtains

$$Q^2 \geqslant \frac{x_{\rm B}}{1-x_{\rm B}} Q'(Q'+2M), \tag{2.34}$$

which indicates that Q^2 has a minimum limit at fixed $x_{\rm B}$ and Q'. If the muon pairs are the expected final states, Q' shall be larger than the mass of a muon pair $Q' \geqslant 2m_\mu$. Therefore, Q^2 must satisfy the limit given by

$$Q^2 \geqslant \frac{4x_{\rm B}}{1-x_{\rm B}} m_\mu(m_\mu + M). \tag{2.35}$$

As DVCS case, Q^2 has a maximum given at fixed $x_{\rm B}$ by

$$Q^2_{\rm max} = \frac{4E^2 M x_{\rm B}}{M x_{\rm B} + 2E}. \tag{2.36}$$

Fig. 2.2 shows the DDVCS $(Q^2, x_{\rm B})$ phase space at some fixed Q'^2 $(4m_\mu^2, 1, 4$ GeV$^2)$ for a 11 GeV beam[1]. Unlike DVCS, which has a triangle-shape $(Q^2, x_{\rm B})$ phase space (Fig. 1.14), DDVCS has a curved-shape $Q^2_{\rm min}$.

[1]I remind that $E = 11$ GeV is kept in the following unless explicitly indicated

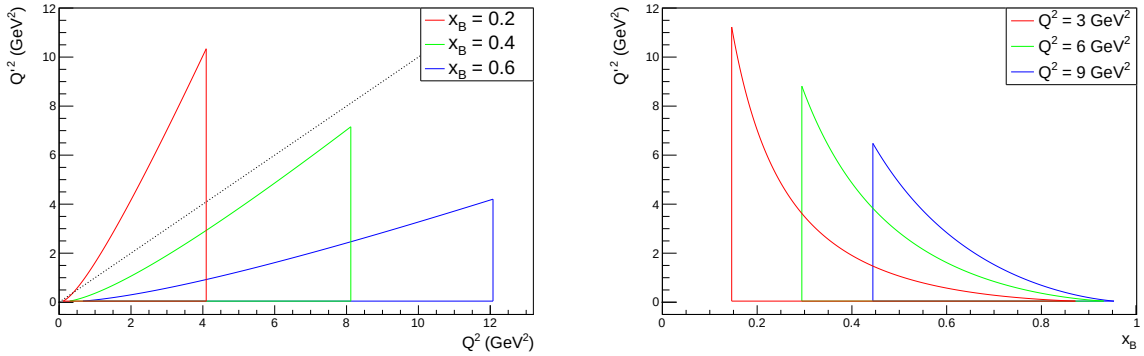

Figure 2.3: DDVCS (Q'^2, Q^2) and $(Q'^2, x_{\rm B})$ phase space. The dotted line in the left panel corresponds $Q^2 = Q'^2$.

Time-like photon view: (Q'^2, Q^2) and $(Q'^2, x_{\rm B})$ phase spaces

From Eq. (2.34), it can also be derived that

$$Q' \leqslant \sqrt{M^2 + \frac{Q^2}{x_{\rm B}} - Q^2} - M, \tag{2.37}$$

expressing the maximal Q' at fixed Q^2 and $x_{\rm B}$. Moreover, if a muon pair is produced, there shall be

$$Q' \geqslant 2m_\mu. \tag{2.38}$$

Fig. 2.3 (left panel) shows the (Q'^2, Q^2) phase space at some fixed $x_{\rm B}$ $(0.2, 0.4, 0.6)$. The general fact here is that the increase in Q^2 expands the Q'^2 range at fixed $x_{\rm B}$ and the increase in $x_{\rm B}$ reduces the the Q'^2 range at fixed Q^2. The dotted line represents the relation $Q'^2 = Q^2$. It is observed that at large $x_{\rm B}$, 0.4 and 0.6 for instance, all the Q'^2 values are in the $Q'^2 < Q^2$ region. Only at small $x_{\rm B}$, Q'^2 values can be in both $Q'^2 < Q^2$ and $Q'^2 > Q^2$ regions. Fig. 2.3 (right panel) also shows the $(Q'^2, x_{\rm B})$ phase space at some fixed Q^2 $(3, 6, 9$ GeV$^2)$ and one can get the same general feature.

Nucleon view: (t, Q^2), $(t, x_{\rm B})$ and (t, Q'^2) phase spaces

The t boundaries are given by Eq. (2.17). Fig. 2.4 (left panel) shows the (t, Q^2) phase space at fixed $x_{\rm B}$ $(0.2, 0.4, 0.6)$ and Q'^2 $(4m_\mu^2, 1, 4$ GeV$^2)$. It can be seen that

(a) the phase spaces shrink when Q'^2 increases ;

(b) the larger Q^2 has the wider t range at fixed $(x_{\rm B}, Q'^2)$, larger $|t_{\rm min}|$ and larger $|t_{\rm max}|$;

(c) the smaller $x_{\rm B}$ also has the wider range in t at fixed (Q^2, Q'^2) but smaller $|t_{\rm min}|$.

Fig. 2.4 (right panel) shows the $(t, x_{\rm B})$ phase space at fixed Q^2 $(3, 6, 9$ GeV$^2)$ and Q'^2 $(4m_\mu^2, 1, 4$ GeV$^2)$, and similar conclusions can be obtained. The left panel of Fig. 2.5 shows the (t, Q'^2) phase space at fixed Q^2 $(3, 6, 9$ GeV$^2)$ and $x_{\rm B} = 0.5$ and the right panel displays the one at fixed $x_{\rm B}$ $(0.2, 0.4, 0.6)$ and $Q^2 = 3$ GeV^2. In addition to the similar general features described above, one also observes that the larger Q^2 and smaller $x_{\rm B}$ enlarge the (t, Q'^2) phase space.

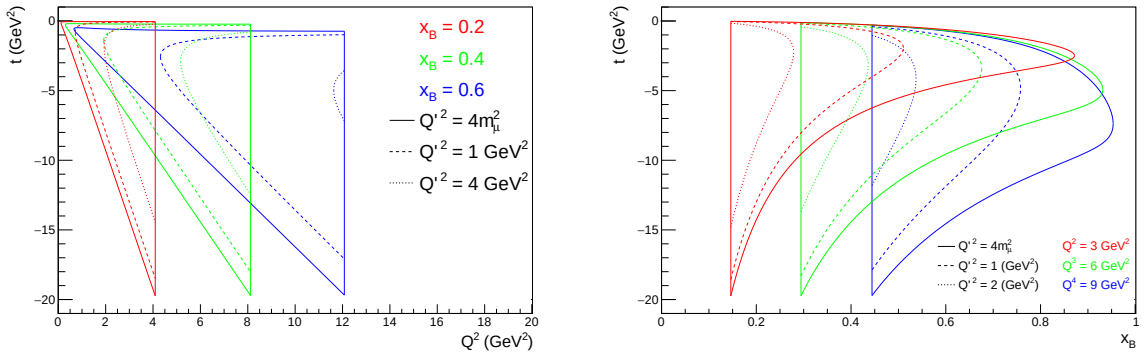

Figure 2.4: DDVCS (t, Q^2) and (t, x_{B}) phase space.

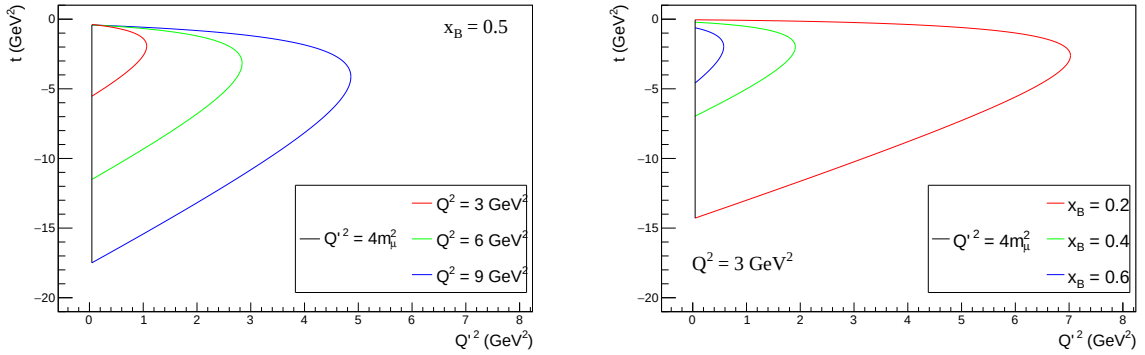

Figure 2.5: DDVCS (t, Q'^2) phase space at $x_{\mathrm{B}} = 0.5$ (left) and $Q^2 = 3$ GeV^2 (right).

GPDs view: (ξ, ξ') phase spaces

For the QCD factorization to be applicable one has to impose the conditions $-t \ll Q^2$ and $Q^2 \gg M^2$. Removing the negligible terms $\sim t/Q^2$ from Eqs. (1.101) and (1.102), the scaling variables rewrite

$$\xi' = \frac{1 - Q'^2/Q^2}{(2 - x_{\mathrm{B}})/x_{\mathrm{B}} - Q'^2/Q^2}, \quad \xi = \frac{1 + Q'^2/Q^2}{(2 - x_{\mathrm{B}})/x_{\mathrm{B}} - Q'^2/Q^2}. \tag{2.39}$$

From the expressions above, one easily get the linear relation between ξ' and ξ at $t = 0$ given by

$$\xi = -\left(\frac{1}{1 - x_{\mathrm{B}}}\right)\xi' + \left(\frac{x_{\mathrm{B}}}{1 - x_{\mathrm{B}}}\right). \tag{2.40}$$

Leaving aside the other phase space, the (ξ, ξ') phase space in Fig. 2.6 (left panel) illustrates the relation at various fixed x_{B} represented by the solid lines. The smaller x_{B} one has, the closer one lies to the TCS region, and $x_{\mathrm{B}} = 0$ results in $\xi = -\xi'$, which is the TCS restriction. Besides, the t-correction for some small $-t$ is represented by the dashed, dotted and dash-dotted lines and acts as a shift to the TCS direction. The extent of the shift depends on the magnitude of t/Q^2.

Furthermore, another linear relation can be also derived from Eq. (2.39),

$$\xi = \left(\frac{1 + Q'^2/Q^2}{1 - Q'^2/Q^2}\right)\xi'. \tag{2.41}$$

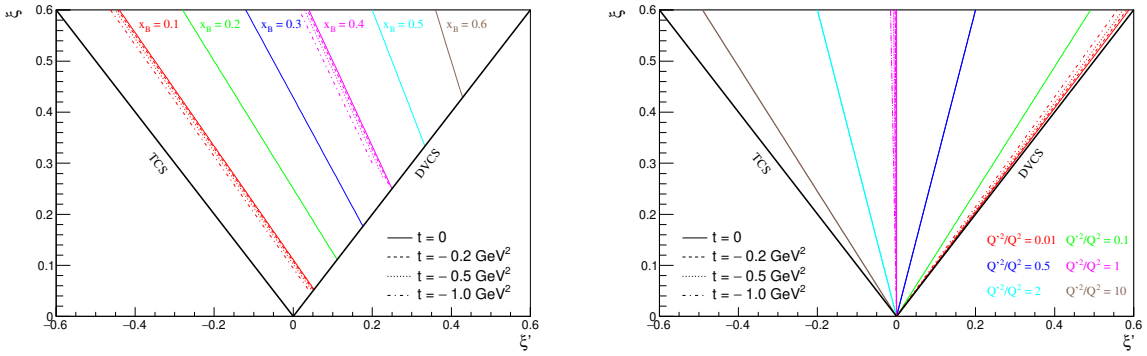

Figure 2.6: (ξ, ξ') phase space for some fixed x_{B} (left) and some fixed ratios Q'^2/Q^2 (right).

Ignoring the other phase space, the relation for some fixed ratios of Q'^2/Q^2 is displayed by the solid lines in the right panel of Fig. 2.6. When the ratio increases, the line rotates from the DVCS side to the TCS side. $Q'^2 = 0$ leads to $\xi = \xi'$ being the DVCS restriction and $Q^2 = 0$ results in $\xi = -\xi'$. Specially, when $Q'^2 = Q^2$ one reaches the zero value of generalized Bjorken variable $\xi' = 0$ pointed out by vertical magenta solid line.

DDVCS can access the CFFs in the region $|\xi'| < \xi$, where the skewness variable ξ ranges in principle in $0 \leqslant \xi \leqslant 1$ as shown in Fig. 1.19. However, for certain kinematics, it has an upper boundary $\xi_{\max}$ that cannot actually exceed an envelope determined by the kinematics condition $|t| \geqslant |t_{\min}|$, and the envelop is given by

$$\xi_{\max} \leqslant \sqrt{-\frac{t}{4M^2 - t}} \tag{2.42}$$

for all possible E, x_{B}, Q^2 and Q'^2. Fig. 2.7 shows the maximal coverage in ξ and ξ' for some fixed t. The coverages at $t = -0.01$, -0.1 and -1 GeV^2 are indicated respectively by the green, yellow and cyan area, and upper limits of the envelopes are represented by the dashed, dotted and dash-dotted lines, respectively. Note that the coverage at large $|t|$ contains the one at small $|t|$. The higher ξ, the larger the coverage of CFFs. To reach large ξ one shall reach large $|t|$. Therefore, to map out the GPDs at large ξ requires high beam energy in order to reach large Q^2 and consequently satisfy the factorization condition at large $-t$.

To conclude, at a fixed x_{B}, one accesses the GPDs in (ξ, ξ') along a line mostly fixed by x_{B} at small $-t$. The accessed maximal ξ-range depends on t, and finally the accessed po-

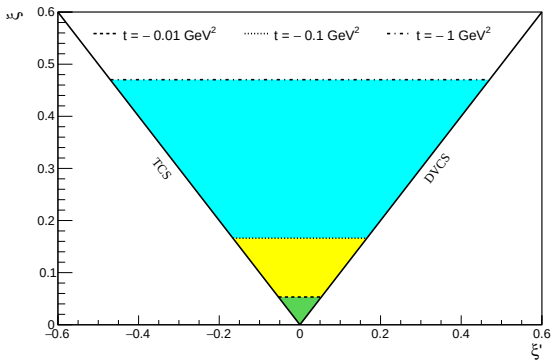

Figure 2.7: (ξ, ξ') maximal coverage for some fixed t.

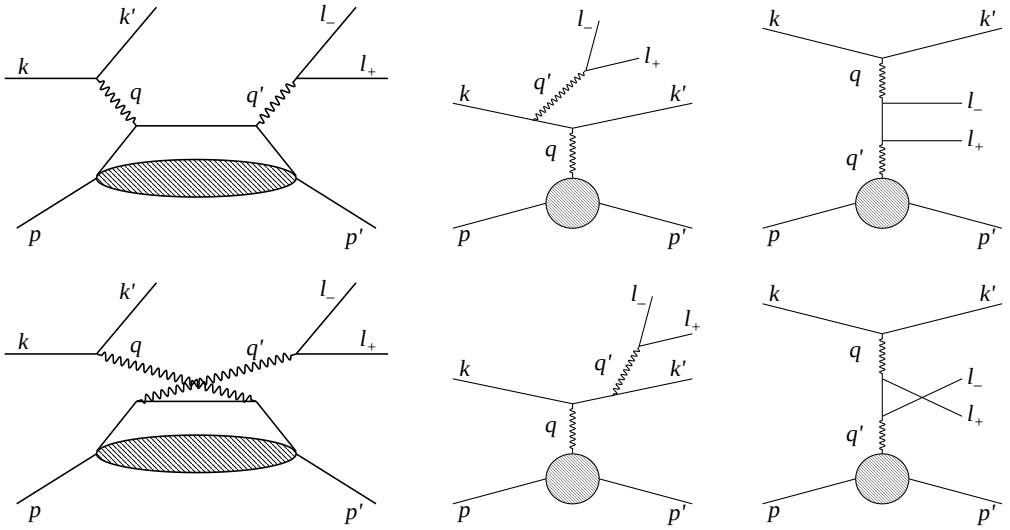

Figure 2.8: The subprocesses contributing to the electroproduction of lepton pairs including DDVCS (left panels), BH1 (middle panels) with the di-lepton emitted by the initial and final electrons, and BH2 (right panels) with the di-lepton virtual production in the nuclear field.

sition within the line is determined by Q^2 and Q'^2. Combining with the other phase space, the specific (ξ, ξ') phase space of some experimental projects is discussed in chapter. 5.

2.2 Cross section

The theoretical formalism and the factorization theorem associated with the DDVCS process have been developed to leading power accuracy in [57], as well as the Fourier expansion of the differential cross section for the exclusive electroproduction of a lepton pair $eN \to eNl^-l^+$. In this section, I briefly present the 7-fold differential cross section at leading order and leading twist for unpolarized targets.

Firstly, I remark that the factorization condition mentioned before, $Q^2 \gg M^2$ and $t \ll Q^2$, is just one part of the full condition. In the DDVCS case, it is the inverse s-channel energy $2P \cdot \bar{q}$ that sets the distance between the quark fields in the Compton scattering amplitude [57] rather than the virtuality Q^2 or $|\bar{q}^2|$. Therefore, to ensure the factorization regime, one has to impose the condition

$$2P \cdot \bar{q} = -\frac{\bar{q}^2}{\xi'} = \frac{1}{2}\left(\frac{2Q^2}{x_{\rm B}} - Q^2 - Q'^2 + t\right) \gg \max\{M^2, -t\}, \tag{2.43}$$

which is named "the generalized Bjorken limit". In this limit, one or both photon virtualities need to be large, namely

$$Q^2 + Q'^2 \gg M^2 \text{ and } -t \ll Q^2 + Q'^2. \tag{2.44}$$

As long as Q^2 and Q'^2 are large, the factorization condition is still satisfied even when $|\bar{q}^2| \simeq 0$ at $Q^2 \simeq Q'^2$. Consequently, the zero ξ'-value can be reached under the factorization regime in the DDVCS process.

The reaction of $eN \to eNl^-l^+$ consists of three undistinguishable interfering processes, depicted in Fig. 2.8: the DDVCS process and two Bethe-Heitler processes denoted BH1

and BH2 respectively. The BH1 process is an analog to the DVCS case (Fig. 1.17), but the BH2, in which the lepton pair production caused by both virtual photon in the nuclear field, is a new mechanism. As mentioned before, they are calculable in QED to a high degree of accuracy at small $-t$, *i.e.* in the momentum transfer region where elastic FFs are precisely known. The 7-fold differential cross section in terms of experimentally measurable variables reads

$$\frac{d^7\sigma}{dx_{\rm B}dQ^2dtdQ'^2d\phi d\Omega_l} = A^{\rm PS}\left|\frac{\mathcal{T}}{e^4}\right|^2 \tag{2.45}$$

being proportional to the square of the total amplitude corresponding to the coherent sum of the three processes, which contains three essentially different contributions,

$$\mathcal{T}^2 = |\mathcal{T}_{\rm BH1} + \mathcal{T}_{\rm BH2}|^2 + |\mathcal{T}_{\rm DDVCS}|^2 + \mathcal{I}, \tag{2.46}$$

with

$$\mathcal{I} = \mathcal{T}_{\rm DDVCS}\mathcal{T}^*_{\rm BH1} + \mathcal{T}^*_{\rm DDVCS}\mathcal{T}_{\rm BH1} + \mathcal{T}_{\rm DDVCS}\mathcal{T}^*_{\rm BH2} + \mathcal{T}^*_{\rm DDVCS}\mathcal{T}_{\rm BH2}. \tag{2.47}$$

The phase space prefactor $A^{\rm PS}$ is given by

$$A^{\rm PS} = \frac{\alpha^4_{\rm em}}{16(2\pi)^3}\frac{x_{\rm B}y^2\beta}{Q^4\sqrt{1+\epsilon^2}} \tag{2.48}$$

Analogous to the DVCS case, the pure BH terms are given in terms of FFs, the pure DDVCS and interference terms are respectively bilinear and linear in CFFs. Therefore, the decomposition of the cross section in terms of beam charge and polarization can be given by

$$\begin{aligned} d^7\sigma &= d^7\sigma^{\rm BH1}_{\rm UU} + d^7\sigma^{\rm BH2}_{\rm UU} + (-e_l)d^7\sigma^{\rm BH12}_{\rm UU} + d^7\sigma^{\rm DDVCS}_{\rm UU} + (-e_l)d^7\sigma^{\rm INT1}_{\rm UU} + d^7\sigma^{\rm INT2}_{\rm UU} \\ &\quad + P_l\left[d^7\sigma^{\rm DDVCS}_{\rm LU} + (-e_l)d^7\sigma^{\rm INT1}_{\rm LU} + d^7\sigma^{\rm INT2}_{\rm LU}\right], \end{aligned} \tag{2.49}$$

where the superscript INT1 and INT2 stand for the contributions of DDVCS interfering with BH1 and BH2, respectively, and BH12 represents the interference contributions between two Bethe-Heitler processes. The helicity-dependent contribution of the imaginary DDVCS amplitude, denoted $d^7\sigma^{\rm DDVCS}_{\rm LU}$ in Eq. (2.49), arises from the interference of twist-2 and twist-3 CFFs and equals to zero in the twist-2 approximation. As for the DDVCS process it is expected to be small and therefore is not presented in the following unless necessary. The contributions as a Fourier expansion in terms of the azimuthal angles, ϕ of the recoiled nucleon and φ_l of a lepton in the final pair, are introduced in the following. Note that θ_l-dependence is embedded inside the Fourier coefficients with the symmetric variable $\tilde{y}$ given by Eq. (2.29). As mentioned previously, φ_l and θ_l are defined in the l^-l^+ CM frame.

2.2.1 Bethe-Heitler contributions

The Bethe-Heitler contributions can be expressed by

$$\begin{aligned} d^7\sigma_{\rm UU}^{\rm BH1} \;\propto\; & \frac{1}{\mathcal{P}_1^2\mathcal{P}_2^2(\phi)}\Big\{ \left[cc_{00}^{\rm BH1} + cc_{02}^{\rm BH1}\cos(2\varphi_l)\right] \\ & + \left[cc_{11}^{\rm BH1}\cos(\varphi_l)\right]\cos(\phi) + \left[cc_{20}^{\rm BH1} + cc_{22}^{\rm BH1}\cos(2\varphi_l)\right]\cos(2\phi) \\ & + \left[cc_{31}^{\rm BH1}\cos(\varphi_l)\right]\cos(3\phi) + \left[cc_{42}^{\rm BH1}\cos(2\varphi_l)\right]\cos(4\phi) \\ & + \left[ss_{11}^{\rm BH1}\sin(\varphi_l)\right]\sin(\phi) + \left[ss_{22}^{\rm BH1}\sin(2\varphi_l)\right]\sin(2\phi) \\ & + \left[ss_{31}^{\rm BH1}\sin(\varphi_l)\right]\sin(3\phi) + \left[ss_{42}^{\rm BH1}\sin(2\varphi_l)\right]\sin(4\phi)\Big\}, \end{aligned} \tag{2.50}$$

$$\begin{aligned} d^7\sigma_{\rm UU}^{\rm BH2} \;\propto\; & \frac{1}{\mathcal{P}_3^2\mathcal{P}_4^2(\theta_l,\varphi_l)}\Big\{ \left[cc_{00}^{\rm BH2} + cc_{20}^{\rm BH2}\cos(2\varphi_l)\right] \\ & + \left[cc_{11}^{\rm BH2}\cos(\varphi_l) + cc_{31}^{\rm BH2}\cos(3\varphi_l)\right]\cos(\phi) \\ & + \left[cc_{02}^{\rm BH2} + cc_{22}^{\rm BH2}\cos(2\varphi_l) + cc_{42}^{\rm BH2}\cos(4\varphi_l)\right]\cos(2\phi) \\ & + \left[ss_{11}^{\rm BH2}\sin(\varphi_l) + ss_{31}^{\rm BH2}\sin(3\varphi_l)\right]\sin(\phi) \\ & + \left[ss_{22}^{\rm BH2}\sin(2\varphi_l) + ss_{42}^{\rm BH2}\sin(4\varphi_l)\right]\sin(2\phi)\Big\}, \end{aligned} \tag{2.51}$$

$$\begin{aligned} d^7\sigma_{\rm UU}^{\rm BH12} \;\propto\; & \frac{1}{\mathcal{P}_1\mathcal{P}_2(\phi)\mathcal{P}_3\mathcal{P}_4(\theta_l,\varphi_l)}\Big\{ \left[cc_{00}^{\rm BH12} + cc_{02}^{\rm BH12}\cos(2\varphi_l)\right] \\ & + \left[cc_{11}^{\rm BH12}\cos(\varphi_l)\right]\cos(\phi) + \left[cc_{20}^{\rm BH12} + cc_{22}^{\rm BH12}\cos(2\varphi_l)\right]\cos(2\phi) \\ & + \left[ss_{11}^{\rm BH12}\sin(\varphi_l)\right]\sin(\phi) + \left[ss_{22}^{\rm BH12}\sin(2\varphi_l)\right]\sin(2\phi)\Big\}. \end{aligned} \tag{2.52}$$

The BH propagators in the denominators are defined by

$$\begin{aligned} (k'+\Delta)^2 &= 4\xi P\cdot\bar{q}\;\mathcal{P}_1(\phi), & (k-\Delta)^2 &= 4\xi P\cdot\bar{q}\;\mathcal{P}_2(\phi), \\ (l_+ +\Delta)^2 &= -4\xi P\cdot\bar{q}\;\mathcal{P}_3(\theta_l,\varphi_l), & (l_- +\Delta)^2 &= -4\xi P\cdot\bar{q}\;\mathcal{P}_4(\theta_l,\varphi_l), \end{aligned} \tag{2.53}$$

and can be expressed in terms of invariants as

$$\begin{aligned} \mathcal{P}_1(\phi) &= \frac{2k\cdot\Delta + Q^2 + Q'^2}{Q^2+Q'^2}, & \mathcal{P}_2(\phi) &= \frac{t - 2k\cdot\Delta}{Q^2+Q'^2}, \\ \mathcal{P}_3(\theta_l,\varphi_l) &= -\frac{m_\mu^2 + 2l_+\cdot\Delta + t}{Q^2+Q'^2}, & \mathcal{P}_4(\theta_l,\varphi_l) &= -\frac{m_\mu^2 + 2l_-\cdot\Delta + t}{Q^2+Q'^2}, \end{aligned} \tag{2.54}$$

and can be expressed in terms of invariants as

with the scalar products given by Eqs. (2.26)-(2.28). Based on the definition of the propagators in Eq. (2.53) and the scalar products in Eq. (2.30), it can be seen that the product $\mathcal{P}_3\mathcal{P}_4$ is related with $\mathcal{P}_1\mathcal{P}_2$ through the interchange $\xi' \leftrightarrow -\xi'$, $y \leftrightarrow \tilde{y}$ and $\phi \leftrightarrow \varphi_l$, namely

$$\mathcal{P}_3\mathcal{P}_4(\xi', y, \tilde{y}, \varphi_l) = \mathcal{P}_1\mathcal{P}_2(-\xi', \tilde{y}, y, \phi), \tag{2.55}$$

and is even function under the interchange of the produced leptons in the pair $l_- \leftrightarrow l_+$, namely

$$\mathcal{P}_3\mathcal{P}_4(\theta_l, \varphi_l) = \mathcal{P}_3\mathcal{P}_4(\pi - \theta_l, \varphi_l + \pi). \tag{2.56}$$

Furthermore, all BH propagators are even functions in the azimuthal angle φ,

$$\mathcal{P}_i(\varphi) = \mathcal{P}_i(2\pi - \varphi) \text{ for } i = \{1, 2, 3, 4\}, \tag{2.57}$$

since they contain only $\cos\varphi$ terms.

2.2.2 DDVCS contribution

The pure DDVCS contribution write

$$\begin{aligned} d^7\sigma_{\rm UU}^{\rm DDVCS} &= A^{\rm PS}A^{\rm DDVCS}\Big\{ cc_{00}^{\rm DDVCS} + \left[cc_{11}^{\rm DDVCS}\cos(\varphi_l)\right]\cos(\phi) \\ &+ \left[cc_{22}^{\rm DDVCS}\cos(2\varphi_l)\right]\cos(2\phi) \\ &+ \left[ss_{11}^{\rm DDVCS}\sin(\varphi_l)\right]\sin(\phi) + \left[ss_{22}^{\rm DDVCS}\sin(2\varphi_l)\right]\sin(2\phi)\Big\}, \end{aligned} \tag{2.58}$$

with the DDVCS kinematical factor

$$A^{\rm DDVCS} = \frac{2\xi'^2}{\left[\xi^2 - \left(1 + \frac{t}{4\bar{q}^2}\right)^2\xi'^2\right]\bar{q}^4}. \tag{2.59}$$

For the pure DDVCS contribution, the Fourier coefficients are a bilinear combination of CFFs, for instance

$$cc_{00}^{\rm DDVCS} = \frac{1}{y^2\tilde{y}^2}\left[2(2-2y+y^2)(2-2\tilde{y}+\tilde{y}^2)\mathcal{C}^{\rm DDVCS} + 16(1-y)(1-\tilde{y})\mathcal{C}_L^{\rm DDVCS}\right] \tag{2.60}$$

with

$$\begin{aligned} \mathcal{C}^{\rm DDVCS} &= (1-\xi^2)(\mathcal{H}\mathcal{H}^* + \widetilde{\mathcal{H}}\widetilde{\mathcal{H}}^*) - \xi^2(\mathcal{H}\mathcal{E}^* + \mathcal{E}\mathcal{H}^* + \widetilde{\mathcal{H}}\widetilde{\mathcal{E}}^* + \widetilde{\mathcal{E}}\widetilde{\mathcal{H}}^*) \\ &- \left(\frac{t}{4M^2} + \xi^2\right)\mathcal{E}\mathcal{E}^* - \xi^2\frac{t}{4M^2}\widetilde{\mathcal{E}}\widetilde{\mathcal{E}}^*, \end{aligned} \tag{2.61}$$

$$\mathcal{C}_L^{\rm DDVCS} = \frac{\xi'^2 - \xi^2}{\xi'^2}\left[(1-\xi^2)\mathcal{H}_L\mathcal{H}_L^* - \xi^2(\mathcal{H}_L\mathcal{E}_L^* + \mathcal{E}_L\mathcal{H}_L^*) - \left(\frac{t}{4M^2} + \xi^2\right)\mathcal{E}_L\mathcal{E}_L^*\right]. \tag{2.62}$$

The CFFs $\mathcal{F}$ in Eq. (2.61) are given by the complex functions of Eq. (1.121). The longitudinal CFFs $\mathcal{F}_L$ in Eq. (2.62) are analogous to the longitudinal structure function of the DIS process. They start at next-to-leading order and are approximated to zero at leading order. I remind that the helicity-dependent DDVCS contribution $d^7\sigma_{\rm LU}^{\rm DDVCS}$ is approximated to zero at leading twist.

2.2.3 Interference contributions

The interference contributions write

$$\begin{aligned} d^7\sigma_{\rm UU}^{\rm INT1} &= \frac{A^{\rm PS}A^{\rm INT}}{\mathcal{P}_1\mathcal{P}_2(\phi)}\Big\{ \big[cc_{01}^{\rm INT1}\cos(\varphi_l)\big] + \big[cc_{10}^{\rm INT1} + cc_{12}^{\rm INT1}\cos(2\varphi_l)\big]\cos(\phi) \\ &+ \big[cc_{21}^{\rm INT1}\cos(\varphi_l)\big]\cos(2\phi) + \big[cc_{32}^{\rm INT1}\cos(2\varphi_l)\big]\cos(3\phi) \\ &+ \big[ss_{12}^{\rm INT1}\sin(2\varphi_l)\big]\sin(\phi) + \big[ss_{21}^{\rm INT1}\sin(\varphi_l)\big]\sin(2\phi) \\ &+ \big[ss_{32}^{\rm INT1}\sin(2\varphi_l)\big]\sin(3\phi)\Big\}, \end{aligned} \tag{2.63}$$

$$\begin{aligned} d^7\sigma_{\rm UU}^{\rm INT2} &= \frac{A^{\rm PS}A^{\rm INT}}{\mathcal{P}_3\mathcal{P}_4(\theta_l,\varphi_l)}\Big\{ \big[cc_{10}^{\rm INT2}\cos(\varphi_l)\big] + \big[cc_{01}^{\rm INT2} + cc_{21}^{\rm INT2}\cos(2\varphi_l)\big]\cos(\phi) \\ &+ \big[cc_{12}^{\rm INT2}\cos(\varphi_l) + cc_{32}^{\rm INT2}\cos(3\varphi_l)\big]\cos(2\phi) \\ &+ \big[ss_{21}^{\rm INT2}\sin(2\varphi_l)\big]\sin(\phi) \\ &+ \big[ss_{12}^{\rm INT2}\sin(\varphi_l) + ss_{32}^{\rm INT2}\sin(3\varphi_l)\big]\sin(2\phi)\Big\}, \end{aligned} \tag{2.64}$$

$$\begin{aligned} d^7\sigma_{\rm LU}^{\rm INT1} &= \frac{A^{\rm PS}A^{\rm INT}}{\mathcal{P}_1\mathcal{P}_2(\phi)}\Big\{ \big[cs_{01}^{\rm INT1}\sin(\varphi_l)\big] + \big[cs_{21}^{\rm INT1}\sin(\varphi_l)\big]\cos(2\phi) \\ &+ \big[sc_{10}^{\rm INT1}\big]\sin(\phi) + \big[sc_{21}^{\rm INT1}\cos(\varphi_l)\big]\sin(2\phi)\Big\}, \end{aligned} \tag{2.65}$$

$$\begin{aligned} d^7\sigma_{\rm LU}^{\rm INT2} &= \frac{A^{\rm PS}A^{\rm INT}}{\mathcal{P}_3\mathcal{P}_4(\theta_l,\varphi_l)}\Big\{ \big[cs_{01}^{\rm INT2} + cs_{21}^{\rm INT2}\cos(2\varphi_l)\big]\sin(\phi) \\ &+ \big[sc_{10}^{\rm INT2}\sin(\varphi_l)\big] + \big[sc_{21}^{\rm INT2}\sin(2\varphi_l)\big]\cos(\phi)\Big\}, \end{aligned} \tag{2.66}$$

with the interference kinematical factor

$$A_{\rm INT} = \frac{2\xi'(1+\xi)}{\left[\xi^2 - \left(1+\frac{t}{4\bar{q}^2}\right)^2\xi'^2\right]\bar{q}^2 t}. \tag{2.67}$$

For the interference contributions, the Fourier coefficients are a linear combination of CFFs. $cc^{\rm INT1,2}$ and $ss^{\rm INT1,2}$ are related to the real part of CFFs, while $cs^{\rm INT1,2}$ and $sc^{\rm INT1,2}$ are related to the imaginary part. For example

$$cc_{10}^{\rm INT1} = \frac{8K}{y^3\tilde{y}^2}\Big[(2-2y+y^2)(2-2\tilde{y}+\tilde{y}^2)\mathrm{Re}\left\{\mathcal{C}_{\rm UU}^{\rm INT}\right\} - 8(1-y)(1-\tilde{y})\mathrm{Re}\left\{\mathcal{C}_{{\rm UU},L}^{\rm INT}\right\}\Big] \tag{2.68}$$

with the linear CFFs combinations

$$\mathcal{C}_{\rm UU}^{\rm INT} = \frac{\xi'}{\xi}\left(F_1\mathcal{H} - \frac{t}{4M^2}F_2\mathcal{E}\right) + \xi(F_1+F_2)\widetilde{\mathcal{H}}, \tag{2.69}$$

$$\mathcal{C}_{{\rm UU},L}^{\rm INT} = \frac{\xi'^2-\xi^2}{\xi\xi'}\left(F_1\mathcal{H}_L - \frac{t}{4M^2}F_2\mathcal{E}_L\right), \tag{2.70}$$

and

$$sc_{10}^{\rm INT1} = -\frac{8\pi K(2-y)(2-2\tilde{y}+\tilde{y}^2)}{y^2\tilde{y}^2}{\rm Im}\left\{\mathcal{C}_{\rm LU}^{\rm INT}\right\} \tag{2.71}$$

with the linear CFFs combination

$$\mathcal{C}_{\rm LU}^{\rm INT} = F_1\mathcal{H} + \xi'(F_1+F_2)\widetilde{\mathcal{H}} - \frac{t}{4M^2}F_2\mathcal{E}. \tag{2.72}$$

The corresponding coefficients in INT2 contributions are given by

$$\left\{cc_{10}^{\rm INT2}, sc_{10}^{\rm INT2}\right\} = \frac{\widetilde{K}y}{K\tilde{y}}\left\{cc_{10}^{\rm INT1}, -sc_{10}^{\rm INT1}\right\} \tag{2.73}$$

being proportional to the same combinations of CFFs respectively. I emphasize that the real and imaginary parts the CFFs above are given by the Eqs. (1.108)-(1.115) and the longitudinal CFFs $\mathcal{F}_L$ contributions are approximated to zero for this study, which focuses on the leading order.

2.3 Cross section integrated over lepton solid angle

As discussed in section 1.3.2, in comparison to DVCS, the DDVCS cross section is small even if integrating over the solid angle of the produced lepton pair. Thus, any measurement of 7-fold differential cross section is too difficult for the current facilities. In order to conduct feasible measurements with reasonable statistics, one can measure the observables in terms of the 5-fold differential cross section integrated over the lepton pair solid angle at a high luminosity and with a large detector acceptance. I present the theoretical description of the integration first and then introduce the experimental observables in the following.

2.3.1 Integration over lepton solid angle

The DDVCS and the BH1 amplitudes are even under the interchange of the produced leptons in the pair $l_- \leftrightarrow l_+$, namely $\theta_l \leftrightarrow \pi - \theta_l$ and $\varphi_l \leftrightarrow \varphi_l + \pi$, while the BH2 amplitude is odd [57]. Therefore, the integration over the solid angle leads to the vanishing of the interference terms between $\mathcal{T}_{\rm BH2}$ and the other two mechanisms. The integrated 5-fold cross section is given by

$$\frac{d^5\sigma}{dx_{\rm B}dQ^2dtdQ'^2d\phi} = \int_0^{2\pi} d\varphi_l \int_{\pi/2-\theta_0}^{\pi/2+\theta_0} d\theta_l \sin\theta_l \ \frac{d^7\sigma}{dx_{\rm B}dQ^2dtdQ'^2d\phi d\Omega_l} \tag{2.74}$$

where the integral over θ_l is in a symmetric interval around the point $\pi/2$ and θ_0 takes any value from $0 < \theta_0 \leqslant \pi/2$. The 5-fold cross section decomposition can be expressed in terms of the beam charge and polarization as

$$d^5\sigma = d^5\sigma_{\rm UU}^{\rm BH1} + d^5\sigma_{\rm UU}^{\rm BH2} + d^5\sigma_{\rm UU}^{\rm DDVCS} + (-e_l)d^5\sigma_{\rm UU}^{\rm INT1} + P_l\left[d^5\sigma_{\rm LU}^{\rm DDVCS} + (-e_l)d^5\sigma_{\rm LU}^{\rm INT1}\right], \tag{2.75}$$

where the helicity-dependent DDVCS contribution $d^5\sigma_{\rm LU}^{\rm DDVCS}$ equals to zero at leading twist. The form is analogous to the DVCS case in Eq. (1.75) expect it contains an additional pure BH2 contribution. All the contributions are presented in the following as a Fourier expansion in ϕ.

Bethe-Heitler contributions

In the 7-fold BH1 contribution of Eq. (2.50), the $cc_{00}^{\rm BH1}$ and $cc_{20}^{\rm BH1}$ harmonic terms are even under the leptons interchange, while the others (odd) vanish from the integration over φ_l. The pure BH1 contribution can be then expressed

$$d^5\sigma_{\rm UU}^{\rm BH1} \propto \frac{1}{\mathcal{P}_1^2\mathcal{P}_2^2(\phi)}\left[c_0^{\rm BH1} + c_2^{\rm BH1}\cos(2\phi)\right], \tag{2.76}$$

where the Fourier coefficients $c_0^{\rm BH1}$, $c_2^{\rm BH1}$ are respectively given by the integral of $cc_{00}^{\rm BH1}$, $cc_{20}^{\rm BH1}$.

For the pure BH2 contribution, one has

$$d^5\sigma_{\rm UU}^{\rm BH2} \propto c_0^{\rm BH2} + c_1^{\rm BH2}\cos(\phi) + c_2^{\rm BH2}\cos(2\phi), \tag{2.77}$$

where the Fourier coefficients $c_0^{\rm BH2}$, $c_1^{\rm BH2}$, $c_2^{\rm BH2}$ are given by the integral of the $\cos 0$, $\cos\phi$, $\cos 2\phi$ harmonic terms of Eq. (2.51), respectively. The BH propagators $\mathcal{P}_3\mathcal{P}_4$ are also integrated. Since each term in Eq. (2.51) becomes a cos-Fourier expansion in φ_l after the integration over θ_l, as shown in Eq. (2.95), the sine harmonics in φ_l drop out from the integration due to the orthogonal property.

DDVCS contribution

The only harmonic term in Eq. (2.58) that does not vanish from the integration is the $cc_{00}^{\rm DDVCS}$ and the 5-fold pure DDVCS contribution writes

$$d^5\sigma_{\rm UU}^{\rm DDVCS} = A^{\rm PS}A^{\rm DDVCS}c_0^{\rm DDVCS}, \tag{2.78}$$

where the coefficient $c_0^{\rm DDVCS}$ is given by the integral of $cc_{00}^{\rm DDVCS}$ as

$$c_0^{\rm DDVCS} = \int_0^{2\pi} d\varphi_l \int_{\pi/2-\theta_0}^{\pi/2+\theta_0} d\theta_l \sin\theta_l \; cc_{00}^{\rm DDVCS}. \tag{2.79}$$

The integral of the components depending on the lepton angles is given by

$$\int_0^{2\pi} d\varphi_l \int_{\pi/2-\theta_0}^{\pi/2+\theta_0} d\theta_l \sin\theta_l \left(\frac{2-2\tilde{y}+\tilde{y}^2}{\tilde{y}^2}\right) = 2\pi\sin\theta_0\left(1+\frac{1}{3}\sin^2\theta_0\right). \tag{2.80}$$

It equals $8\pi/3$ when integrating over the full range of θ_l, *i.e.* $\theta_0 = \pi/2$, and becomes about 62% over the half of the full range when $\theta_0 = \pi/4$. Consequently, the Fourier coefficient of the 5-fold pure DDVCS contribution of full range integration writes

$$c_0^{\rm DDVCS} = \frac{16\pi(2-2y+y^2)}{3y^2}\,\mathcal{C}^{\rm DDVCS} \tag{2.81}$$

Interference contributions

The only harmonic term in Eq. (2.63) that survives the integration is the cc_{10}^{INT1} and the 5-fold unpolarized INT1 contribution writes

$$d^5\sigma_{\mathrm{UU}}^{\mathrm{INT1}} = \frac{A^{\mathrm{PS}}A^{\mathrm{INT}}}{\mathcal{P}_1\mathcal{P}_2(\phi)} c_1^{\mathrm{INT1}} \cos(\phi), \tag{2.82}$$

where the coefficient c_1^{INT1} is given by the integral of cc_{10}^{INT1} analogously to Eq. (2.79). For the integration over the full range of θ_l, one has

$$c_1^{\mathrm{INT1}} = \frac{64\pi K(2-2y+y^2)}{3y^3} \,\mathrm{Re}\left\{\mathcal{C}_{\mathrm{UU}}^{\mathrm{INT}}\right\}, \tag{2.83}$$

Similarly, the 5-fold helicity-dependent INT1 contribution writes

$$d^5\sigma_{\mathrm{LU}}^{\mathrm{INT1}} = \frac{A^{\mathrm{PS}}A^{\mathrm{INT}}}{\mathcal{P}_1\mathcal{P}_2(\phi)} s_1^{\mathrm{INT1}} \sin(\phi), \tag{2.84}$$

with the coefficient s_1^{INT1} given by the integral of ss_{10}^{INT1}. For the θ_l-full-range integration, s_1^{INT1} reads

$$s_1^{\mathrm{INT1}} = -\frac{64\pi^2 K(2-y)}{3y^2} \,\mathrm{Im}\left\{\mathcal{C}_{\mathrm{LU}}^{\mathrm{INT}}\right\}. \tag{2.85}$$

The BH propagators $\mathcal{P}_1\mathcal{P}_2$ are kinematics factors with a ϕ dependence entering into the denominator of the cross section contributions. Consequently, the $\cos\phi$ or $\sin\phi$ moment of the cross section can not directly access the Fourier coefficients. However, their full expressions are calculable through Eqs. (2.54), (2.26) and (2.28) at a fixed kinematic point $(x_{\mathrm{B}}, Q^2, t, Q'^2, \phi)$.

Applying the approximation for introducing the symmetric variables, the propagators can be given by using Eqs. (2.30)-(2.33) as

$$\begin{aligned}\mathcal{P}_1\mathcal{P}_2(\phi) \;\approx\; & -\frac{1}{y^2}\Bigg\{\left[(1-y)+y(1-y)\left(\frac{t}{Q^2+Q'^2}\right)\right] \\ & -2\left[2-y\left(1-\frac{t}{Q^2+Q'^2}\right)\right] K\cos\phi + 4K^2\cos^2\phi\Bigg\}.\end{aligned} \tag{2.86}$$

It is obvious that the ϕ dependence can be neglected only when $K \ll 1-y$. Neglecting the kinematically suppressed term $\sim t/(Q^2+Q'^2)$ and keeping the leading and sub-leading terms only, the formula simplify considerably,

$$\mathcal{P}_1\mathcal{P}_2(\phi) \approx -\frac{1}{y^2}\left[(1-y)-2(2-y)K\cos\phi\right]. \tag{2.87}$$

When the generalized Bjorken limit is fulfilled, to the degree that the kinematically suppressed terms are negligible, the approximations mentioned above are good enough to describe the contributions. Then, the 5-fold cross section contributions integrated over the full range of the final lepton solid angle are expressed in term of the experimental variables, respectively, by

$$d^5\sigma_{\mathrm{UU}}^{\mathrm{DDVCS}} \;\approx\; \frac{\alpha_{\mathrm{em}}^4}{12\pi^2}\frac{x_{\mathrm{B}}(2-2y+y^2)}{Q^6Q'^2}\,\mathcal{C}^{\mathrm{DDVCS}}, \tag{2.88}$$

$$d^5\sigma_{\mathrm{UU}}^{\mathrm{INT1}} \;\approx\; \frac{\alpha_{\mathrm{em}}^4}{3\pi^2}\frac{(2-2y+y^2)yK'\cos\phi}{Q^4Q'^2t\left[\sqrt{1-y}-2(2-y)K'\cos\phi\right]} \,\mathrm{Re}\left\{\mathcal{C}_{\mathrm{UU}}^{\mathrm{INT}}\right\}, \tag{2.89}$$

$$d^5\sigma_{\mathrm{LU}}^{\mathrm{INT1}} \;\approx\; -\frac{\alpha_{\mathrm{em}}^4}{3\pi}\frac{(2-y)y^2K'\sin\phi}{Q^4Q'^2t\left[\sqrt{1-y}-2(2-y)K'\cos\phi\right]} \,\mathrm{Im}\left\{\mathcal{C}_{\mathrm{LU}}^{\mathrm{INT}}\right\}, \tag{2.90}$$

where

$$K' = \frac{\sqrt{t_{\min} - t}\sqrt{|(1-x_{\rm B})Q^2 - x_{\rm B}Q'^2|}}{Q^2 + Q'^2}. \tag{2.91}$$

The kinematical factor $K' > 0$ has positive value, and when it is non-negligible the $d^5\sigma^{\rm INT1}_{\rm UU}$ contribution therefore has larger absolute magnitude at $\phi = 0$ than at $\phi = \pi$. I emphasize that when $Q^2 + Q'^2$ becomes of order M^2 or $-t$ the approximations break down and one must use the full expressions.

2.3.2 Integration over ϕ and θ_l

The magnitude of interference contributions depends on the relative strength of the BH amplitudes with respect to the DDVCS one. The BH1 amplitude becomes smaller when one goes from the the space-like region $\xi' > 0$ ($Q^2 > Q'^2$) to the time-like region $\xi' < 0$ ($Q^2 < Q'^2$), while the BH2 amplitude acts contrarily and dominates the cross section except when one approaches the limit $Q'^2 \to 0$ [57]. In the time-like region, the INT1 contributions therefore becomes considerably small, but one can alternatively measure the observables sensitive to INT2 contributions.

Due to the antisymmetric property of the INT2 contributions under the interchange of the final leptons in the pair, they drop out from the integration over the lepton solid angle. In order to access the INT2 contribution, one can do the azimuthal integration in another way to interpret data:

$$\frac{d^5\Sigma}{dx_{\rm B}dQ^2dtdQ'^2d\varphi_l} = \int_0^{2\pi} d\phi \int_{\pi/2-\theta_0}^{\pi/2+\theta_0} d\theta_l \sin\theta_l \; \frac{d^7\sigma}{dx_{\rm B}dQ^2dtdQ'^2d\phi d\Omega_l}. \tag{2.92}$$

Here I use the symbol Σ denoting the 5-fold cross section to discriminate it from the previous one. The decomposition form is given by

$$\begin{aligned} d^5\Sigma \;\; = \;\; & d^5\Sigma^{\rm BH1}_{\rm UU} + d^5\Sigma^{\rm BH2}_{\rm UU} + (-e_l)d^5\Sigma^{\rm BH12}_{\rm UU} + d^5\Sigma^{\rm DDVCS}_{\rm UU} + (-e_l)d^5\Sigma^{\rm INT1}_{\rm UU} + d^5\Sigma^{\rm INT2}_{\rm UU} \\ & + P_l\left(d^5\Sigma^{\rm DDVCS}_{\rm LU} + d^5\Sigma^{\rm INT2}_{\rm LU}\right), \end{aligned} \tag{2.93}$$

where the helicity-dependent DDVCS contribution $d^5\Sigma^{\rm DDVCS}_{\rm LU}$ equals to zero at leading twist. In comparison to the 7-fold form in Eq. (2.49), the only term that drop out is the helicity-dependent INT1 contribution, in which every single Fourier harmonic is odd under the substitution of $\phi \to \phi + \pi$ and $\theta_l \to \pi - \theta_l$. All the contributions as a Fourier expansion in φ_l are presented in the following.

Bethe-Heitler contributions

For the pure 7-fold BH1 contribution of Eq. (2.50), the integration over ϕ removes all sine terms in ϕ, but the cosine terms survive due to the cosine terms of $\mathcal{P}_1\mathcal{P}_2$ in the denominator. The $cc^{\rm BH1}_{00}$, $cc^{\rm BH1}_{20}$, $cc^{\rm BH1}_{02}$, $cc^{\rm BH1}_{22}$ and $cc^{\rm BH1}_{42}$ harmonic terms are even under the substitution of $\theta_l \to \pi - \theta_l$, while the others are odd and therefore vanish from the integration over θ_l. Then, one has

$$d^5\Sigma^{\rm BH1}_{\rm UU} \propto C^{\rm BH1}_0 + C^{\rm BH1}_2 \cos(2\varphi_l), \tag{2.94}$$

where $C^{\rm BH1}_0$ is given by the integrals of the $cc^{\rm BH1}_{00}$, $cc^{\rm BH1}_{20}$ harmonic terms of Eq. (2.50), and $C^{\rm BH1}_2$ is given by the integrals of the $cc^{\rm BH1}_{02}$, $cc^{\rm BH1}_{22}$, $cc^{\rm BH1}_{42}$ harmonic terms of Eq. (2.50).

For the pure 7-fold BH2 contribution of Eq. (2.51), the integration over ϕ removes all sine and cosine terms in ϕ. The only remaining terms is the $cc_{00}^{\rm BH2}$ and $cc_{20}^{\rm BH2}$. As a consequence of the symmetry of the product $\mathcal{P}_3\mathcal{P}_4$, see Eq. (2.56), the integration over $d\theta_l$ in a symmetric interval around the point $\theta_l = \pi/2$ gives for any (anti)symmetric moment $\tau(\theta_l)$ the following characteristic cos-Fourier expansion (for any integer r) [57]:

$$\int_{\pi/2-\theta_0}^{\pi/2+\theta_0} d\cos\theta_l \frac{\tau(\theta_l)}{[\mathcal{P}_3\mathcal{P}_4]^r} = \sum_{n=0,1,\cdots} \tau_n(\theta_0) \left\{ \begin{array}{c} \cos[(2n+1)\varphi_l] \\ \cos(2n\varphi_l) \end{array} \right\} \text{for} \left\{ \begin{array}{c} \tau(\theta_l) = -\tau(\pi-\theta_l) \\ \tau(\theta_l) = \tau(\pi-\theta_l)) \end{array} \right\}. \tag{2.95}$$

The $cc_{00}^{\rm BH2}$ and $cc_{20}^{\rm BH2}$ harmonic terms are even under the substitution of $\theta_l \to \pi - \theta_l$, and their integration over θ_l expands into even cos-expansions in terms of $\cos(2n\varphi_l)$. Eventually, the 5-fold pure BH2 contribution writes

$$d^5\Sigma_{\rm UU}^{\rm BH2} \propto C_0^{\rm BH2} + C_2^{\rm BH2}\cos(2\varphi_l) + C_4^{\rm BH2}\cos(4\varphi_l) + \cdots \tag{2.96}$$

Similarly for the BH12 contribution of Eq. (2.52), the $c_{00}^{\rm BH12}$, $c_{20}^{\rm BH12}$, $c_{02}^{\rm BH12}$ and $c_{22}^{\rm BH12}$ terms being odd under the θ_l substitution and the $c_{11}^{\rm BH12}$ being even survive from the integration over ϕ. Their integration over θ_l expands into both even and odd cos-expansion, and one has then

$$d^5\Sigma_{\rm UU}^{\rm BH12} \propto C_1^{\rm BH12}\cos(\varphi_l) + C_2^{\rm BH12}\cos(\varphi_l)\cos(2\varphi_l) + \cdots \tag{2.97}$$

DDVCS contribution

The only harmonic term in Eq. (2.58) surviving the integration is still the azimuthal independent term $cc_{00}^{\rm DDVCS}$ and the 5-fold pure DDVCS contribution writes

$$d^5\Sigma_{\rm UU}^{\rm DDVCS} = A^{\rm PS}A^{\rm DDVCS}C_0^{\rm DDVCS}, \tag{2.98}$$

where the coefficient $C_0^{\rm DDVCS}$ is given by the integral of $cc_{00}^{\rm DDVCS}$ as

$$C_0^{\rm DDVCS} = \int_0^{2\pi} d\phi \int_{\pi/2-\theta_0}^{\pi/2+\theta_0} d\theta_l \sin\theta_l \; cc_{00}^{\rm DDVCS}. \tag{2.99}$$

Since $cc_{00}^{\rm DDVCS}$ is independent on the angles, $C_0^{\rm DDVCS}$ is given by the right-hand side of Eq. (2.80) and related to the CFFs similarly to Eq. (2.81) when integration over the full range of θ_l. Therefore, the 5-fold pure DDVCS contributions with respect to the two azimuthal integrations have the same magnitude at leading twist.

Interference contributions

Following the same approach, the interference contributions in terms of φ_l can be obtained. The unpolarized INT1 contribution reads

$$d^5\Sigma_{\rm UU}^{\rm INT1} \propto C_0^{\rm INT1} + C_2^{\rm INT1}\cos(2\varphi_l). \tag{2.100}$$

For the INT2 contributions, the only terms that survive the integration over ϕ are the Fourier harmonic terms with the coefficients $cc_{10}^{\rm INT2}$ and $sc_{10}^{\rm INT2}$ given by the relation of Eq. (2.73). Then, one has

$$d^5\Sigma_{\rm UU}^{\rm INT2} = 2\pi \int_{\pi/2-\theta_0}^{\pi/2+\theta_0} d\theta_l \sin\theta_l \frac{A^{\rm PS}A^{\rm INT}}{\mathcal{P}_3\mathcal{P}_4(\theta_l,\varphi_l)} \; cc_{10}^{\rm INT2}\cos(\varphi_l), \tag{2.101}$$

$$d^5\Sigma_{\rm LU}^{\rm INT2} = 2\pi \int_{\pi/2-\theta_0}^{\pi/2+\theta_0} d\theta_l \sin\theta_l \frac{A^{\rm PS}A^{\rm INT}}{\mathcal{P}_3\mathcal{P}_4(\theta_l,\varphi_l)} \; sc_{10}^{\rm INT2}\sin(\varphi_l), \tag{2.102}$$

where the terms being even under the θ_l substitution give even cos-expansions in the expression:

$$d^5\Sigma_{\rm UU}^{\rm INT2} = 2\pi A^{\rm PS} A^{\rm INT} \cos(\varphi_l) \left[C_1^{\rm INT2} + C_2^{\rm INT2} \cos(2\varphi_l) + \cdots \right], \quad (2.103)$$

$$d^5\Sigma_{\rm LU}^{\rm INT2} = 2\pi A^{\rm PS} A^{\rm INT} \sin(\varphi_l) \left[S_1^{\rm INT2} + S_2^{\rm INT2} \cos(2\varphi_l) + \cdots \right]. \quad (2.104)$$

To obtain the coefficients above, one need the full expression of the product $\mathcal{P}_3\mathcal{P}_4$ given by the Eqs. (2.54), (2.27) and (2.28) at a fixed kinematic point $(x_{\rm B}, Q^2, t, Q'^2, \theta_l, \varphi_l)$. It is rather lengthy, but simplify considerably in kinematics where t, M^2 and m_μ^2 can be neglected compared to terms going with $Q^2 + Q'^2$ as

$$\mathcal{P}_3\mathcal{P}_4 \approx \frac{\sin^2\theta_l}{4} \approx \frac{\tilde{y}-1}{\tilde{y}^2}, \quad (2.105)$$

which has been noticed in [58]. Indeed, Eq. (2.105) is the leading term of the expression obtained by using Eqs. (2.30)-(2.33), which reads

$$\mathcal{P}_3\mathcal{P}_4 \approx \frac{\sin^2\theta_l}{4} \left(1 + 4K'' \frac{\cos\theta_l}{\sin\theta_l} \cos\varphi_l - 4K''^2 \cos^2\varphi_l \right) \quad (2.106)$$

with

$$K'' = \frac{\sqrt{Q'^2/Q^2}\sqrt{t_{\rm min} - t}\sqrt{|(1-x_{\rm B})Q^2 - x_{\rm B}Q'^2|}}{Q^2 + Q'^2} \quad (2.107)$$

It can be seen that the product $\mathcal{P}_3\mathcal{P}_4$ of lepton propagators goes to zero at $\sin\theta_l = 0$ in this approximation. Closer inspection reveals that when $\sin\theta_l$ becomes of order $t/(Q^2+Q'^2)$ or $m_\mu^2/(Q^2+Q'^2)$ the approximations break down and one must use the full expressions. Using the approximation of Eq. (2.105), the integral of the θ_l-dependent components in the INT2 contributions is given by

$$\int_{\pi/2-\theta_0}^{\pi/2+\theta_0} d\theta_l \sin\theta_l \left(\frac{\tilde{y}^2}{\tilde{y}-1} \right) \left(\frac{2 - 2\tilde{y} + \tilde{y}^2}{\tilde{y}^3} \right) \widetilde{K} = K'' \left(3\theta_0 - \frac{\sin 2\theta_0}{2} \right) \quad (2.108)$$

when $\theta_0 = \pi/2$, namely integrating over the full range in θ_l, one gets $3\pi K''/2$. It becomes about 39% over the half of the full range when $\theta_0 = \pi/4$. Eventually, the 5-fold INT2 contributions integrated over the full range of the final lepton solid angle are expressed in term of the experimental variables, respectively, by

$$d^5\Sigma_{\rm UU}^{\rm INT2} \approx -\frac{3\alpha_{\rm em}^4}{8\pi} \frac{(2 - 2y + y^2) K'' \cos\varphi_l}{Q^4 Q'^2 t} \, {\rm Re}\left\{ \mathcal{C}_{\rm UU}^{\rm INT} \right\}, \quad (2.109)$$

$$d^5\Sigma_{\rm LU}^{\rm INT2} \approx -\frac{3\alpha_{\rm em}^4}{8} \frac{(2-y) y K'' \sin\varphi_l}{Q^4 Q'^2 t} \, {\rm Im}\left\{ \mathcal{C}_{\rm LU}^{\rm INT} \right\}. \quad (2.110)$$

The expressions above are valid only when one sufficiently satisfies the generalized Bjorken limit. It can be seen that the $d^5\Sigma^{\rm INT2}$ contributions access the same linear CFFs combinations accessed by the corresponding $d^5\sigma^{\rm INT1}$, however, the magnitudes of the contribution are different, depending on different kinematic factors. Neglecting the ϕ-dependent subleading term of $\mathcal{P}_1\mathcal{P}_2$ in the denominators of Eqs. (2.89) and (2.90), the ratio of the absolute magnitudes of $d^5\Sigma^{\rm INT2}$ to $d^5\sigma^{\rm INT1}$, at the same corresponding azimuthal angles, can be roughly expressed as

$$\left| \frac{d^5\Sigma^{\rm INT2}(\varphi)}{d^5\sigma^{\rm INT1}(\varphi)} \right| \approx \frac{9\pi}{8} \frac{\sqrt{Q'^2/Q^2}}{\sqrt{y^2/(1-y)}}. \quad (2.111)$$

In the space-like region, one has $Q'^2/Q^2 < 1$ (see the right panel of Fig. 2.6) and large Q^2 supporting the factorization regime, thus, $d^5\sigma^{\rm INT1}$ has a relatively considerable magnitude, especially at small Q'^2. Thus, it is appropriate to measure observables responsive to $d^5\sigma^{\rm INT1}$ in this region. When one goes to the time-like region where $Q'^2/Q^2 > 1$, $d^5\sigma^{\rm INT1}$ becomes very small while $d^5\Sigma^{\rm INT2}$ becomes significant, particularly when $Q^2 \to 0$ at large Q'^2. Then, one shall perform measurements of observables sensitive to $d^5\Sigma^{\rm INT2}$. Let's discuss how we access the CFFs through the specific experimental observables in the next section.

2.4 Experimental observables

Neglecting the twist-3 heilicity-dependent DDVCS contributions and considering 100% beam polarization, the experimental observables in terms of the 5-fold differential cross sections are listed in the following.

2.4.1 5-fold cross sections with polarized electron beam

With polarized electron beam, the 5-fold unpolarized cross section and beam spin cross section difference for DDVCS measurements are built as

$$\begin{aligned}
\sigma^-_{\rm UU}(\phi) &= \frac{1}{2}\left(d^5\sigma^-_{\rightarrow} + d^5\sigma^-_{\leftarrow}\right) = d^5\sigma^{\rm BH1}_{\rm UU} + d^5\sigma^{\rm BH2}_{\rm UU} + d^5\sigma^{\rm DDVCS}_{\rm UU} + d^5\sigma^{\rm INT1}_{\rm UU}, \\
\Delta\sigma^-_{\rm LU}(\phi) &= \frac{1}{2}\left(d^5\sigma^-_{\rightarrow} - d^5\sigma^-_{\leftarrow}\right) = d^5\sigma^{\rm INT1}_{\rm LU},
\end{aligned} \tag{2.112}$$

which are the integrals over the final lepton solid angle and eventually consist of the Fourier harmonics in the nucleon azimuthal angle ϕ. In order to single out the polarized INT2 contribution, one can also follow the other integration scheme to obtain

$$\begin{aligned}
\Sigma^-_{\rm UU}(\varphi_l) = \frac{1}{2}\left(d^5\Sigma^-_{\rightarrow} + d^5\Sigma^-_{\leftarrow}\right) &= d^5\Sigma^{\rm BH1}_{\rm UU} + d^5\Sigma^{\rm BH2}_{\rm UU} + d^5\Sigma^{\rm BH12}_{\rm UU} \\
&\quad + d^5\Sigma^{\rm DDVCS}_{\rm UU} + d^5\Sigma^{\rm INT1}_{\rm UU} + d^5\Sigma^{\rm INT2}_{\rm UU} \\
\Delta\Sigma^-_{\rm LU}(\varphi_l) = \frac{1}{2}\left(d^5\Sigma^-_{\rightarrow} - d^5\Sigma^-_{\leftarrow}\right) &= d^5\Sigma^{\rm INT2}_{\rm LU},
\end{aligned} \tag{2.113}$$

containing only harmonics in the lepton azimuthal angle φ_l after the integration over ϕ and the lepton polar angle θ_l.

Similarly to the DVCS case, the beam spin cross section differences are of great interest, since they are directly proportional to the imaginary part of the linear CFFs combination $\mathcal{C}^{\rm INT}_{\rm LU}$ given by Eq. (2.72). At leading twist approximation, they can be expressed by

$$\Delta\sigma^-_{\rm LU}(\phi) = \mathcal{K}_{\rm LU}(\phi)\ {\rm Im}\left\{F_1\mathcal{H} + \xi'(F_1+F_2)\widetilde{\mathcal{H}} - \frac{t}{4M^2}F_2\mathcal{E}\right\}, \tag{2.114}$$

and similar relation holds for $\Delta\Sigma^-_{\rm LU}(\varphi_l)$. The azimuthal-angle-dependent factor $\mathcal{K}_{\rm LU}$ can be read off from the corresponding Fourier coefficients, where the phase space prefactor $A^{\rm PS}$, kinematical factor of the interference contribution $A^{\rm INT}$, and most of all, the corresponding integration and the propagators should be exactly taken into account. Sec. 6.1.1 will present the specific expression of $\mathcal{K}_{\rm LU}$ for the extraction of the CFFs combination. In Eq. (2.114), the kinematical factors ξ' and t being small, the measurements of the beam

spin cross section differences on a proton target are mainly sensitive to $\mathrm{Im}\mathcal{H}^p(\xi',\xi,t)$, being the proton singlet GPD $H^p_+(\xi',\xi,t)$. Due to the small value of F_1^n and the cancellation between u and d polarized parton distributions in $\widetilde{\mathcal{H}}^n$, the measurements on a neutron target provide access to $\mathrm{Im}\mathcal{E}^n(\xi',\xi,t)$, which is the neutron singlet GPD $E^n_+(\xi',\xi,t)$.

Since the imaginary parts of $\mathcal{H}$, $\mathcal{E}$ and $\xi'\widetilde{\mathcal{H}}$ are antisymmetric in ξ', as displayed in Eqs. (1.119) and (1.120), one experts the beam spin cross section differences with different sign in the space-like and time-like region, and becoming zero at $\xi'=0$.

Actually, $\Delta\sigma^-_{\mathrm{LU}}(\phi)$ is complicated by the presence of the twist-three DDVCS contribution $d^5\sigma^{\mathrm{DDVCS}}_{\mathrm{LU}}$. Moreover, although one can get rid of all the BH terms by QED calculations, the unpolarized cross section σ^-_{UU} is still a mix of the bilinear and linear CFFs combinations coming from the DDVCS and INT1 contributions, respectively. The unpolarized cross section Σ^-_{UU} has more contributions. To separate them, the cross sections with positron beam are needed.

2.4.2 5-fold cross sections with polarized electron and positron beam

Using polarized electron and polarized positron beam, one can measure the experimental observables built as

$$\begin{aligned}
\sigma_{\mathrm{UU}}(\phi) &= \frac{1}{4}\left[\left(d^5\sigma^-_{\rightarrow}+d^5\sigma^-_{\leftarrow}\right)+\left(d^5\sigma^+_{\rightarrow}+d^5\sigma^+_{\leftarrow}\right)\right] = d^5\sigma^{\mathrm{BH1}}_{\mathrm{UU}}+d^5\sigma^{\mathrm{BH2}}_{\mathrm{UU}}+d^5\sigma^{\mathrm{DDVCS}}_{\mathrm{UU}},\\
\Delta\sigma^{\mathrm{C}}_{\mathrm{UU}}(\phi) &= \frac{1}{4}\left[\left(d^5\sigma^-_{\rightarrow}+d^5\sigma^-_{\leftarrow}\right)-\left(d^5\sigma^+_{\rightarrow}+d^5\sigma^+_{\leftarrow}\right)\right] = d^5\sigma^{\mathrm{INT1}}_{\mathrm{UU}},\\
\Delta\sigma_{\mathrm{LU}}(\phi) &= \frac{1}{4}\left[\left(d^5\sigma^-_{\rightarrow}-d^5\sigma^-_{\leftarrow}\right)+\left(d^5\sigma^+_{\rightarrow}-d^5\sigma^+_{\leftarrow}\right)\right] = 0,\\
\Delta\sigma^{\mathrm{C}}_{\mathrm{LU}}(\phi) &= \frac{1}{4}\left[\left(d^5\sigma^-_{\rightarrow}-d^5\sigma^-_{\leftarrow}\right)-\left(d^5\sigma^+_{\rightarrow}-d^5\sigma^+_{\leftarrow}\right)\right] = d^5\sigma^{\mathrm{INT1}}_{\mathrm{LU}},
\end{aligned} \tag{2.115}$$

where $\Delta\sigma_{\mathrm{LU}}$ equals to zero only at leading twist and should include the twist-3 $d^5\sigma^{\mathrm{DDVCS}}_{\mathrm{LU}}$ contribution. Its contamination totally drops out in the $\Delta\sigma^{\mathrm{C}}_{\mathrm{LU}}$, as a direct benefit of combining electron and positron beam DDVCS observables. The interference contribution and the DDVCS contribution are singled out from each cross section, which offers a cleaner platform for the extraction of CFFs. Following the other integration scheme, one also obtains

$$\begin{aligned}
\Sigma_{\mathrm{UU}}(\varphi_l) &= \frac{1}{4}\left[\left(d^5\Sigma^-_{\rightarrow}+d^5\Sigma^-_{\leftarrow}\right)+\left(d^5\Sigma^+_{\rightarrow}+d^5\Sigma^+_{\leftarrow}\right)\right]\\
&= d^5\Sigma^{\mathrm{BH1}}_{\mathrm{UU}}+d^5\Sigma^{\mathrm{BH2}}_{\mathrm{UU}}+d^5\Sigma^{\mathrm{DDVCS}}_{\mathrm{UU}}+d^5\Sigma^{\mathrm{INT2}}_{\mathrm{UU}},\\
\Delta\Sigma^{\mathrm{C}}_{\mathrm{UU}}(\varphi_l) &= \frac{1}{4}\left[\left(d^5\Sigma^-_{\rightarrow}+d^5\Sigma^-_{\leftarrow}\right)-\left(d^5\Sigma^+_{\rightarrow}+d^5\Sigma^+_{\leftarrow}\right)\right] = d^5\Sigma^{\mathrm{BH12}}_{\mathrm{UU}}+d^5\Sigma^{\mathrm{INT1}}_{\mathrm{UU}},\\
\Delta\Sigma_{\mathrm{LU}}(\varphi_l) &= \frac{1}{4}\left[\left(d^5\Sigma^-_{\rightarrow}-d^5\Sigma^-_{\leftarrow}\right)+\left(d^5\Sigma^+_{\rightarrow}-d^5\Sigma^+_{\leftarrow}\right)\right] = d^5\Sigma^{\mathrm{INT2}}_{\mathrm{LU}},\\
\Delta\Sigma^{\mathrm{C}}_{\mathrm{LU}}(\varphi_l) &= \frac{1}{4}\left[\left(d^5\Sigma^-_{\rightarrow}-d^5\Sigma^-_{\leftarrow}\right)-\left(d^5\Sigma^+_{\rightarrow}-d^5\Sigma^+_{\leftarrow}\right)\right] = 0,
\end{aligned} \tag{2.116}$$

where $\Delta\Sigma_{\mathrm{LU}}$ equals to $d^5\Sigma^{\mathrm{INT2}}_{\mathrm{LU}}$ only at leading twist and should also include the twist-3 $d^5\Sigma^{\mathrm{DDVCS}}_{\mathrm{LU}}$ contribution. In this case, one cannot get rid of its contamination by introducing opposite beam charge. In $\Sigma_{\mathrm{UU}}(\varphi_l)$, the INT2 contribution is contaminated by the DDVCS contribution. However, one can get rid of the DDVCS term by taking advantage of σ_{UU},

since $d^5\Sigma_{\rm UU}^{\rm DDVCS}$ and $d^5\sigma_{\rm UU}^{\rm DDVCS}$ are independent on ϕ or φ_l and have the same value when they are integrated over the identical interval in θ_l in the leading twist approximation.

At leading twist and leading order, $\Delta\sigma_{\rm UU}^{\rm C}$, as well as $\Sigma_{\rm UU}$ subtracting its BH and DDVCS contributions, are directly proportional to the real part of the linear CFFs combination $\mathcal{C}_{\rm UU}^{\rm INT}$ given by Eq. (2.69),

$$\Delta\sigma_{\rm UU}^{\rm C}(\phi) = \mathcal{K}_{\rm UU}(\phi)\ {\rm Re}\left\{\frac{\xi'}{\xi}\left(F_1\mathcal{H} - \frac{t}{4M^2}F_2\mathcal{E}\right) + \xi(F_1+F_2)\widetilde{\mathcal{H}}\right\}. \tag{2.117}$$

I remind that, unlike Eq. (2.114), there shall be longitudinal CFFs originating from next-to-leading order in the CFFs combination. The kinematical factor $\mathcal{K}_{\rm UU}$ can be read off as mentioned before, see more details in Sec. 6.1.1. For a proton target, one realizes that ${\rm Re}\mathcal{H}^p(\xi',\xi,t)$ is suppressed by a kinematical factor ξ'/ξ, thus with decreasing $|\xi'|$ the contribution of ${\rm Re}\widetilde{\mathcal{H}}^p(\xi',\xi,t)$ begins to be important. Similarly, ${\rm Re}\mathcal{E}^n(\xi',\xi,t)$ is accessed by the measurements of a neutron target.

In Eq. (2.117) $\widetilde{\mathcal{H}}$ seems to be dominant at $|\xi'|\to 0$, however, its real part also becomes zero at $\xi'=0$, since ${\rm Re}\widetilde{\mathcal{H}}(-\xi',\xi,t) = -{\rm Re}\widetilde{\mathcal{H}}(\xi',\xi,t)$ is antisymmetric in ξ'. Therefore, the beam charge cross section difference also goes to zero at $\xi'=0$ and has the sign change behavior due to the antisymmetric property of the real parts of $\xi'\mathcal{H}$, $\xi'\mathcal{E}$ and $\widetilde{\mathcal{H}}$, as displayed in Eqs. (1.117) and (1.118).

In order to obtain more information on the other GPDs, the observable with target polarization are needed. As mentioned before, in the current state of polarized target technology, a fixed-target DDVCS experiment is not achievable. However, it can be achieved in the collider experiment, such as the EIC program. They are not discussed here but the polarized-nucleon formalism can be found in [57].

2.4.3 Asymmetries

Only the asymmetries in terms of $d^5\sigma$ are presented here. With polarized electron beam, one measures the BSA defined as

$$A_{\rm LU}^{-}(\phi) = \frac{\Delta\sigma_{\rm LU}^{-}(\phi)}{\sigma_{\rm UU}^{-}(\phi)} = \frac{d^5\sigma_{\rm LU}^{\rm INT1}}{d^5\sigma_{\rm UU}^{\rm BH1} + d^5\sigma_{\rm UU}^{\rm BH2} + d^5\sigma_{\rm UU}^{\rm DDVCS} + d^5\sigma_{\rm UU}^{\rm INT1}}. \tag{2.118}$$

The access to ${\rm Im}\{\mathcal{C}_{\rm LU}^{\rm INT}\}$ via the BSA is mostly complicated by the presence of ${\rm Re}\{\mathcal{C}_{\rm UU}^{\rm INT}\}$ in the denominator. Again, this entanglement can be cancelled by the application of beam charge, and then one can build the unpolarized and polarized Beam Charge Asymmetries as

$$A_{\rm UU}^{\rm C}(\phi) = \frac{\Delta\sigma_{\rm UU}^{\rm C}(\phi)}{\sigma_{\rm UU}(\phi)} = \frac{d^5\sigma_{\rm UU}^{\rm INT1}}{d^5\sigma_{\rm UU}^{\rm BH1} + d^5\sigma_{\rm UU}^{\rm BH2} + d^5\sigma_{\rm UU}^{\rm DDVCS}}, \tag{2.119}$$

$$A_{\rm LU}^{\rm C}(\phi) = \frac{\Delta\sigma_{\rm LU}^{\rm C}(\phi)}{\sigma_{\rm UU}(\phi)} = \frac{d^5\sigma_{\rm LU}^{\rm INT1}}{d^5\sigma_{\rm UU}^{\rm BH1} + d^5\sigma_{\rm UU}^{\rm BH2} + d^5\sigma_{\rm UU}^{\rm DDVCS}}, \tag{2.120}$$

The access to ${\rm Re}\{\mathcal{C}_{\rm UU}^{\rm INT}\}$ and ${\rm Im}\{\mathcal{C}_{\rm LU}^{\rm INT}\}$ via the BCAs are still complicated by the presence of $\mathcal{C}^{\rm DDVCS}$ in the denominator, making the physical interpretation more involved in comparison with measuring absolute cross sections. On the other hand, asymmetries measurements have the benefit that many experimental uncertainties cancel out because of the cross section ratio. Therefore, one can also perform these measurements as a first

step of the investigation. The azimuthal moments of the BCAs can also give direct access to the linear CFFs combinations only if the DDVCS contribution is negligible.

With respect to the BH2 contribution in the denominator, one shall notice the fact that it has large magnitude when θ_l approaches the edges of the phase space $\theta_l = 0, \pi$ due to small value of the propagators in Eq. (2.106). Therefore, the maginitudes of the asymmetries will be suppressed. To partly get rid of this problem, instead of integrating over the full range of θ_l, one rather has to sum over a restricted domain and exclude the endpoint regions, such as $[\pi/4, 3\pi/4]$. Even though the integration over $[\pi/4, 3\pi/4]$ in θ_l also reduces the magnitude of the nominators of the asymmetries, it still benifits the asymmetry measures, since the BH2 contribution generally dominates the cross section. Furthermore, the extent of BH2's decrease are greater than the the other contributions for a decreasing interval in θ_l, which one can roughly get from Eqs. (2.80) and (2.108).

Chapter 3

Model-predicted observables

To give quantitative estimates of the observables and provide some insights into the procedure of extracting the GPDs from DDVCS experiments, I have used the VGG model for computing the cross sections of the electroproduction of muon pairs off proton targets. Both the 5-fold cross section $d^5\sigma$ and $d^5\Sigma$ have been investigated at different kinematics to obtain a quantitative view of the sensitivities to kinematics and GPDs. The interference contribution to the cross section is particularly are highlighted since offering eventual access to a linear combinations of CFFs.

3.1 Estimates with VGG

The GPD model used in the calculations is as follows. The (x, ξ)-dependence of the GPDs is parameterized by using DDs ansatz, where the parameters are chosen as $b_{\rm val} = 1$, $b_{\rm sea} = 5$, $J_u = 0.3$ and $J_d = 0.1$. For the quark distributions, the MRST02 NNLO parameterization [64] at scale $\mu^2 = 1$ GeV^2 is used. The t-dependence of the GPD H is parameterized by using modified Regge model, given by Eq. (1.59), where the Regge slope is chosen as $\alpha' = 1.098$. For the t-dependences of the other GPDs, the t-factorized ansatz is used. This GPD model is also used throughout the rest of this document. As discussed in Sec. 2.4, the GPD H is dominant in the observables for proton unpolarized targets. Therefore, the observables shown in this section include only GPD H.

The kinematical variables have been chosen as a fixed set of ($Q^2 = 1.25$ GeV^2, $t = -0.15$ GeV^2, $\xi = 0.135$) and varying ξ', in order to investigate the ξ' dependence of the observables. Note that the range of ξ' in principle is $|\xi'| < \xi$, however, it is constrained here by the phase spaces and the muon pair mass. Eventually, ξ' varies approximately from -0.06 to 0.11. The integration over final muon polar angle θ_l has been performed for the full range between 0 and π, namely $\theta_0 = \pi/2$ in Eqs. (2.74) and (2.92).

3.1.1 Cross sections as functions of the azimuthal angles

The 5-fold unpolarized cross sections, $\sigma^-_{\rm UU}(\phi)$ and $\Sigma^-_{\rm UU}(\varphi_l)$, at $\xi' = 0.06$ are displayed by the solid black curves in Fig. 3.1 and their contributions are represented by the colored curves. Note that the unit for the cross sections is pb/GeV^6, implying the necessity of a high luminosity for the measurements. For this moderate ξ', it is obviously seen that the BH2 contributions (red dashed curves) are dominant. I remind that BH1 contributions (red dotted curves) become significant when $Q'^2 \to 0$, namely $\xi' \to \xi$. The DDVCS contributions (green curves) are significant and cannot be neglected. Although the DDVCS

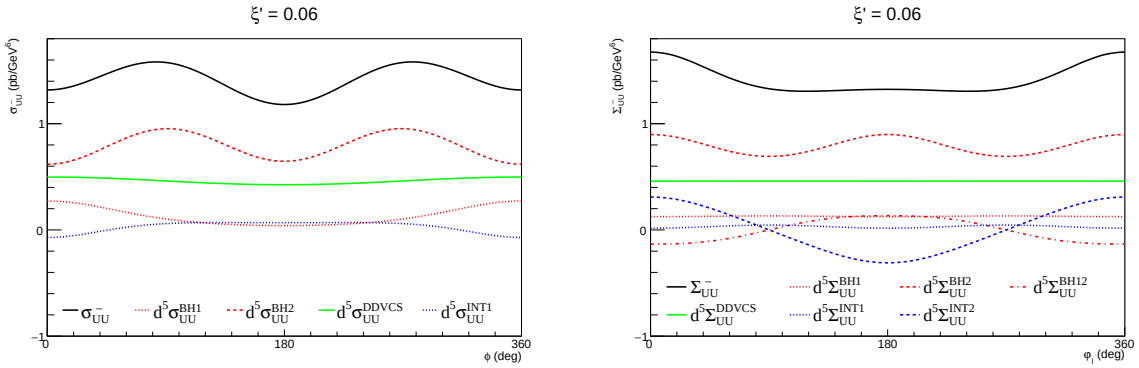

Figure 3.1: $\sigma^{-}_{\rm UU}(\phi)$ (left panel) and $\Sigma^{-}_{\rm UU}(\varphi_l)$ (right panel) at $\xi' = 0.06$.

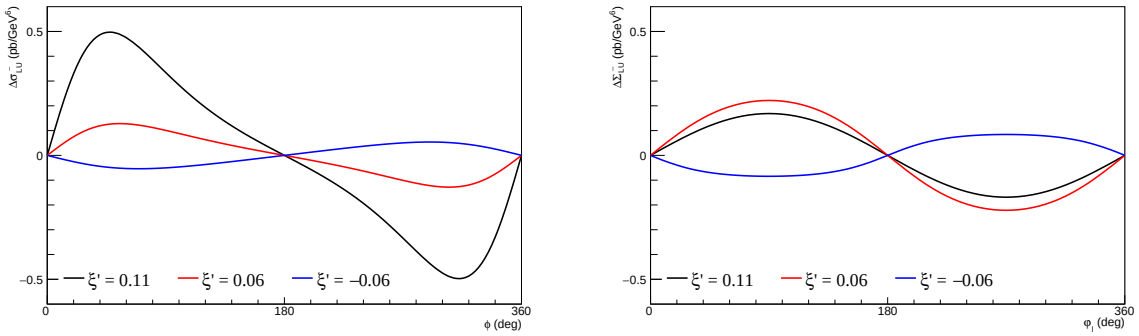

Figure 3.2: $\Delta\sigma^{-}_{\rm LU}(\phi)$ (left panel) and $\Delta\Sigma^{-}_{\rm LU}(\varphi_l)$ (right panel) at $\xi' = 0.11,\ 0.06,\ -0.06$.

contributions dominate the CFFs involving parts, they are related to the bilinear CFFs combination. For the real part of the CFFs in a linear fashion, accessed through the unpolarized interference contributions, additional positron beam is needed to single out them in the beam charge cross section differences. The unpolarized INT1 (blue dotted curves) and INT2 (blue dashed curve) contributions are relative small, and their measurements therefore require even higher luminosities. With respect to $\Sigma^{-}_{\rm UU}(\varphi_l)$ (right panel in Fig. 3.1), the unpolarized INT1 contribution (blue dotted curves) is much smaller than the INT2 contribution (blue dashed curve). Therefore, the latter is more appropriate for the extraction of the real part of the CFFs, which is singled out in $\Sigma_{\rm UU}(\varphi_l)$, the sum of unpolarized cross section with electron and positron given by Eq. (2.116).

The 5-fold beam spin cross section differences, $\Delta\sigma^{-}_{\rm LU}(\phi)$ and $\Delta\Sigma^{-}_{\rm LU}(\varphi_l)$, at $\xi' = 0.11$ (black curves), 0.06 (red curves), -0.06 (green curves) are shown in Fig. 3.2. They include only the helicity-dependent INT1 and INT2 contributions, $d^5\sigma^{\rm INT1}_{\rm LU}$ and $d^5\Sigma^{\rm INT2}_{\rm LU}$, respectively. Their sign change behavior can be readily seen when ξ' changes sign. For $\Delta\sigma^{-}_{\rm LU}(\phi)$, the magnitude at $\xi' = 0.11$ is larger than $\xi' = 0.06$ since the BH1 contribution becomes significant, while $\Delta\Sigma^{-}_{\rm LU}(\varphi_l)$ acts contrarily since the BH2 contribution becomes small when one approaches $\xi' = \xi$.

3.1.2 Azimuthal moments as functions of ξ'

Fig. 3.1 and 3.2 show the examples for the specific ξ', which offer the basic picture on the ϕ dependence of the observables. For the ξ' dependence, it is more convenient to investigate the azimuthal moments of the observables. For any observable $d^5\sigma(\phi)$, its

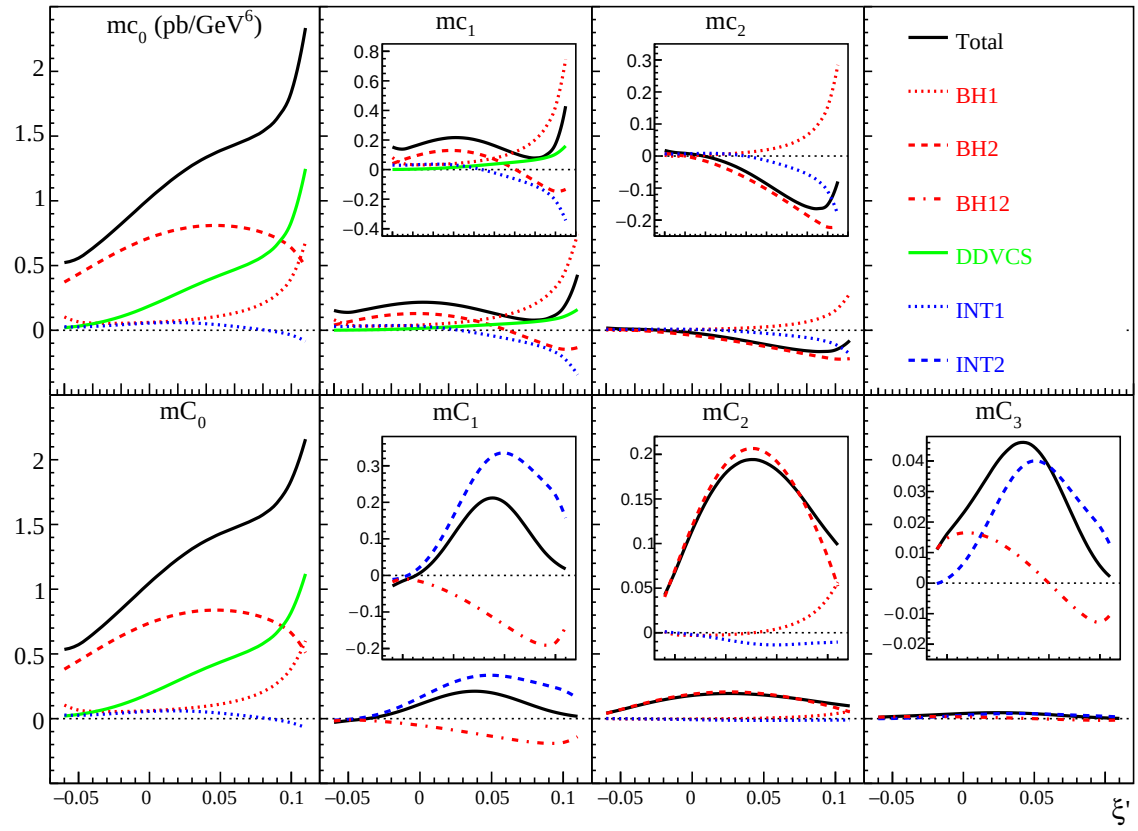

Figure 3.3: The cosine moments of the unpolarized cross section as functions of ξ'. The upper panels show the moments of $\sigma^{-}_{\rm UU}(\phi)$ and the bottom panels show the moments of $\Sigma^{-}_{\rm UU}(\varphi_l)$. The scale of each panel is unified while the internal panels display with different scales in the y-axis for visual clarity. The black solid curves represent the total moments and the colored curves stand for the non-zero moments of the corresponding contributions.

azimuthal moments are given by

$$\begin{aligned} mc_0 &= \frac{1}{2\pi}\int_0^{2\pi} d\phi\; d^5\sigma(\phi), \\ mc_n &= \frac{1}{\pi}\int_0^{2\pi} d\phi\; d^5\sigma(\phi)\cos(n\phi), \\ ms_n &= \frac{1}{\pi}\int_0^{2\pi} d\phi\; d^5\sigma(\phi)\sin(n\phi), \end{aligned} \tag{3.1}$$

where $n = 1, 2, 3\cdots$. The azimuthal moments of any observable $d^5\Sigma(\varphi_l)$, denoted by mC_0, mC_n and mS_n instead, are given by the similar expressions integrated over φ_l.

Moments of the unpolarized cross section

Fig. 3.3 show the cosine moments of the unpolarized cross sections and the corresponding contributions. With respect to the total moments represented by the black solid curves, the cos0 moments are dominant and higher order moments are much smaller.

The BH1 contributions $d^5\sigma^{\rm BH1}_{\rm UU}$ and $d^5\Sigma^{\rm BH1}_{\rm UU}$ are given by Eqs. (2.76) and (2.94), respectively. The red dotted curves in Fig. 3.3 present their non-zero moments as functions

of ξ'. It can be readily seen that the BH1 contributions are small in the time-like region ($\xi' < 0$), especially for $d^5\sigma_{\rm UU}^{\rm BH1}$, and become significant when ξ' increases. The cos0 moments are dominant and higher order moments are much smaller except $mc_1^{\rm BH}$. The presence of a significant $mc_1^{\rm BH}$ is inconsistent with Eq. (2.76). The possible explanation is that this inconsistency is attributed to the accuracy of the VGG calculation and the approximations used in Belitsky and Müller formalism. The VGG calculation is regarded as an accurate tool for the estimation of BH processes at small t, while the formalism in [57] is developed at leading order approximation. Moreover, the nucleon mass corrections are neglected and only leading and subleading terms are kept in the scalar products of Eq. (2.30) when introducing the symmetric variables, which are the cornerstone for the deduction of the 7-fold cross section and the (anti)symmetric properties of the Fourier coefficients. Therefore, the $mc_1^{\rm BH}$ shall be related to an accurate Fourier coefficient $cc_1^{\rm BH}$ which survives from the integration over the muon angle and does not exist in [57].

The BH2 contributions $d^5\sigma_{\rm UU}^{\rm BH2}$ and $d^5\Sigma_{\rm UU}^{\rm BH2}$ are given by Eqs. (2.77) and (2.96), respectively. The red dashed curves in Fig. 3.3 present their non-zero moments, where one can find that the magnitudes of BH2 moments are in general larger than the BH1 ones except for the region of $\xi' \to \xi$ where the BH2 moments become less significant. One easily sees the dominance of the cos0 moments.

The BH12 contribution survives only in $\Sigma_{\rm UU}^{-}$, given by Eq. (2.97). The red dash-dotted curves in Fig. 3.3 present their non-zero moments and the $\cos(3\varphi_l)$ moment $mC_3^{\rm BH12}$ comes from the second term in Eq. (2.97) , which can be decomposed following

$$\cos(\varphi_l)\cos(2\varphi_l) = \frac{\cos(\varphi_l)}{2} + \frac{\cos(3\varphi_l)}{2}. \tag{3.2}$$

The $\cos(\varphi_l)$ moment $mC_1^{\rm BH12}$ shows its dominance and consists of the contributions from the $C_1^{\rm BH12}$ and $C_2^{\rm BH12}$ Fourier harmonics.

The DDVCS contribution $d^5\sigma_{\rm UU}^{\rm DDVCS}$ is given by Eq. (2.78) and $d^5\Sigma_{\rm UU}^{\rm DDVCS}$ equals to $d^5\sigma_{\rm UU}^{\rm DDVCS}$ at leading twist. They have the most concise expression, containing only cos0 Fourier harmonics without the entanglement of the BH propagators. The green solid curves in Fig. 3.3 present their non-zero moments. The presence of the $\cos\phi$ moment $mc_1^{\rm DDVCS}$ in $d^5\sigma_{\rm UU}^{\rm DDVCS}$ is inconsistent with Eq. (2.78). It is caused by the minimal twist-3 corrections to restore gauge invariance in the VGG calculation. For $d^5\Sigma_{\rm UU}^{\rm DDVCS}$, the twist-3 effect drops out from the integration over ϕ, resulting in the absence of $\cos\varphi_l$ and the slight difference between the cos0 moments. For the current kinematics, the DDVCS contribution is small in the time-like region and becomes significant in the space-like region especially in the limit $\xi' \to \xi$.

The unpolarized contribution $d^5\sigma_{\rm UU}^{\rm INT1}$ is given by Eq. (2.82) and offers access to the real part of the linear CFFs combination $\mathcal{C}_{\rm UU}^{\rm INT}$. Experimentally, this contribution can be singled out in the beam charge cross section by introducing positron beam, as shown in Eq. (2.115). The blue dotted curves in the upper panels of Fig. 3.3 present its non-zero moments. The $\cos(\phi)$ moment $mc_1^{\rm INT1}$ dominates while the $\cos(2\phi)$ moment $mc_2^{\rm INT1}$ caused by the minimal twist-3 correction is small. The presence of the moderate $mc_0^{\rm INT1}$ is inconsistent with Eq. (2.76). The possible explanation is that it might result from the interference between the accurate BH1 term related with $mc_1^{\rm BH1}$ and DDVCS term with minimal twist-3 and therefore is not present in Eq. (2.82). For the current kinematics, the ξ' dependence of $d^5\sigma_{\rm UU}^{\rm INT1}$ is similar to the BH1 and DDVCS contribution, having significant magnitude only in the space-like region. Therefore, extracting $\mathrm{Re}\{\mathcal{C}_{\rm UU}^{\rm INT}\}$ from $d^5\sigma_{\rm UU}^{\rm INT1}$ is more challenging in the time-like region.

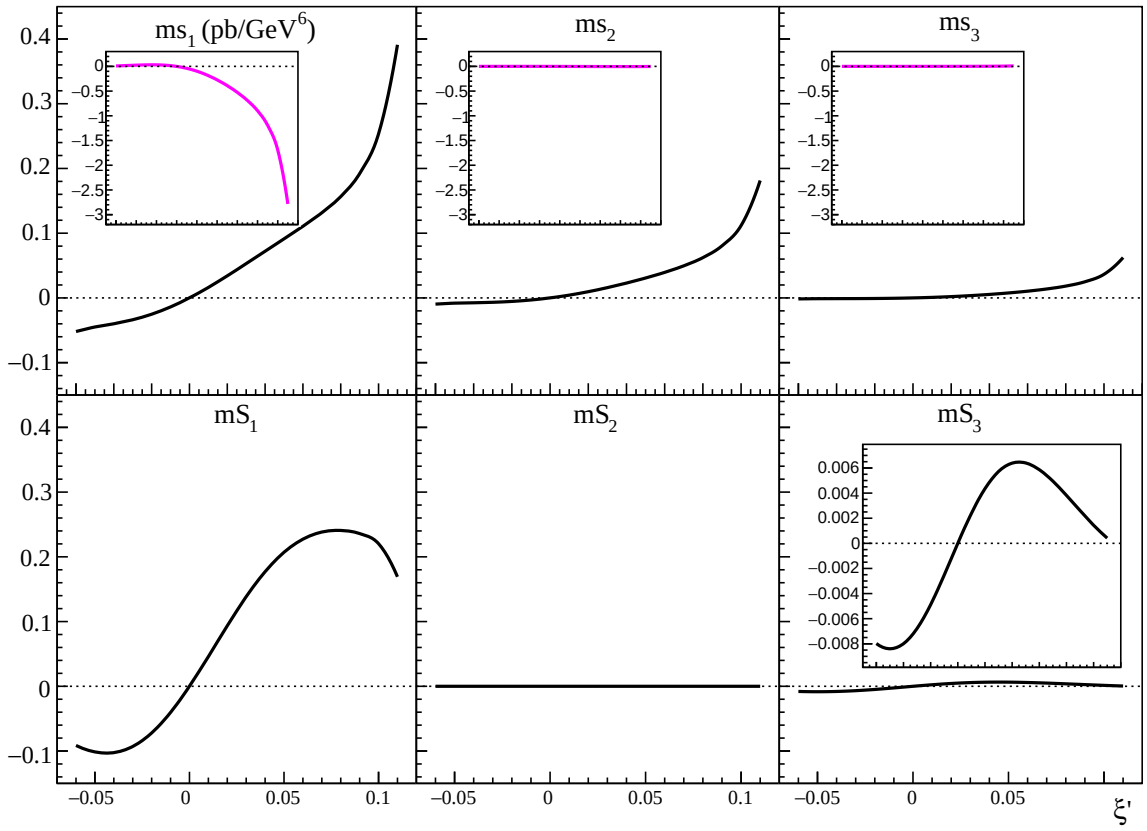

Figure 3.4: The sine moments of the beam spin cross section difference as functions of ξ'. The upper panels show the moments of $\Delta\sigma^{-}_{\rm LU}(\phi)$ and the bottom panels show the moments of $\Delta\Sigma^{-}_{\rm UU}(\varphi_l)$. The scale of each panel is unified. The internal panel in the bottom right panel for mS_3 display with different scales in the y-axis for visual clarity. The black solid curves represent the moments of $\Delta\sigma^{-}_{\rm LU}(\phi)$ and the magenta solid curves stand for the moments extracted from $\mathcal{P}_1\mathcal{P}_2 \cdot \Delta\sigma^{-}_{\rm LU}(\phi)$.

The unpolarized contributions $d^5\Sigma^{\rm INT1}_{\rm UU}$ and $d^5\Sigma^{\rm INT2}_{\rm UU}$ are given by Eqs. (2.100) and (2.103), respectively. They also offer access to the real part of the linear CFFs combination. Experimentally, these contributions can be derived indirectly by introducing positron beam, as discussed in Sec. 2.4.2. Their non-zero moments are presented by the blue dotted (INT1) and dashed (INT2) curves in Fig. 3.3. It can be seen that the moments of $d^5\Sigma^{\rm INT1}_{\rm UU}$ have much smaller magnitudes than $d^5\Sigma^{\rm INT2}_{\rm UU}$. Thus, it is easier to extract the CFFs from $d^5\Sigma^{\rm INT2}_{\rm UU}$, which also provides access to $\mathrm{Re}\{\mathcal{C}^{\rm INT}_{\rm UU}\}$. The $\cos(\varphi_l)$ moment $mC^{\rm INT2}_1$ is dominant and the $\cos(3\varphi_l)$ moment $mC^{\rm INT2}_3$ comes from the second term of Eq. (2.103) through Eq. (3.2). In comparison with the $d^5\sigma^{\rm INT1}_{\rm UU}$ contribution, $d^5\Sigma^{\rm INT1}_{\rm UU}$ has a wider ξ' range with relatively significant magnitude since it is partly driven by the dominant BH2 process. In the time-like region, it is better to alternatively extract $\mathrm{Re}\{\mathcal{C}^{\rm INT}_{\rm UU}\}$ from $d^5\Sigma^{\rm INT1}_{\rm UU}$.

Moments of the beam spin cross section difference

The beam spin cross section difference $\Delta\sigma^{-}_{\rm LU}(\phi)$ includes only the helicity-dependent contribution $d^5\sigma^{\rm INT1}_{\rm LU}$ given by Eq. (2.84) and $\Delta\Sigma^{-}_{\rm UU}(\varphi_l)$ includes only $d^5\Sigma^{\rm INT2}_{\rm LU}$ given by Eq. (2.104). They offer access to the imaginary part of the linear CFFs combination

$\mathcal{C}^{\rm INT}_{\rm LU}$. The black solid curves in Fig. 3.4 present their sine moments. Due to the entanglement of the BH propagators in the $d^5\sigma^{\rm INT1}_{\rm LU}$ contributions, as shown in Eq. (2.84), one shall also investigate the moments calculated through the substitution of $\mathcal{P}_1\mathcal{P}_2 \cdot d^5\sigma^{\rm INT1}_{\rm LU}$ for $d^5\sigma^{\rm INT1}_{\rm LU}$ in Eq. (3.1), presented by the magenta curves in Fig. 3.4. They are zero for the $\sin(2\phi)$ and $\sin(3\phi)$ moments when getting rid of the entanglement, which implies that the non-zero values of $ms_2^{\rm INT1}$ and $ms_3^{\rm INT1}$ just result from the numerical integration and the VGG calculation is consistent with Eq. (2.84). For $\Delta\Sigma^{-}_{\rm UU}(\varphi_l)$, it can be seen that the $\sin(\varphi_l)$ moment $mS_1^{\rm INT1}$ are dominant. The $\sin(3\varphi_l)$ moment $ms_3^{\rm INT1}$ has a small magnitude and results from the second term of Eq. (2.104) through

$$\sin(\varphi_l)\cos(2\varphi_l) = \frac{\sin(3\varphi_l)}{2} - \frac{\sin(\varphi_l)}{2}. \tag{3.3}$$

Moreover, It can be observed that the moments change sign from $\xi' < 0$ to $\xi' > 0$. Similarly, extracting $\mathrm{Im}\{\mathcal{C}^{\rm INT}_{\rm LU}\}$ from $d^5\sigma^{\rm INT1}_{\rm LU}$ is very challenging in the time-like region, where one better perform the extraction from $d^5\Sigma^{\rm INT2}_{\rm LU}$.

Basic on the GPD formalism, both $\mathrm{Re}\{\mathcal{C}^{\rm INT}_{\rm UU}\}$ and $\mathrm{Im}\{\mathcal{C}^{\rm INT}_{\rm LU}\}$ are antisymmetric functions in ξ'. Thus, measurements in either space-like or time-like region offers the full map of $\mathrm{Re}\{\mathcal{C}^{\rm INT}_{\rm UU}\}$ and $\mathrm{Im}\{\mathcal{C}^{\rm INT}_{\rm LU}\}$. Therefore, measurements in both region offers additional tests for the universality of the GPD formalism.

3.2 Dominance of the CFF $\mathcal{H}$

3.2.1 CFFs

The calculation is here performed including the 4 GPDs. The kinematical variables are the same as in the previous section. The CFFs as functions of ξ' are displayed in Fig. 3.5, where $\widetilde{\mathcal{E}}$ is not presented since it does not enter the interference contributions. The CFF $\widetilde{\mathcal{E}}$ only enters into the pure DDVCS contributions and eventually has negligible impact on the unpolarized cross section. In Fig. 3.5, it can be easily seen that the CFFs are (anti)symmetric in ξ', given by Eqs. (1.117) to (1.120). In addition, the real and imaginary parts of $\mathcal{H}$ (red curves) are dominant with respect to the magnitudes of the CFFs. For proton target, the contributions of $\mathcal{E}$ (green curves) and $\widetilde{\mathcal{H}}$ (blue curves) are suppressed by the small kinematics factors and the sensitivities to them can be foreseen to be very

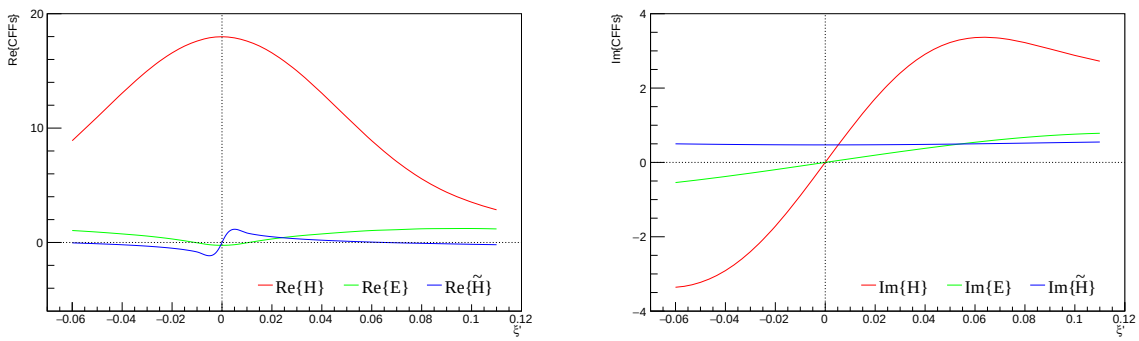

Figure 3.5: The real (left panel) and imaginary (right panel) parts of the CFFs as function of ξ' in the VGG calculation at $\xi = 0.135$.

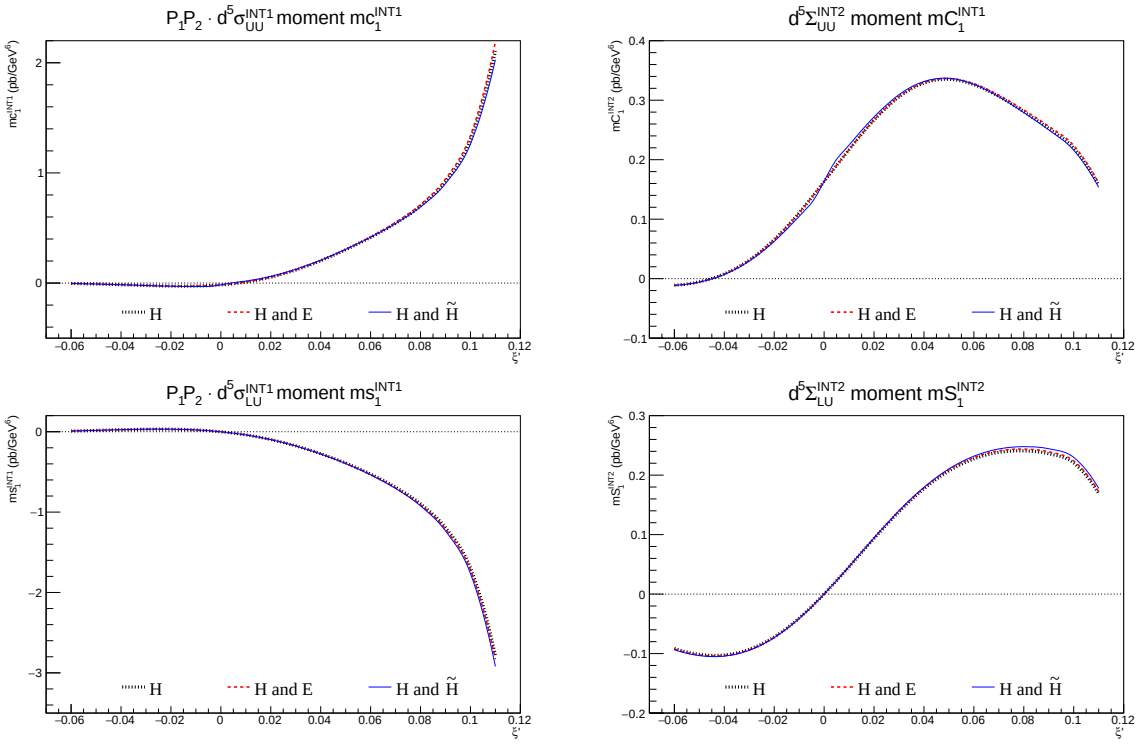

Figure 3.6: The dominant moments in the interference contributions at $\xi = 0.135$. Left upper panel: the $\cos(\phi)$ moment $mc_1^{\rm INT1}$ of $d^5\sigma_{\rm UU}^{\rm INT1}$; Right upper panel: the $\cos(\varphi_l)$ moment $mC_1^{\rm INT2}$ of $d^5\Sigma_{\rm UU}^{\rm INT2}$; Left bottom panel: the $\sin(\phi)$ moment $ms_1^{\rm INT1}$ of $d^5\sigma_{\rm LU}^{\rm INT1}$; Right bottom panel: the $\sin(\varphi_l)$ moment $mS_1^{\rm INT2}$ of $d^5\Sigma_{\rm UU}^{\rm INT2}$. The thick black dotted curves correspond to the calculation including only $\mathcal{H}$, the red dashed curves include $\mathcal{H}$ and $\mathcal{E}$ and the blue solid curves include $\mathcal{H}$ and $\widetilde{\mathcal{H}}$.

small at the current kinematics. Note that the wiggle around the point $\xi' \to 0$ of the blue curve in the left panel arise from the numerical convolution of Re$\widetilde{\mathcal{H}}$.

3.2.2 Azimuthal moments

The dominant moments of the interference contributions, $mc_1^{\rm INT1}$, $mC_1^{\rm INT2}$, $ms_1^{\rm INT1}$ and $mS_1^{\rm INT2}$, are shown in Fig. 3.6. At the current kinematics, they are dominated by the CFF $\mathcal{H}$ and hardly sensitive to the CFF $\mathcal{E}$ or $\widetilde{\mathcal{H}}$ for both the real and imaginary parts.

3.2.3 Theoretical sensitivity to $\widetilde{\mathcal{H}}$

According to Belitsky and Müller formalism, there shall be some sensitivity to the CFFs $\widetilde{\mathcal{H}}$ other than the strong dominance of $\mathcal{H}$, though I concentrate only on unpolarized proton target. Eq. (2.117) displays that Re$\mathcal{H}$ is suppressed by a kinematical factor ξ'/ξ and Re$\widetilde{\mathcal{H}}$ is suppressed by ξ. In order to find the sensitivity to $\widetilde{\mathcal{H}}$, I have investigated ξ' dependence of the interference contributions at a larger ξ. As shown in Fig. 2.7, $-t$ shall be large as well in order to cover large ξ. Eventually, The kinematical variables have been chosen as a fixed set of ($Q^2 + Q'^2 = 8$ GeV^2, $t = -0.825$ GeV^2, $\xi = 0.4$) and varying ξ'. The large value of the sum of the virtualities not only opens the phase space to enlarge the accessible ξ' range, but also supports factorization regime at the same time ($2P \cdot \bar{q} \approx 10$ GeV^2). Eventually, ξ' varies approximately from -0.36 to 0.37.

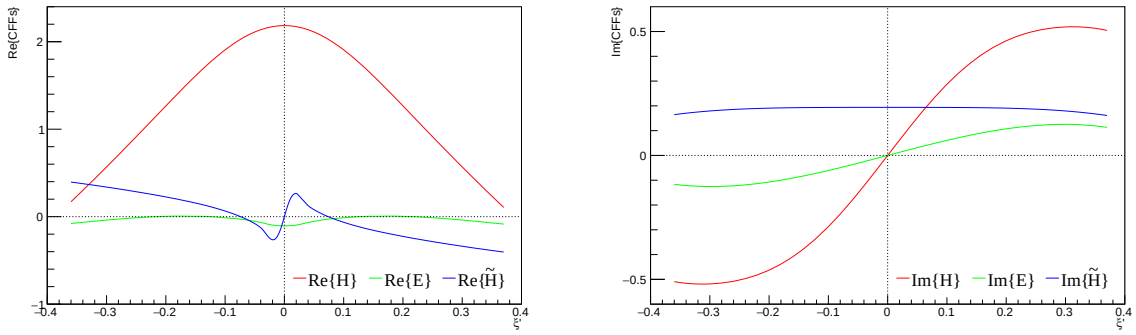

Figure 3.7: The real (left panel) and imaginary (right panel) parts of the CFFs as function of ξ' in the VGG calculation at $\xi = 0.4$.

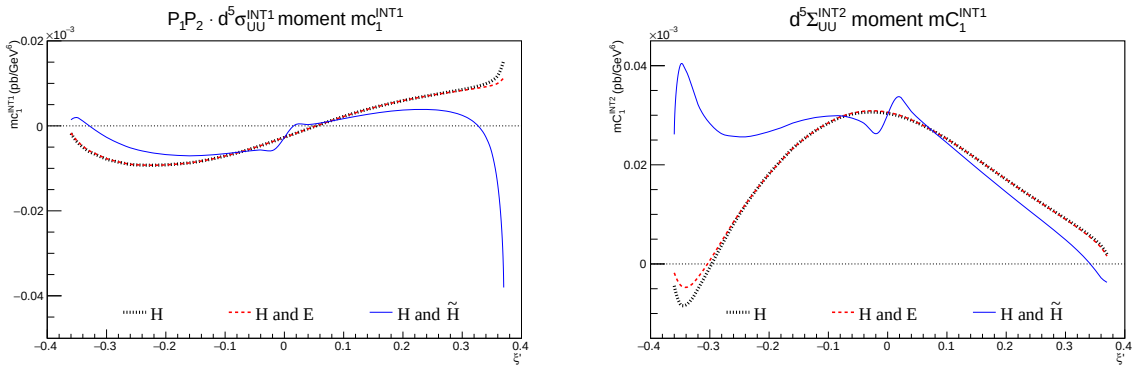

Figure 3.8: The dominant moments in the unpolarized interference contributions at $\xi = 0.4$. The styles of curves are the same as Fig. 3.6.

Fig. 3.7 shows that the CFFs as functions of ξ' for the kinematical set of $\xi = 0.4$. Comparing with Fig. 3.5, the CFFs decrease generally by one order of magnitude and result in small cross sections, which are further suppressed kinematically due to the large $-t$ and virtualities. Therefore, the measurements for this kinematical set are very challenging and demand an extreme high luminosity. It can also be seen from the comparison that the dominance of $\mathcal{H}$ (red curves) becomes less significant, especially for the real part at the edges, namely in the region of $\xi' \to \pm\xi$.

The dominant moment $mc_1^{\rm INT1}$ in $d^5\sigma_{\rm UU}^{\rm INT1}$ and $mC_1^{\rm INT2}$ in $d^5\Sigma_{\rm UU}^{\rm INT2}$ are shown in Fig. 3.8. The dominance of Re$\mathcal{H}$ still holds in general but the sensitivity to Re$\widetilde{\mathcal{H}}$ is much more obvious and becomes even dominant when one approaches the edges. At the edge of the space-like region, namely $\xi' \to \xi$, $d^5\sigma_{\rm UU}^{\rm INT1}$ is strongly sensitive to Re$\widetilde{\mathcal{H}}$ and so is $d^5\Sigma_{\rm UU}^{\rm INT2}$ in the time-like region. Similar feature can also be found for the helicity-dependent interference contributions, as shown in Fig. 3.9. However, the sensitivity to Im$\widetilde{\mathcal{H}}$ is weaker. Therefore, the way one processes the data, namely the way of the integration over the angles, not only determines the ξ' dependence of the observables for the CFFs extraction but also impacts the ξ' dependence of CFFs.

However, one can notice the magnitudes of the moments are very small. They are 10^4 to 10^5 smaller than the ones in Fig. 3.6, making the measurements extremely difficult. In practice, the CFF $\mathcal{H}$ always dominates the observables for proton unpolarized targets. Therefore, the extraction of the GPD H information shall be set as the main goal for the proton DDVCS experiments at JLab 12 GeV.

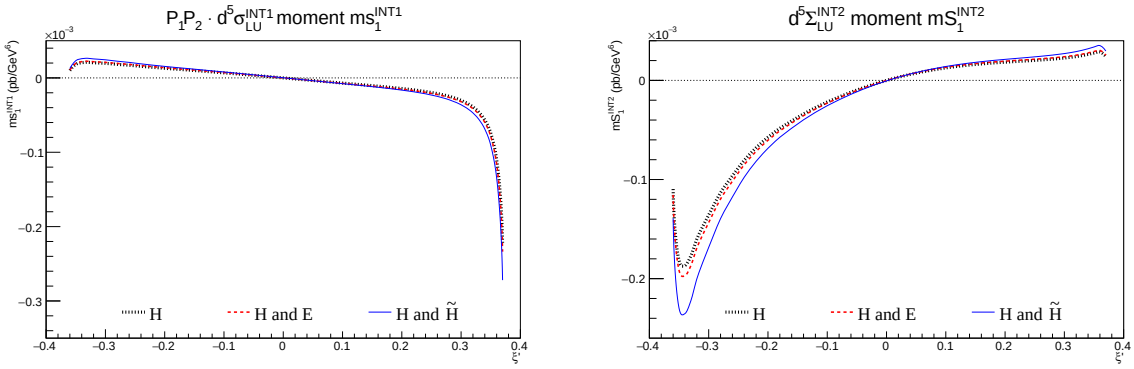

Figure 3.9: The dominant moments in the helicity-dependent interference contributions at $\xi = 0.4$. The styles of curves are the same as Fig. 3.6.

3.3 Sensitivities to the other CFFs

As discussed in Sec. 2.4, the interference contributions are sensitive to the CFF $\mathcal{E}$ for the unpolarized neutron target, and the GPD E can be therefore investigated through neutron DDVCS. Moreover, different combinations of CFFs enter the observables with polarized nucleons, which are sensitive to the CFFs beside $\mathcal{H}$ [56]. For example, the longitudinal target spin cross section difference $\Delta\sigma_{\rm UL}^{-}$, measured by using unpolarized electrons and longitudinal polarized nucleons, is related with the imaginary part of CFFs by

$$\Delta\sigma_{\rm UL}^{-} \sim {\rm Im}\left\{F_1\widetilde{\mathcal{H}} + \xi'\left(F_1+F_2\right)\left(\mathcal{H} + \frac{\xi}{1+\xi}\mathcal{E}\right) + \cdots\right\}, \tag{3.4}$$

and the double spin cross section difference $\Delta\sigma_{\rm LL}^{-}$, measured by using polarized electrons and longitudinal polarized nucleons, is related with the real part of CFFs by

$$\Delta\sigma_{\rm LL}^{-} \sim {\rm Re}\left\{\frac{\xi'}{\xi}F_1\widetilde{\mathcal{H}} + \xi\left(F_1+F_2\right)\left(\mathcal{H} + \frac{\xi}{1+\xi}\mathcal{E}\right) + \cdots\right\}. \tag{3.5}$$

The observables clearly offer access to the CFF $\widetilde{\mathcal{H}}$ for longitudinal polarized protons and the measurements would be possibly performed at the future EIC facilities.

Chapter 4

DDVCS events generation

DDVCS experimental pseudo-data consist of two components: the magnitude of the observable and the corresponding uncertainty. The magnitude of the observable can be directly obtained by using the VGG code at a given kinematical point. For the statistical uncertainty, the number of events within the kinematical bin shall be well evaluated. As the DDVCS cross section is extremely small, the kinematical bin shall be large in order to obtain a high statistics. The DDVCS cross section is not a linear function in each variables and its variation within a large kinematical bin can be huge. Therefore, the number of events shall be evaluated by an dedicated event generator, in which the phase space is divided into tiny bins and the cross section within each tiny bin can be approximately considered as linear function. However, an powerful and reliable event generator for the DDVCS process requires a massive table of 7-fold cross section, which is not yet developed. Therefore, a "quasi" event generator for the exclusive electroproduction of muon pairs off a proton target has been developed, in which the 5-fold cross section integrated over the lepton solid angle and the adopted GPDs are calculated by using the VGG model. The goal of developing such a quasi event generator is to derive reliable statistical errors for the observables in terms of the 5-fold cross section. The dependence of the muon angle is lost in the event generator and corrections is needed when applying to the limited acceptance of muon angles, which is discussed in the next chapter. I stress that the event generator is only used for the evaluation of the statistical error and not for the generation of the magnitude of the observable.

4.1 Development of the event generator

The development of the event generator follows the steps below:

(a) A grid covering the full phase space of interest is adopted to divide the 5-dimensional phase space $(x_{\mathrm{B}}, Q^2, t, Q'^2, \phi)$ into small bins such that one can approximately consider the integrated cross section as the differential cross section at the bin center multiplied by the bin widths.

(b) The bins whose geometric centers lie within the kinematically authorized phase space might not be fully occupied in the calculation of the integrated cross section. Therefore, bin weights are introduced representing the occupancy rate determined by a Monte Carlo method. The bin weight computation is performed with respect to the 4-dimensional phase space $(x_{\mathrm{B}}, Q^2, t, Q'^2)$, since the ϕ bins are always fully occu-

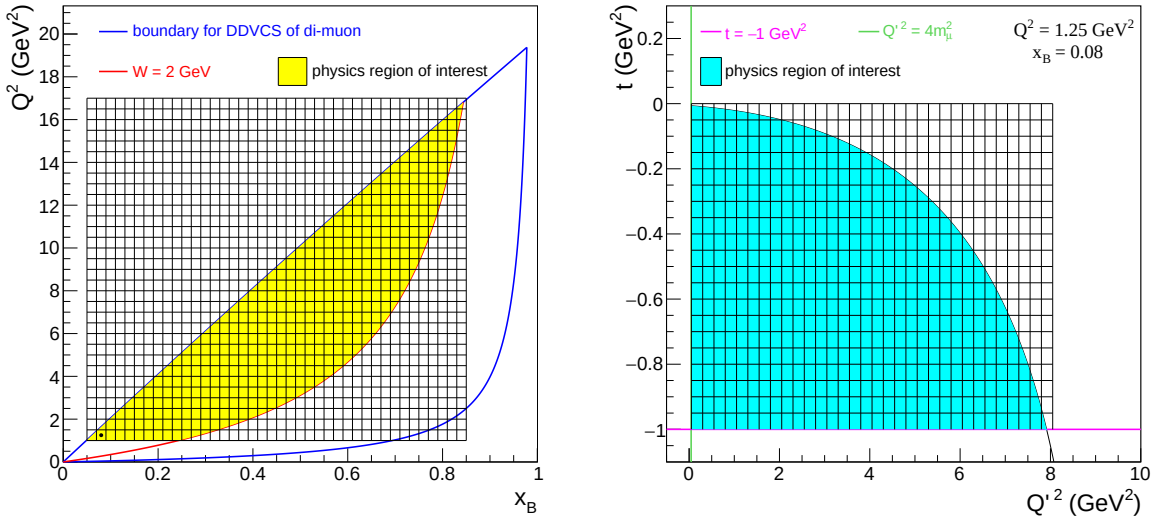

Figure 4.1: The grid adopted for the event generator. Left panel: the grid in the $(Q^2, x_{\rm B})$ plane. Right panel: the grid in the (t, Q'^2) plane at $Q^2 = 1.25$ GeV^2 and $x_{\rm B} = 0.08$, corresponding to the black solid circle in the left panel.

pied. The bins whose geometric centers lie outside of the kinematically authorized phase space are not considered in the determination of the number of events.

(c) The number of events for each 5-dimensional bin $(x_{\rm B}, Q^2, t, Q'^2, \phi)$, is computed as

$$N = \frac{d^5\sigma}{dx_{\rm B}dQ^2dtdQ'^2d\phi} \cdot \Delta x_{\rm B} \cdot \Delta Q^2 \cdot \Delta t \cdot \Delta Q'^2 \cdot \Delta\phi \cdot w_{\rm b} \cdot \mathcal{L} \cdot T, \tag{4.1}$$

where $w_{\rm b}$ is the bin weight, $\mathcal{L}$ is the luminosity and T is the running time.

(d) The final step is making the continuous distributions in the kinematical variables with respect to all the events. For each 5-dimensional bin $(x_{\rm B}, Q^2, t, Q'^2, \phi)$, the Q^2 value of the event i out of N events is assigned by

$$Q_i^2 = Q_c^2 + \Delta Q^2 \cdot \left(r_i - \frac{1}{2}\right), \tag{4.2}$$

where Q_c^2 is the value at the bin center, ΔQ^2 is the bin width and r_i is a random number between 0 and 1. The values in $x_{\rm B}$, t and Q'^2 are assigned simultaneously by a similar approach. The assignment runs iteratively until the values are kinematically authorized. Using the assigned values, the values in ξ' and ξ of each event are calculated through Eqs.(1.101) and (1.102). The assigned kinematical values for all the events are stored in a root file.

The finer grid one adopt for the event generator, the better projection one can derive. In consideration of the computing power and time, the following 5-dimensional grid of bins has been adopted for the event generator (see Fig. 4.1):

- 40 bins in $x_{\rm B}$ from 0.05 to 0.85, $\Delta x_{\rm B} = 0.02$;
- 32 bins in Q^2 from 1 to 17 GeV^2, $\Delta Q^2 = 0.5$ GeV^2;

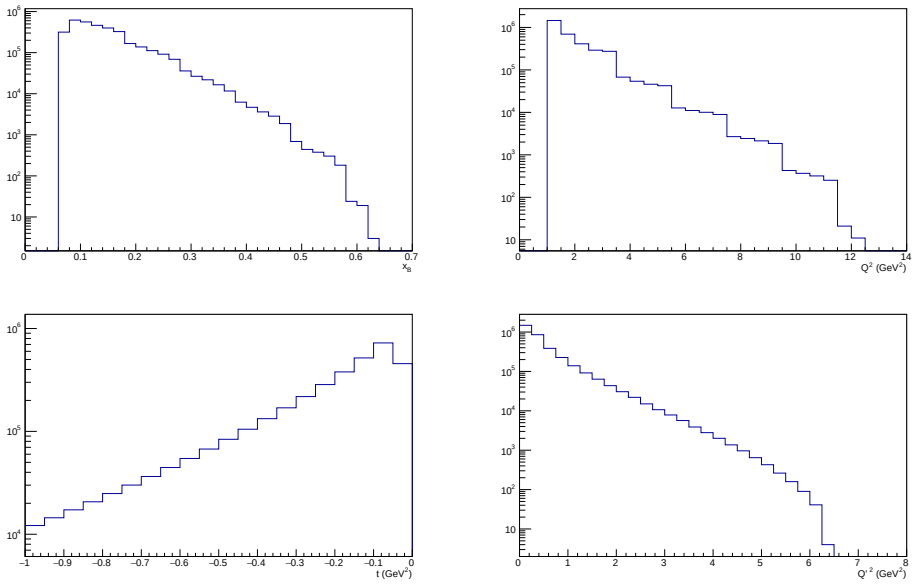

Figure 4.2: Distributions of kinematic variables for DDVCS events: x_{B} distribution (top left panel), Q^2 distribution (top right panel), t distribution (bottom left panel), and Q'^2 distribution (bottom right panel).

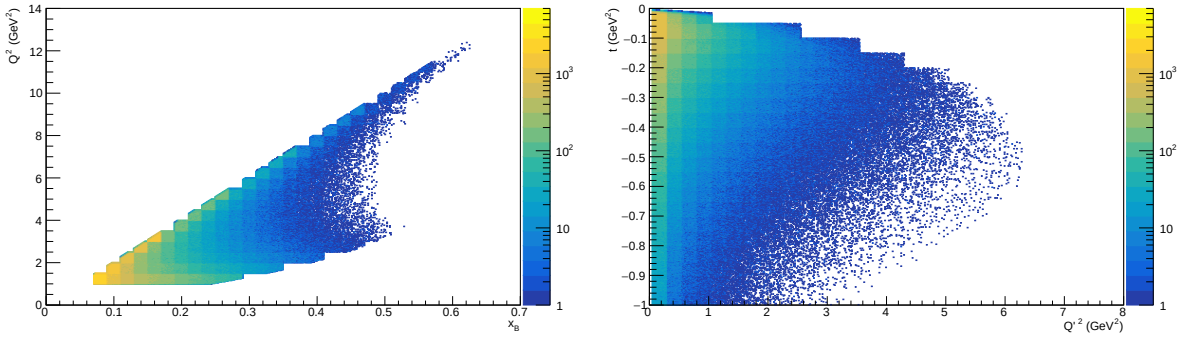

Figure 4.3: Distributions of kinematic variables for DDVCS events: the distribution in (Q^2, x_{B}) (left panel) and distribution in (t, Q'^2) (Right panel).

- 20 bins in t from 0 to -1 GeV^2, $\Delta t = 0.05$ GeV^2;
- Multiple bins in Q'^2 from $4m_\mu^2$ to Q'^2_{max}, $\Delta Q'^2 = 0.25$ GeV^2;
- 24 bins in ϕ from 0° to 360°, $\Delta\phi = 15°$,

where Q'^2_{max} is determined following Eq. (2.37).

Eventually, about 3×10^4 bins in the 4-dimensional hypervolume of $(x_{\mathrm{B}}, Q^2, t, Q'^2)$ have the kinematically authorized bin center and make about 7×10^5 bins in the 5-dimensional hypervolume of $(x_{\mathrm{B}}, Q^2, t, Q'^2, \phi)$ for the event generator. With respect to the Monte Carlo computation of the bin weights, 10^7 times iterations have been performed for each bin.

Fig. 4.2 illustrates the distributions of kinematic variables for DDVCS events when $\mathcal{L} = 10^{36}$ cm^{-2}·s^{-1} and $T = 50$ days. Globally speaking, the number of events roughly follows an exponential distribution in each variable. In another word, the events concentrate in

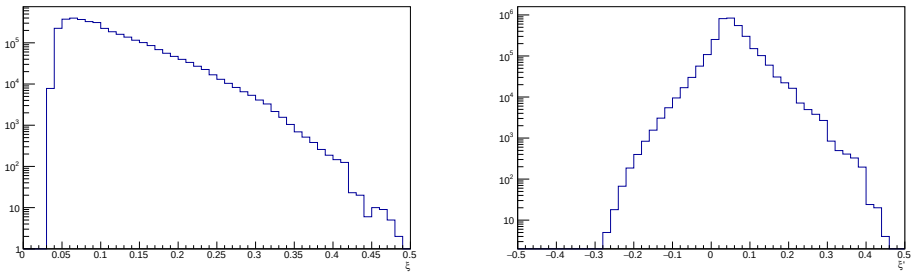

Figure 4.4: Distributions of kinematic variables for DDVCS events: ξ distribution (left panel) and ξ' distribution (right panel).

the region of small Q^2, $x_{\rm B}$, $|t|$ and Q'^2. Similar feature can be also seen from Fig. 4.3, showing the events distribution in the $(Q^2, x_{\rm B})$ and (t, Q'^2) planes.

4.2 Binning

Since the significance of DDVCS measurements is the access to GPDs as a function of its three arguments independently, the 5-dimensional grid of bins for the observables shall be made with respect to ξ, ξ', t, Q^2 and ϕ. The distributions of ξ and ξ' are shown in Fig. 4.4. The number of events deceases exponentially in ξ, while the events concentrate in the region of $|\xi'|$ close to 0 and decrease dramatically when $|\xi'|$ increases. In order to eventually be able to investigate ξ' dependence of CFFs at fixed ξ, t and Q^2 and derive relatively good statistical errors for the observables, the following 5-dimensional grid of bins has been adopted:

- 6 bins in ξ [0.03, 0.06, 0.09, 0.12, 0.15, 0.2, 0.3];
- 8 bins in ξ' [−0.19, −0.09, −0.03, 0, 0.03, 0.06, 0.09, 0.15, 0.25];
- 5 bins in $-t$ [0.1, 0.2, 0.3, 0.45, 0.65, 1 GeV^2];
- 5 bins in Q^2 [1, 1.5, 2.25, 3.25, 4.75, 6.75 GeV^2];
- 12 bins in ϕ, each 30° wide.

The grid of bins is illustrated by the black lines in Fig. 4.5. In order to investigate the dependence of the cross section on single kinematical varibles while keeping the other variables invariant, one shall estimate the observable at the bin center. Therefore, the bins whose geometric centers lie outside of the kinematically authorized phase space are abandoned.

I stress that the binning above is only used to obtain the number of events for the evaluation of statistical errors. The cross section to be investigated remains the 5-fold differential cross section with respect to $(x_{\rm B}, Q^2, t, Q'^2, \phi)$, namely $\frac{d^5\sigma}{dx_{\rm B}dQ^2dtdQ'^2d\phi}$. For example, the 5-dimensional bin i has the kinematical variables denoted $(\xi'_i, \xi_i, t_i, Q^2_i, \phi_i)$ at the bin center. The corresponding values of $x_{{\rm B}i}$ and Q'^2_i can be derived through Eqs.(1.101) and (1.102). The magnitude of $d^5\sigma_i$ is calculated at $(x_{{\rm B}i}, Q^2_i, t_i, Q'^2_i, \phi_i)$, *i.e.* the kinematics at the bin center, by using VGG code. The number of events N_i is derived from the event generator by selecting the kinematical variables within the 5-dimensional

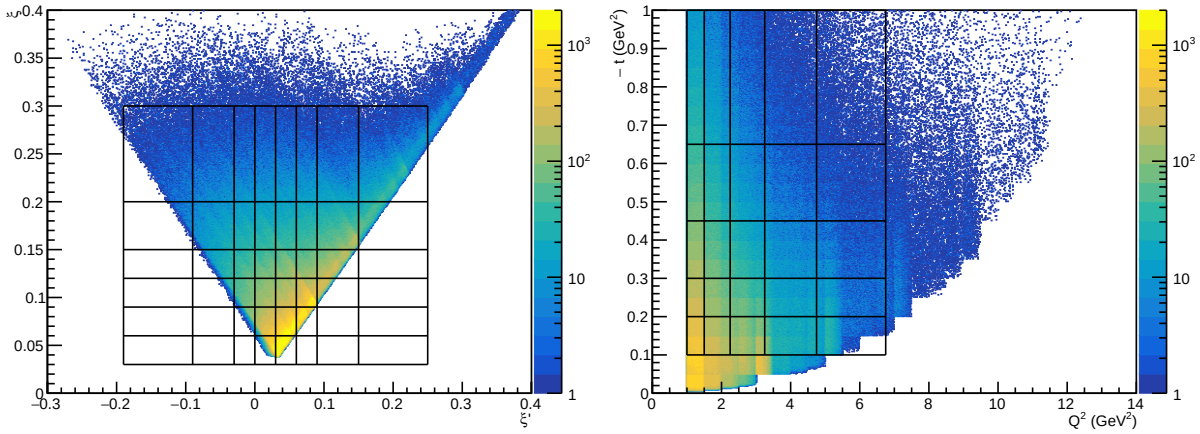

Figure 4.5: Distributions of kinematic variables for DDVCS events: the distribution in (ξ, ξ') (left panel) and distribution in (t, Q^2) (right panel).

$(\xi', \xi, t, Q^2, \phi)$ hypervolume of the bin. The observable for the bin i eventually consists of the $d^5\sigma_i$ and its statistical error, which is given by

$$\frac{\delta(d^5\sigma_i)}{d^5\sigma_i} = \frac{1}{\sqrt{N_i}}. \tag{4.3}$$

For the real data, the average value of the cross section is obtained from the number of events in the 5-dimensional $(\xi, \xi', t, Q^2, \phi)$ bin. However, the cross section might not vary linearly across the width of a bin, which would result in the cross section at the bin center not coinciding with the average value of the cross section in that bin. Therefore, bin centering corrections must be considered and determined. One can divide each bin over $(\xi, \xi', t, Q^2, \phi)$ into multiple smaller bins, calculate the BH cross section at the center of each of the smaller bins (CS_{av}), and separately calculate the BH cross section at the center of the large bin (CS_c). The bin centering correction is then defined as

$$B(\xi, \xi', t, Q^2, \phi) = \frac{CS_c}{CS_{av}}, \tag{4.4}$$

which must be included in the calculation of the cross section. The reason of using BH cross section instead of total cross section is that BH processes are accurately calculable and dominate the total cross section.

On the current stage of experimental projections, the cross section at the bin center is directly calculated by the VGG model.

4.3 Observables in an ideal situation

Assuming that the measurements are performed in the ideal situation that all the particles of the final state can be detected with 100% efficiency and the beam polarization is also 100%, the number of events for each bin can be directly derive from the event generator without any correction. When the running time is equally divided for each beam helicity and charge, the statistical errors of the observables in Eqs. (2.112) and (2.115) are then

given by

$$\delta(\sigma^{-}_{\rm UU}) = \delta(\Delta\sigma^{-}_{\rm LU}) = \frac{\sigma^{-}_{\rm UU}}{\sqrt{N}}, \tag{4.5}$$

$$\delta(\sigma_{\rm UU}) = \delta(\Delta\sigma^{\rm C}_{\rm UU}) = \delta(\Delta\sigma_{\rm LU}) = \delta(\Delta\sigma^{\rm C}_{\rm LU}) = \frac{\sigma_{\rm UU}}{\sqrt{N}}, \tag{4.6}$$

where N is the sum of the number of events for each beam helicity and charge. Whereas, the statistical errors on asymmetries (A) in Eqs. (2.118)-(2.120) depend on the values of the asymmetry, through the formula

$$\delta A = \frac{\sqrt{1-A^2}}{\sqrt{N}}. \tag{4.7}$$

The calculation of the number of events has been done for a luminosity $\mathcal{L} = 10^{37}$ cm^{-2}·s^{-1} (corresponding to roughly 1μA on a 40 cm long liquid hydrogen target) and for $T = 50$ days running time.

Fig. 4.6 shows an example of $\sigma^{-}_{\rm UU}$, the unpolarized cross section with only electron beam, as functions of ϕ with statistic errors at $\xi = 0.135$. The unpolarized cross section with very small statistical errors can be obtained. Fig. 4.7 shows an example of $A^{-}_{\rm LU}$ (BSA) as functions of ϕ with statistic errors at $\xi = 0.135$. The expected accuracy can be also obtained at a high level. The BSA is considerable in the region of $\xi' = -0.06$ and $\xi' \geqslant 0.045$ but very small when $\xi' = -0.015$ and 0.015, caused by the imaginary CFFs combination being zero at $\xi' = 0$. It can be seen that the measurements of the BSA is challenging for the bins at large $-t$. At a moderate ξ', for instance $\xi' = 0.075$, the BSA becomes large when Q^2 increases. Although the error bars become large, the expected accuracy is still significant in this case. Unlike the unpolarized cross section, the accuracy of the BSA would strongly degrades with a 10 times smaller luminosity. Fig. 4.8 shows an example of $A^{\rm C}_{\rm UU}$ (BCA) as functions of ϕ with statistic errors at $\xi = 0.135$ when one has additional 50 days running with positron beam at the same luminosity. The expected accuracy stays at the level between the unpolarized cross section and the BSA. Contrary to the BSA, the measurements of the BCA is challenging for the bins at small $-t$. When one has 10 times less the luminosity, the accuracy of the BCA remains at an acceptable level.

The expected accuracy of the observables is presented in the Appendix A for the remaining covered bins in ξ.

In summary, the evaluated observables of a DDVCS experiment indicate a high degree of feasibility at $\mathcal{L} = 10^{37}$ cm^{-2}·s^{-1} in an ideal life. The unpolarized cross section with very small statistics error can be obtained. Although the BCA or the beam charge cross section difference has less precision, a better extraction of the real part of CFFs can be performed. The BSA or the beam spin cross section difference can also be obtained accurately for most of the covered bins, and it is the most powerful tools to directly access the totally unexplored GPDs phase space, otherwise inaccessible. The realistic projections with specific experimental setups are presented in the next chapter.

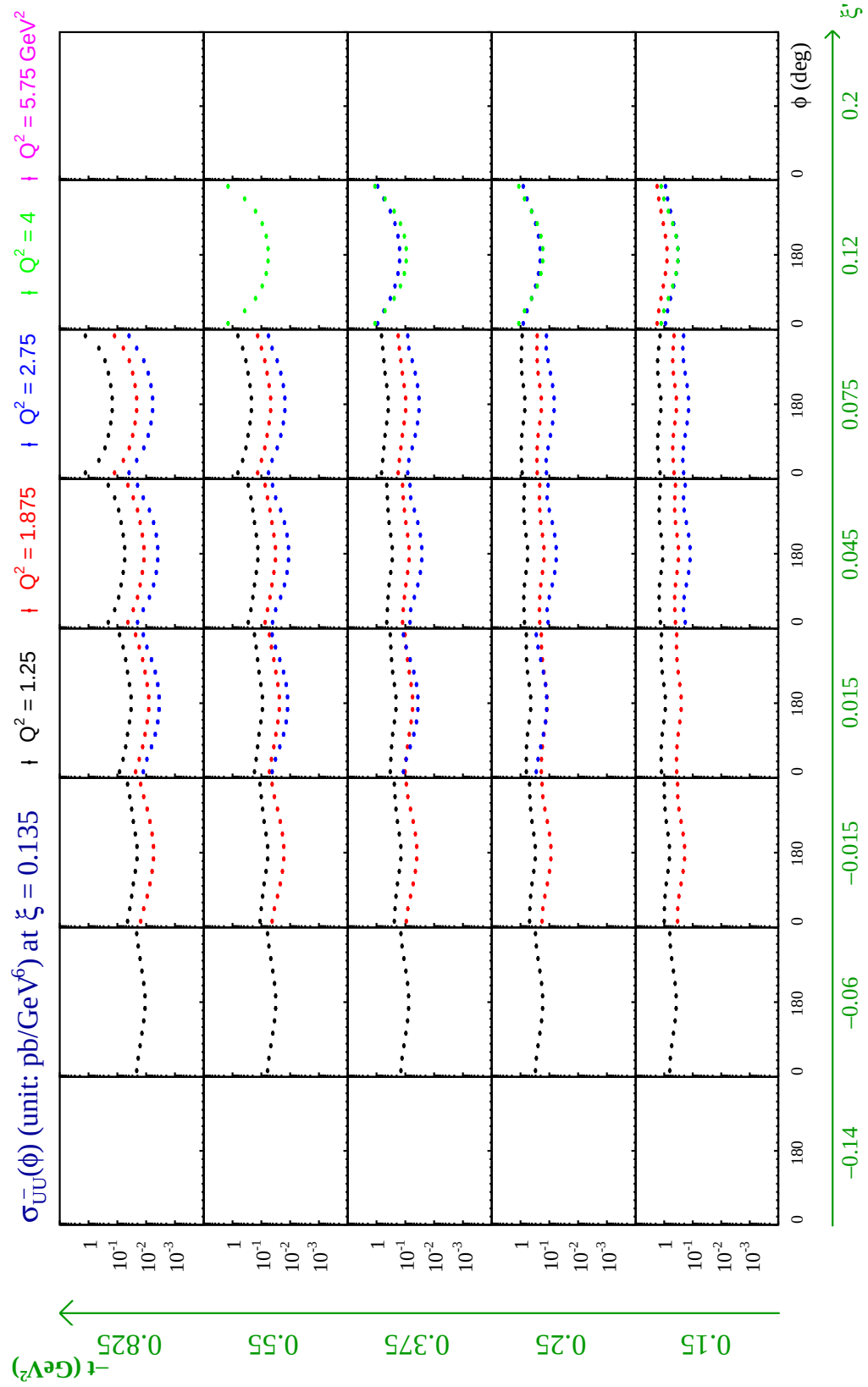

Figure 4.6: The expected accuracy on $\sigma_{UU}^{-}(\phi)$ for all the covered bins in ξ' , $-t$ and Q^2 at fixed $\xi = 0.135$. The error bars reflect the statistical uncertainties for an ideal situation and a 50 days run at $\mathcal{L} = 10^{37}$ cm^{-2}·s^{-1}. Note a logarithmic scale for the y-axis of the panels and the unit being pb/GeV^6.

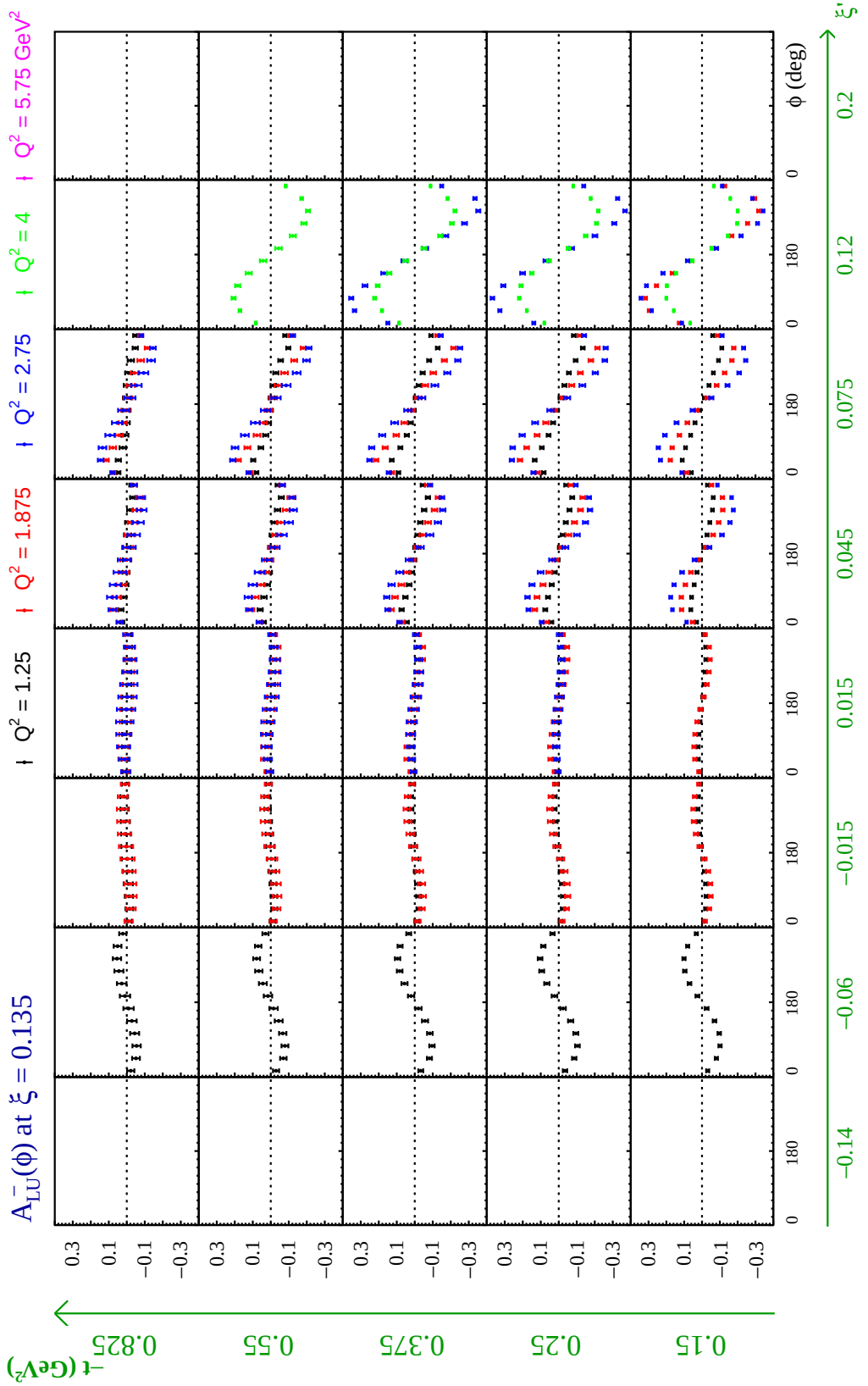

Figure 4.7: The expected accuracy on $A_{\mathrm{LU}}^{-}(\phi)$ for all the covered bins in ξ' , $-t$ and Q^2 at fixed $\xi = 0.135$ for an ideal situation and a 50 days run at $\mathcal{L} = 10^{37}$ cm^{-2}·s^{-1}.

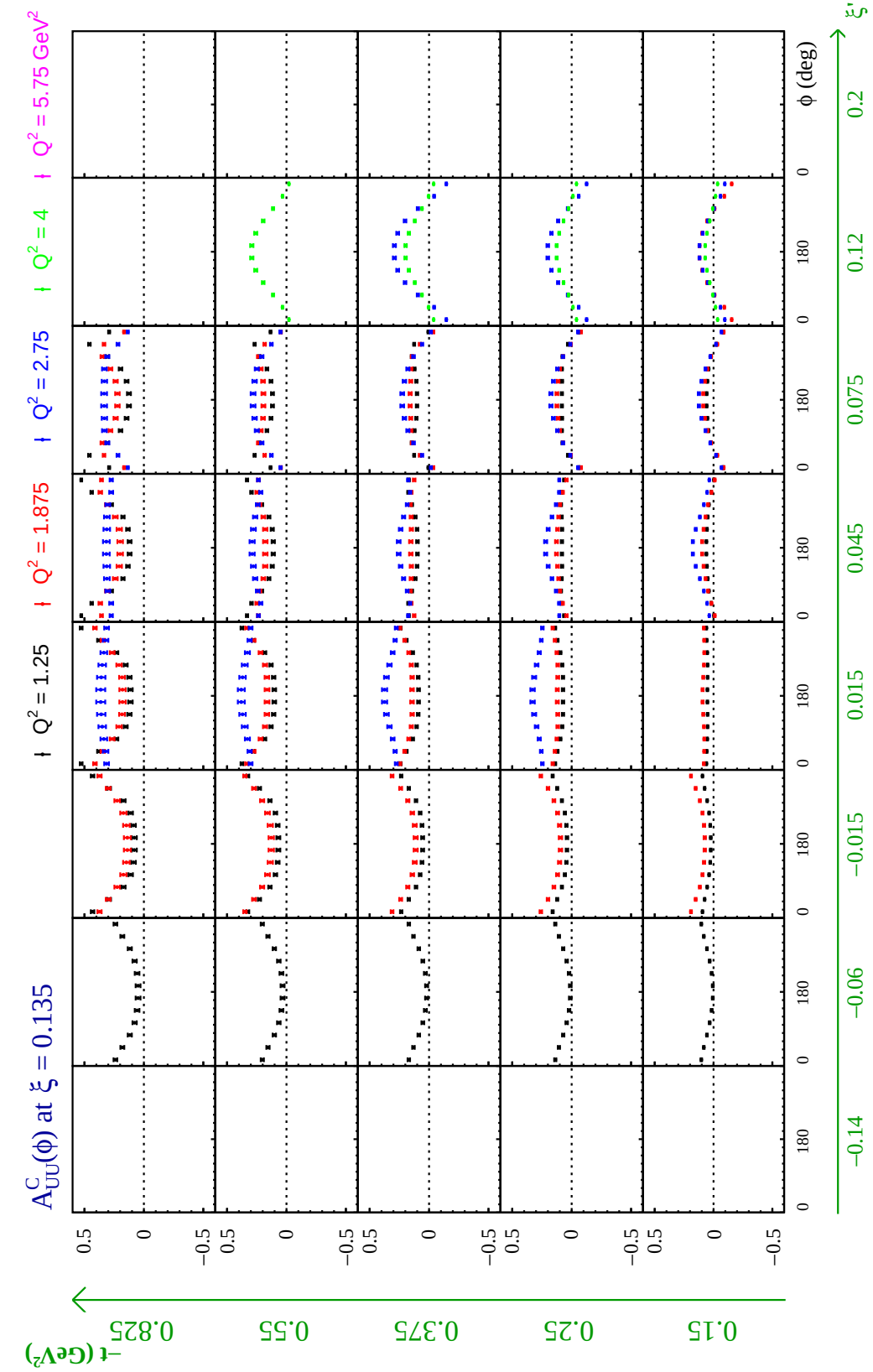

Figure 4.8: The expected accuracy on $A_{UU}^{C}(\phi)$ for all the covered bins in ξ' , $-t$ and Q^2 at fixed $\xi = 0.135$ for an ideal situation and 50 days with electron beam and 50 days with positron beam runs at $\mathcal{L} = 10^{37}$ cm^{-2}·s^{-1}.

Chapter 5

Experimental projections

With respect to the experimental setup, there are two typical scenarios for DVCS measurements at JLab. The first dedicated DVCS experiment [41] in Hall A used the high luminosity scenario, which detected the scattered electron in the High Resolution Spectrometers (HRS, $\delta p/p \approx 10^{-4}$ for momentum) on one side of the beam and the real photon in an electromagnetic calorimeter ($\delta E/E \approx 4\%$ for energy) on the other side. This scenario was kept for following DVCS experiments at 6 GeV and 12 GeV. In this case, measurements require high luminosities and are limited over a relatively narrow phase space due to the small acceptance of the detectors. Another approach is the large acceptance scenario. For instance, the CLAS collaboration used a large acceptance spectrometer with a lesser resolution ($\delta p/p \approx 10^{-2}$ for momentum) to measure the DVCS process [42, 53] by detecting the three particles of the final state over a much broader phase space than in Hall A. The CLAS12 collaboration also pursues this scenario for the current DVCS/TCS measurements in Hall B.

For the anticipated measurements of the $ep \to ep\mu^-\mu^+$ process, the detection of the scattered electron can also follow the two scenarios using the existing spectrometers. For the muon detection, however, a dedicated muon detector with large acceptance is the only realistic choice for statistically significant measurements of the 5-fold cross sections or corresponding asymmetries. Since the muon detector does not exist at the moment, the two scenarios are both discussed here in order to provide some insights about the eventual experimental setup and the development of the muon detector. Therefore, an ideal muon detector with 4π acceptance and 100% efficiency has been firstly considered in the evaluation of the experimental projection of chapter 4. The purpose was to determine the generic conditions of the feasibility of a DDVCS experiment. In this chapter, more realistic projections are performed with the parameters of some existing detectors. The experimental observables have been calculated only in terms of $d^5\sigma$, namely the 5-fold cross section integrated over the final muon solid angle. One can certainly analyze the same data by means of the integration over the nucleon azimuthal angle and the final muon polar angle, *i.e.* $d^5\Sigma$, but this aspect is not included in the following.

5.1 Kinematics for the high luminosity scenario

It is indeed predicted that the Beam Spin Asymmetry (BSA) should have an opposite sign in the $Q'^2 < Q^2$ and $Q'^2 > Q^2$ regions due to the sign change of the imaginary part of the DDVCS amplitude [56, 57, 60, 62, 63]. This special sign change behavior in BSA is a distinctive signature of the DDVCS process. Here I introduce two experimental schemes

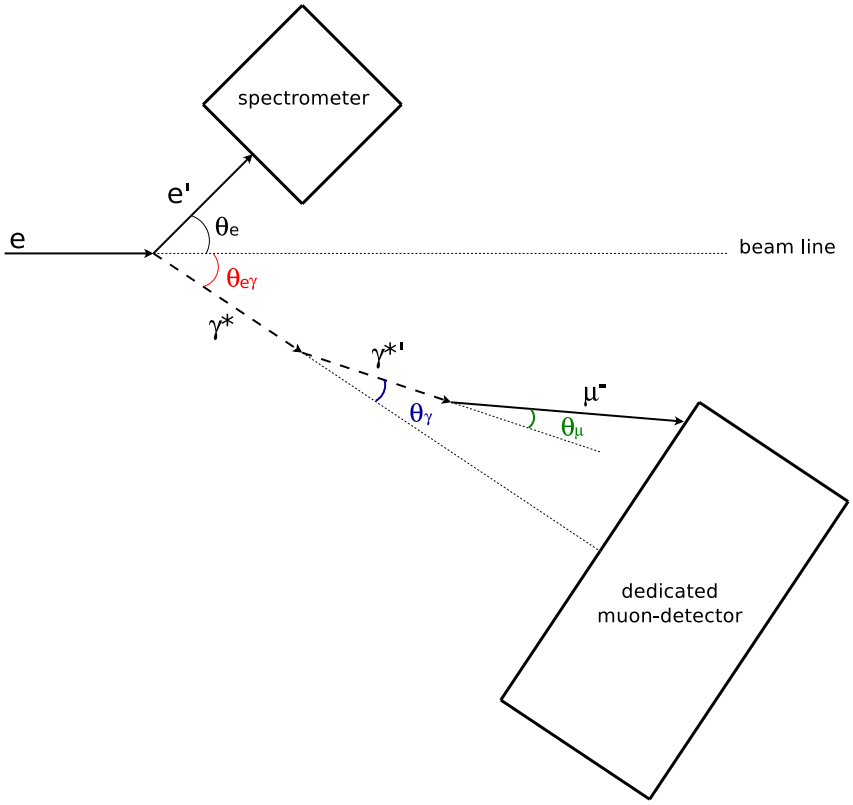

Figure 5.1: Illustration for the experimental setup of the high luminosity scenario. The polar angles are defined in the lab frame.

of the high luminosity scenario intending at an experimental determination of the change of the BSA-sign.

5.1.1 Experimental setup

Fig. 5.1 illustrates the experimental setup for the high luminosity scenario, where the spectrometer is located on one side of the beam line and the dedicated muon detector is on the other. One can use existing spectrometers, such as the Super High Momentum Spectrometers (SHMS) of Hall C, to detect the scattered electron at suitable Q^2, $x_{\rm B}$ bins. The detection of muons would be conducted by a dedicated muon detector. I only present the phase spaces with respect to the detection of scattered electrons and the virtuality of time-like photons at the initial step of DDVCS in order to obtain the suitable phase spaces, in which we can achieve the experimental plan. The explored GPDs phase space is presented as well.

5.1.2 Q' scan scenario

A first possibility to demonstrate the BSA sign-change could be to scan the Q'^2 dependence of the BSA at fixed $(Q^2, x_{\rm B})$. One fixes Q^2 and $x_{\rm B}$ experimentally by means of selection of the scattered electron energy and angle in a spectrometer though Eqs. (1.61) and (1.62). Fig. 5.2 (left panel) shows the $(Q^2, x_{\rm B})$ phase space with additional physics constraints: (a) the bottom black curve is $Q^2_{\rm min}$ when $Q' = 2m_\mu$, which ensures the production of a muon pair; (b) the blue line is $Q^2 = 1$ GeV^2, a minimal restriction to favor the reaction at the parton level; (c) the red curve is $W = 2$ GeV, the minimal center of mass energy

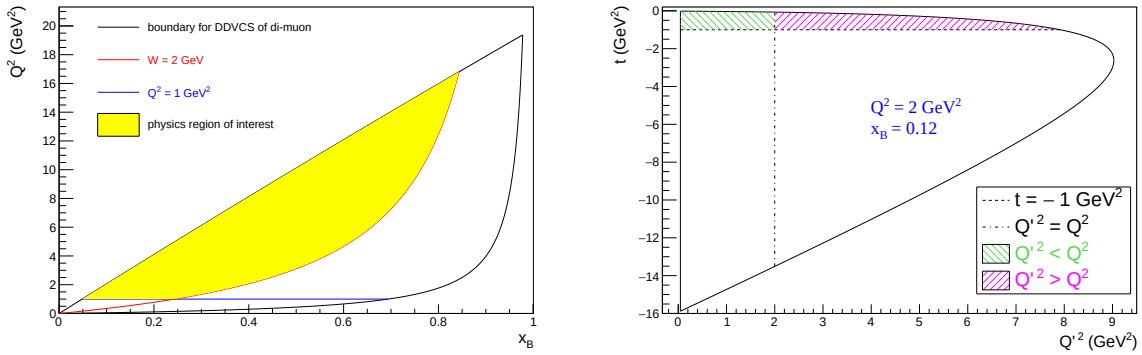

Figure 5.2: Left panel: $(Q^2, x_{\rm B})$ phase space with physics constraints. Right Panel: (t, Q'^2) phase space at $(Q^2, x_{\rm B}) = (2\ {\rm GeV}^2, 0.12)$.

to ensure the deep inelastic scattering regime. The region delimited by these constraints is the physics region of interest, the yellow area, where one can select $(Q^2, x_{\rm B})$ points. The candidates do not reach very high Q^2 that are likely unreachable at JLab energies because of the very small cross section magnitude.

As mentioned before, the difference between the two virtualities can cause the sign change of the beam spin asymmetry (BSA). Therefore, the selected $(Q^2, x_{\rm B})$ points shall cover both $Q'^2 < Q^2$ and $Q'^2 > Q^2$ region at relatively small $-t$, at least smaller than 1 GeV^2 in order to support the factorization regime. Fig. 5.2 (right panel) displays the behavior of one selected $(Q^2, x_{\rm B})$ point in the corresponding (t, Q'^2) phase space, where (a) the solid curve is the boundary of the (t, Q'^2) phase space; (b) the dashed line represents $t = -1$ GeV^2; (c) the dashed-dotted line stands for $Q'^2 = Q^2$; (d) the green shaded area represents the allowed $Q'^2 < Q^2$ region; (e) the magenta shaded area represents the allowed $Q'^2 > Q^2$ region. As Fig. 5.3 shows, when $x_{\rm B} = 0.27$ the $Q'^2 > Q^2$ region becomes tiny and disappears when $x_{\rm B} = 0.32$. It implies that there exists an upper limit in $x_{\rm B}$ for covering both regions. Fig. 5.4 (left panel) shows $t_{\rm min}$ at $Q'^2 = Q^2$ as a function of $x_{\rm B}$, in which it can be easily observed that the $Q'^2 > Q^2$ region cannot be explored above $x_{\rm B} \sim 0.31$ no matter the photon virtualities. Actually, the constraint $-t < 1$ GeV^2 is only a rough form of $-t/Q^2 \ll 1$, which means $-t$ shall be much smaller than Q^2 and as small as possible at small Q^2. In order to get enough coverage for the $Q'^2 > Q^2$ region, $x_{\rm B} = 0.25$ seems to be the maximum measurable value, named "constraint of interest".

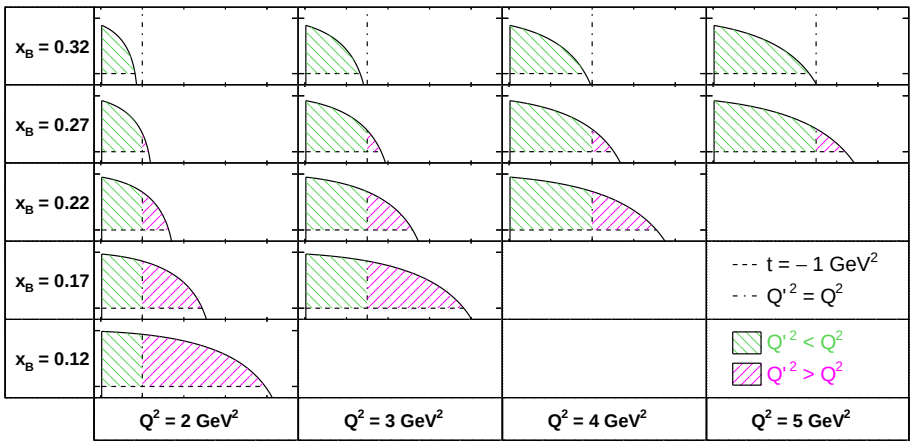

Figure 5.3: (t, Q'^2) phase spaces of the $(Q^2, x_{\rm B})$ points up to disagreeing with the request.

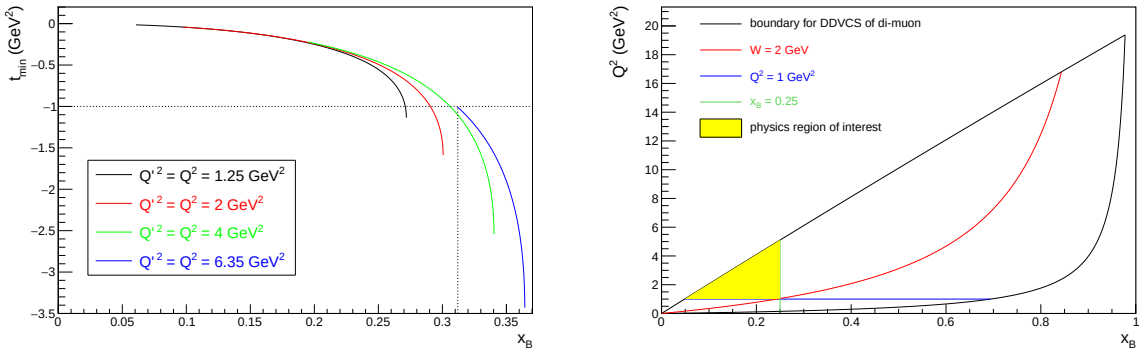

Figure 5.4: Left panel: $t_{\rm min}$ at $Q'^2 = Q^2$ as a function of $x_{\rm B}$. Right panel: $(Q^2, x_{\rm B})$ phase space with the constraint of interest.

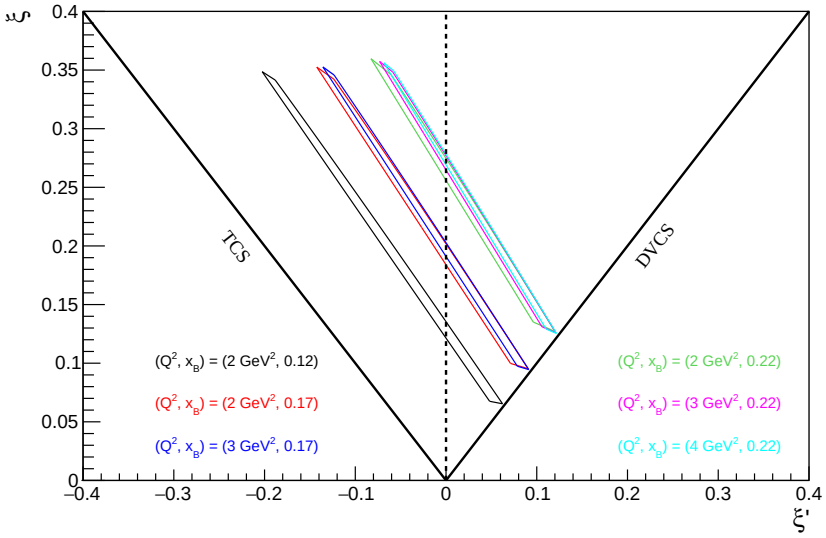

Figure 5.5: (ξ, ξ') phase space of some $(Q^2, x_{\rm B})$ points at $|t_{\rm min}| < |t| < -1$ GeV^2.

Fig. 5.4 (right panel) shows the $(Q^2, x_{\rm B})$ phase space where the constraint of interest is inserted.

From Eqs. (1.101) and (1.102) one can get the (ξ, ξ') phase space of proper $(Q^2, x_{\rm B})$ points at $|t|$ varying from $|t_{\rm min}|$ to 1 GeV^2, as shown in Fig. 5.5. The shown $(Q^2, x_{\rm B})$ points cover both positive and negative ξ' region when scanning all possible Q'^2. As discussed above, the BSA is predicted to change sign when $\xi' = 0$ represented by the black dashed line. The BSA measurements at a few fixed kinematics not only can test the universality of the GPD formalism, but also can provide the opportunity to measure the unknown GPDs values within $|\xi'| < \xi$ region, which offer additional GPD constraints on the model-dependent deconvolution of experimental observables. Since the (ξ, ξ') phase space has strong sensitivity to $x_{\rm B}$ and tiny to Q^2, and high Q^2 causes small cross section magnitude, low Q^2 is expected to be the most suitable initial virtuality. Moreover, at low Q^2 the phase space has a larger coverage in $x_{\rm B}$.

In an anticipated DDVCS experiment, the detection of the muon pairs in the final state is mandatory. Each of the available spectrometers at JLab can be a choice for the DDVCS experiment.

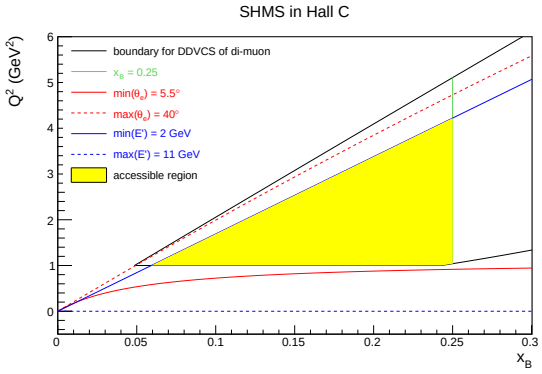

Figure 5.6: (Q^2, x_{B}) phase space with SHMS constraints.

The Super High Momentum Spectrometers (SHMS) of the 12 GeV upgrade in Hall C enables measurements of charged particles with momenta approaching that of the beam highest energy. Together with its companion, the HMS, this makes Hall C capable of studying deep exclusive reactions at the highest momentum transfers with appropriate high luminosity [65]. It has central momentum: 2 - 11 GeV and scattering angle: 5.5° - 40°. As shown in Fig. 5.6, it is suitable to use the SHMS, which hardly limits the region of interest, for the high luminosity scenario. In conclusion, the SHMS designed for 12 GeV upgrade have abilities to play the role for a DDVCS experiment to achieve our physics aims in terms of the electron view.

5.1.3 Fixed Q' scenario

Additional contributions from vector meson decay would most likely degrade the small physics signal in a DDVCS experiment. Although the contribution of the ρ-meson resonance to the BSA turns out to be small in a perturbative QCD estimate [55], the selection of the final virtual photon mass Q' simply above 1.8 GeV would minimize eventual contamination from vector mesons decay. As a second scenario towards the demonstration of the BSA sign-change, measurements can also be foreseen at fixed Q' and different (Q^2, x_{B}). This approach can also obtain BSA in both $Q'^2 < Q^2$ and $Q'^2 > Q^2$ regions. Adding this $Q' = 1.8$ GeV constraint in the (Q^2, x_{B}) phase space, the suitable kinematics can be obtained in order to guide the measurement of scattered electrons using a spectrometer, as shown in Fig. 5.7 (left panel). It can be seen that the (Q^2, x_{B}) phase space is further limited by the green curve representing the minimal Q^2 at $Q' = 1.8$ GeV. The suitable x_{B} can be directly obtained covering both $Q^2 < Q'^2$ (cyan area) and $Q^2 > Q'^2$ (yellow area) regions separated by the dashed line representing $Q^2 = Q'^2 = 3.24$ GeV^2. The (Q^2, x_{B}) phase space of interest further constrained with the SHMS acceptance is shown in the right panel.

Fig. 5.8 shows the (t, Q^2) phase space for some x_{B} values considering $-t < 1$ GeV^2 constraint. Due to the minimal momentum of SHMS (blue line) cutting the $Q^2 > Q'^2$ region (green shaded area), the small x_{B} is rejected; the large x_{B} rejects the $Q^2 < Q'^2$ region (magenta shaded area), being the same as in the scheme of Q' scan. As mentioned before, the constraint $-t < 1$ GeV^2 is only a rough form of $Q^2/(-t) \gg 1$. Therefore, measurements at a small $-t$, especially when one goes low in Q^2, is necessary for supporting the factorization regime, for instance $-t < 0.5$ GeV^2 (red line). In order to obtain suitable coverage of Q^2 in both regions, $x_{\mathrm{B}} = 0.22$ seems to be the optimal value meeting physics requirements. In comparison to the scanned Q', the fixed Q' scheme not only has

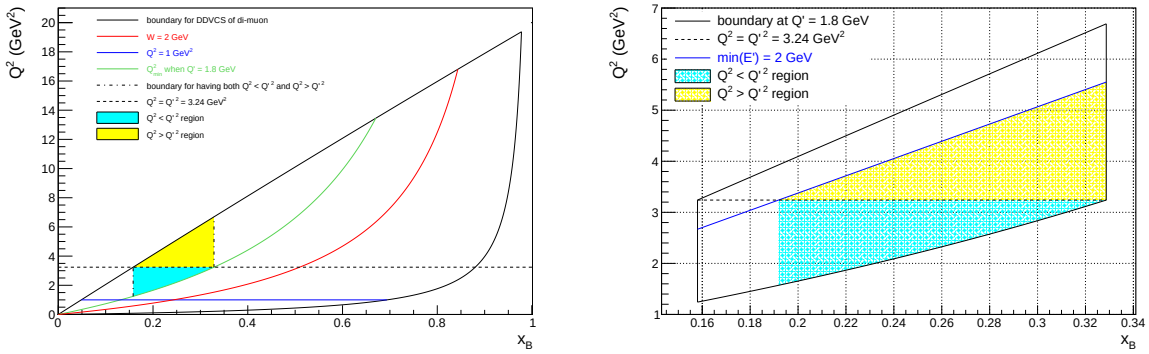

Figure 5.7: (Q^2, x_{B}) phase space at $Q' = 1.8$ GeV with the physics constraints (left) and experimental ones (right).

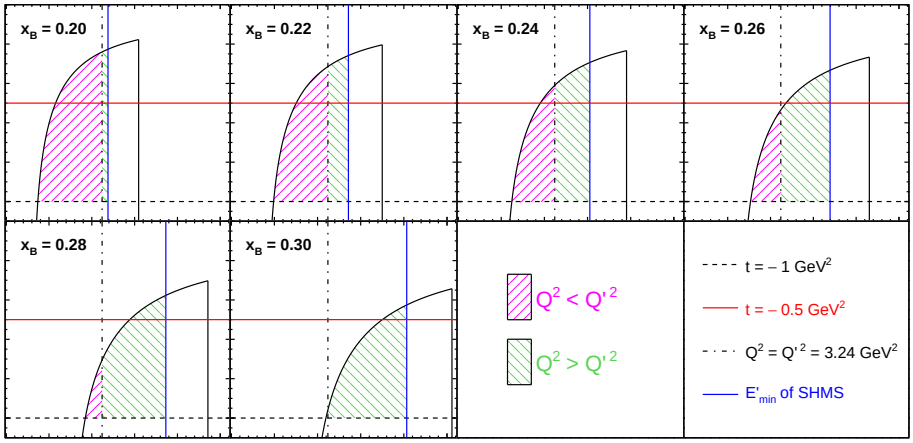

Figure 5.8: (t, Q^2) phase spaces at some x_{B} and fixed $Q' = 1.8$ GeV^2 up to disagreeing with the request.

very limited phase space but also calls for higher luminosity.

5.1.4 Feasibility analysis

On one hand, the muon detector shall be centered in the direction of the momentum of the time-like virtual photon without crossing the beam pipe, as shown in Fig. 5.1. Therefore, the polar angle in the lab frame between the space-like photon and the incident electron must be larger than the one between the muons and the space-like photon, namely $\theta_{e\gamma} > \theta_\gamma + \theta_\mu$. Fig. 5.9 shows the results of the simulation of the polar angle acceptance for typical kinematics for the scheme of Q' scan. Under the cut of $-t < 0.5$ GeV^2, θ_γ is constrained below a maximum of 5.7°, as shown in the top left panel of Fig. 5.9. Since the fixed Q^2 and x_{B} lead to a fixed $\theta_{e\gamma} = 8.3°$, the requirement of not crossing the beam pipe is reached. However, θ_μ covers the full range even after the cut, as shown in the top right panel of Fig. 5.9. Thus, the muons are only detected when $\theta_\mu < 2.6°$ for the full azimuthal coverage, resulting in extremely poor statistics. Moreover, the muons of the pair need to be detected to reconstruct the kinematics. The bottom panel of Fig. 5.9 displays the opening angle of two muons in pairs, which varies up to 180° and centres at 35°. Therefore, the measurements with SHMS makes the muon detection very difficult.

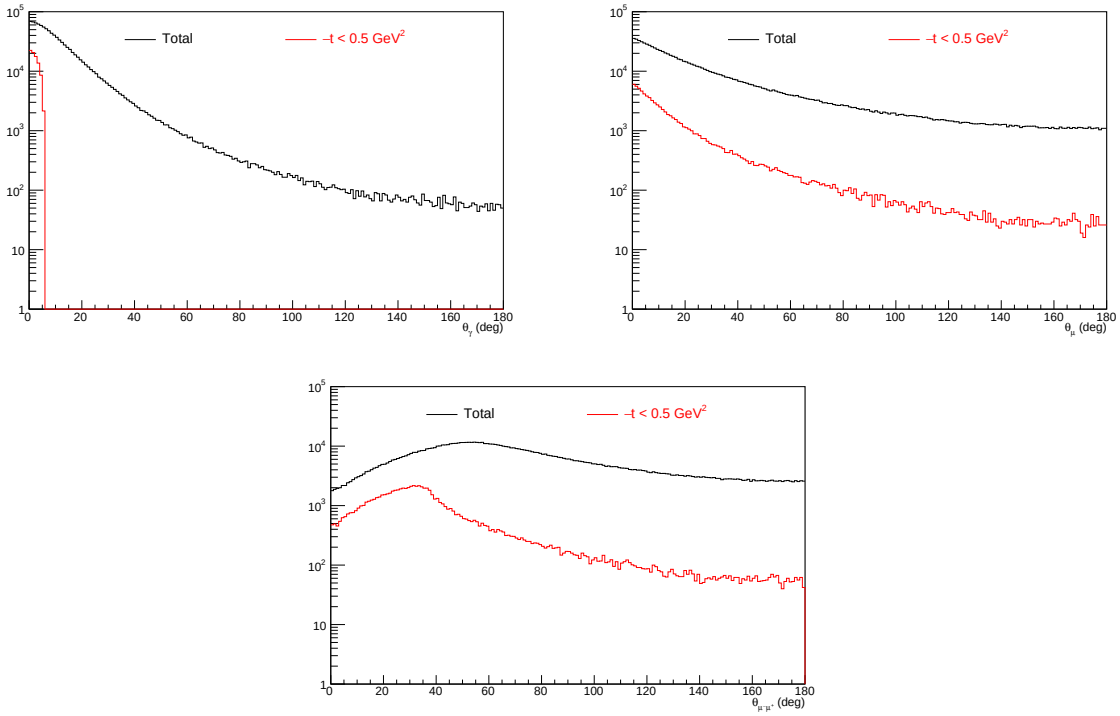

Figure 5.9: Top left panel: θ_γ acceptance. Top right panel: θ_μ acceptance. Bottom panel: the openning angle of two muons in pairs. The black histograms stand for the acceptance without any cuts and the red histograms for the acceptance under the cut of $-t < 0.5$ GeV^2. The kinematical variables used here are $Q^2 = 2$ GeV^2, $x_\mathrm{B} = 0.17$ and any possible Q'^2.

On the other hand, SHMS has only ± 40 mrad vertical acceptance unlike large acceptance spectrometers, such as SoLID in Hall A and CLAS12 in Hall B, owning 2π azimuthal coverage. So the azimuthal acceptance of SHMS for ϕ_e is 80 mrad. The number of events measured by SHMS is then $2\pi/0.08 \approx 80$ times less than by SoLID or CLAS12 when other conditions are the same. Thus, the measurements with SHMS need 80 times higher luminosity in order to obtain the same quality of statistics for the observables. As discussed before, 10^{37} cm^{-2}·s^{-1} is demonstrated to be a reasonable value for the BSA measurements in the ideal situation. Simply speaking, the measurements with SHMS need at least 10^{39} cm^{-2}·s^{-1} in practice but only investigate a small phase space for a 50 days run.

5.2 The large acceptance scenario

The CEBAF Large Acceptance Spectrometer of the 12 GeV upgrade (CLAS12) in Hall B has a full 2π azimuthal coverage and a very large acceptance in polar angle, 5° to 35° for the forward detector (FD), 35° to 125° for the central detector, even larger with the backward detector. However, a DDVCS experiment demands extremely high luminosity which brings much more incident particles with respect to detectors than their limits. The CLAS12 detectors must be modified to allow for high luminosity. In [62], it was proposed to detect the muon pairs from time-like photon in the CLAS12 FD and scattered electrons in a new PbWO4 calorimeter mounted in place of the CLAS12 high threshold Cherenkov counter. The Solenoidal Large Intensity Device (SoLID) in Hall A is dedicated to run at high luminosity also has a full 2π azimuthal coverage. For the J/Ψ configuration of the

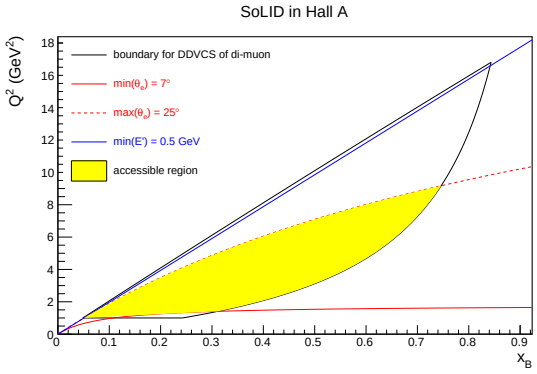

Figure 5.10: (Q^2, x_{B}) phase space with SoLID constraints.

SoLID spectrometer, the polar angle acceptance is 7° to 25°, as shown in Fig. 5.10. The phase-space loss concerns the high Q^2-region where the number of events is small (see Fig. 4.2 and 4.3). A realistic study of DDVCS with the SoLID spectrometer is presented in the following, .

5.2.1 SoLID spectrometer

The SoLID spectrometer is based on the CLEO II solenoidal magnet [66]. Solenoidal geometry is the most suitable arrangement for high luminosity capabilities because of the trapping effect of the magnetic field on low energy background particles acting therefore as detector shielding. The detection capabilities developped for the experiments are essential for GPDs study, and particularly for a DDVCS experimental program. DDVCS involves the detection of muon pairs produced around the virtual photon defined by the scattered electron. In such a case, a full and symmetrical azimuthal angle coverage is a minimal requirement to allow for the determination of angular harmonics from the observables. The additionnal DDVCS constraint is the high luminosity needed to compensate small cross section. SoLID is especially designed to achieve these goals and would be ideally suited for a DDVCS program [63]. The SoLID detection system is built around the solenoidal field of the CLEO II magnet having an uniform axial central field of 1.5 T and a ±0.2% field uniformity. The main technology developped for the high luminosity purpose of the SoLID detector are Gas Electron Multiplier (GEM) systems arranged in three layers [67]. They allow tracking at high rates and are providing the momentum measurement capabilities of the spectrometer.

As shown in Fig. 5.11, the target is located outside of the detector for the J/Ψ setup. The experiment is designed to detect electron-positron pairs from the J/Ψ decay and is planned for running at 3 μA on a 15 cm long liquid hydrogen target, corresponding to the instantaneous luminosity 1.2×10^{37} cm^{-2}·s^{-1}. The Forward Angle Electromagnetic Calorimeter (FAEC) covers polar angles from 7° to 15° and part of the FAEC at large angle will be reconfigured in a Large Angle Electromagnetic Calorimeter (LAEC) located inside the detector to cover angles from 15° to 25°. The main trigger of that experiment is the 3-fold coincidence between the scattered electron and the two leptons from the J/Ψ decay. This triple coincidence yields a moderate trigger rate (a few kHz) allowing to run parasitically other trigger type. Additionally, the expected detector resolutions, 2% in momentum, 0.6 mrad in polar angle and 5 mrad in azimuthal angle, would be also suitable for a DDVCS experiment.

With respected to the muon detection, it is proposed in [63] to complement the SoLID

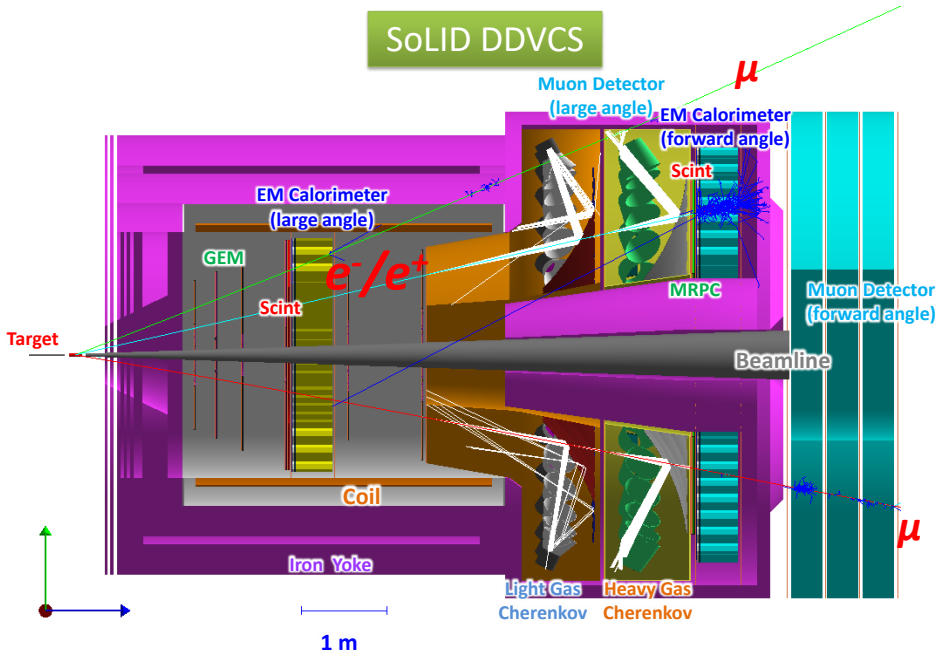

Figure 5.11: J/Ψ-μ configuration of the SoLID spectrometer for a parasitic DDVCS experiment.

detector package with muon detection capabilities over a large angular phase space, as shown in Fig. 5.11. Such addition would not only establish the capability to achieve a di-muon DDVCS experimental program. The parasitic data taking of the DDVCS experiment would be parallel to the J/Ψ experiment run and would involve supplementing the J/Ψ setup with the muon detection system (J/Ψ-μ setup).

5.2.2 Acceptance of SoLID

According to the SoLID Geant4 detector simulation with energy loss in materials [68], the J/Ψ-μ configuration of SoLID has the prelimilary acceptance parameters:

- The electron acceptance covers 7°-15° with the momentum threshold of $E' > 0.5$ GeV for the FAEC and 15°-25° with $E' > 0.2$ GeV for the LAEC.
- The muon acceptance covers 7°-15° with the momentum threshold $P_\mu > 1.5$ GeV for the forward angle muon chambers and 15°-25° with $P_\mu > 1$ GeV for the large angle muon chambers.

Due to the limited acceptance of the muon polar angle in the lab frame, the muon polar angle θ_l in the l^-l^+ CM frame does not cover the full range. With respect to the evaluation of the cross section at the bin center, the integration of $d^7\sigma$ over the solid angle needs to be adjusted to the proper interval of θ_l. In order to obtain the boundary of θ_l for the integration, an acceptance simulation has been developed specifically. The simulation is performed with uniform distributions for 7 kinematical variables, Q^2, $x_{\rm B}$, Q'^2, θ^*_γ, ϕ, θ_l and φ_l (see the definitions in Sec. 2.1.1), to determine kinematics of the final-state muon pairs in the lab frame with the z axis being aligned to the beam direction (beam frame). The muon polar angles are denoted $\theta_{\mu 1}$ and $\theta_{\mu 2}$ in the beam frame and the corresponding

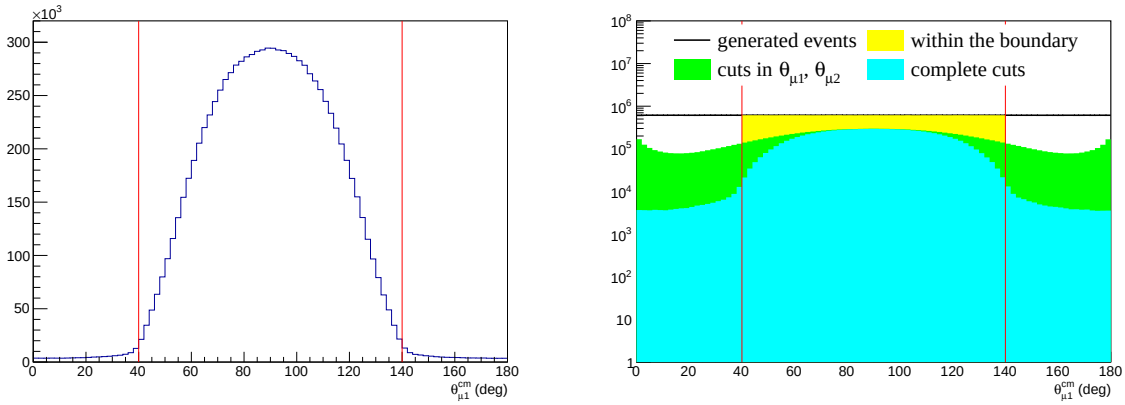

Figure 5.12: Global spectrum of $\theta^{\rm cm}_{\mu 1}$ with SoLID acceptance.

polar angles in $l^- l^+$ CM frame are denoted $\theta^{\rm cm}_{\mu 1}$ and $\theta^{\rm cm}_{\mu 2}$ in the following. When the SoLID fiducial cuts for the scattered electron and the pair of muons in pairs together with the physics cuts ($Q^2 > 1$ GeV^2 and $-t < 1$ GeV^2) are included, the boundary of θ_l can be derived. For example, the global spectrum of $\theta^{\rm cm}_{\mu 1}$ is shown in the left panel of Fig. 5.12. It can be seen that the distribution is symmetric and centered at 90°. The threshold for the determination of the boundary is defined as 10% of the maximum, which gives the 40°-140° interval in the global case as shown by the red lines.

With a limited acceptance for the muon detection, the detected exclusive events do not directly reflect the 5-fold cross section integrated over the corresponding range in $\theta^{\rm cm}_{\mu 1}$. Therefore, the number of the events cannot be directly calculated by Eq. 4.1 and need to include a muon acceptance efficiency E_μ. The right panel of Fig. 5.12 shows the global distribution of $\theta^{\rm cm}_{\mu 1}$ for generated events (black curve), the SoLID cuts only for $\theta_{\mu 1}$ and $\theta_{\mu 2}$ (green histogram) and the complete SoLID cuts (cyan histogram). Thus, the muon acceptance efficiency E_μ is defined as

$$E_\mu = \frac{N_d}{N_g}, \tag{5.1}$$

where N_d stands for the number of DDVCS events accepted by SoLID and N_g for the one generated within the boundary (yellow histogram). The global muon acceptance efficiency is $E_\mu = 32\%$ for the J/Ψ-μ configuration of SoLID.

To obtain the pseudo-data, the same grid of bins is adopted as in the ideal situation in Sec. 4.2 . The boundary of $\theta^{\rm cm}_{\mu 1}$ and the muon acceptance efficiency E_μ for each bin

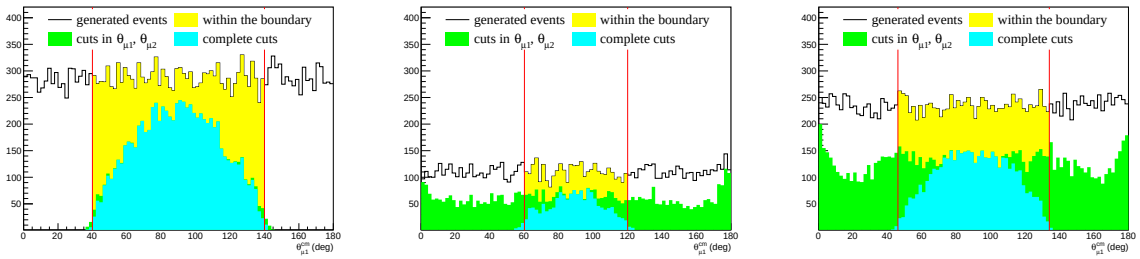

Figure 5.13: The spectra of $\theta^{\rm cm}_{\mu 1}$ for three specific bins centred at $\xi = 0.135$, $-t = 0.25$ GeV^2, $\xi' = -0.06$ (left) and 0.075 (middle and right), and $Q^2 = 1.25$ (left and middel) and 1.875 GeV^2 (right).

can be different and are determined specifically. For example, Fig. 5.13 shows the spectra of $\theta_{\mu 1}^{\rm cm}$ for three specific bins. The $\theta_{\mu 1}^{\rm cm}$ intervals are respectively 40°-140°, 60°-120° and 45°-135° represented by the red lines. The muon acceptance efficiencies E_μ are 56%, 46% and 44% respectively. Moreover, the region of interest in the $(Q^2, x_{\rm B})$ plane is not fully covered by SoLID due to the limited electron acceptance. Some bins might be partially occupied, as shown in the right panel of Fig. 5.10. Thus, the electron acceptance efficiency E_e also need to be included for the calculation of the number of events, which follows the same approach as for the the bin weight in 4.1. For the three bins above, the electron acceptance efficiencies E_e are respectively 87%, 53% and 100%.

5.2.3 Observables with SoLID

Assuming the acceptance efficiency is independent on the beam polarization and charge, the BSA and BCA at the bin center are calculated directly in term of the 5-fold cross section integrated over the limited range of $\theta_{\mu 1}^{\rm cm}$, due to the cancellation of the efficiency in the numerator and denominator.

With respect to the number of events for each bin, one shall in principle use a dedicated event generator using 7-fold fine bins and 7-fold differential cross section. This computer demanding method is approached here. I use here the quasi event generator developed in Sec. 4.1 by introducing some corrections based on the SoLID configuration. The number of events N for each bin is given by

$$N = N_{\rm id} \cdot F(\theta_0) \cdot E_e \cdot E_\mu \cdot E_d, \tag{5.2}$$

where $N_{\rm id}$ is the number of events given by the event generator for the ideal case, E_e and E_μ are respectively the electron and muon acceptance efficiencies and E_d is the global detection efficiency for the three final-state particle. Since $N_{\rm id}$ indicates the full coverage of the muon angle, a function $F(\theta_0)$ need to be included for the proper integration interval of $\theta_{\mu 1}^{\rm cm}$. I recall that the integration over the symmetric interval of $\theta_{\mu 1}^{\rm cm}$ decreases by a factor determined by the boundary, see Eq. (2.80), in comparison with the integration over the full range. For an interval $[\pi/2 - \theta_0, \pi/2 + \theta_0]$,

$$F(\theta_0) = \frac{\sin\theta_0 \left(3 + \sin^2\theta_0\right)}{4}. \tag{5.3}$$

Note that Eq. (2.80) is only applicable to the BH1, DDVCS, INT1 contributions in the cross section integrated over the lepton solid angle but not to BH2 contributions. The approximation of the total cross section following Eq. (2.80) is made here. For the global case, the interval of 40°-140° gives $F(\theta_0 = 50°) = 0.69$.

Considering 85% polarized electron beam for $\mathcal{L} = 1.2 \times 10^{37}$ cm^{-2}·s^{-1}, 50 days running and a global detection efficiency of $E_d = 50\%$, Fig. 5.14 displays distributions of kinematical variables for DDVCS events with the J/Ψ-μ configuration of SoLID. The left panel of Fig. 5.15 shows the results of the evaluation of $A_{\rm LU}^{-}(\phi)$ (BSA) as functions of ϕ with statistic errors for the three bins above. Considering additional 50 days running with unpolarized positron beam for $\mathcal{L} = 1.1 \times 10^{37}$ (corresponding to 1 μA on a 40 cm long liquid hydrogen target), the BCA can also be obtained with a good precision, as shown in the right panel of Fig. 5.15. For all the covered bins for the J/Ψ-μ configuration of SoLID, the expected accuracy of the observables is presented in the Appendix B.

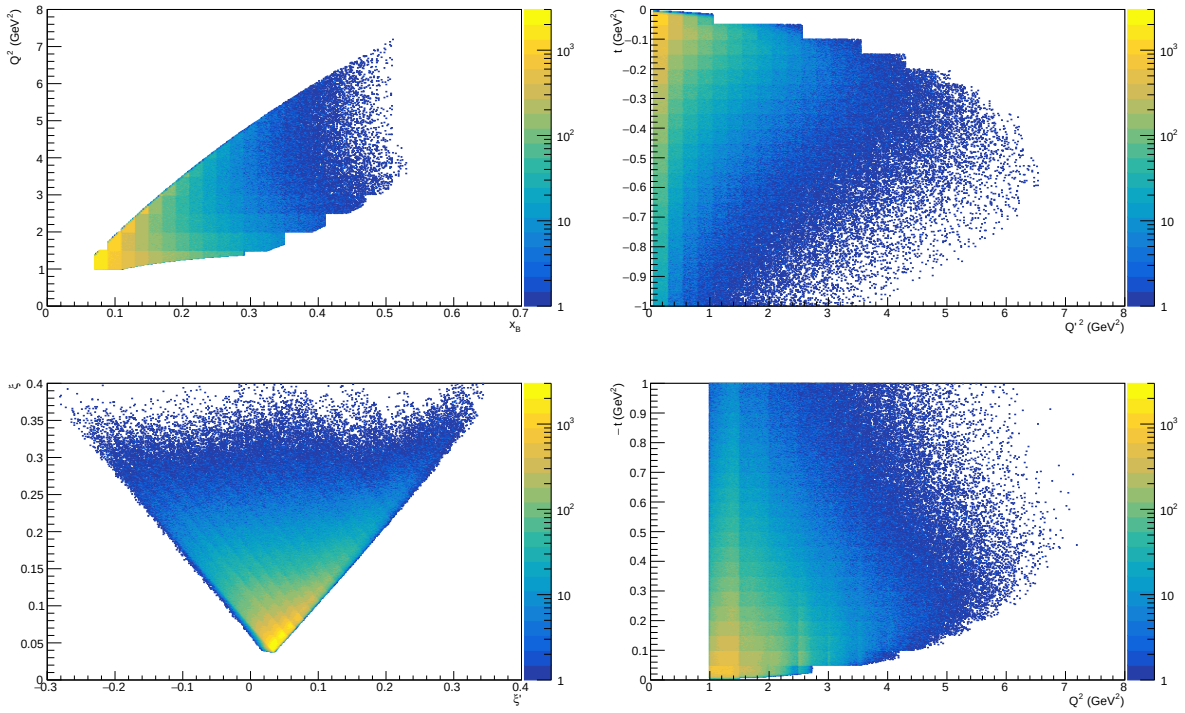

Figure 5.14: The distributions of kinematical variables for DDVCS events with the J/Ψ-μ configuration of SoLID: the distribution in $(Q^2, x_{\rm B})$ (top left panel), distribution in (t, Q'^2) (top right panel), distribution in (ξ, ξ') (bottom left panel), and distribution in $(-t, Q^2)$ (bottom right panel).

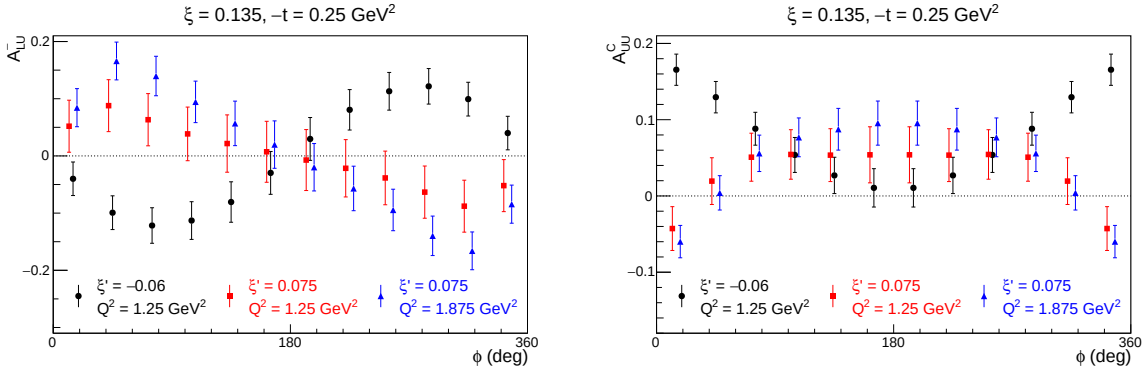

Figure 5.15: The expected accuracy on $A^{-}_{\rm LU}(\phi)$ (left panel) and $A^{\rm C}_{\rm UU}(\phi)$ (right panel) for three specific bins.

In summary, the expected asymmetries and statistics for the J/Ψ-μ configuration of SoLID demonstrate the actual feasibility of the experiment. In order to minimize contamination from meson decay, a minimum value of the final virtual photon mass is required ($Q'^2 > 3$ GeV^2) inspired from photoproduction experiments. However, the final experimental value of this cut may be lower depending on the true cross section for the electroproduction of meson at DDVCS kinematics. There exists some indications [55] supporting reduced cross sections that would allow to relax this cut and access high counting rate regions. The parasitic project here would answer such questions while simultaneously providing a set of experimental data for di-muon electroproduction at different physics regimes. However, in the high ξ region where DDVCS asymmetries are predicted to be small (Appendix B), statistics will most likely be not large enough for a significant impact. Thus, higher luminosities are needed to investigate this domain, which could be achieved by a dedicated DDVCS detector or a modified CLAS12.

Chapter 6

Extraction of the CFFs

The attempts to determine CFFs from experimental data mostly fall into two categories: global fits and local fits. With respect to the global fits, the free coefficients of a CFF parameterization are matched to experimental data. Kinematical bins are not treated independently. Interpolating between measurements of the same observable on neighboring kinematic bins is feasible. Extrapolating out of the probed kinematical domain constrained by measurements becomes possible too. However the estimation of the systematic uncertainty associated to the choice of a parameterization is an extremely difficult task. On the other hand, the local fits determine CFFs independently between different kinematical bins. This amounts to a sampling of CFFs over the probed kinematical domain. The model-dependence of the result is low, but the problem is often ill-posed by lack of uniqueness.

In the following, two approaches are applied to extract CFFs information from the DDVCS pseudo-data. Firstly, two specific linear CFFs combinations mentioned in Sec. 2.4 are directly obtained from cross section differences. With limited number of observables over the current kinematical domain, the CFFs combinations are the maximum information one can obtain uniquely and model-independently. Such CFFs information certainly offers constraints on CFFs and can contribute to the global fits program, such as the recent DVCS global fits studies [69, 70] within the PARTONS framework [71]. Then, a local fitting inspired from the one of the DVCS process [72, 73, 74, 75, 76, 77, 78] is discussed and applied to extract the CFFs from the DDVCS pseudo-data at given (ξ', ξ, t, Q^2) points.

6.1 Extraction of the CFFs combinations

As discussed in Sec. 2.4, the beam spin cross section difference $\Delta\sigma^{-}_{\mathrm{LU}}$ and the beam charge cross section difference $\Delta\sigma^{\mathrm{C}}_{\mathrm{UU}}$ are of great interest, since $\Delta\sigma^{-}_{\mathrm{LU}}$ is directly proportional to the imaginary part of the linear CFFs combination $\mathcal{C}^{\mathrm{INT}}_{\mathrm{LU}}$ given by Eq. (2.72) and $\Delta\sigma^{\mathrm{C}}_{\mathrm{UU}}$ is, in the absence of longitudinal CFF $\mathcal{F}_L$, proportional to the real part of the linear CFFs combination $\mathcal{C}^{\mathrm{INT}}_{\mathrm{UU}}$ given by Eq. (2.69). The process and results of extracting the linear CFFs combinations from the pseudo-data in the ideal situation are presents here.

6.1.1 The extraction method

The pseudo-data consist of 12 data points in ϕ for each (ξ', ξ, t, Q^2) bin. For the bin i centered at ϕ_i, being $\Delta\phi_i$ wide, I denote the value of the cross section difference by $\Delta\sigma^{-}_{\mathrm{LU}}(\phi_i)$ and $\Delta\sigma^{\mathrm{C}}_{\mathrm{UU}}(\phi_i)$ and its errors by $\delta\Delta\sigma^{-}_{\mathrm{LU}}(\phi_i)$ and $\delta\Delta\sigma^{\mathrm{C}}_{\mathrm{UU}}(\phi_i)$. Thus, the combinations are

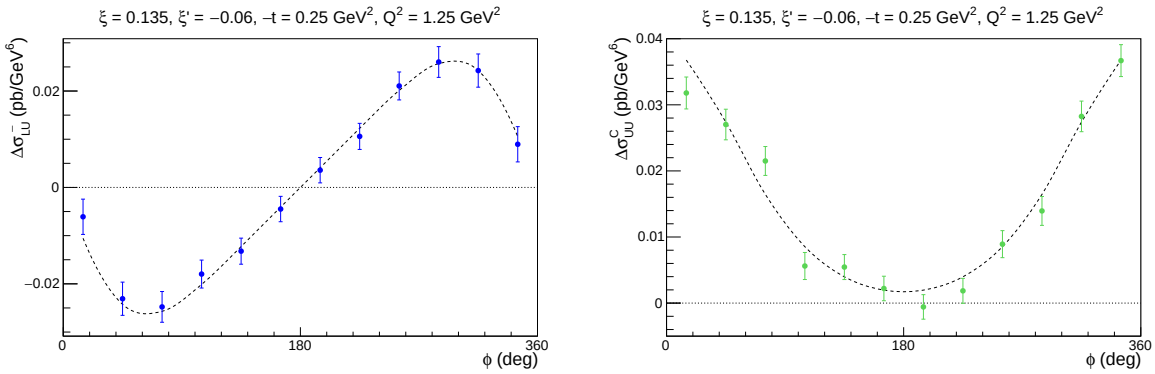

Figure 6.1: The smeared pseudo-data of $\Delta\sigma^{-}_{\rm LU}$ (left panle) and $\Delta\sigma^{\rm C}_{\rm UU}$(right panel) at $\xi = 0.135$, $\xi' = -0.06$, $-t = 0.25$ GeV^2 and $Q^2 = 1.25$ GeV^2 at $\mathcal{L} = 10^{37}$ cm$^{-2}\cdot$s^{-1}.

obtained through modified moments following

$$\mathrm{Im}\left\{\mathcal{C}^{\rm INT}_{\rm LU}\right\} = \frac{1}{\pi}\sum_{i=1}^{12}\left[\frac{\mathcal{P}_1\mathcal{P}_2(\phi_i)K_s}{A^{\rm PS}A^{\rm INT}}\right]\Delta\sigma^{-}_{\rm LU}(\phi_i)\Delta\phi_i\sin\phi_i, \tag{6.1}$$

$$\mathrm{Re}\left\{\mathcal{C}^{\rm INT}_{\rm UU}\right\} = \frac{1}{\pi}\sum_{i=1}^{12}\left[\frac{\mathcal{P}_1\mathcal{P}_2(\phi_i)K_c}{A^{\rm PS}A^{\rm INT}}\right]\Delta\sigma^{\rm C}_{\rm UU}(\phi_i)\Delta\phi_i\cos\phi_i, \tag{6.2}$$

where

$$K_s = -\frac{3y^2}{64\pi^2K(2-y)}, \tag{6.3}$$

$$K_c = \frac{3y^3}{64\pi K(2-2y+y^2)}, \tag{6.4}$$

are the kinematical prefactors of the Fourier coefficients $s_1^{\rm INT1}$ in Eq. (2.85) and $c_1^{\rm INT1}$ in Eq. (2.83), respectively. The statistical errors of the extracted combinations are given by

$$\left(\delta\mathrm{Im}\left\{\mathcal{C}^{\rm INT}_{\rm LU}\right\}\right)^2 = \frac{1}{\pi^2}\sum_{i=1}^{12}\left\{\left[\frac{\mathcal{P}_1\mathcal{P}_2(\phi_i)K_s}{A^{\rm PS}A^{\rm INT}}\right]\Delta\phi_i\sin\phi_i\right\}^2\cdot\left[\delta\Delta\sigma^{-}_{\rm LU}(\phi_i)\right]^2, \tag{6.5}$$

$$\left(\delta\mathrm{Re}\left\{\mathcal{C}^{\rm INT}_{\rm UU}\right\}\right)^2 = \frac{1}{\pi^2}\sum_{i=1}^{12}\left\{\left[\frac{\mathcal{P}_1\mathcal{P}_2(\phi_i)K_c}{A^{\rm PS}A^{\rm INT}}\right]\Delta\phi_i\cos\phi_i\right\}^2\cdot\left[\delta\Delta\sigma^{\rm C}_{\rm UU}(\phi_i)\right]^2. \tag{6.6}$$

Smearing

In order to make the pseudo-data more realistic, the central value of the cross section differences is smeared according to a Gaussian probability distribution whose standard deviation is equal to the error bar. Fig. 6.1 shows an example of the smearing effects, where the colored points present the smeared pseudo-data and the dashed curves show the theoretical estimate of observables.

6.1.2 The expected results

Using the smeared pseudo-data, the linear CFFs combinations are obtained for all covered $(x_{\rm B}, Q^2, t, Q'^2)$ bins, shown in Appendix. C. Fig. 6.2 shows the results as functions of ξ'

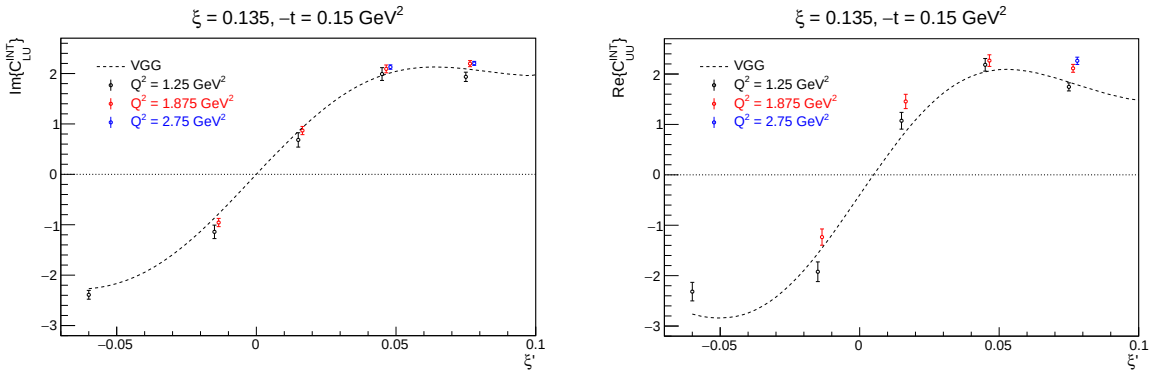

Figure 6.2: The linear CFFs combinations $\mathrm{Im}\left\{\mathcal{C}^{\mathrm{INT}}_{\mathrm{LU}}\right\}$ (left panels) and $\mathrm{Re}\left\{\mathcal{C}^{\mathrm{INT}}_{\mathrm{UU}}\right\}$ (right panels) as functions of ξ' at $\xi = 0.135$, $-t = 0.15$ GeV^2 and $Q^2 = 1.25$ (black points), 1.875 (red points), 2.75 (blue points) GeV^2, extracted from the pseudo-data at $\mathcal{L} = 10^{37}$ cm$^{-2} \cdot$ s^{-1}. The points are slightly offset in ξ' for visual clarity.

at specific ξ and t. It can be seen that the extracted CFFs combinations recover the theoretical curves with good accuracy. Such experimental measurements will provide unprecedented CFFs constraints at $\xi' \neq \xi$.

6.2 Local fits of the CFFs

Based on the merging of the well-established VGG code, a local fitting code has been specifically developed for the DDVCS process. It consists in taking the eight CFFs as free parameters and, using the BH and DDVCS leading-twist amplitudes, to fit at a fixed kinematics simultaneously the ϕ-distributions of a set of experimental observables. The VGG code uses its own models for the GPDs but in fact any GPD model can be used. When the range of variation of the CFFs is limited, the dominant CFFs contributing to the observables which are fitted are obtained from the fit procedure with finite error bars. These error bars are mainly due to the correlations between the CFFs. Rather than the error on the experimental data, they reflect the influence of the other sub-dominant CFFs [77, 78]. Except for the limits imposed on the variation of the CFFs, it has the merit of being mostly model-independent as there is no need to assume and hypothesize any functional shape for the CFFs. It has been proved in [72, 73] that the fitting code is reliable and powerful to extract all CFFs, given enough observables. If only limited observables are available, limits and constraints can still be derived for specific CFFs, as shown in [74, 75, 76] for JLab and HERMES DVCS data.

6.2.1 Monte Carlo studies

In this section, some examples of the simulations are presented in order to test and demonstrate the reliability and robustness of the fitting method. Considering the least constrained case and most challenging case, only two observables, σ^{-}_{UU} and $\Delta\sigma^{-}_{\mathrm{LU}}$ in Eq. (2.112), are fitted. The fitting with four observables, σ_{UU}, $\Delta\sigma^{\mathrm{C}}_{\mathrm{UU}}$, $\Delta\sigma_{\mathrm{LU}}$ and $\Delta\sigma^{\mathrm{C}}_{\mathrm{LU}}$ in Eq. (2.115), is also presented.

Each observable receives contributions from several CFFs, which are strongly correlated. Thus, the extraction of 8 CFFs from only two or four observables, with finite experimental uncertainties, is an underconstrained problem. However, some observables

E (GeV)	x_{B}	Q'^2 (GeV^2)	Q^2 (GeV^2)	$-t$ (GeV^2)	ξ	ξ'
11	0.138	1.012	2.75	0.25	0.105	0.045

Table 6.1: The particular kinematics for the simulations.

$a(\mathrm{Re}\mathcal{H})$	$a(\mathrm{Re}\mathcal{E})$	$a(\mathrm{Re}\widetilde{\mathcal{H}})$	$a(\mathrm{Re}\widetilde{\mathcal{E}})$
0.790050	1.336966	3.864845	1.450441
$a(\mathrm{Im}\mathcal{H})$	$a(\mathrm{Im}\mathcal{E})$	$a(\mathrm{Im}\widetilde{\mathcal{H}})$	$a(\mathrm{Im}\widetilde{\mathcal{E}})$
-1.485952	0.587110	-2.346204	-2.134648

Table 6.2: The generated CFF multipliers for the simulations.

are dominated by and mostly sensitive to one or two CFFs compared to the others. For instance, σ^{-}_{UU} is particularly sensitive to the real part of $\mathcal{H}$ and $\Delta\sigma^{-}_{\mathrm{LU}}$ is dominated by the imaginary part of $\mathcal{H}$. Other CFFs contributing to these observables are kinematically suppressed. Therefore, the range of variation of the CFFs is limited in a conservative way. While keeping the 8 CFFs in the fit, this reduces the underconstrained problem to fitting the one or two dominant CFFs to the one or two experimental observables. The influence of the non-dominant CFFs, over the domain in which they are allowed to vary, is then reflected in the resulting uncertainty on the dominant CFFs extracted. The mostly model-dependent input in this approach is the definition of the range of variation of the CFFs. In addition, the nucleon mass correction and higher twist effects for the calculation of the amplitude also enter the fitting code as a model-dependent factor.

Pseudo-data generation

The first step of this study consists in generating the pseudo-data for the fit. A particular set of kinematical variable shown in Table 6.1 is taken. Then, the 8 CFFs entering the DDVCS amplitude are generated randomly. In order to keep the problem realistic, they are chosen to vary within a bounded 8-fold hypervolume, whose limits are defined as ± 5 times the CFFs predicted by the VGG model. It is chosen not to generate the CFF values themselves but rather their "multipliers", namely their deviations from the VGG CFFs. The CFFs entering the DDVCS amplitude are then the product of these multipliers by the VGG reference CFFs. The randomly generated CFF multipliers are denoted $a(\mathcal{F})$ and their values for generating the cross sections are shown in Table 6.2. Some of the multipliers are very far from 1. They correspond probably to quite unrealistic CFFs. However, exploring such a large range of values should make the fitting code more robust and convincing.

The goal of this study is to see if the 8 original randomly generated CFF multipliers, or some of them, can be retrieved under realistic conditions. Therefore, the calculated cross sections are smeared according to the statistical errors obtained in Chapter 4. Fig. 6.3 shows the unpolarized cross section and beam spin cross section difference generated with the 8 random CFFs. The fit is carried out with only 6 points in ϕ spread in steps of 30° between 15° and 165°, since little improvement is observed in fitting more ϕ values.

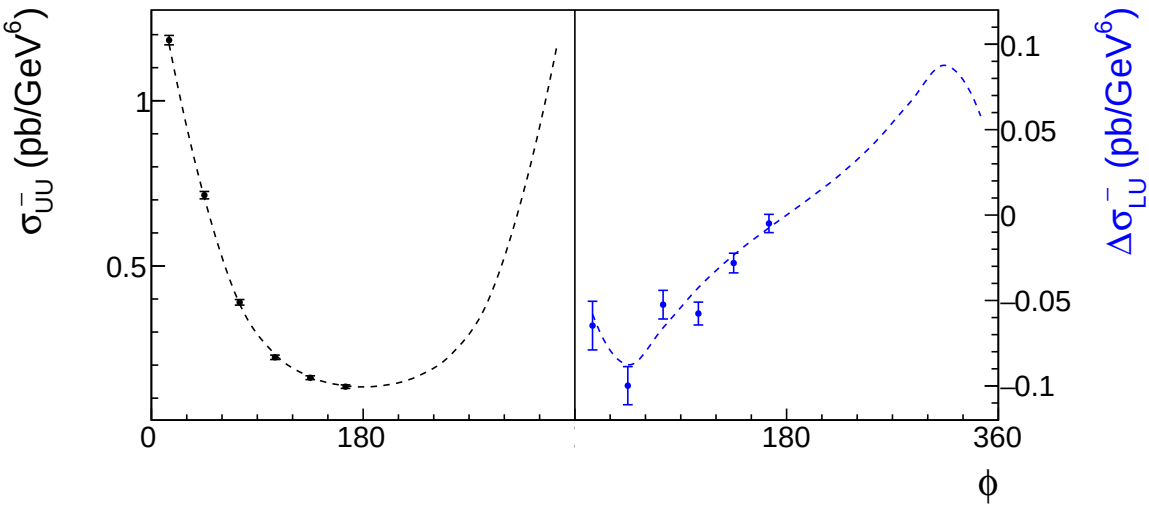

Figure 6.3: σ^-_{UU} (left) and $\Delta\sigma^-_{LU}$ (right) generated from 8 randomly generated CFF multipliers (Table 6.2) for the kinematics in Table 6.1. The dashed curves presents the originally generated distribution. The points presents the pseudo-data smeared according to the statistical errors evaluated for an ideal detector with $\mathcal{L} = 10^{36}$ cm$^{-2} \cdot$ s^{-1} and 50 days run.

Pseudo-data fitting

The second step of the study consists in fitting the generated ϕ distributions leaving the 8 CFFs as free parameters, ignoring any information about the initial generated values. The idea is to match as much as possible real conditions. However, the condition for the fitting procedure to converge is to limit the hyperspace in which the 8 CFFs are allowed to vary. The choice of the values of the boundaries is the only model-dependent input. In this study, the same hyperspace in which the 8 CFFs were originally generated, namely ± 5 times the VGG CFFs., is chosen. Similarly to the generation of the CFFs, the multipliers of the VGG CFFs are fitted, rather than the absolute CFFs themselves, with the goal to retrieve the originally generated ones. Using the least square method, the quantity to be minimized is

$$\chi^2 = \sum_{i=1}^{n} \frac{(\sigma_i^{theo} - \sigma_i^{exp})^2}{(\delta\sigma_i^{exp})^2}, \tag{6.7}$$

where σ_i^{theo} is the theoretical cross section depending on the CFFs multipliers, σ_i^{exp} is the corresponding value of the pseudo- or experimental data and $\delta\sigma_i^{exp}$ is its associated error bar. The index i runs over all the available ϕ points of all the observables to be fitted for a given (ξ', ξ, t, Q^2) bin. The MIGRAD minimizer of MINUIT [79] is used to perform the fit, with the MINOS subpackage for the error analysis. This method allows to explore in a gradual and automatic way the χ^2 landscape around the minimum and define one-standard-deviation uncertainties for each parameter when it reaches $\chi^2 + 1$. It is costly in terms of computing time but can find the global minimum (or minima) of the non-linear problem, reducing the risk of falling into local minima. When the problem is severely underconstrained and has strong correlations between the parameters, this is the only way to determine the error.

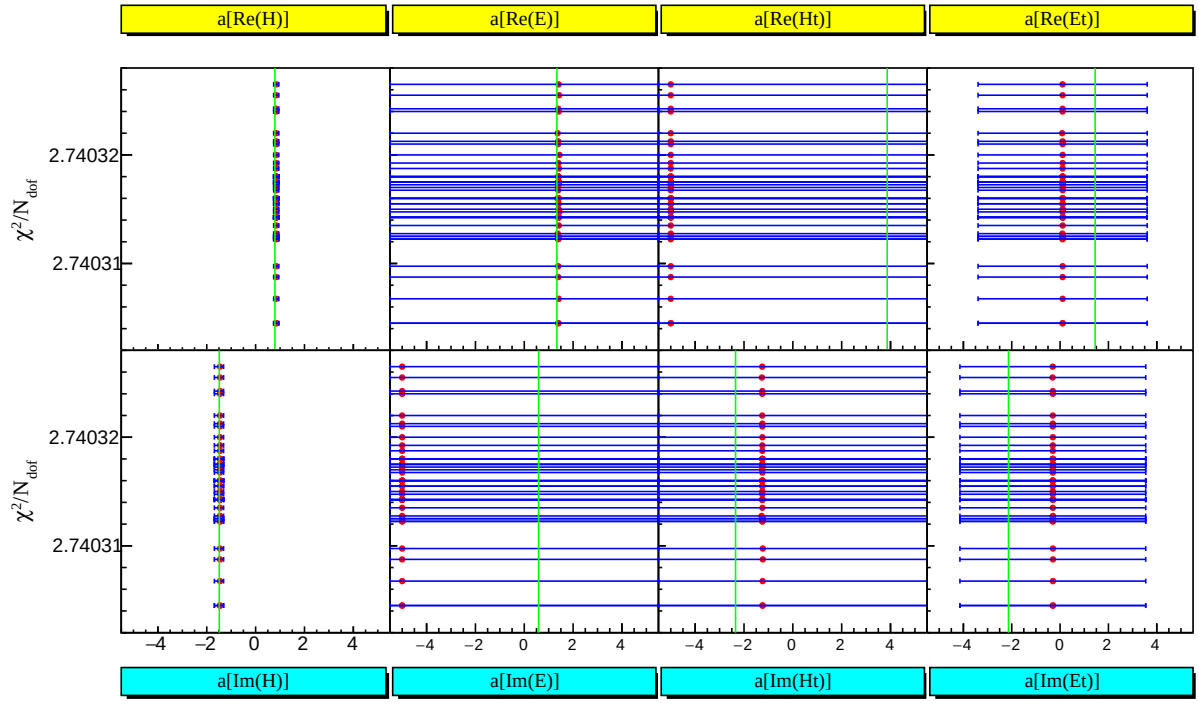

Figure 6.4: Results of a series of fits, differing by their randomly generated starting values, of σ_{UU}^{-} and $\Delta\sigma_{LU}^{-}$ smeared pseudo-data of Fig. 6.3. The red dots show for each fit, on the x-axis, the values of the CFFs multipliers which minimize the problem and, on the y-axis, the corresponding minimal value of reduced χ^2. The blue error bars indicate the uncertainties derived from the MINOS analysis. The green vertical lines indicate the CFF multiplier values used for the generation of the pseudo-data in Table. 6.2.

Fitting the specifically smeared pseudo-data of σ_{UU}^{-} and $\Delta\sigma_{LU}^{-}$ in Fig. 6.3 for dozens of times with various starting points randomly selected in $[-5, 5]$, the red dots in Fig. 6.4 shows the results of the fits for the 8 CFF multipliers as a function of reduced χ^2. The blue error bars indicate the one-standard-deviation uncertainties corresponding to $\chi^2 + 1$. The non-finite error bars for the CFFs $\mathcal{E}$ and $\widetilde{\mathcal{H}}$ mean that the $\chi^2 + 1$ value lies out of the ± 5 times VGG CFF range. It can be interpreted as the whole range of values for the associated parameter can accommodate the fit with relatively equally good χ^2. In other words, the corresponding CFF multiplier is essentially unconstrained and therefore no particular confidence and meaning can be given to the quoted numerical value. Obviously, the result of the fit is not dependent on the particular starting values of the 8 CFFs. It can also be observed that only CFF $\mathcal{H}$, very close to the originally generated values (green lines), can be retrieved from the fit with good minimum and accuracy, $\chi^2/N_{dof} \approx 2.74$ and about 15% uncertainties for both $a(\mathrm{Re}\mathcal{H})$ and $a(\mathrm{Im}\mathcal{H})$. The result actually implies that σ_{UU}^{-} and $\Delta\sigma_{LU}^{-}$ are dominantly sensitive to the CFFs $\mathrm{Re}\mathcal{H}$ and $\mathrm{Im}\mathcal{H}$.

Fitting the pseudo-data of σ_{UU}^{-} and $\Delta\sigma_{LU}^{-}$ in Fig. 6.3 for dozens of times with different random smearings, Fig. 6.5 shows the results of the fits for the 8 CFF multipliers as a function of reduced χ^2. Each fit yields a different solution and different values in χ^2/N_{dof} from 1 to 4. However, it is remarkable that the originally generated values of $a(\mathrm{Re}\mathcal{H})$ and $a(\mathrm{Im}\mathcal{H})$ mostly lies within the error bars (mostly about 20%) of the fitted ones. A closer look (see the top panels of Fig. 6.6) reveals that the values of $a(\mathrm{Re}\mathcal{H})$ and $a(\mathrm{Im}\mathcal{H})$ (red dots) are not exactly centered on the originally generated values (green lines). The origin of such shifts is the random smearing of the data that can accidentally bias the ϕ

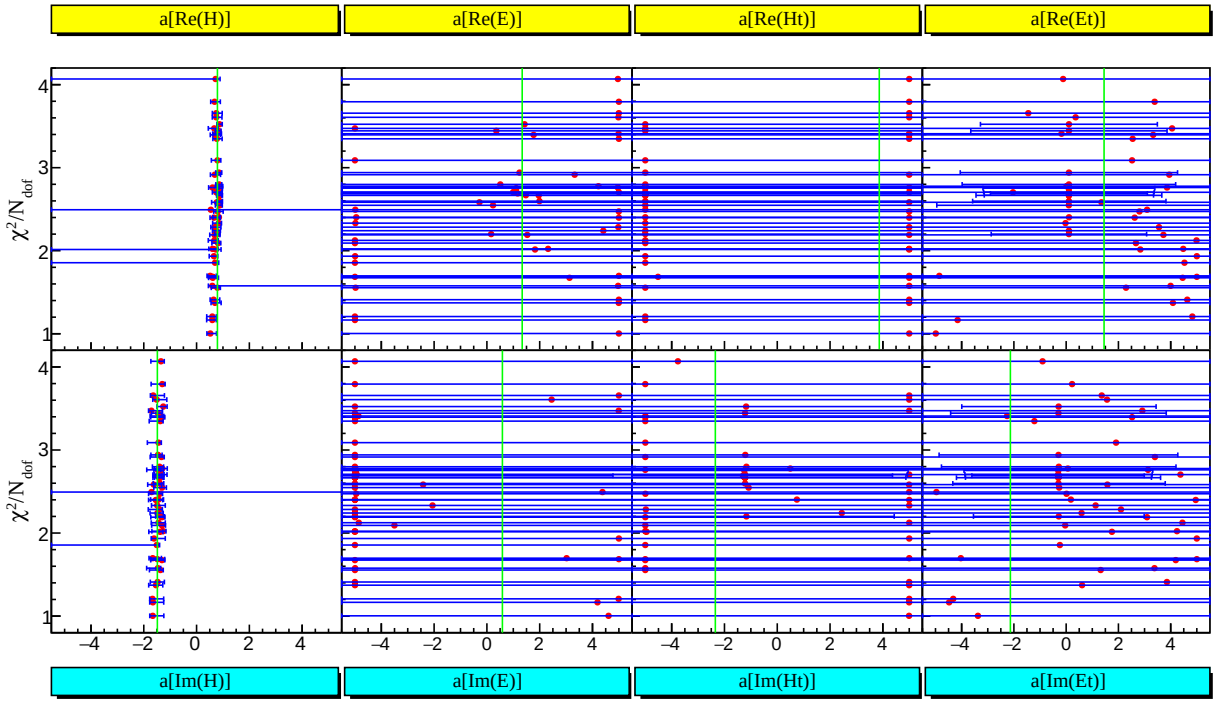

Figure 6.5: Results of a series of fits, differing by their different random smearings, of σ^{-}_{UU} and $\Delta\sigma^{-}_{LU}$ pseudo-data.

distributions in a given direction. It can also be seen that there are chances that the fit does not converge and/or ends up with non-finite error bars for $a(\mathrm{Re}\mathcal{H})$ and/or $a(\mathrm{Im}\mathcal{H})$, also resulting from the random smearings for the pseudo-data. The fit is very challenging for the low statistics data.

It has been proved in [77] that the more observables one fit, the smaller and more symmetric the error bars on the resulting fitted CFFs can be derived, together with the less dependence on the the allowed domain of variation of the CFFs. This feature can be also observed in Fig. 6.6, where the bottom panels shows the resulting fitted $a(\mathrm{Re}\mathcal{H})$ and $a(\mathrm{Im}\mathcal{H})$ derived from the fits of σ_{UU}, $\Delta\sigma^{C}_{UU}$, $\Delta\sigma_{LU}$ and $\Delta\sigma^{C}_{LU}$ for dozens of times with different random smearings. In order to compare the impact of number of observables, the statistical errors for the 4 observables are evaluated in the same condition as for the 2 observables, namely $\mathcal{L} = 10^{36}$ cm$^{-2} \cdot$ s^{-1} and 50 days in total. In comparison with the fits with the 2 observables, the fits with the 4 observables results in smaller errors on the fitted $a(\mathrm{Re}\mathcal{H})$ and $a(\mathrm{Im}\mathcal{H})$, higher degree of concentration on the originally generated values and smaller values in χ^2/N_{dof} (from 0.5 to 3). The other CFFs still cannot be retrieved with the 4 observables, since the generation and fitting are performed at leading twist approxiamtion, where they are all dominated by the CFF $\mathcal{H}$ and do not provide essential constraints on CFFs other than $\mathcal{H}$. The observables with neutron and nucleon polarization offer the additional constraints and meanwhile improve the accuracy of the fitted $\mathcal{H}$.

Since the problem is severely underconstrained and the available observables predicted by VGG model are dominantly sensitive to $\mathrm{Re}\mathcal{H}$ and $\mathrm{Im}\mathcal{H}$, the fits with only CFF $\mathcal{H}$ are also tested. Fig. 6.7 shows the results of these fits, differing by their different random smearings, of 2 observables, σ^{-}_{UU} and $\Delta\sigma^{-}_{LU}$ (top panels), and 4 observables, σ_{UU}, $\Delta\sigma^{C}_{UU}$, $\Delta\sigma_{LU}$ and $\Delta\sigma^{C}_{LU}$ (bottom panels). The originally generated values of $a(\mathrm{Re}\mathcal{H})$ and $a(\mathrm{Im}\mathcal{H})$ mostly lies within the error bars (about 6%) of the fitted ones, even though the

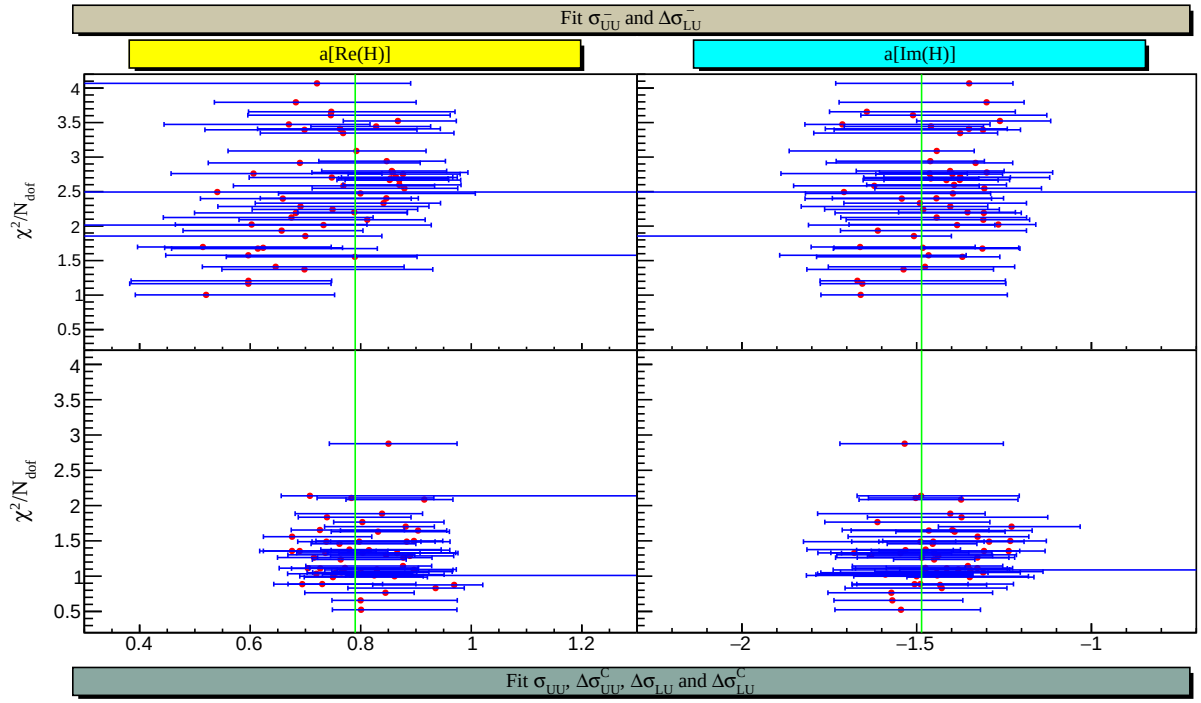

Figure 6.6: Fitted $a(\mathrm{Re}\mathcal{H})$ (left panels) and $a(\mathrm{Im}\mathcal{H})$ (right panels) derived from a series of fits, differing by their different random smearings, of 2 observables, σ^{-}_{UU} and $\Delta\sigma^{-}_{\mathrm{LU}}$ (top panels), and 4 observables, σ_{UU}, $\Delta\sigma^{\mathrm{C}}_{\mathrm{UU}}$, $\Delta\sigma_{\mathrm{LU}}$ and $\Delta\sigma^{\mathrm{C}}_{\mathrm{LU}}$ (bottom panels).

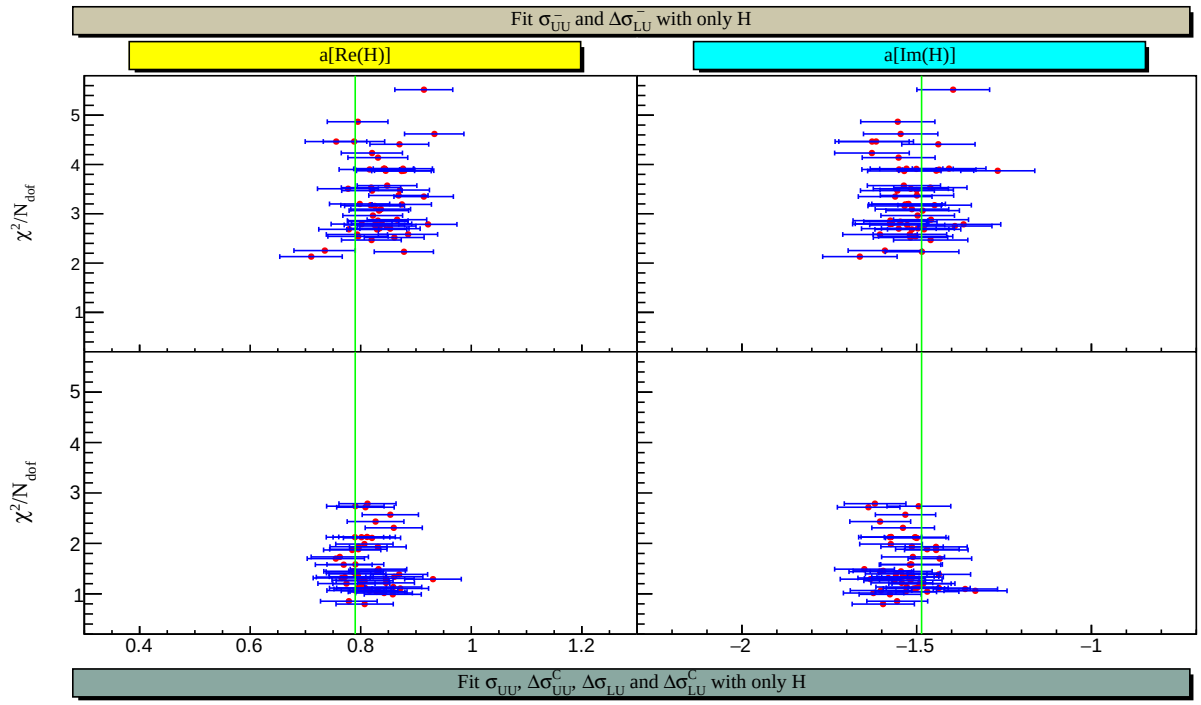

Figure 6.7: Results of the fits when only CFF $\mathcal{H}$ is included and the other CFFs are set to zero.

pseudo-data are generated with 8 VGG CFFs. The error bars of fitted CFFs are no more asymmetric due to the absence of the correlation between $\mathcal{H}$ and the others, which are set to zero for the fits. These results actually indicate the strong sensitivity of the available pseudo-data to the CFF $\mathcal{H}$ again.

Altogether, the Monte Carlos studies above proves that the fitting method is reliable and robust and CFF $\mathcal{H}$ can be conservatively obtained when the smearing does not distort the pseudo-data.

6.2.2 Application

Here I apply the fit method (with 8 CFF as free parameters) to the pseudo-data derived in the ideal situation discussed in Chapter 4. The pseudo-data are smeared according to errors evaluated for 50 days and two luminosities, 10^{36} cm$^{-2} \cdot$ s^{-1} and 10^{37} cm$^{-2} \cdot$ s^{-1}. When the statistics of the pseudo-data is too poor, the fits mostly will not converge and/or end up with non-finite error. Thus, I only carry out the fit on the pseudo-data fulfilling a certain statistics requirement: the errors on minimal σ^{-}_{UU} at $\phi = 165^{\circ}$ need to be smaller than 10% and the errors on the maximal BSA and BCA need to be smaller than 100%. There are 120 (ξ', ξ, t, Q^2) bins satisfying the requirement at 10^{36} cm$^{-2} \cdot$ s^{-1} and 266 at 10^{37} cm$^{-2} \cdot$ s^{-1}.

Fig. 6.8 shows the fitting results for Im$\mathcal{H}$ as a function of ξ' at $\xi = 0.135$, $-t = 0.25$ GeV^2 and $Q^2 = 1.25$ GeV^2. The CFF Im$\mathcal{H}$, defined in Eq. 1.112, actually is the singlet GPD $H^+(x, \xi, t)$ at $x = \xi'$, which is a asymmetric function in ξ' (see the dashed curve in the bottom panel). Thus, $\Delta\sigma^{-}_{\mathrm{LU}}$ (and $\Delta\sigma^{\mathrm{C}}_{\mathrm{LU}}$) is very small around $\xi' = 0$, where it offers weak constraints on Im$\mathcal{H}$. This feature makes the fit very challenging in this region. For example, the fitted CFF multipliers (top panel) at $\xi' = -0.015$ have non-finite errors and the corresponding fitted CFF values (bottom panel) are not presented, regarded as unsuccessful fit. The successfully fitted Im$\mathcal{H}$, namely with finite errors, appearing in the bottom panel of Fig. 6.8 mostly lies in the space-like region ($\xi' > 0$). This is caused by the smallness of $\Delta\sigma^{-}_{\mathrm{LU}}$ (and $\Delta\sigma^{\mathrm{C}}_{\mathrm{LU}}$) in the time-like region ($\xi' < 0$), as discussed in Sec. 2.3.2. However, the GPD H^+ in the time-like region can be deduced through its model-independent asymmetry in ξ' and eventually mapped out over the full phase space. Simultaneously, the fitted Re$\mathcal{H}$ is derived from the fit, as shown in Fig. 6.9. With the additional constraints, fitting with 4 observables seems to have higher probabilities than with 2 observables to end up with finite error bars, as shown at $\xi' = \pm 0.015$. This is simply due to the real part of the linear CFFs combination in the beam charge cross section difference.

In summary, the fit method specially developed for DDVCS shows it is possible to extract the imaginary (singlet GPD) and real part of the CFFs $\mathcal{H}$ from the pseudo-data. For all the bins meeting the statistics requirement, the results of the fits are presented in the Appendix D.

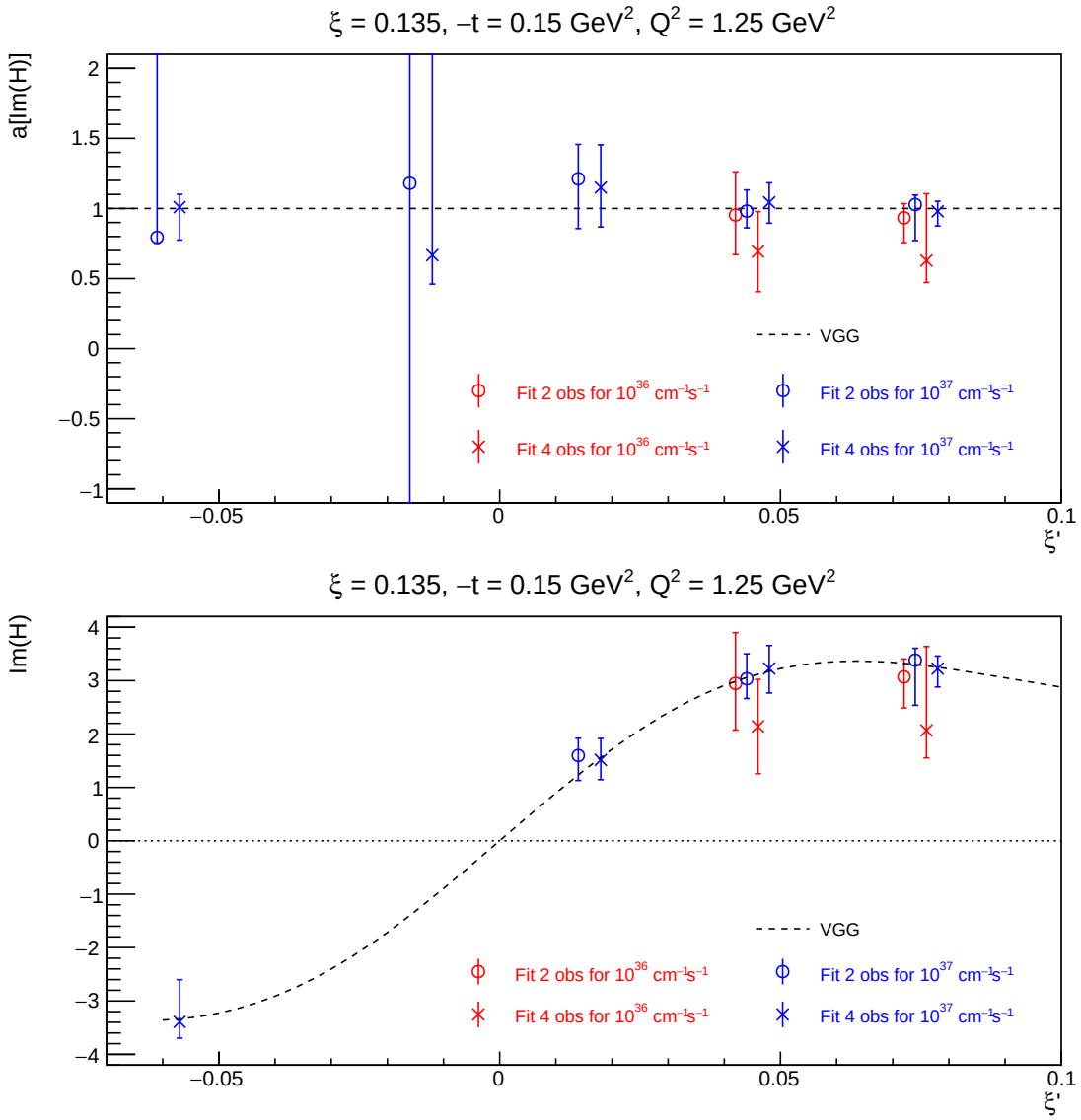

Figure 6.8: Fitted Im$\mathcal{H}$ CFF multiplier (top panel) and CFF itself (bottom panel) as functions of ξ' at $\xi = 0.135$, $-t = 0.25$ GeV^2 and $Q^2 = 1.25$ GeV^2. The red marks correspond the fits to the data at 10^{36} cm$^{-2}\cdot$s^{-1} and the blue ones at 10^{37} cm$^{-2}\cdot$s^{-1}. The open circles correspond the fits of σ^{-}_{UU} and $\Delta\sigma^{-}_{\mathrm{LU}}$, and the crosses correspond the fits of σ_{UU}, $\Delta\sigma^{\mathrm{C}}_{\mathrm{UU}}$, $\Delta\sigma_{\mathrm{LU}}$ and $\Delta\sigma^{\mathrm{C}}_{\mathrm{LU}}$. The dashed curves represent the originally generated VGG CFF.

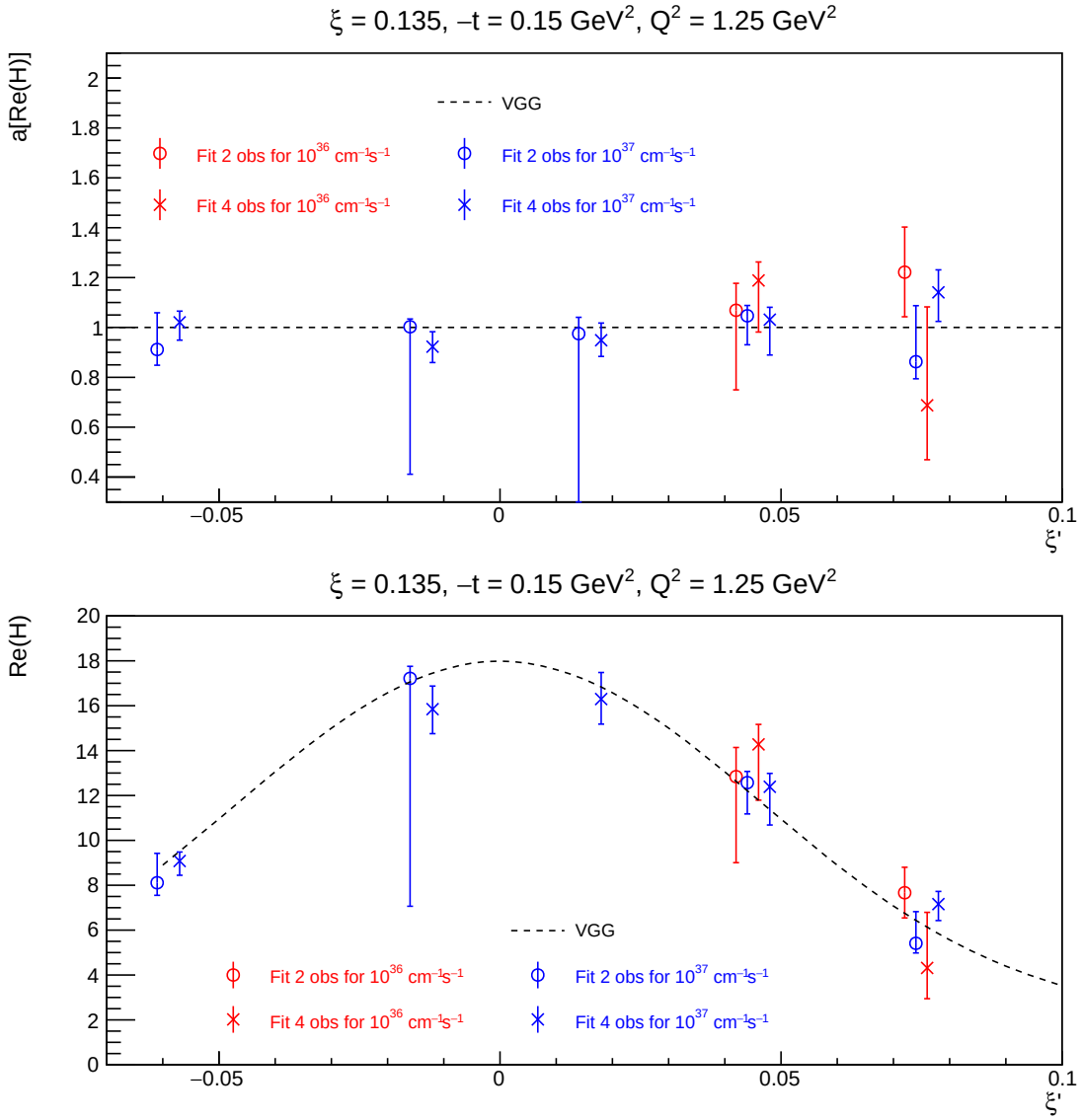

Figure 6.9: Fitted Re$\mathcal{H}$ CFF multiplier (top panel) and CFF itself (bottom panel) as functions of ξ' at $\xi = 0.135$, $-t = 0.25$ GeV^2 and $Q^2 = 1.25$ GeV^2. The convention for curves and points is the same as in Fig. 6.8.

Conclusion

Generalized Parton Distributions contain a wealth of information and have become a powerful paradigm to study the structure and dynamics of the nucleon. Encoding the correlations between the parton, i.e. quarks and gluons, of the nucleon, GPDs allows 3-dimensional imaging of the nucleon from the dynamical link between the transverse position and the longitudinal momentum of partons. As a result of these position-momentum correlations, GPDs provide a way to measure the unknown orbital momentum contribution of quarks to the total spin of the nucleon.

Double Deeply Virtual Compton Scattering is one of the cleanest reaction accessing GPDs. The electroproduction of a lepton pair $eN \to eNl^-l^+$, which is sensitive to the DDVCS amplitude, provides the only experimental framework for a decoupled measurement of GPDs(x, ξ, t) as a function of both the average momentum fraction x and the transferred one ξ. This unique feature of DDVCS is of relevance, among others, for the determination of the transverse parton densities and the distribution of nuclear forces.

Because of complex antisymmetrization concerns, the production of muon pairs appear the only feasible and promising channel for the investigation of DDVCS with electron and positron beams, asking, in the JLab experimental context, for the availability of a muon detector. The DDVCS process is most challenging from the experimental point of view due to the small magnitude of the cross section. The measurements of DDVCS observables require high luminosity and large acceptance detectors for reasonable statistics. Thus, measurements of the observables in terms of the 5-fold differential cross section is more realistic than the full differential cross section measurements. The leading-twist formulas of the cross section integrated over final lepton solid angle and over final lepton polar angle and nucleon azimuthal angle have been deduced to obtain the theoretical ground of the phenomenological studies of the DDVCS process discussed in the present work.

At JLab 12 GeV kinematics, the DDVCS observables with unpolarized targets have been evaluated by using VGG model and show a dominant sensitivity to the CFFs $\mathcal{H}$. The model-predicted projections of a DDVCS experiment indicate a high degree of feasibility at a luminosity of 10^{37} cm^{-2}·s^{-1} with exclusive final states completely detected. A more realistic study is supporting feasibility with large acceptance and reasonable luminosity as opposed to small acceptance and very high luminosity. A more detailed study with SoLID spectrometer shows a realistic possibility for the measurements with the J/Ψ configuration complemented by muon detection capabilities.

Numerical methods have been specifically developed for the extraction of CFFs. Considering polarized electron and positron beams, two specific linear combinations of CFFs with a good accuracy have been extracted from simulated experimental pseudo-data at a luminosity of 10^{37} cm^{-2}·s^{-1}. Covering a broad kinematics phase space, it is highly possible to obtain, by applying a local fitter algorithm, the dependence of the CFF $\mathcal{H}$ on its three arguments independently, where the GPD H singlet is directly given by the extracted imaginary part of the CFF $\mathcal{H}$.

SoLID project is moving forward and the design of various detectors of SoLID spectrometer is being optimized. The DDVCS measurements with SoLID is considered as the most promising DDVCS experiment in the future.

In order to reveal the spin puzzle of the nucleon, the knowledge of the GPD E is still needed. The measurements on a neutron target offer the sensitivity to the GPD E and become then of direct relevance in the determination of the quark angular momentum. To access the other GPDs, the measurements of the observables with polarized target are required. In the current state of polarized target technology, a fixed-target DDVCS experiment is not achievable. However, it can be achieved at the future EIC facility. The observables with polarized nucleon related to complementary combinations of CFFs will provide additional constraints on the CFFs other than $\mathcal{H}$, which will also benefit the extraction of $\mathcal{H}$ in the local fit.

Appendix A

Observables in the ideal situation

When $\mathcal{L} = 10^{37}$ cm^{-2}·s^{-1} and $T = 50$ days, the observables for the covered bins in $\xi = 0.045,\ 0.075,\ 0.105,\ 0.175$ and 0.25 are shown in the following figures. Fig. A.1-A.5 display the expected accuracy of the unpolarized cross section, Fig. A.6-A.10 display the expected accuracy of the BSA and Fig. A.11-A.15 display the expected accuracy of the BCA with additional 50 days running of positron beam.

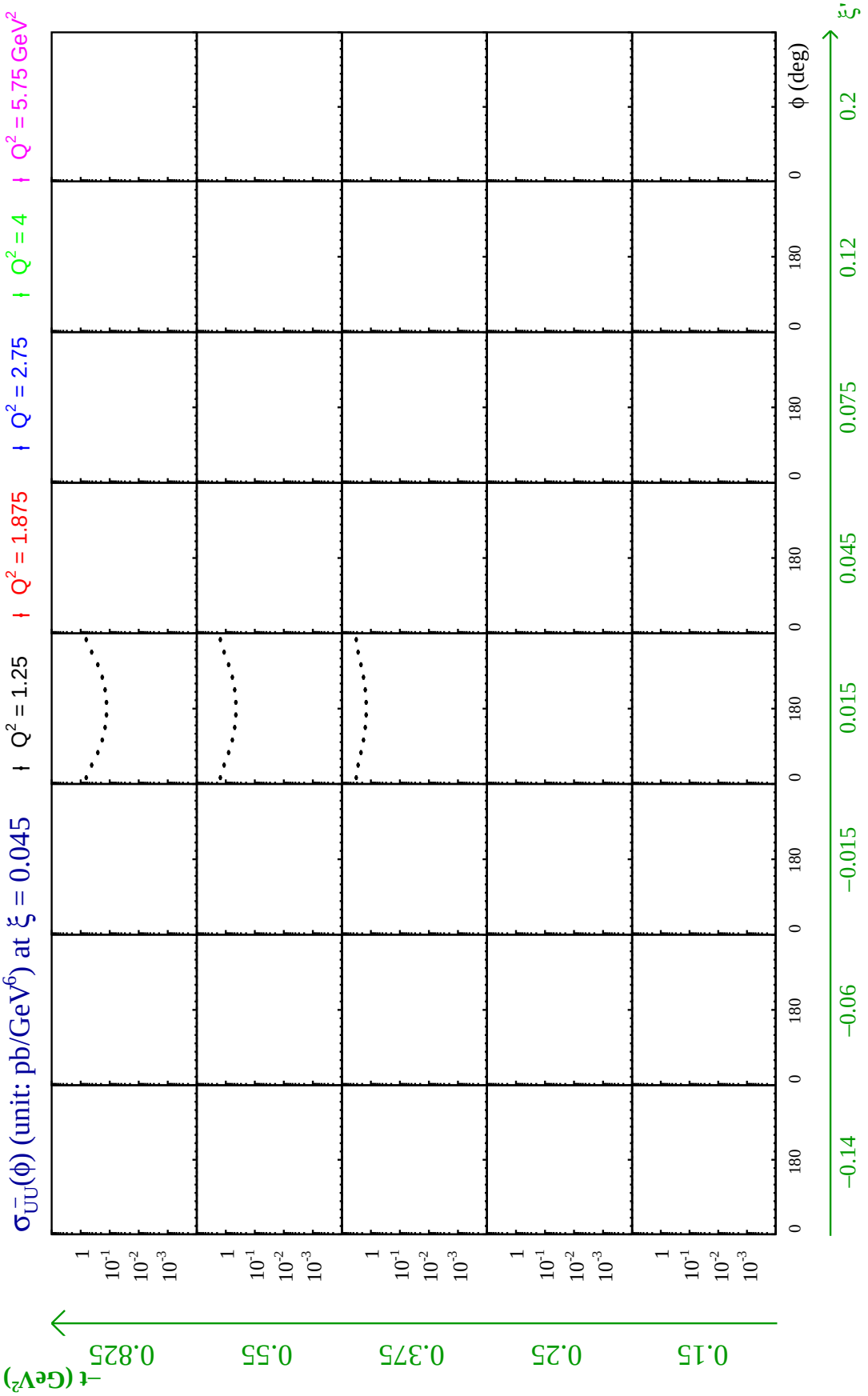

Figure A.1: $\sigma^{-}_{UU}(\phi)$ at $\xi = 0.045$.

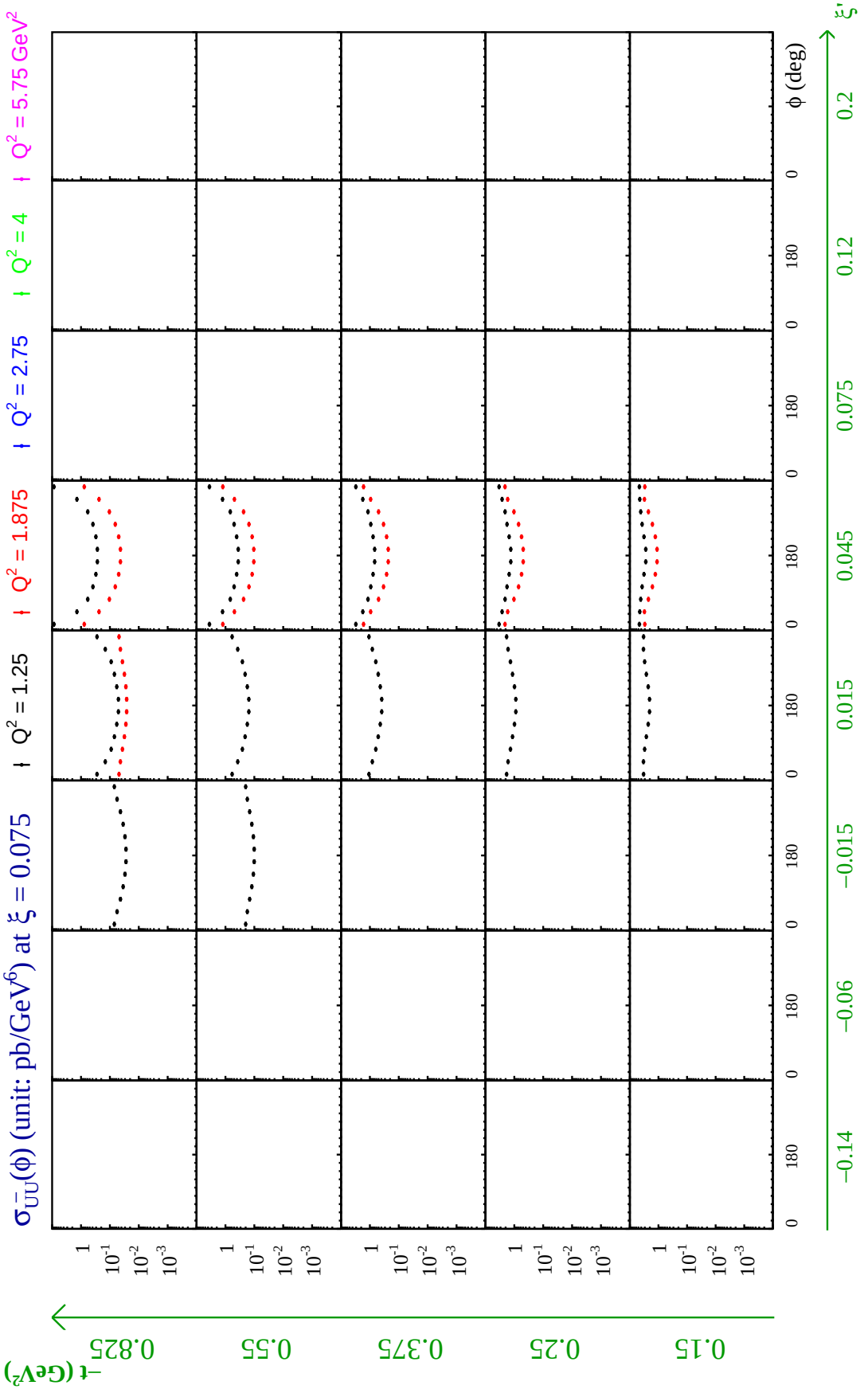

Figure A.2: $\sigma^{-}_{UU}(\phi)$ at $\xi = 0.075$.

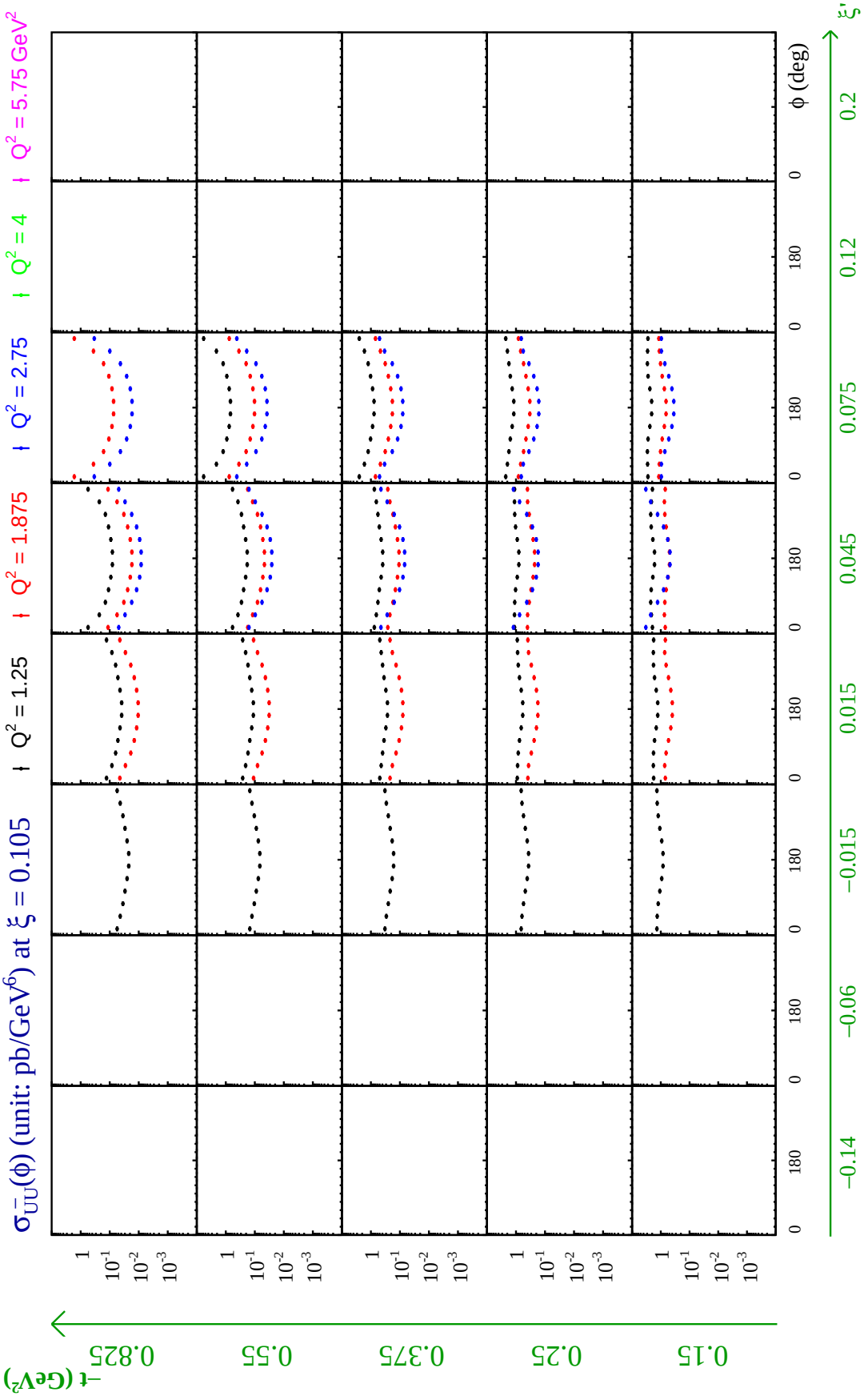

Figure A.3: $\sigma^{-}_{UU}(\phi)$ at $\xi = 0.105$.

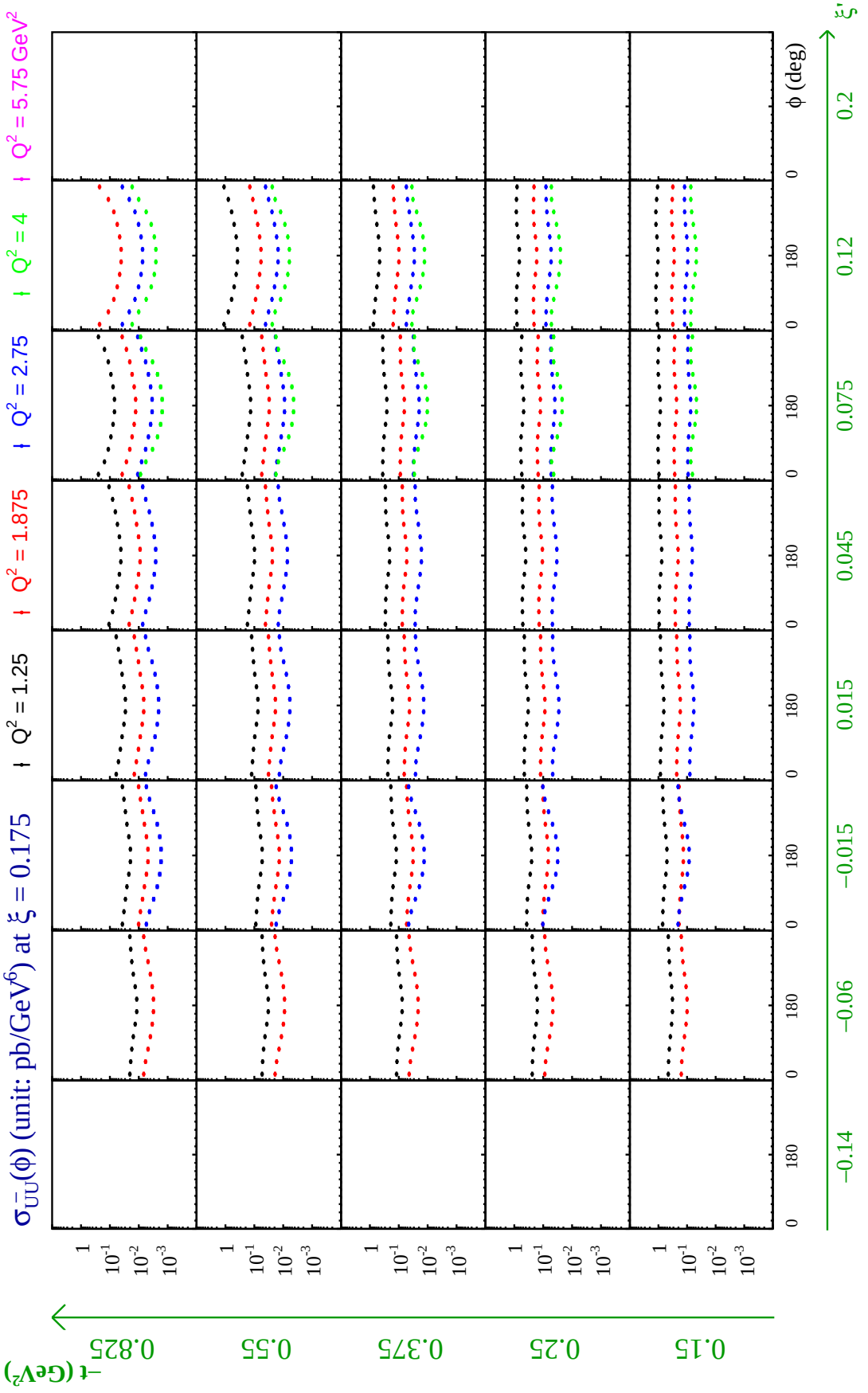

Figure A.4: $\sigma^{-}_{UU}(\phi)$ at $\xi = 0.175$.

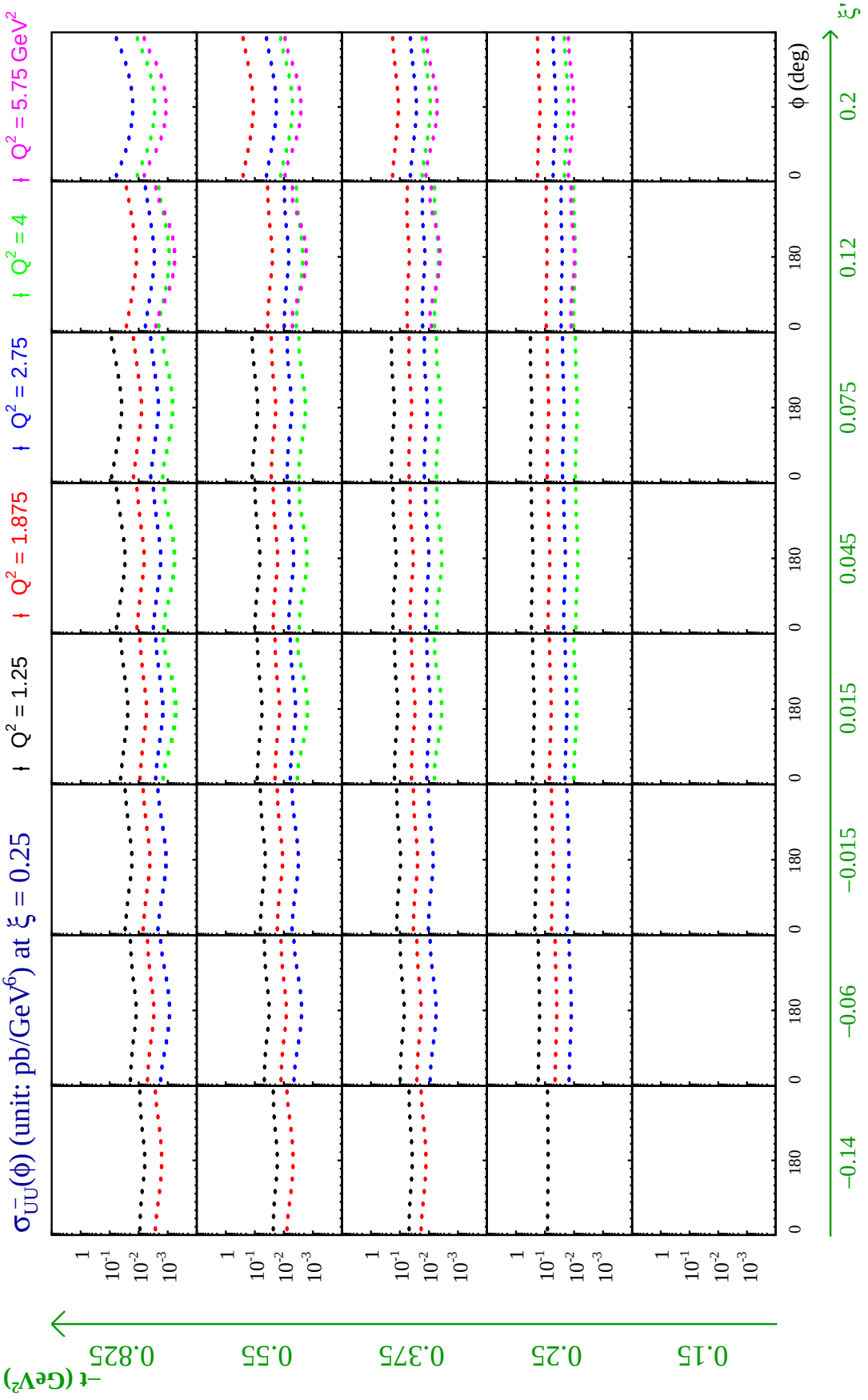

Figure A.5: $\sigma^-_{UU}(\phi)$ at $\xi = 0.25$.

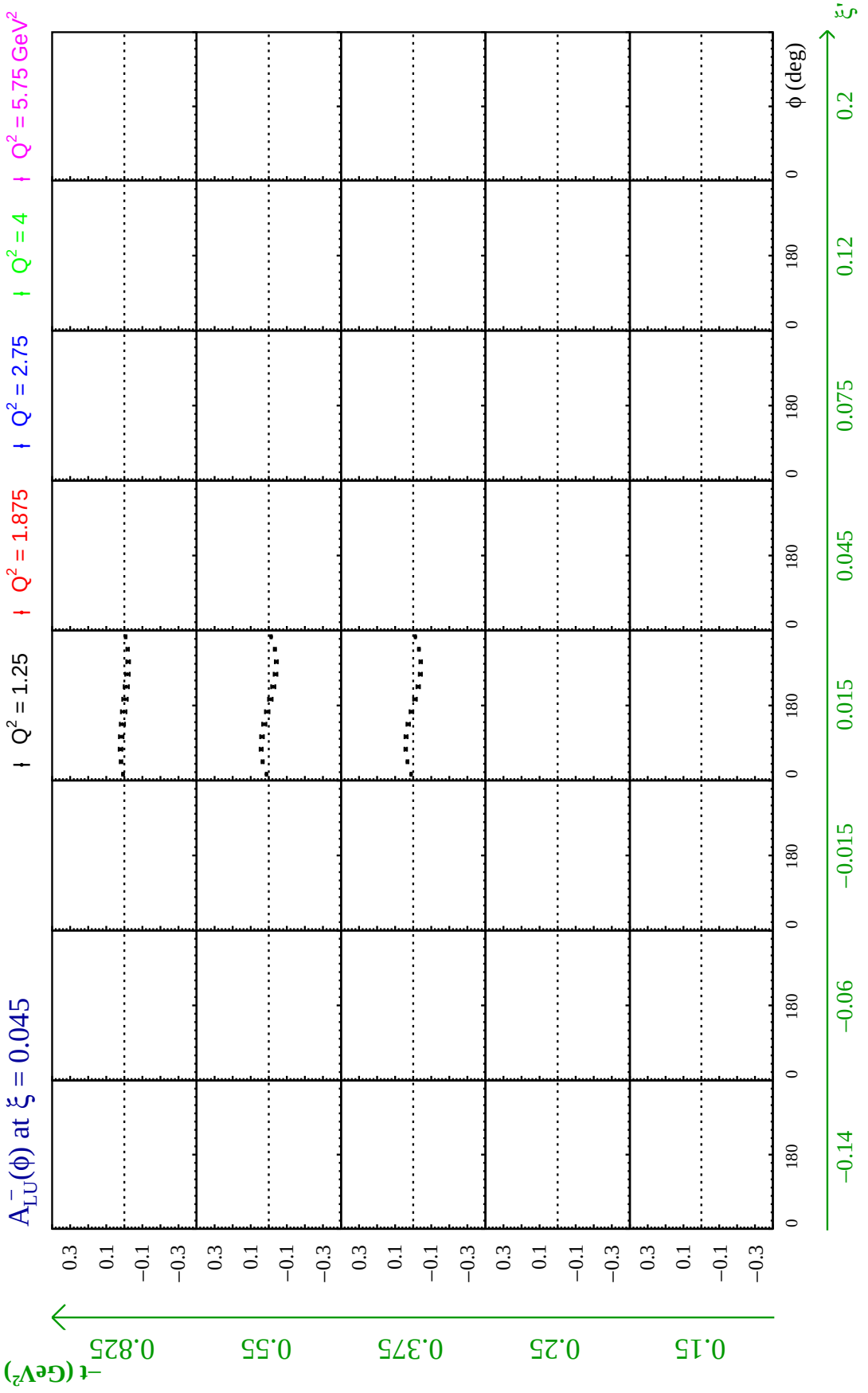

Figure A.6: $A_{\mathrm{LU}}^{-}(\phi)$ at $\xi = 0.045$.

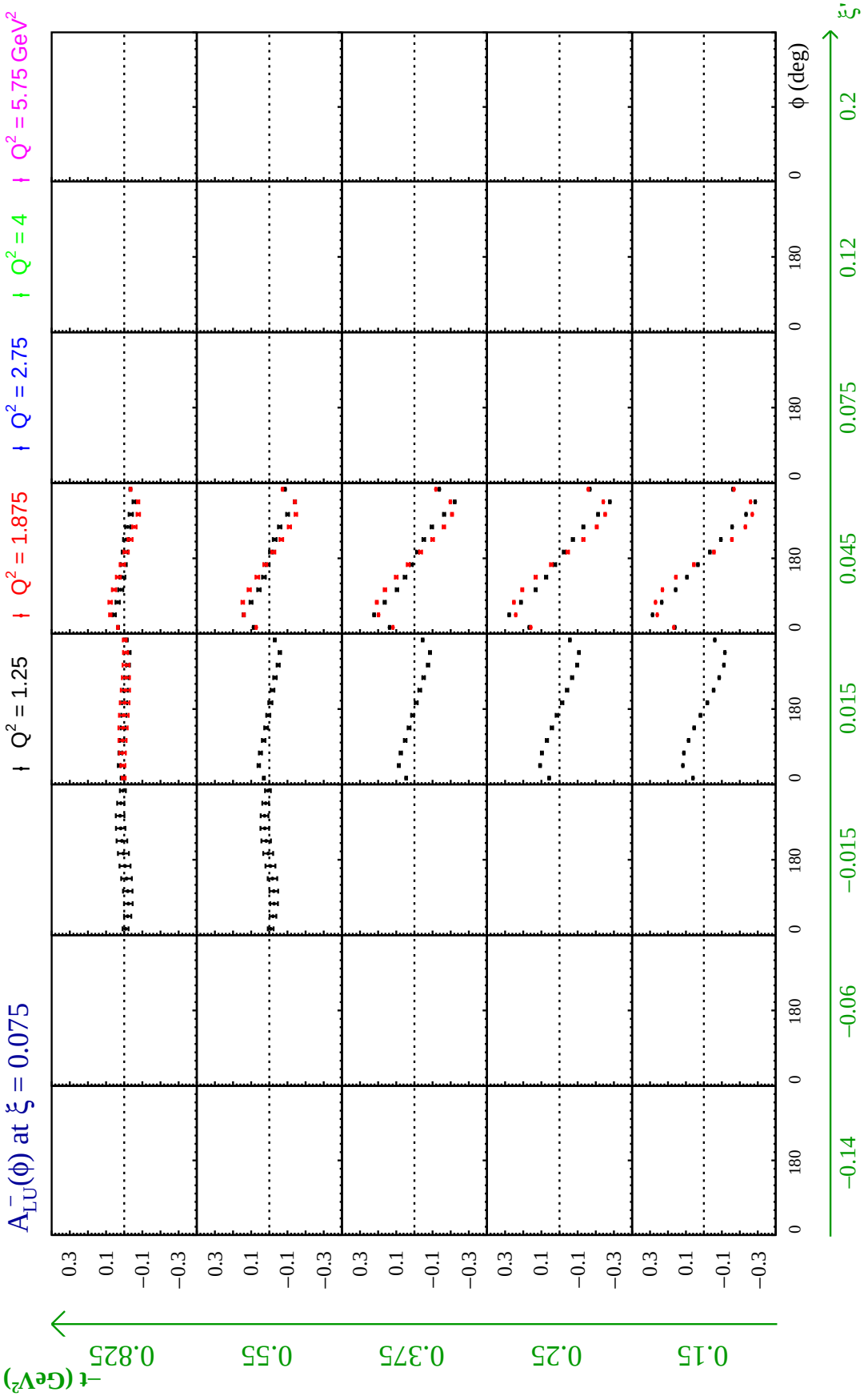

Figure A.7: $A_{LU}^{-}(\phi)$ at $\xi = 0.075$.

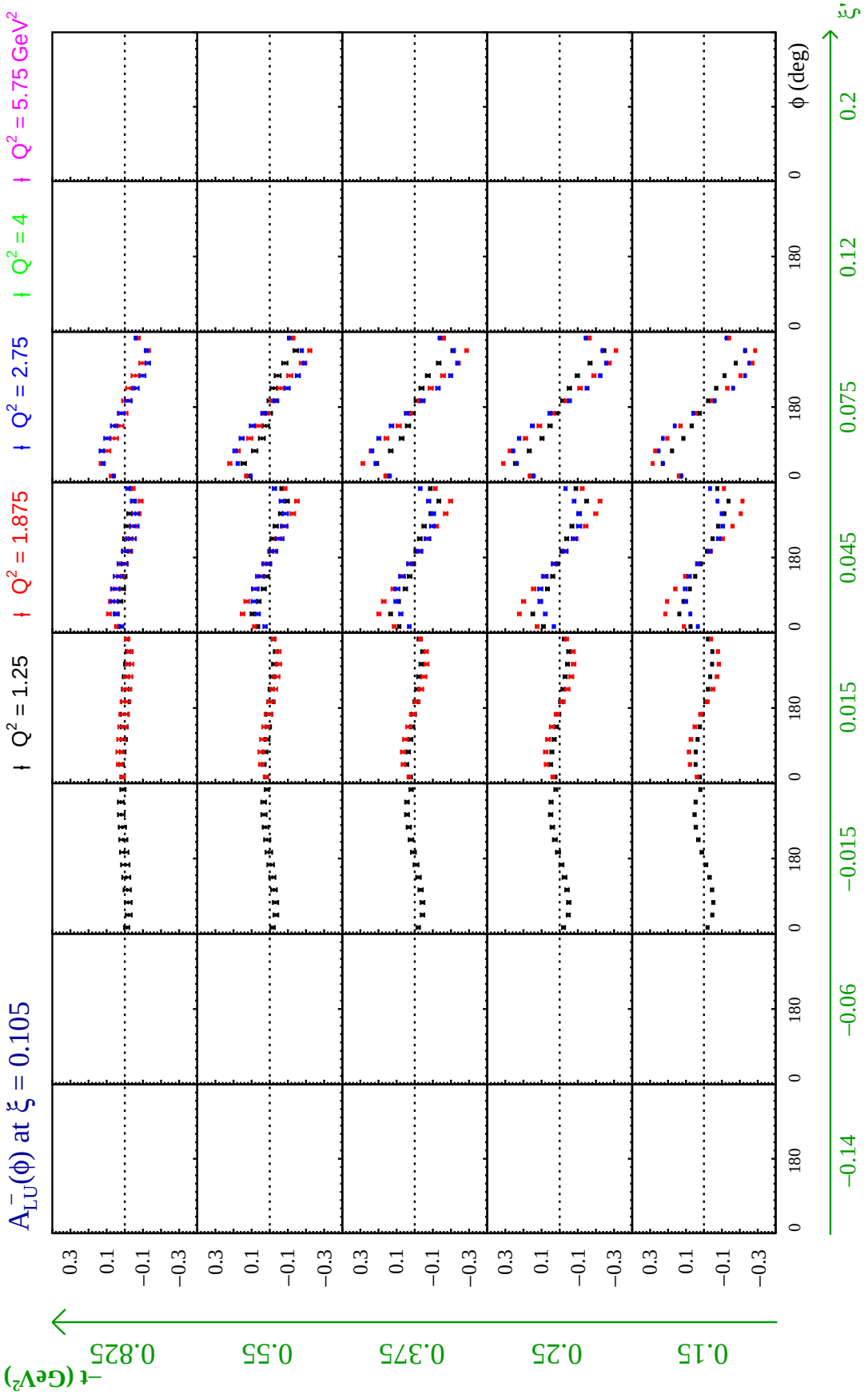

Figure A.8: $A_{\mathrm{LU}}^{-}(\phi)$ at $\xi = 0.105$.

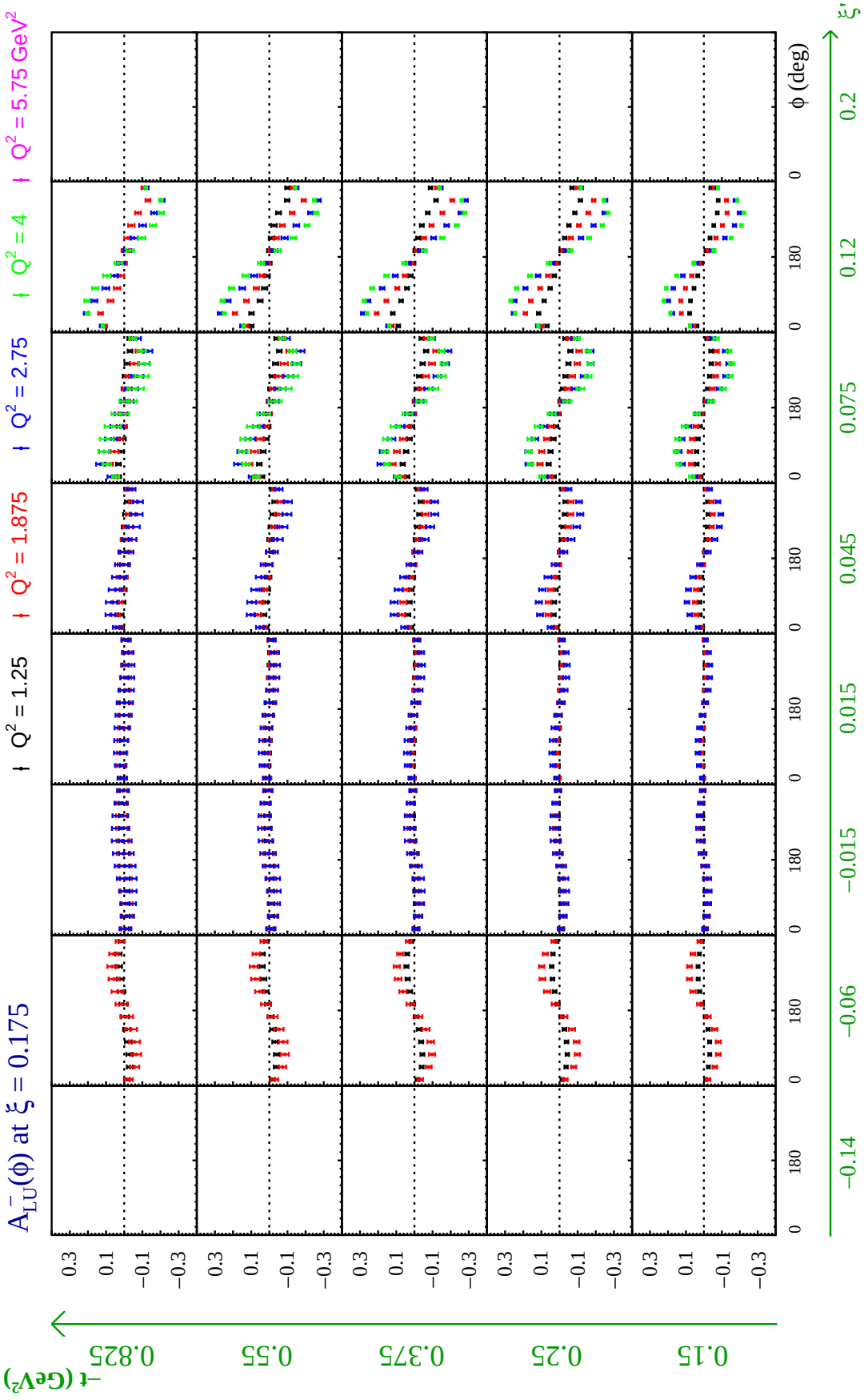

Figure A.9: $A_{LU}^{-}(\phi)$ at $\xi = 0.175$.

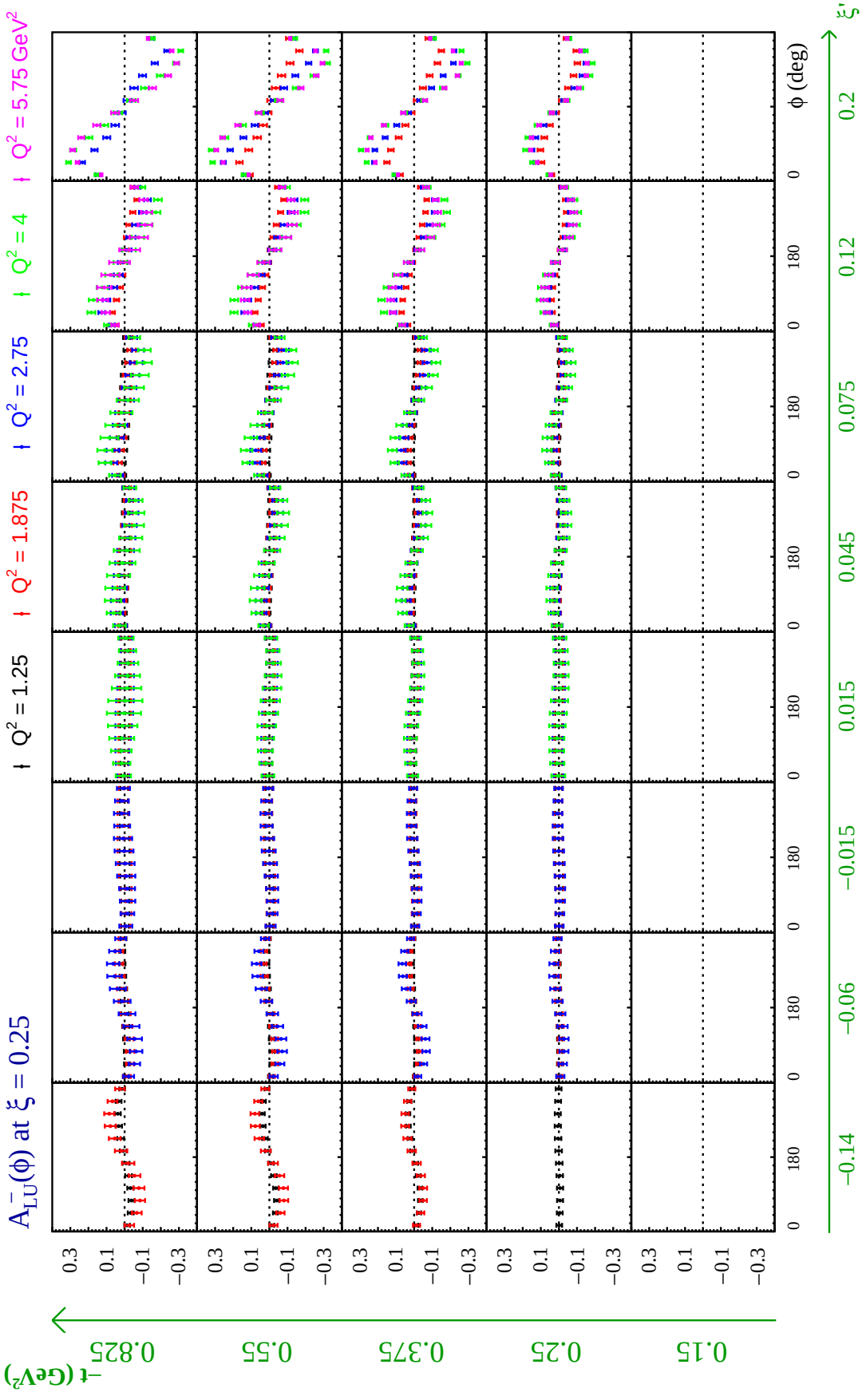

Figure A.10: $A_{\mathrm{LU}}^{-}(\phi)$ at $\xi = 0.25$.

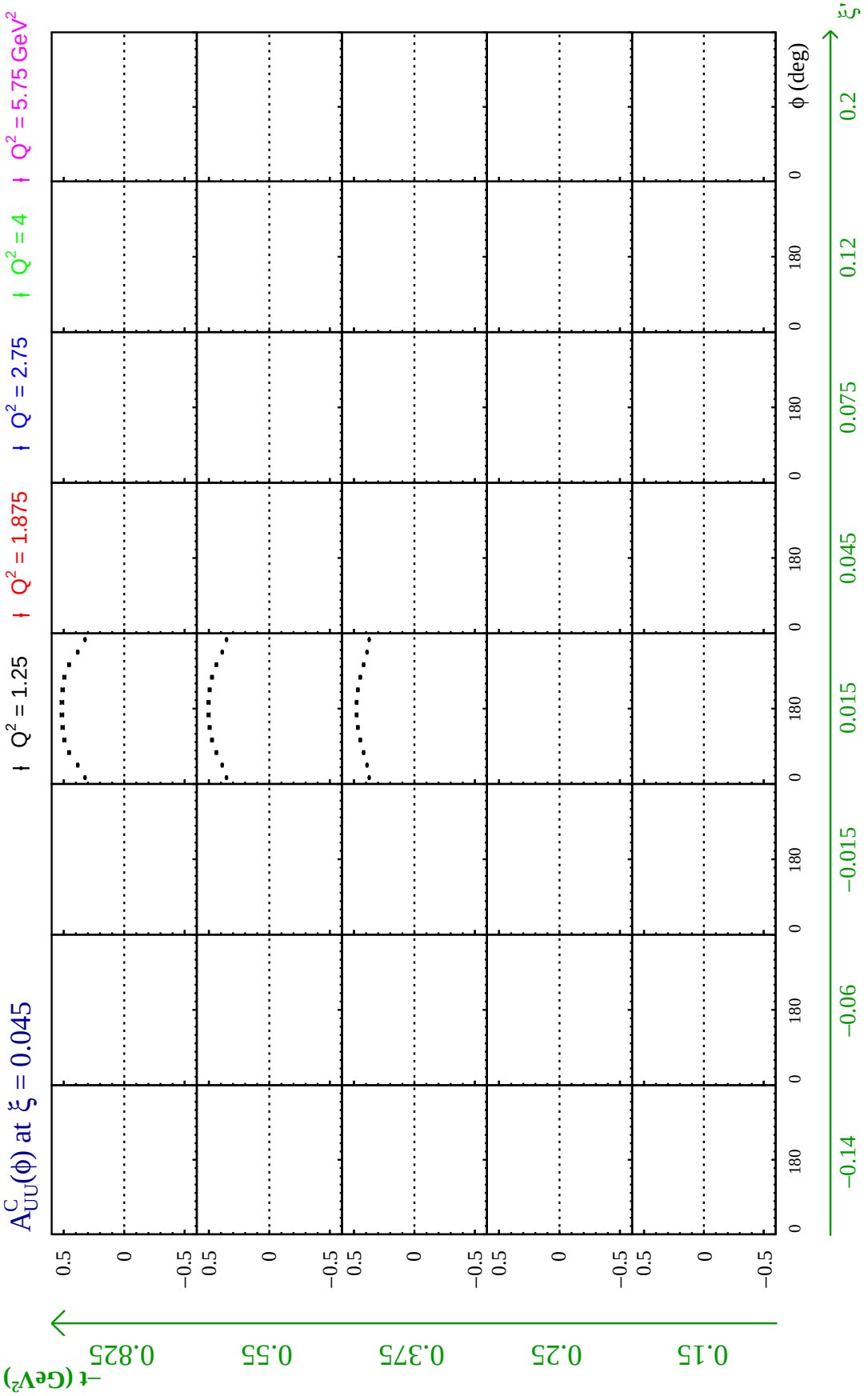

Figure A.11: $A_{UU}^{C}(\phi)$ at $\xi = 0.045$.

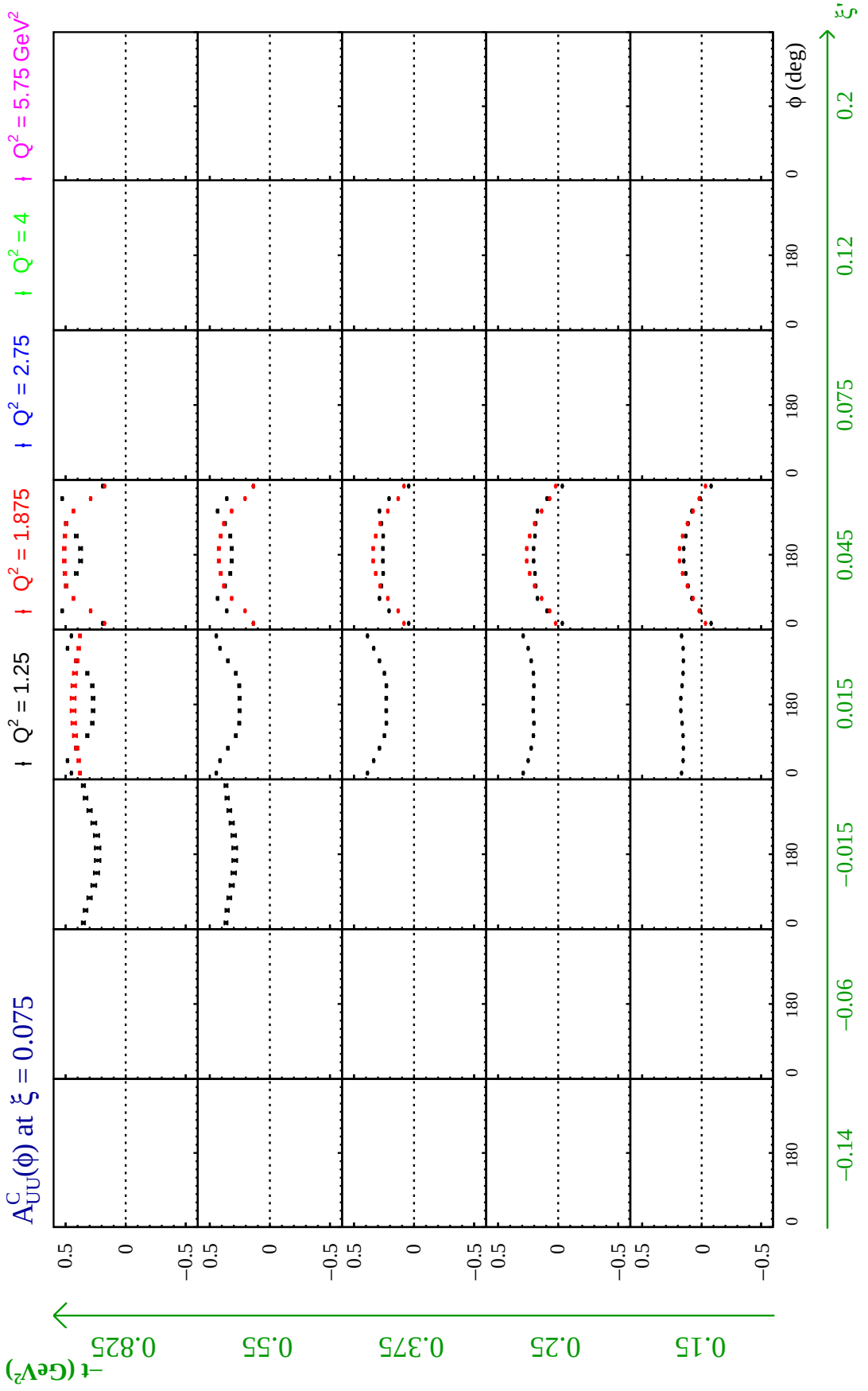

Figure A.12: $A_{UU}^{C}(\phi)$ at $\xi = 0.075$.

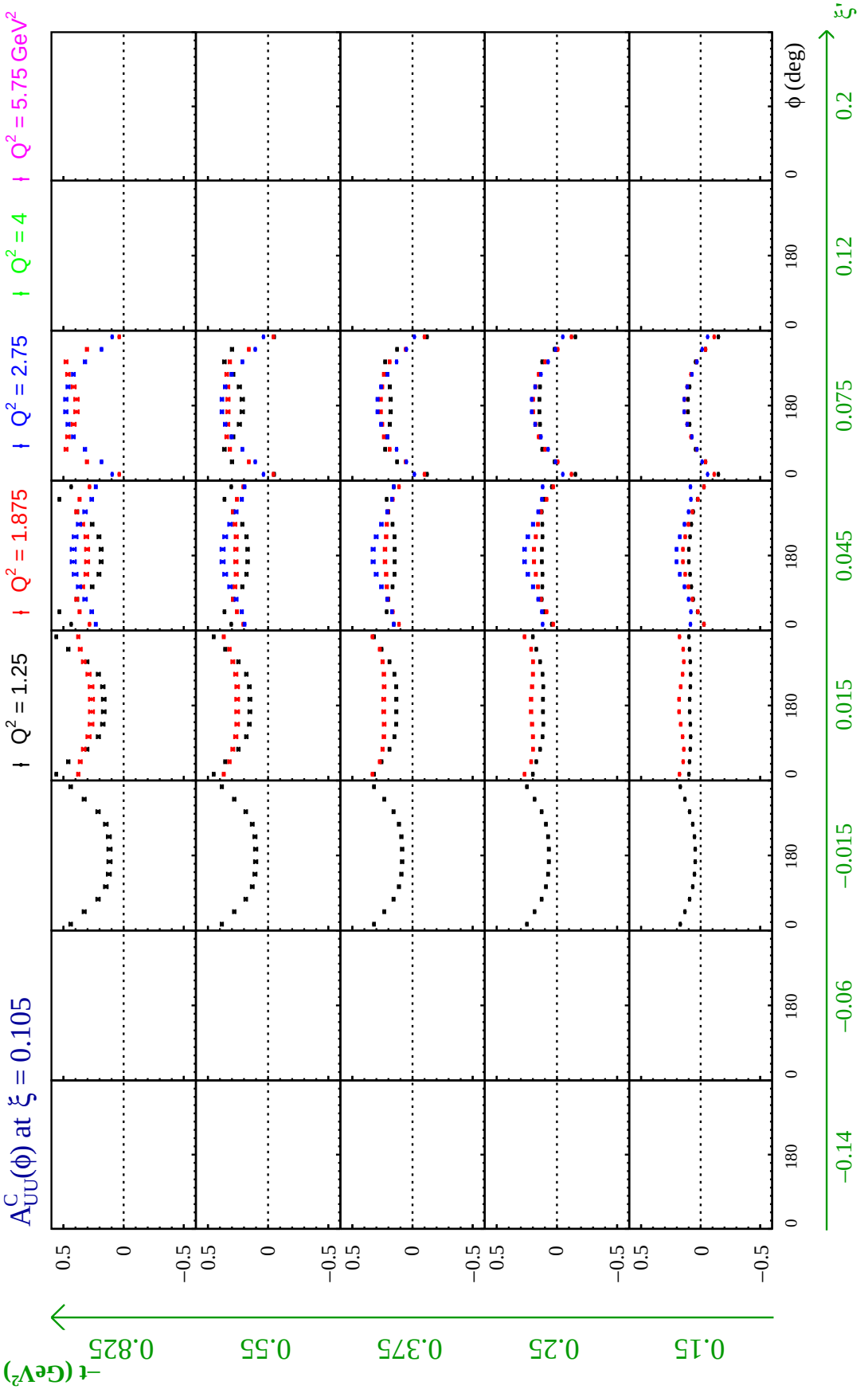

Figure A.13: $A_{UU}^{C}(\phi)$ at $\xi = 0.105$.

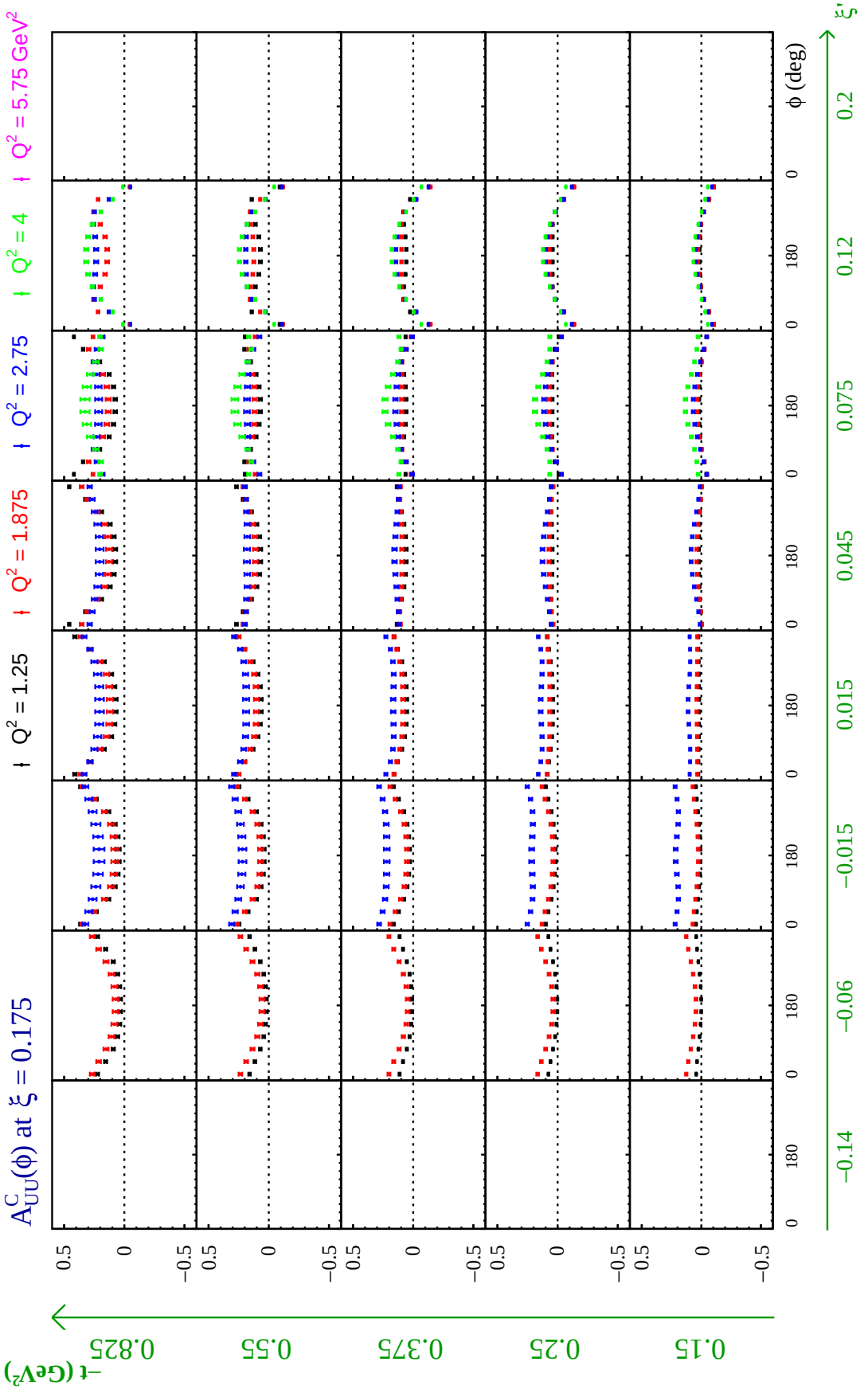

Figure A.14: $A_{UU}^{C}(\phi)$ at $\xi = 0.175$.

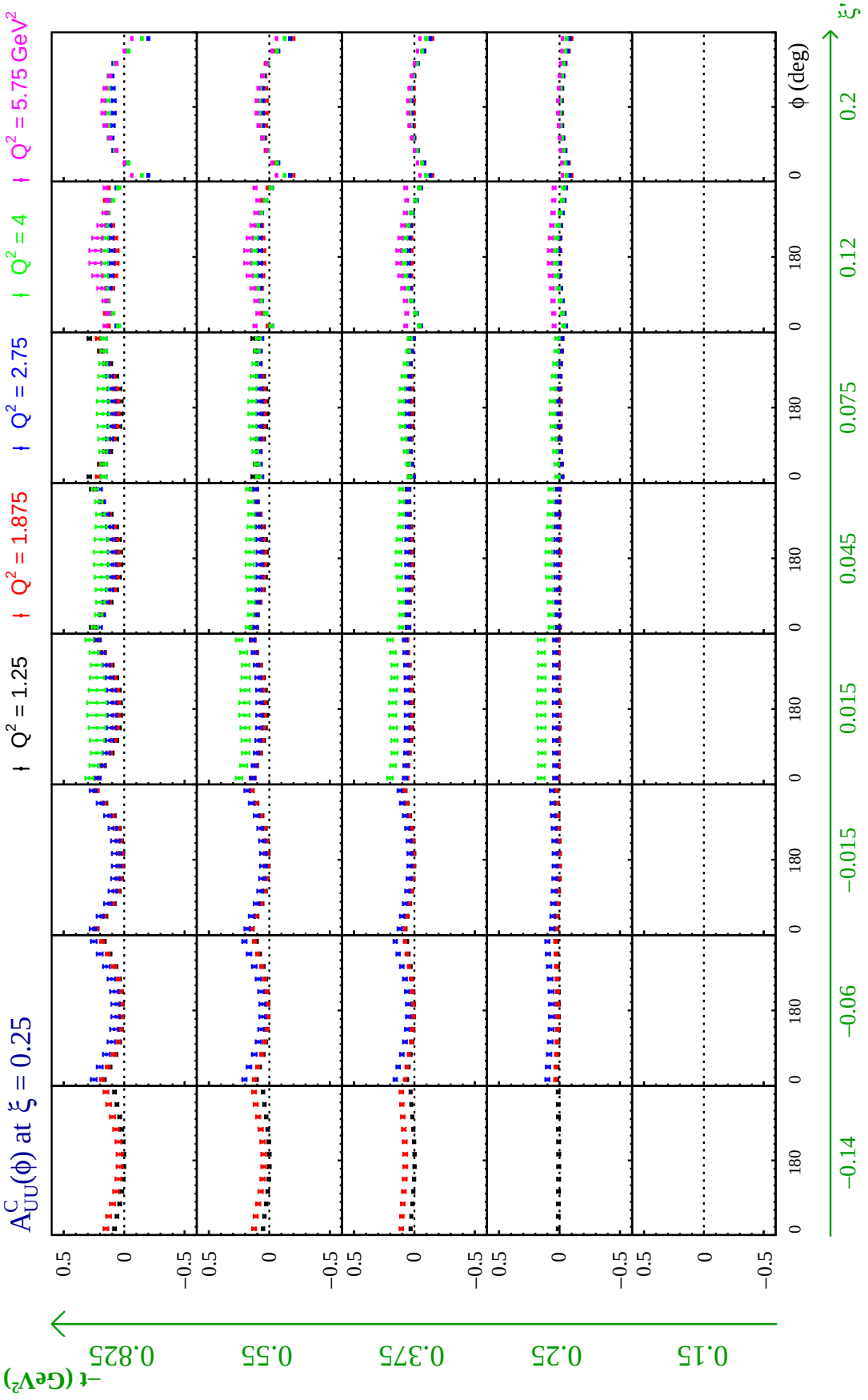

Figure A.15: $A_{UU}^{C}(\phi)$ at $\xi = 0.25$.

Appendix B

Observables with SoLID

With the J/Ψ-μ configuration of SoLID for 50 days, the observables for the covered bins in ξ = 0.045, 0.075, 0.105, 0.135, 0.175 and 0.25 are shown in the following figures. Fig. B.1-B.6 display the expected accuracy of the BSA and Fig. B.7-B.12 display the expected accuracy of the BCA with additional 50 days running of positron beam.

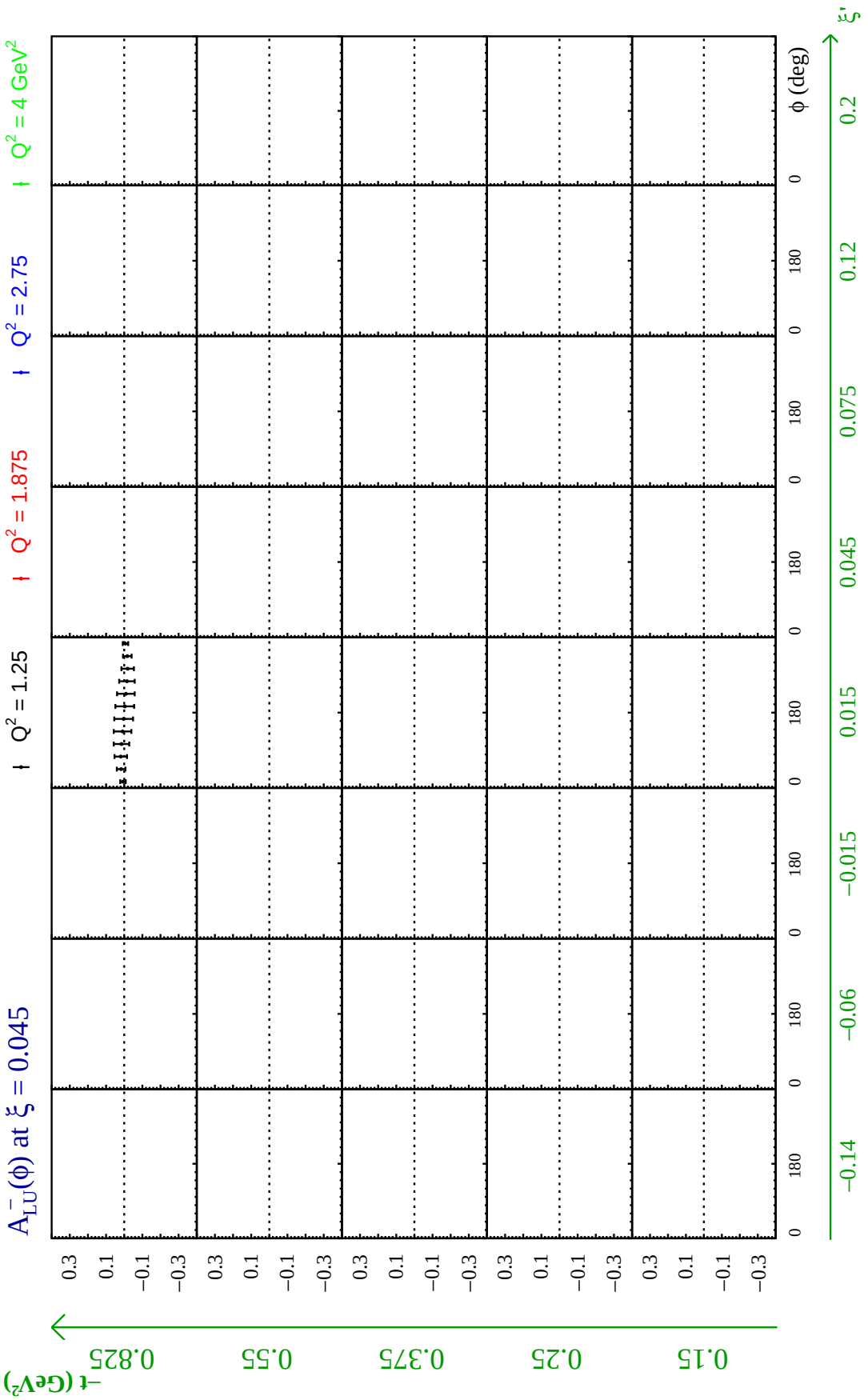

Figure B.1: $A_{\mathrm{LU}}^{-}(\phi)$ at $\xi = 0.045$.

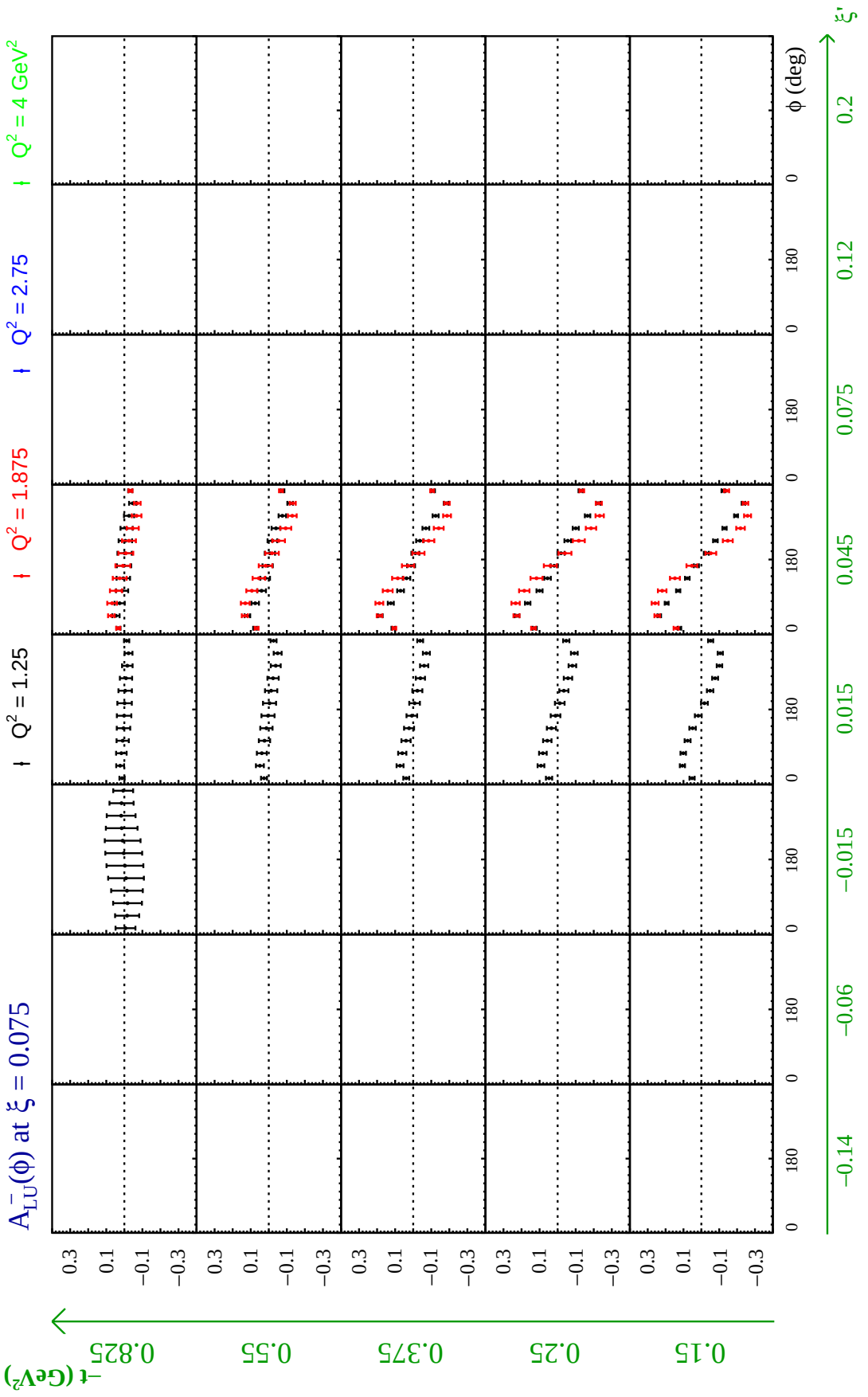

Figure B.2: $A_{\mathrm{LU}}^{-}(\phi)$ at $\xi = 0.075$.

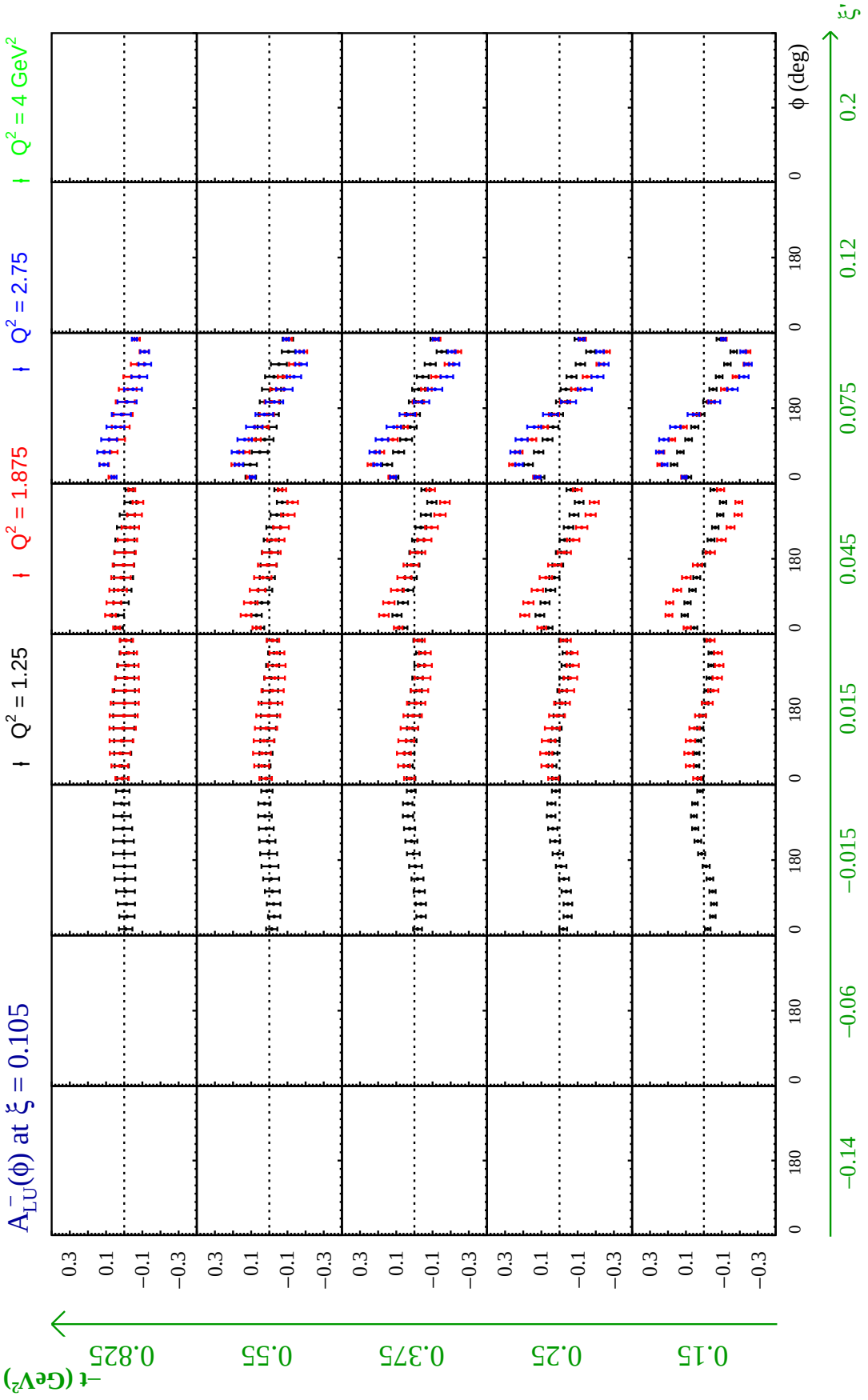

Figure B.3: $A_{LU}^{-}(\phi)$ at $\xi = 0.105$.

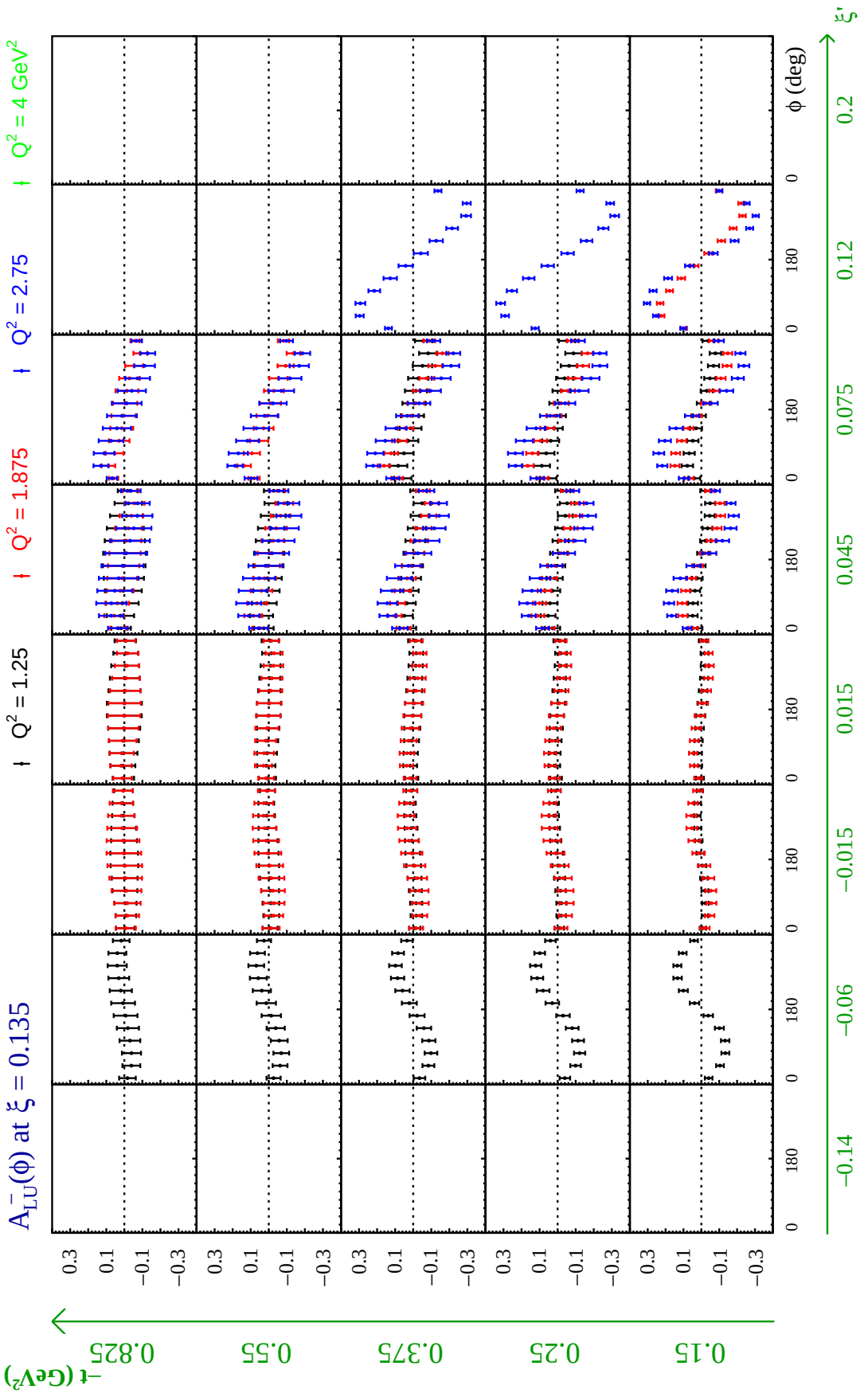

Figure B.4: $A_{\mathrm{LU}}^{-}(\phi)$ at $\xi = 0.135$.

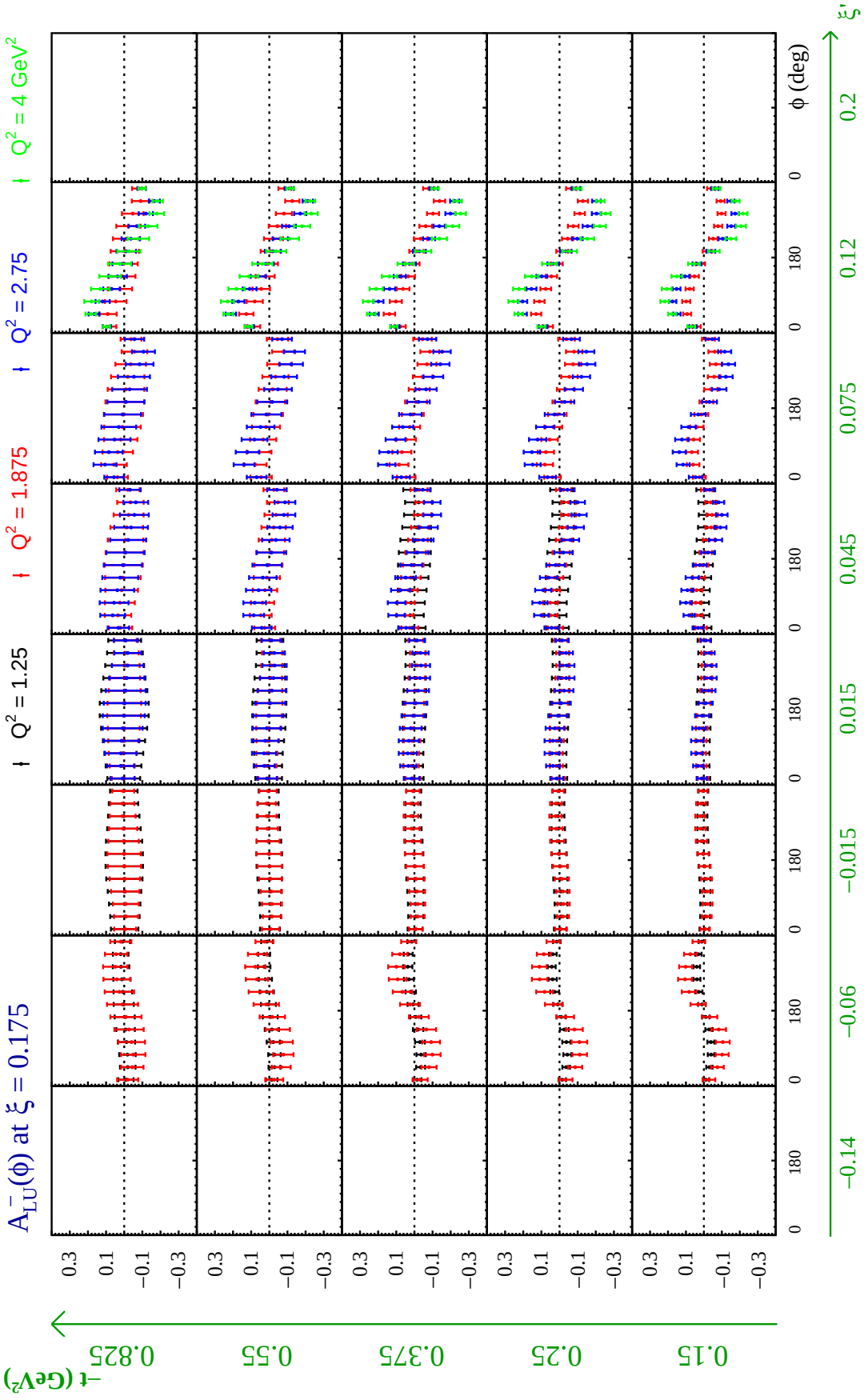

Figure B.5: $A_{LU}^{-}(\phi)$ at $\xi = 0.175$.

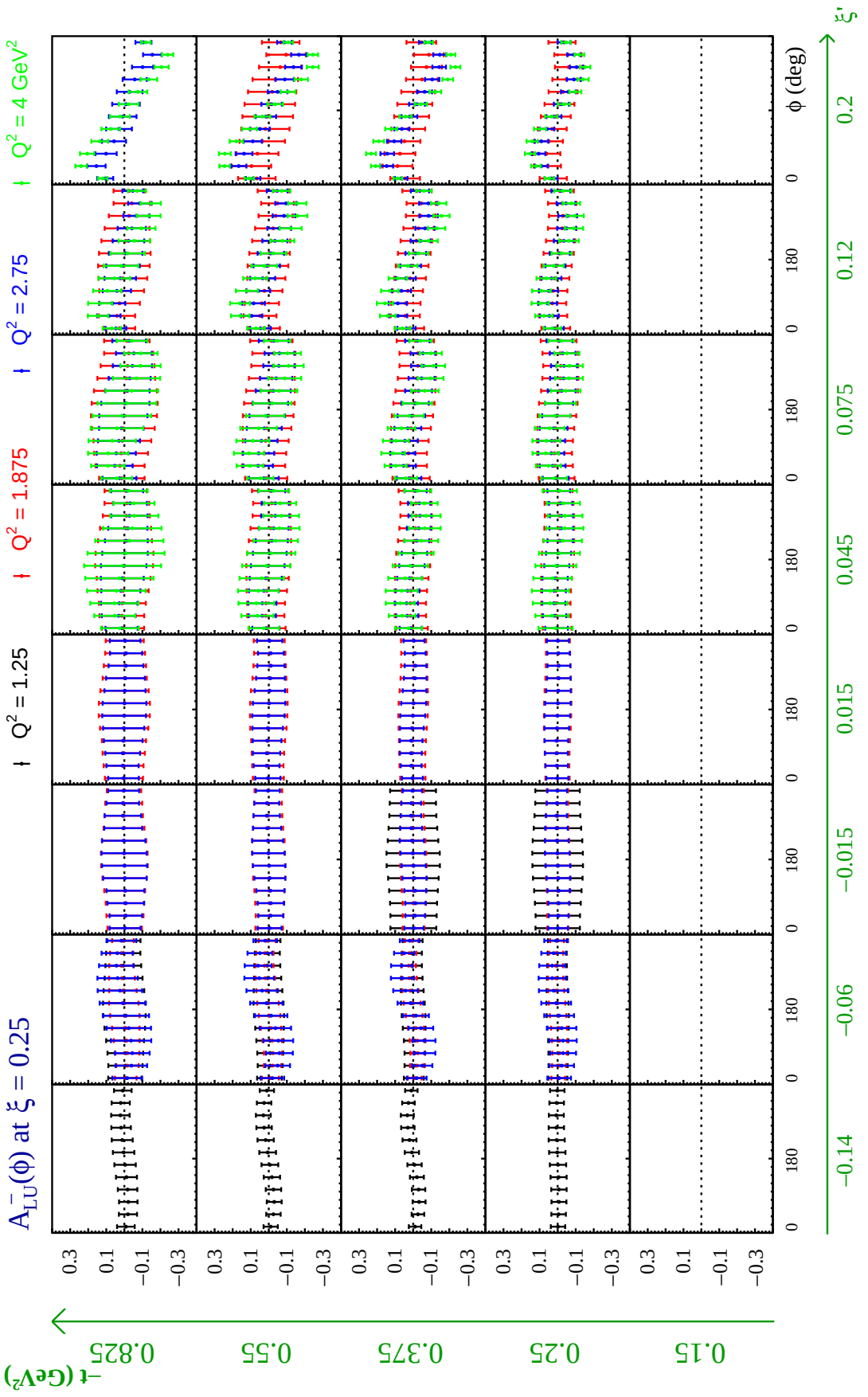

Figure B.6: $A_{\mathrm{LU}}^{-}(\phi)$ at $\xi = 0.25$.

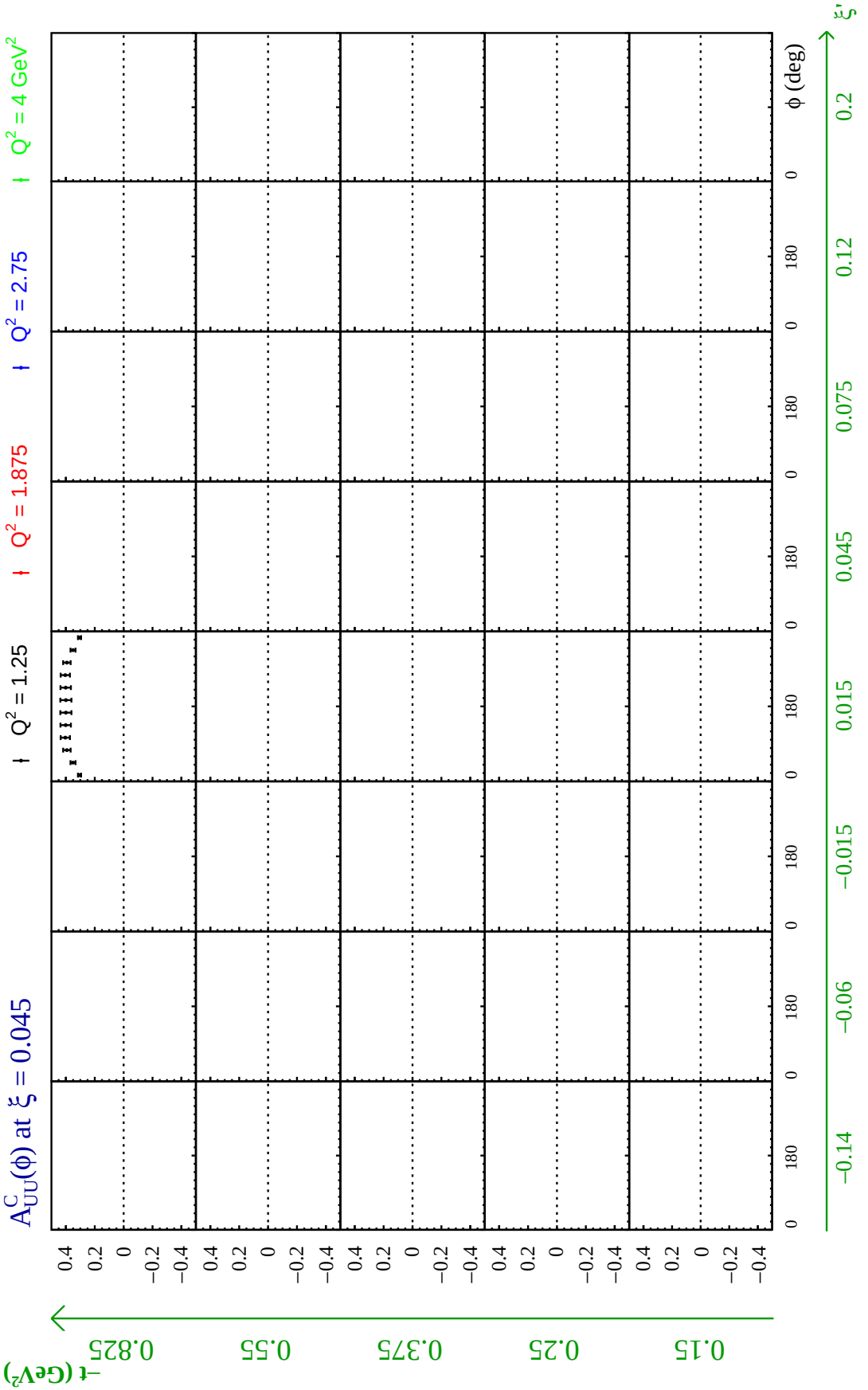

Figure B.7: $A_{\mathrm{UU}}^{\mathrm{C}}(\phi)$ at $\xi = 0.045$.

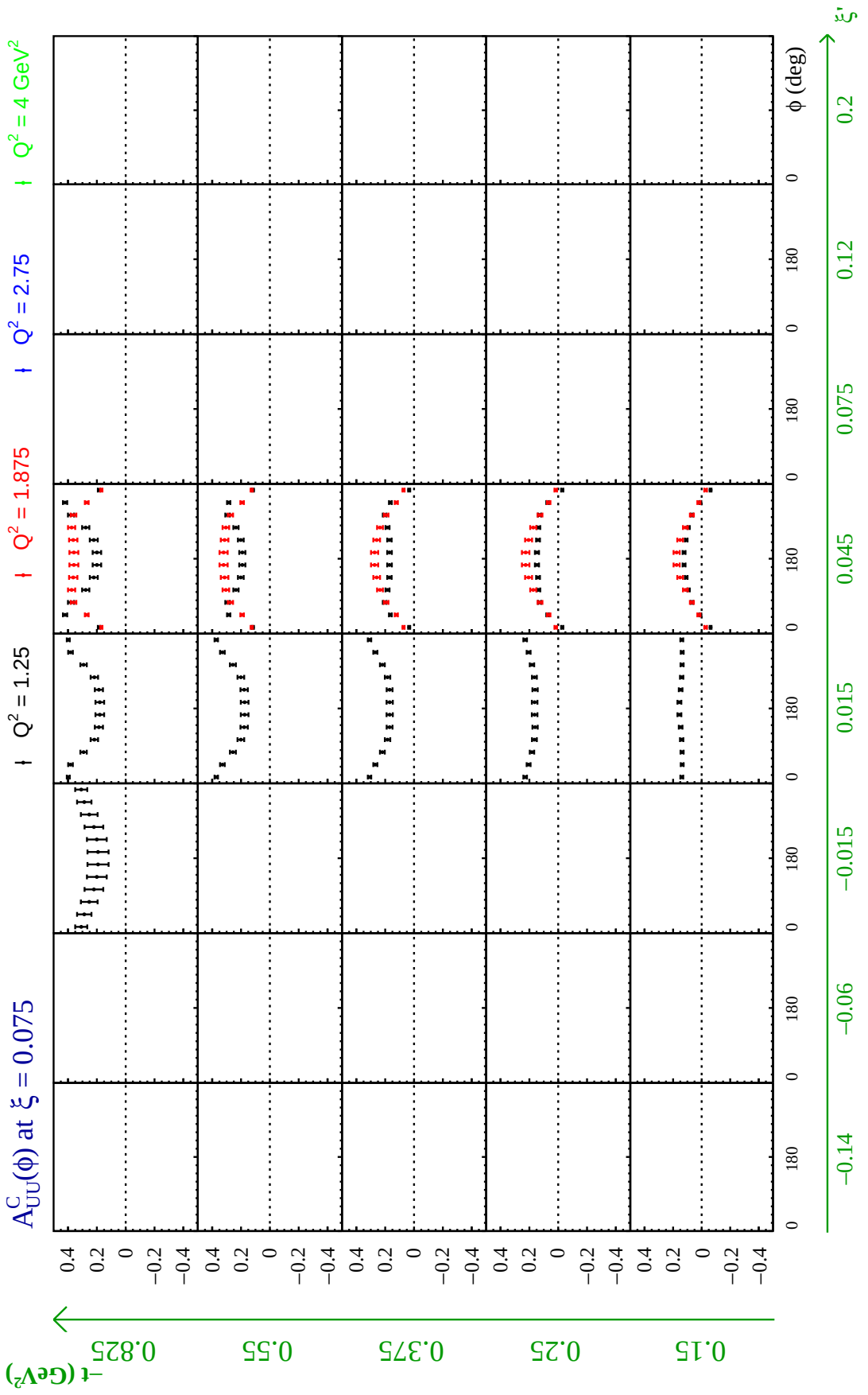

Figure B.8: $A_{\mathrm{UU}}^{\mathrm{C}}(\phi)$ at $\xi = 0.075$.

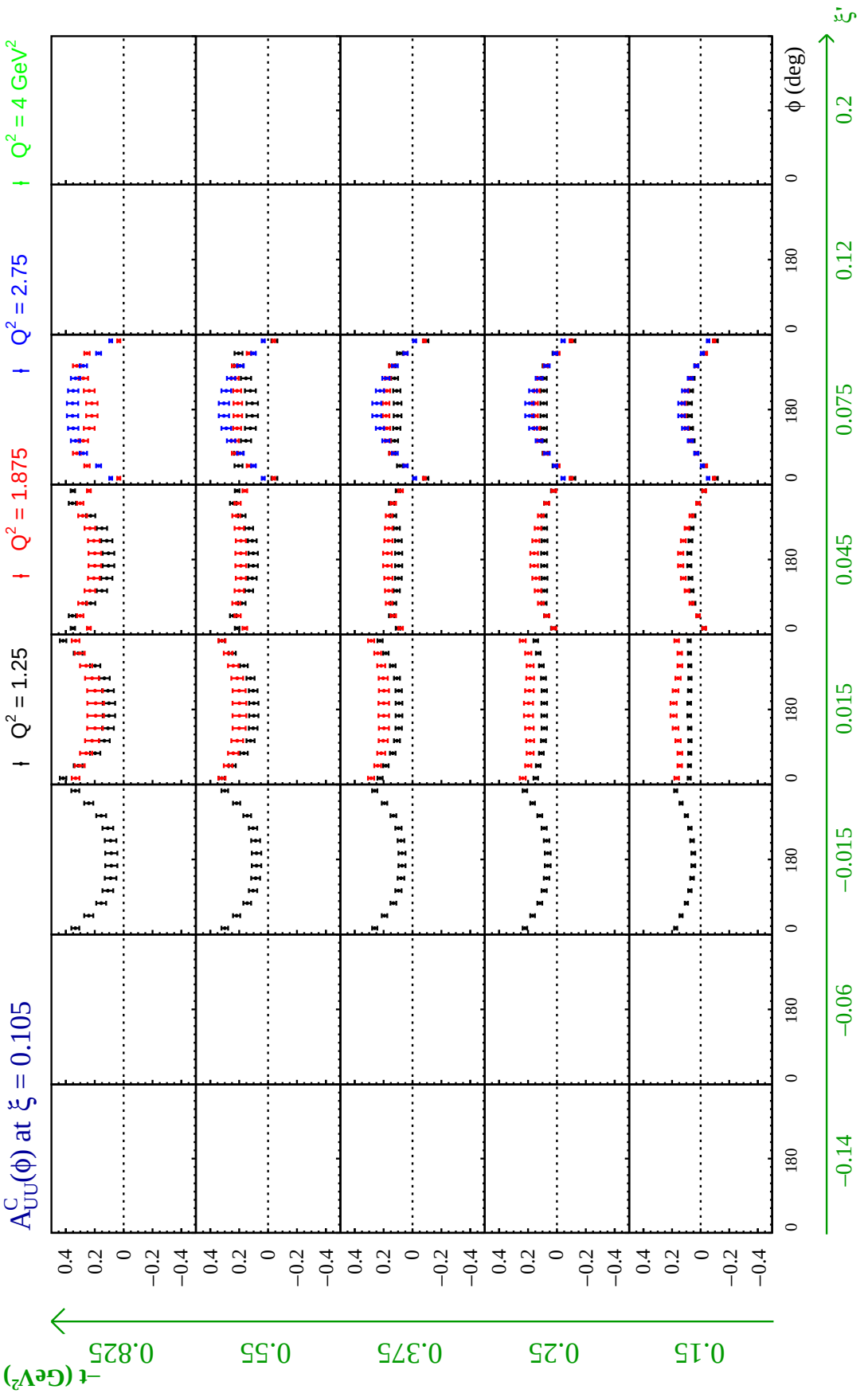

Figure B.9: $A_{UU}^{C}(\phi)$ at $\xi = 0.105$.

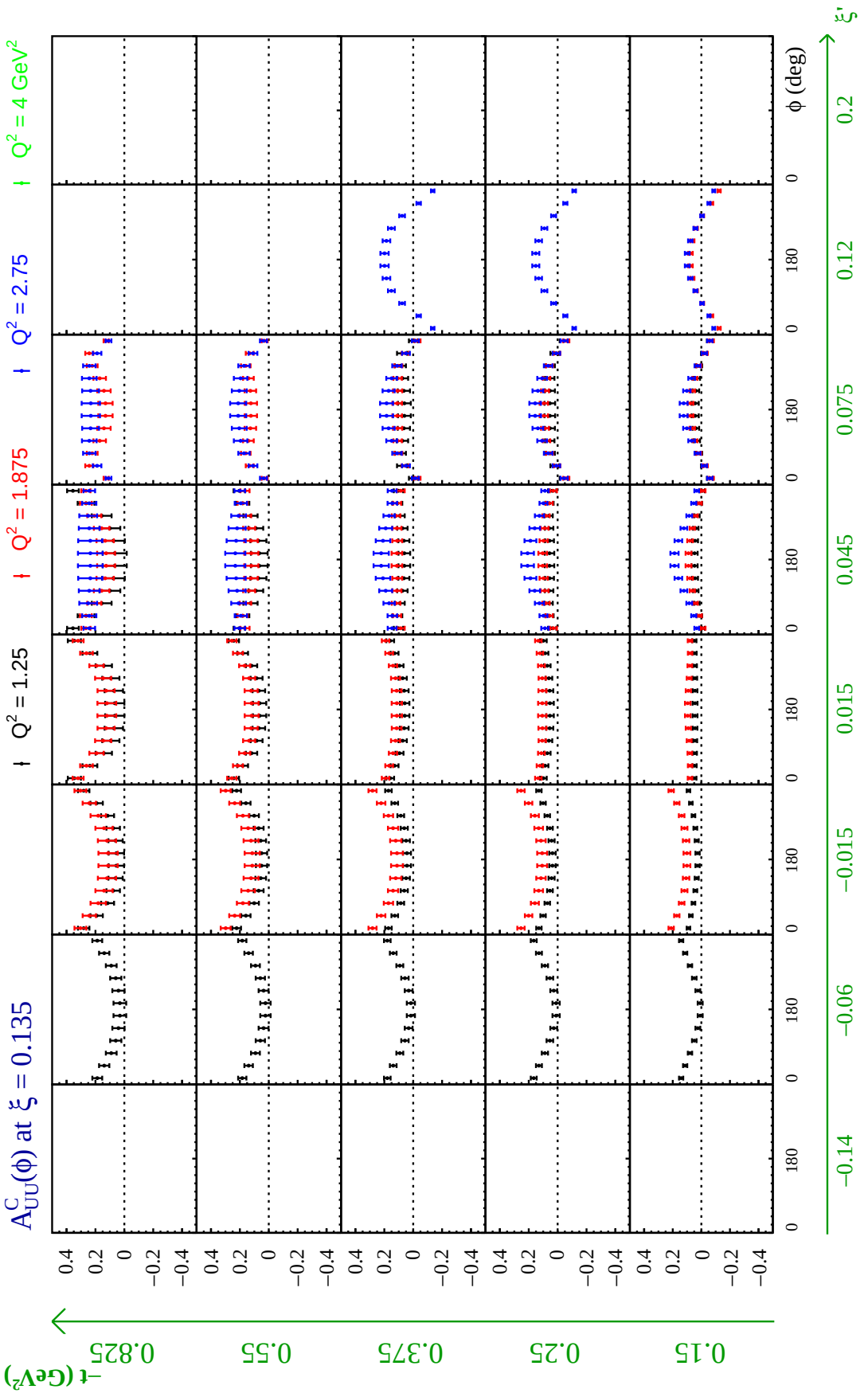

Figure B.10: $A_{UU}^{C}(\phi)$ at $\xi = 0.135$.

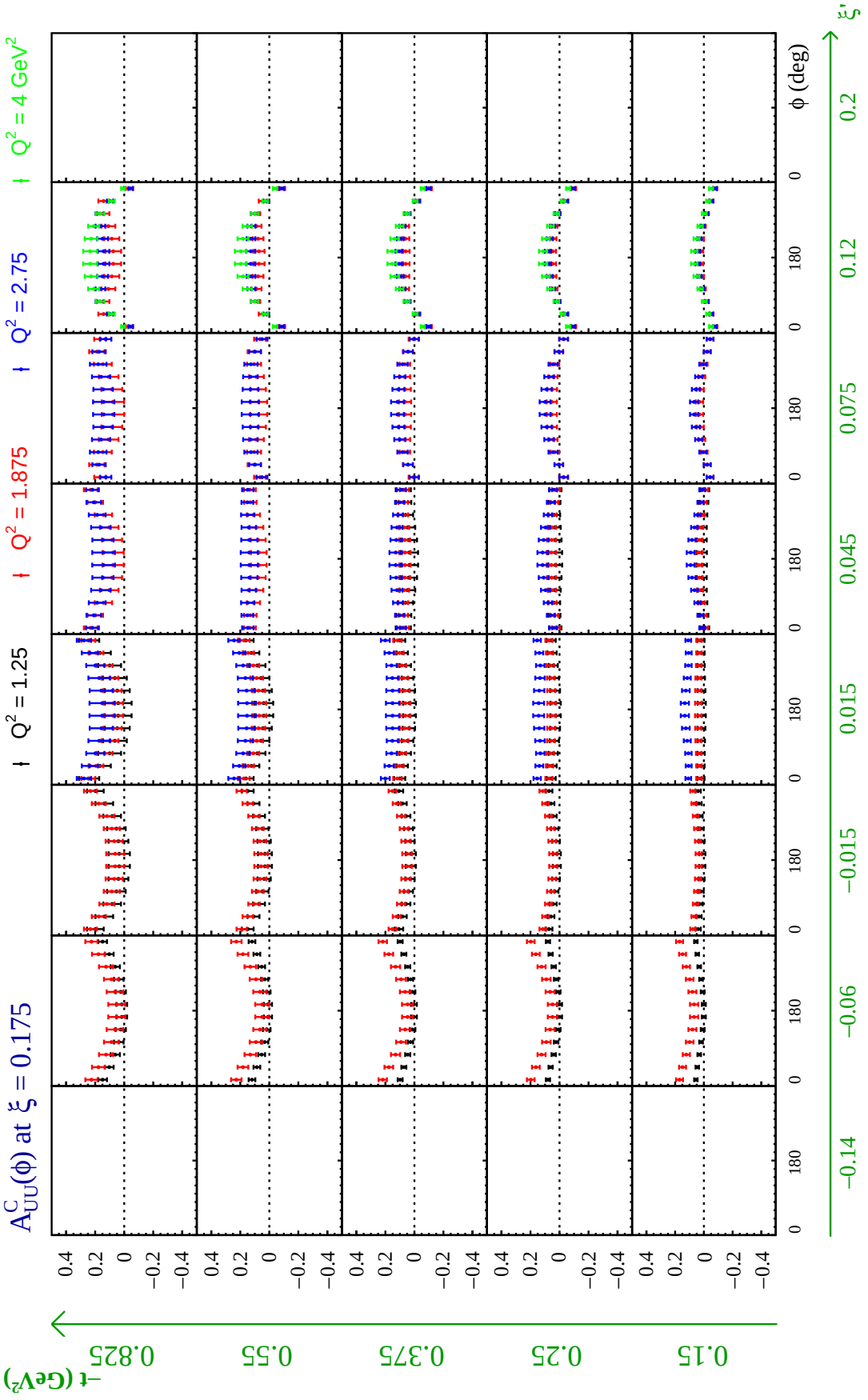

Figure B.11: $A_{UU}^{C}(\phi)$ at $\xi = 0.175$.

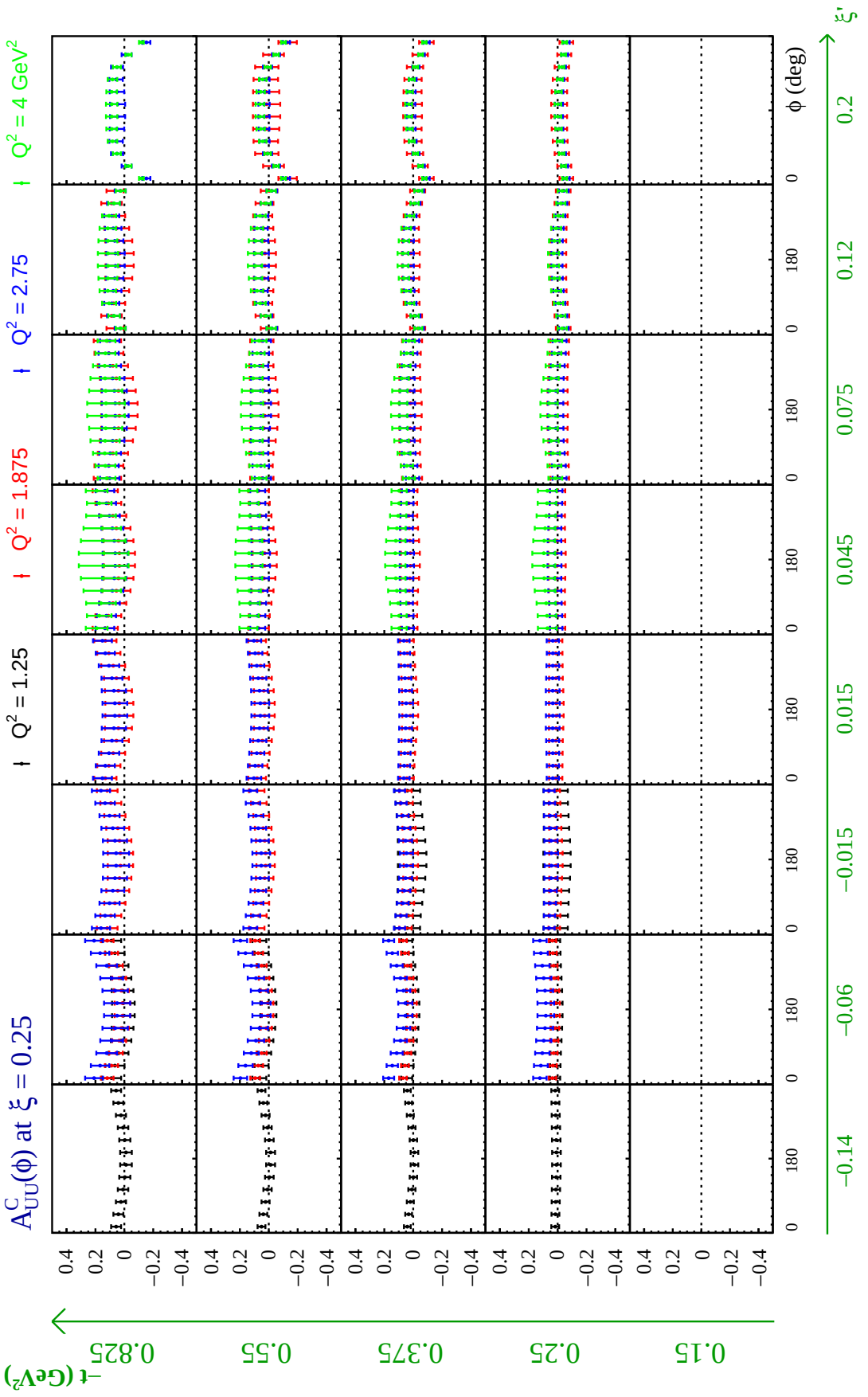

Figure B.12: $A_{UU}^{C}(\phi)$ at $\xi = 0.25$.

Appendix C

Extracted linear CFFs combinations

The linear CFFs combinations as functions of ξ' extracted from the covered bins are shown in the following figures for $\xi = 0.045,\ 0.075,\ 0.105,\ 0.135,\ 0.175$ and 0.25. Fig. C.1-C.6 display the expected accuracy of the extracted imaginary part of linear CFFs combination

$$\mathcal{C}_{\mathrm{LU}}^{\mathrm{INT}} = F_1\mathcal{H} + \xi'(F_1 + F_2)\widetilde{\mathcal{H}} - \frac{t}{4M^2}F_2\mathcal{E}, \tag{C.1}$$

and Fig. C.7-C.12 display the expected accuracy of extracted real part of linear CFFs combination

$$\mathcal{C}_{\mathrm{UU}}^{\mathrm{INT}} = \frac{\xi'}{\xi}\left(F_1\mathcal{H} - \frac{t}{4M^2}F_2\mathcal{E}\right) + \xi(F_1 + F_2)\widetilde{\mathcal{H}}. \tag{C.2}$$

The results of $\mathrm{Im}\{\mathcal{C}_{\mathrm{LU}}^{\mathrm{INT}}\}$ are extracted from $\Delta\sigma_{\mathrm{LU}}^{-}$, based on the pseudo-data in the ideal situation at $\mathcal{L} = 10^{37}\ \mathrm{cm}^{-2}\cdot\mathrm{s}^{-1}$ for 50 days running of polarized electron beam, while the results of $\mathrm{Re}\{\mathcal{C}_{\mathrm{UU}}^{\mathrm{INT}}\}$ are extracted from $\Delta\sigma_{\mathrm{UU}}^{\mathrm{C}}$, based on the pseudo-data in the ideal situation at $\mathcal{L} = 10^{37}\ \mathrm{cm}^{-2}\cdot\mathrm{s}^{-1}$ for additional 50 days running of unpolarized positron beam.

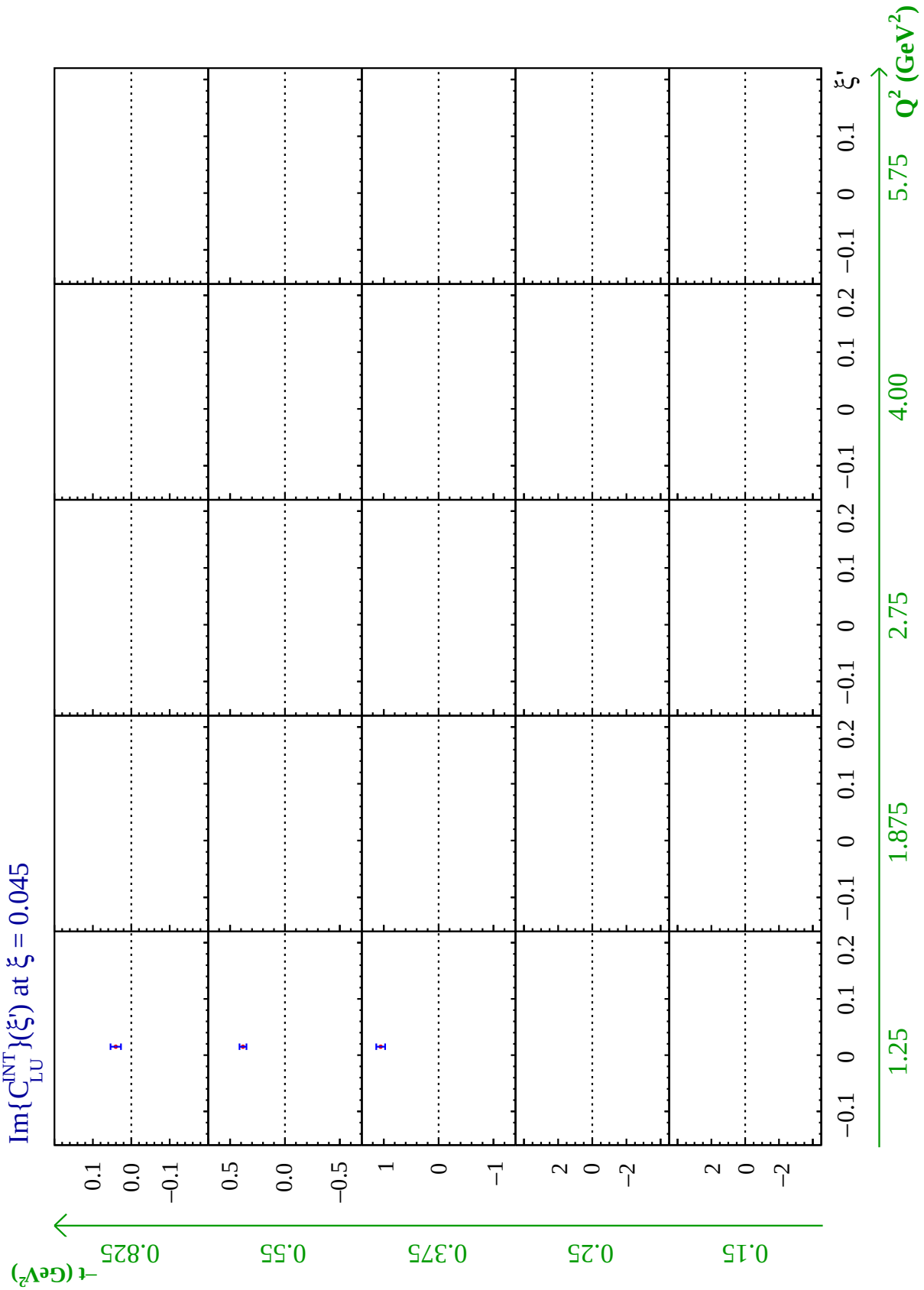

Figure C.1: $\mathrm{Im}\{\mathcal{C}_{\mathrm{LU}}^{\mathrm{INT}}\}(\xi')$ at $\xi = 0.045$.

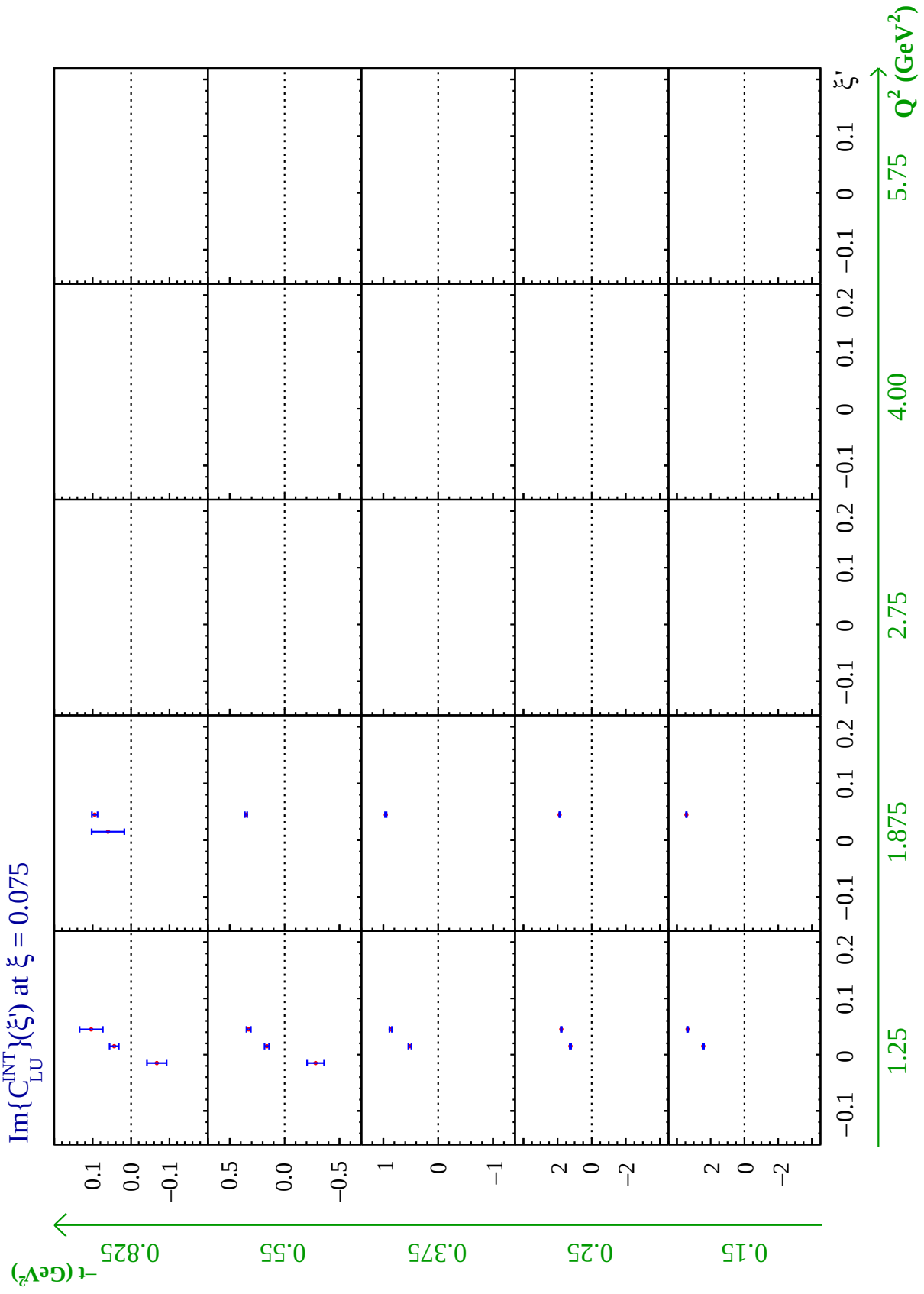

Figure C.2: $\mathrm{Im}\{\mathcal{C}_{\mathrm{LU}}^{\mathrm{INT}}\}(\xi')$ at $\xi = 0.075$.

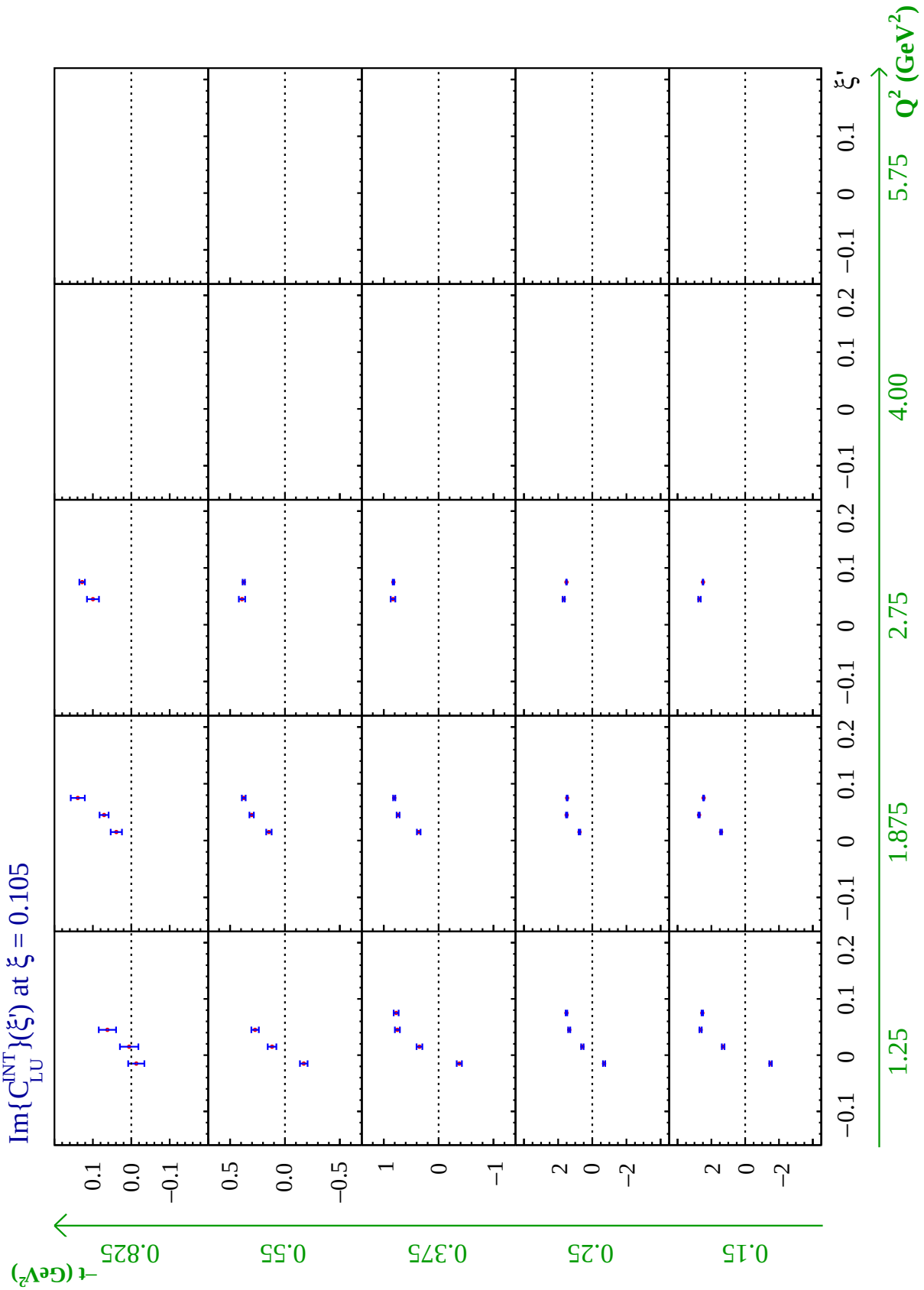

Figure C.3: $\mathrm{Im}\{\mathcal{C}^{\mathrm{INT}}_{\mathrm{LU}}\}(\xi')$ at $\xi = 0.105$.

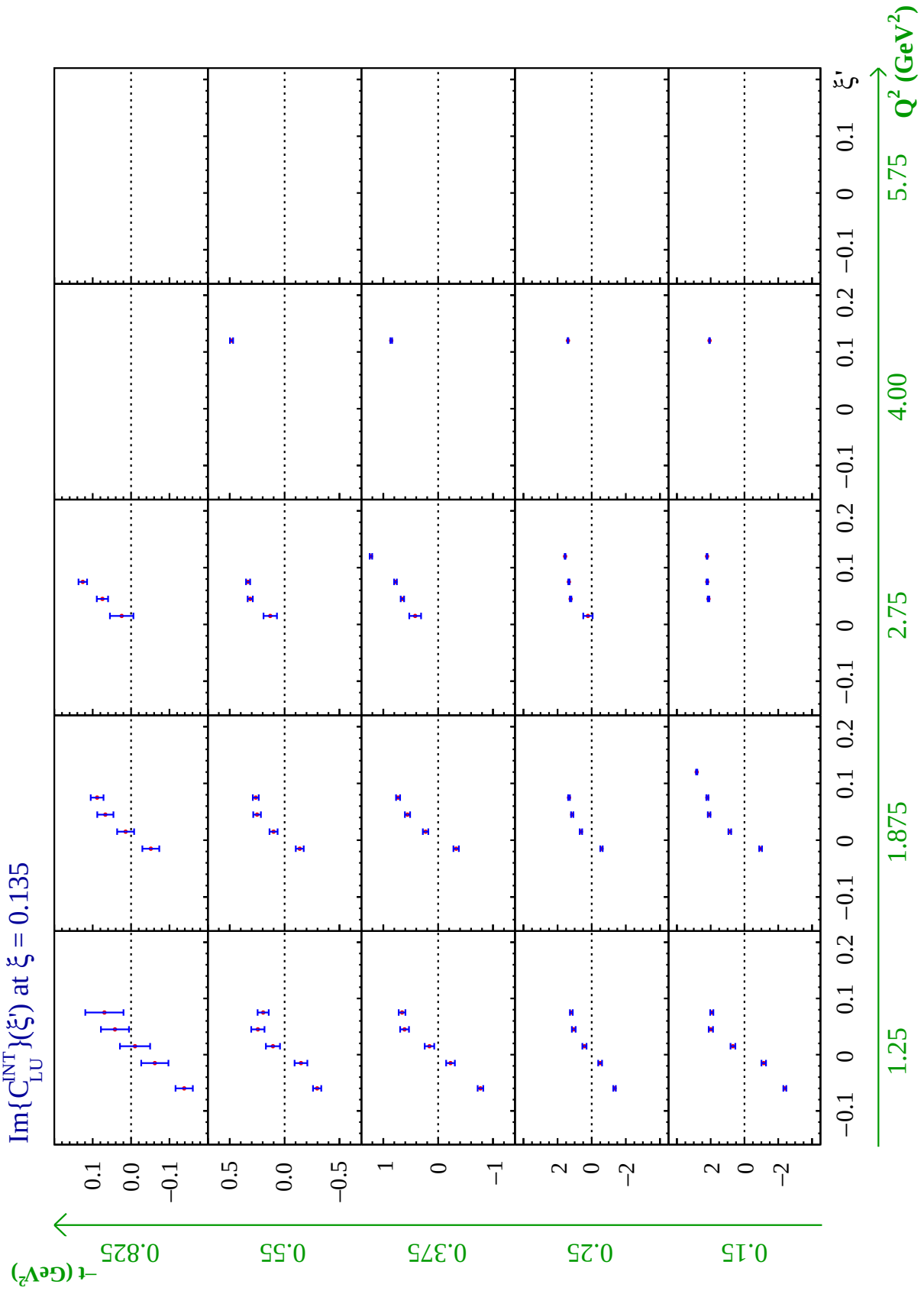

Figure C.4: $\mathrm{Im}\{\mathcal{C}_{\mathrm{LU}}^{\mathrm{INT}}\}(\xi')$ at $\xi = 0.135$.

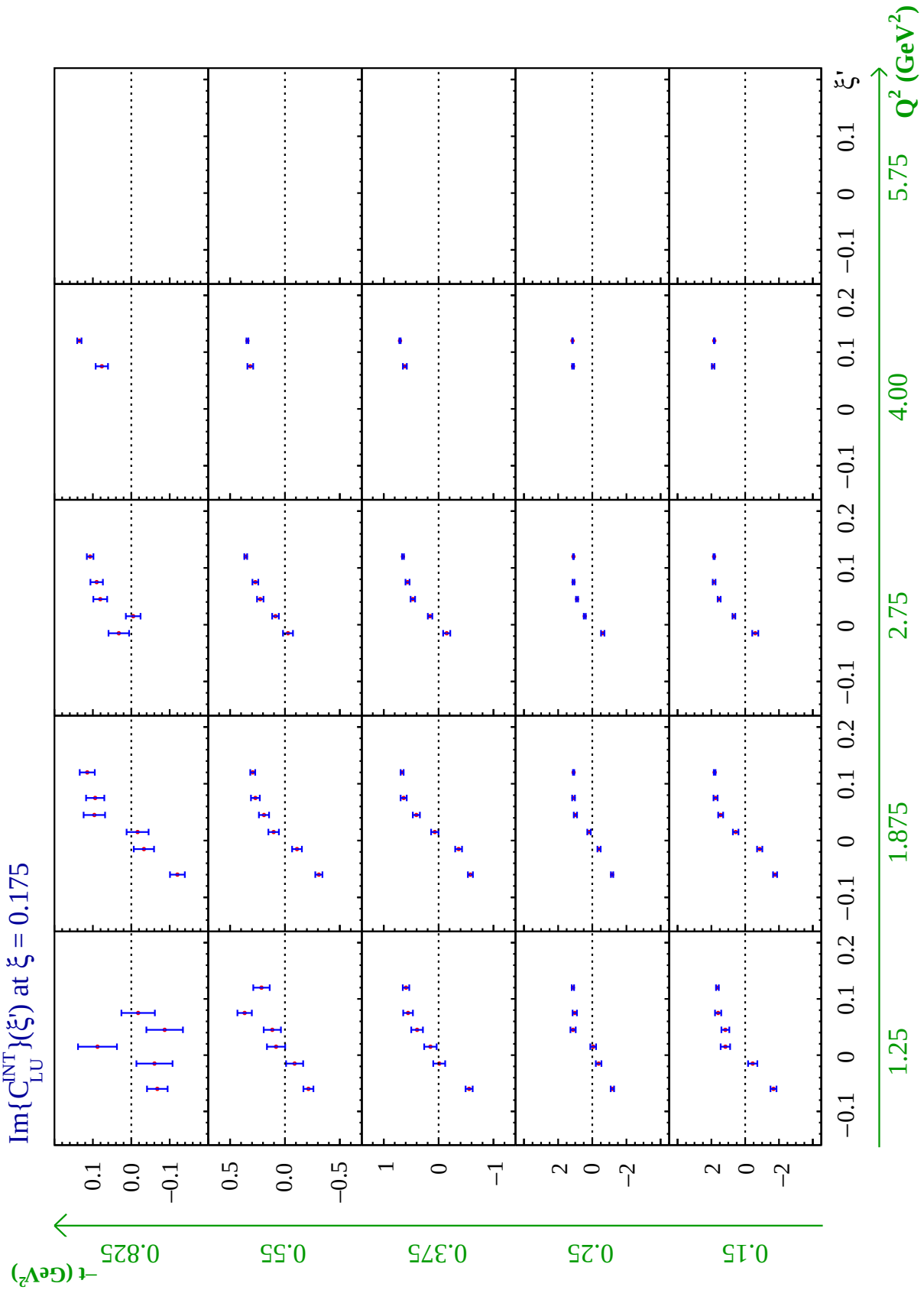

Figure C.5: $\mathrm{Im}\{\mathcal{C}_{\mathrm{LU}}^{\mathrm{INT}}\}(\xi')$ at $\xi = 0.175$.

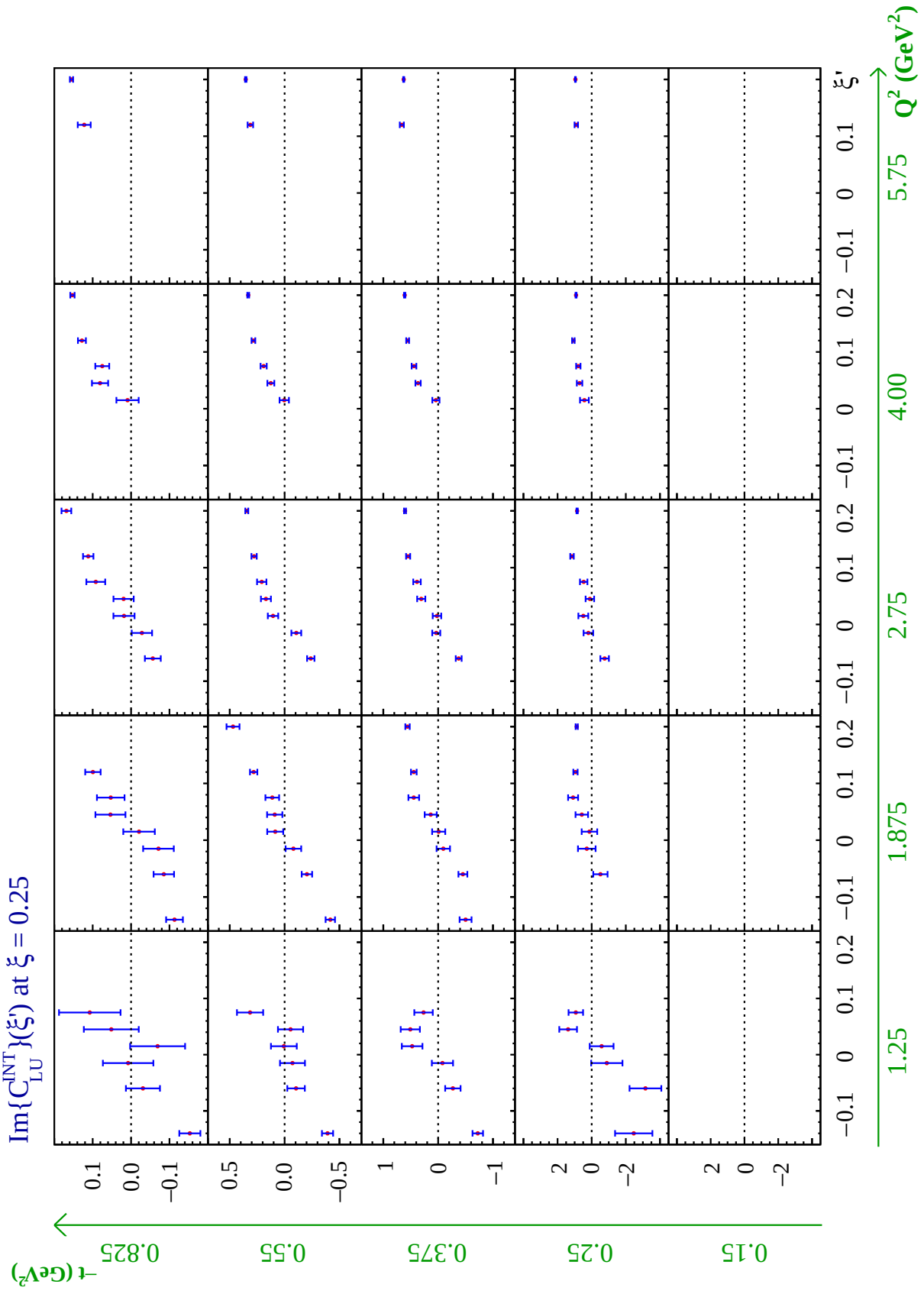

Figure C.6: $\mathrm{Im}\{\mathcal{C}_{\mathrm{LU}}^{\mathrm{INT}}\}(\xi')$ at $\xi = 0.25$.

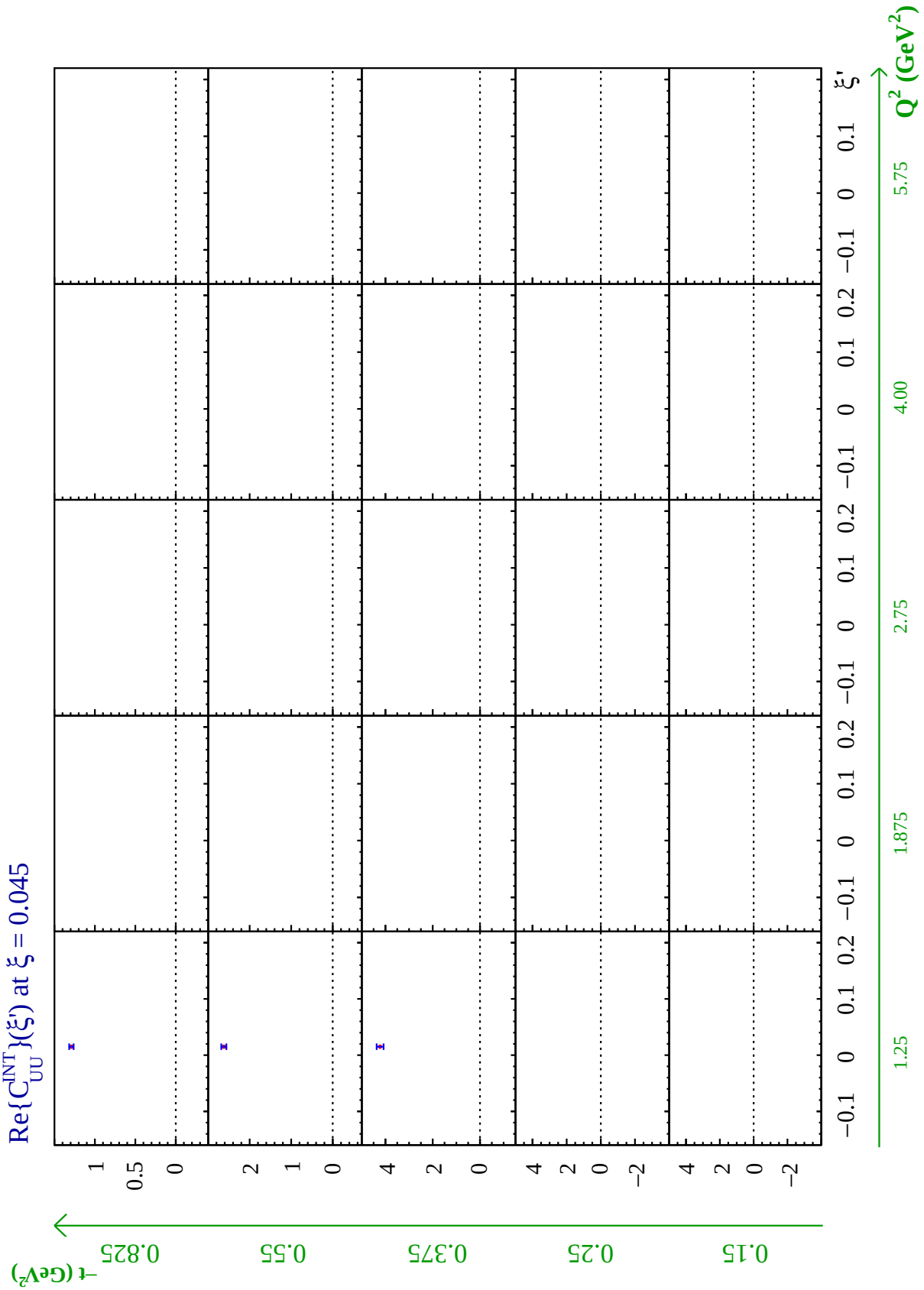

Figure C.7: $\mathrm{Re}\{\mathcal{C}_{\mathrm{UU}}^{\mathrm{INT}}\}(\xi')$ at $\xi = 0.045$.

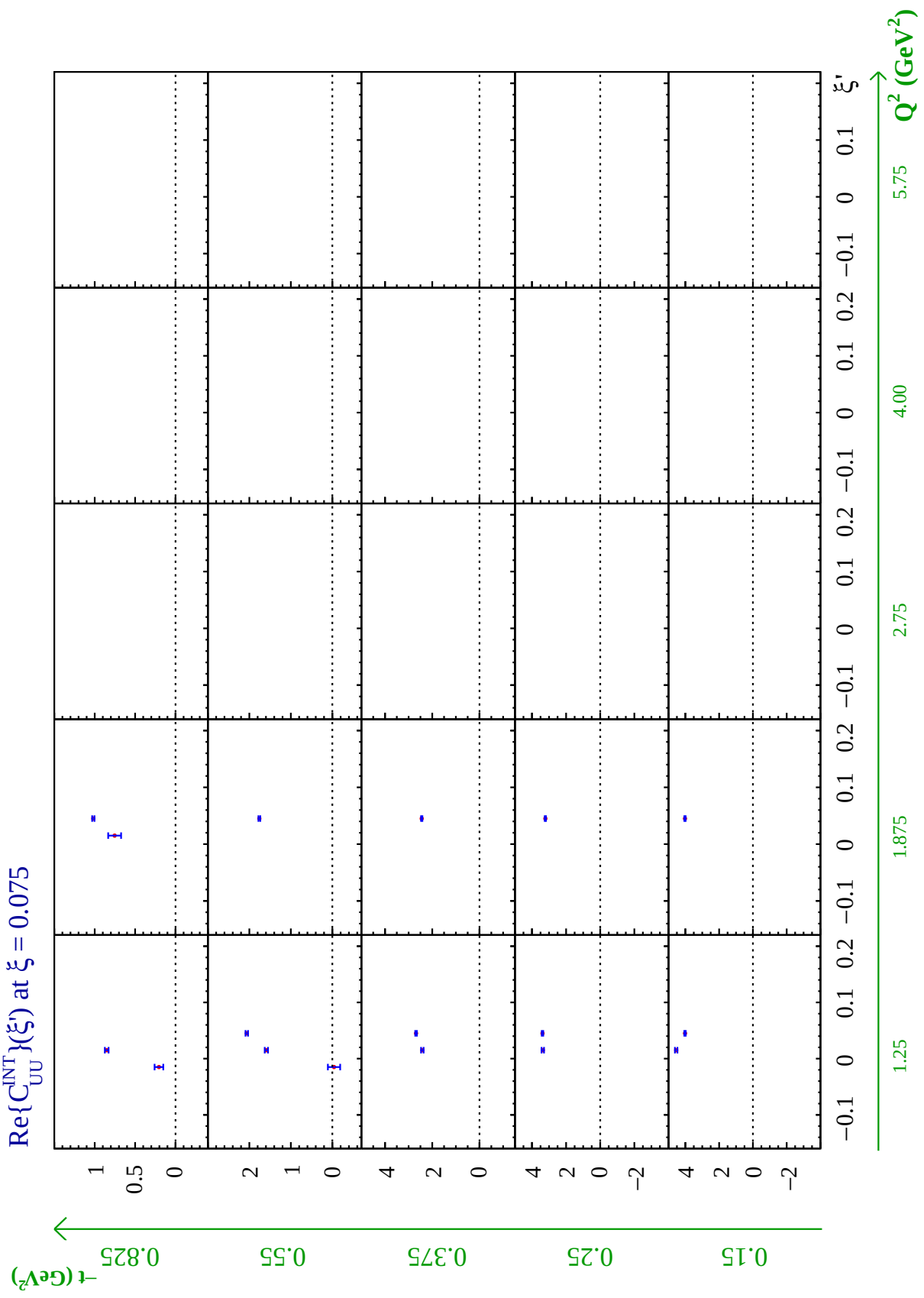

Figure C.8: $\mathrm{Re}\{\mathcal{C}_{\mathrm{UU}}^{\mathrm{INT}}\}(\xi')$ at $\xi = 0.075$.

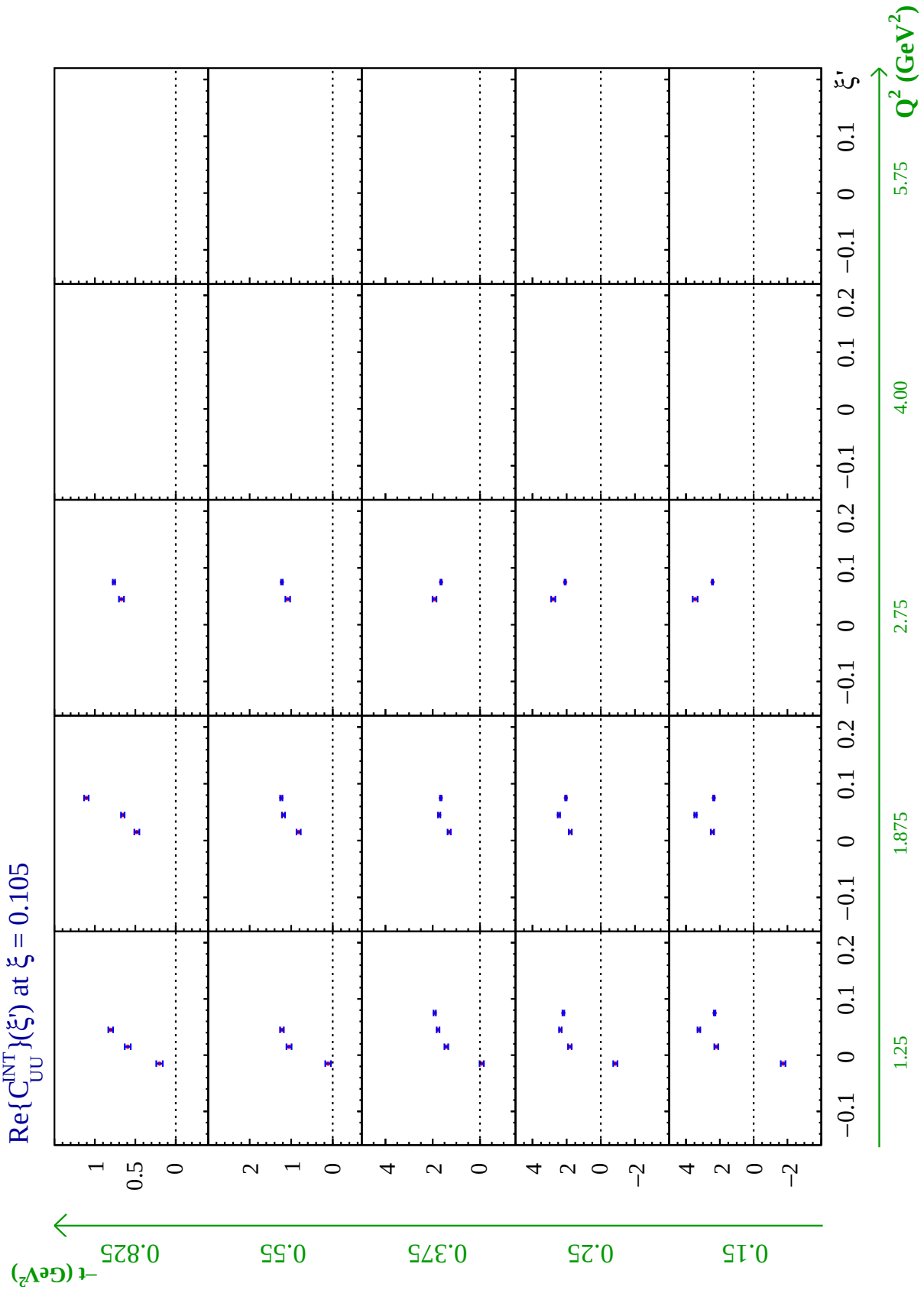

Figure C.9: $\mathrm{Re}\{\mathcal{C}_{\mathrm{UU}}^{\mathrm{INT}}\}(\xi')$ at $\xi = 0.105$.

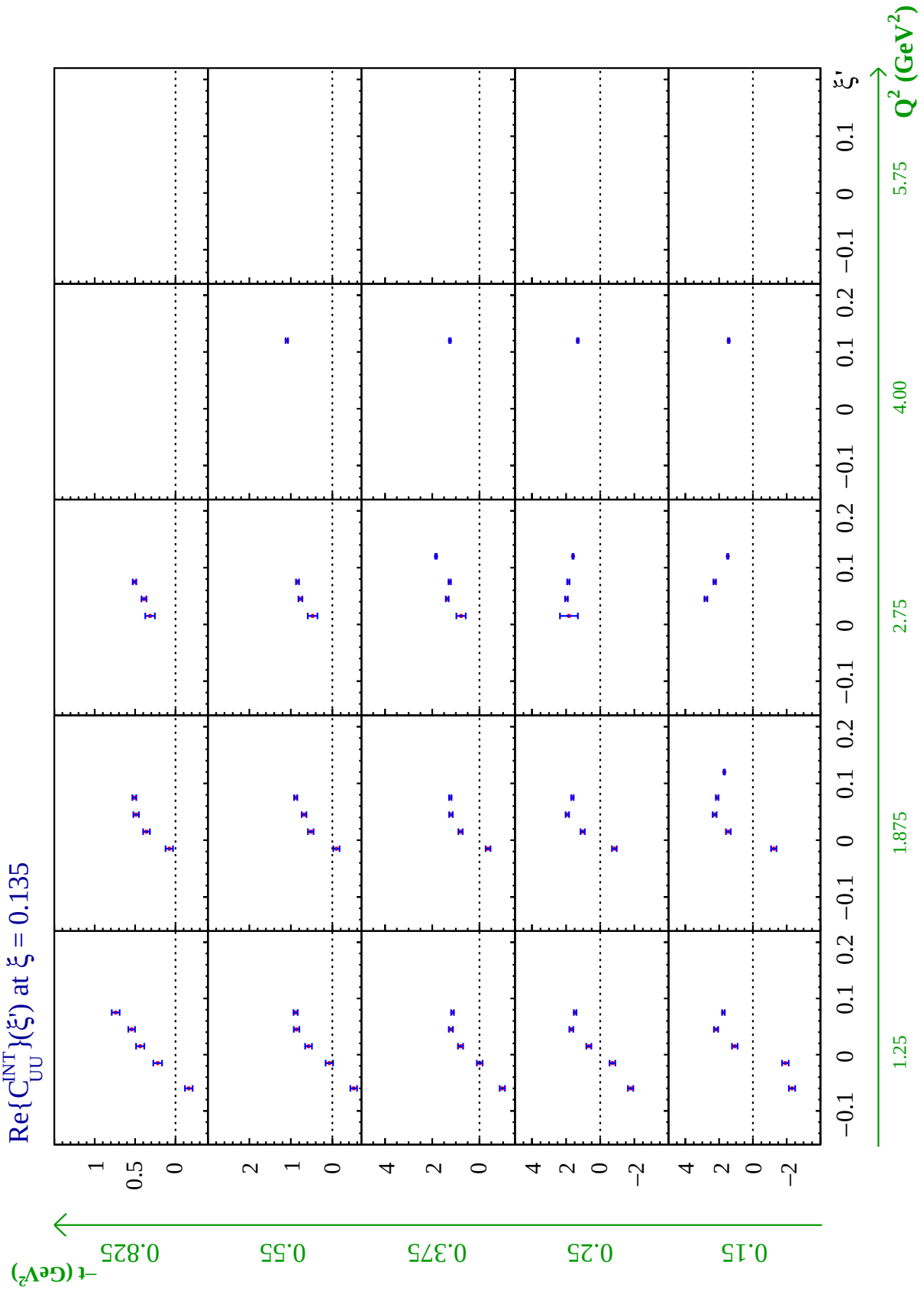

Figure C.10: $\mathrm{Re}\{\mathcal{C}_{\mathrm{UU}}^{\mathrm{INT}}\}(\xi')$ at $\xi = 0.135$.

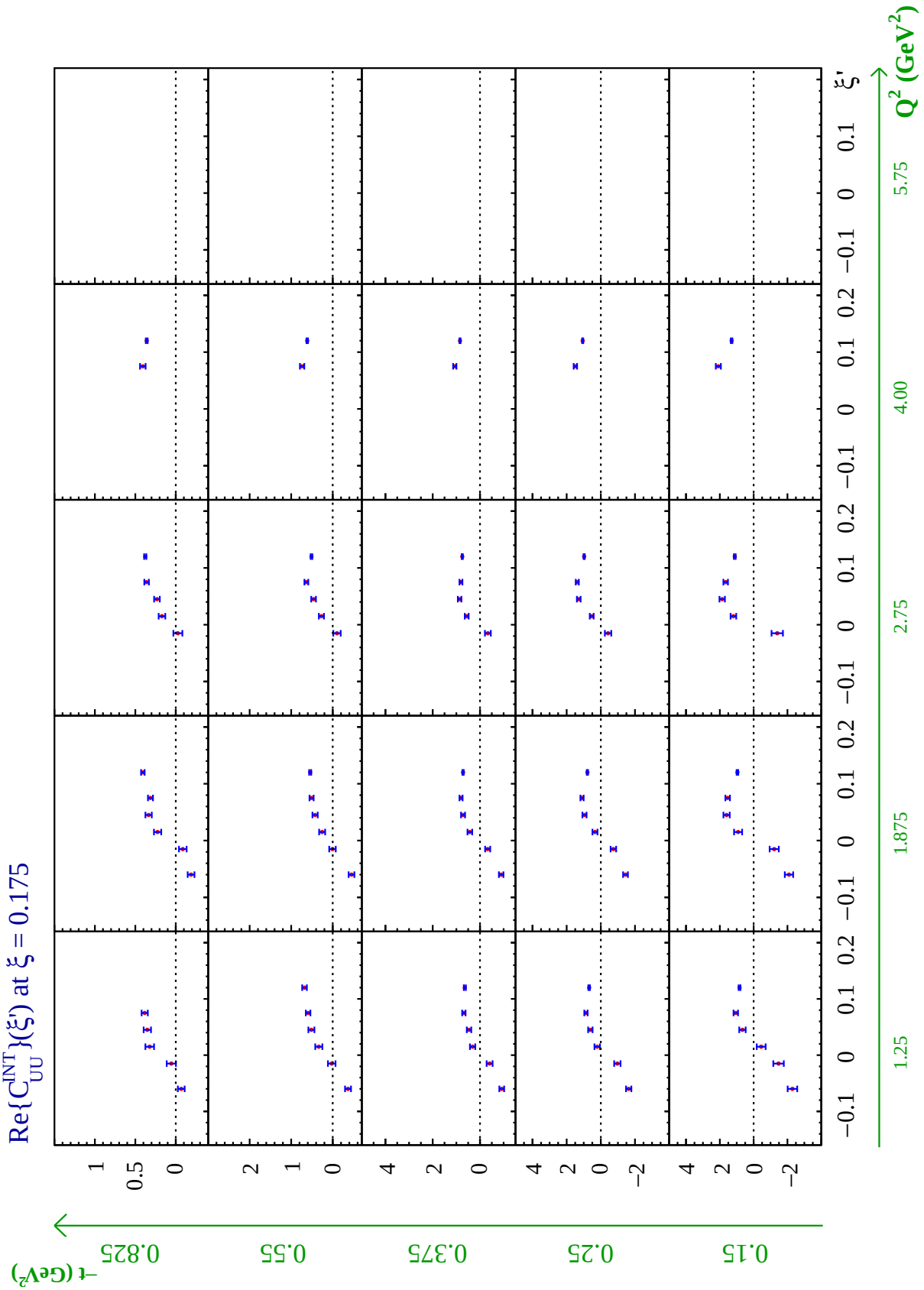

Figure C.11: $\mathrm{Re}\{\mathcal{C}_{\mathrm{UU}}^{\mathrm{INT}}\}(\xi')$ at $\xi = 0.175$.

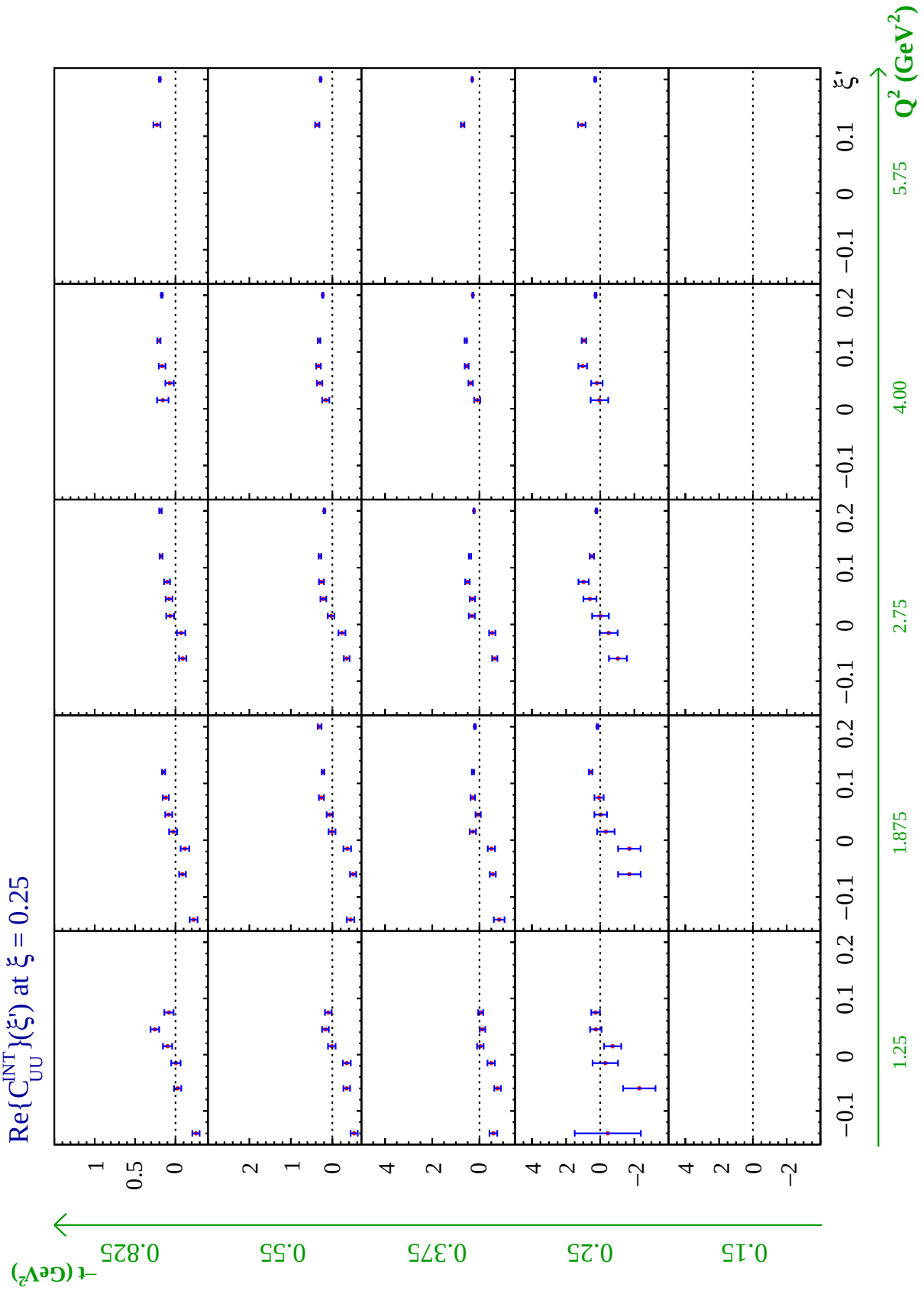

Figure C.12: $\mathrm{Re}\{\mathcal{C}_{UU}^{INT}\}(\xi')$ at $\xi = 0.25$.

Appendix D

Extracted CFFs $\mathcal{H}$

When the statistics of the pseudo-data is too poor, the fits mostly will not converge and/or end up with non-finite error. Thus, I only carry out the fit on the pseudo-data fulfilling a certain statistics requirement: the errors on minimal σ^{-}_{UU} at $\phi = 165°$ need to be smaller than 10% and the errors on the maximal BSA and BCA need to be smaller than 100%. There are 120 (ξ', ξ, t, Q^2) bins satisfying the requirement at 10^{36} cm$^{-2} \cdot$ s^{-1} and 266 at 10^{37} cm$^{-2} \cdot$ s^{-1} for 50 days run. The results presented here are obtained when fitting σ_{UU}, $\Delta\sigma^{\mathrm{C}}_{\mathrm{UU}}$, $\Delta\sigma_{\mathrm{LU}}$ and $\Delta\sigma^{\mathrm{C}}_{\mathrm{LU}}$ simultaneously.

Fig. D.1-D.4 show the fitting results at $\xi = 0.045$, where Fig. D.1 for the fitted CFFs multiplier $a(\mathrm{Im}\mathcal{H})$, Fig. D.2 for the resulting value of $\mathrm{Im}\mathcal{H}$, Fig. D.3 for the fitted CFFs multiplier $a(\mathrm{Re}\mathcal{H})$,, and Fig. D.4 for the resulting value of $\mathrm{Re}\mathcal{H}$. Fig. D.5-D.24 follow the same pattern and show the results at $\xi = 0.075,\ 0.105,\ 0.135,\ 0.175$ and 0.25. Note that the resulting value CFFs are presented only for the converging fits and the finite error bars. In each figure, the red points stand for the results obtained at $\mathcal{L} = 10^{36}$ cm$^{-2} \cdot$ s^{-1} and the blue points at $\mathcal{L} = 10^{37}$ cm$^{-2} \cdot$ s^{-1}. Note that the blue points are offset by +0.005 in ξ' for visual clarity.

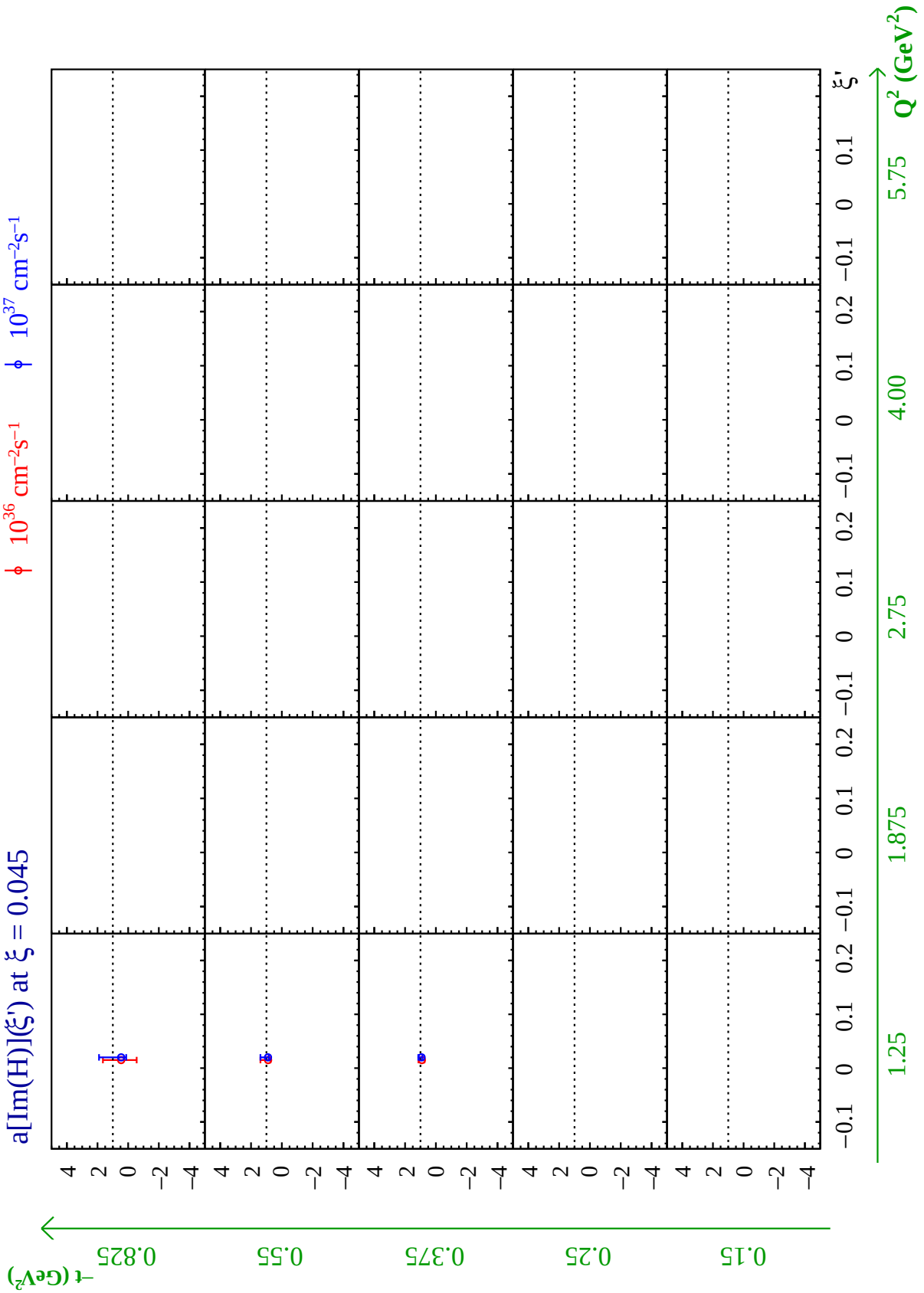

Figure D.1: $a(\mathrm{Im}\mathcal{H})$ at $\xi = 0.045$.

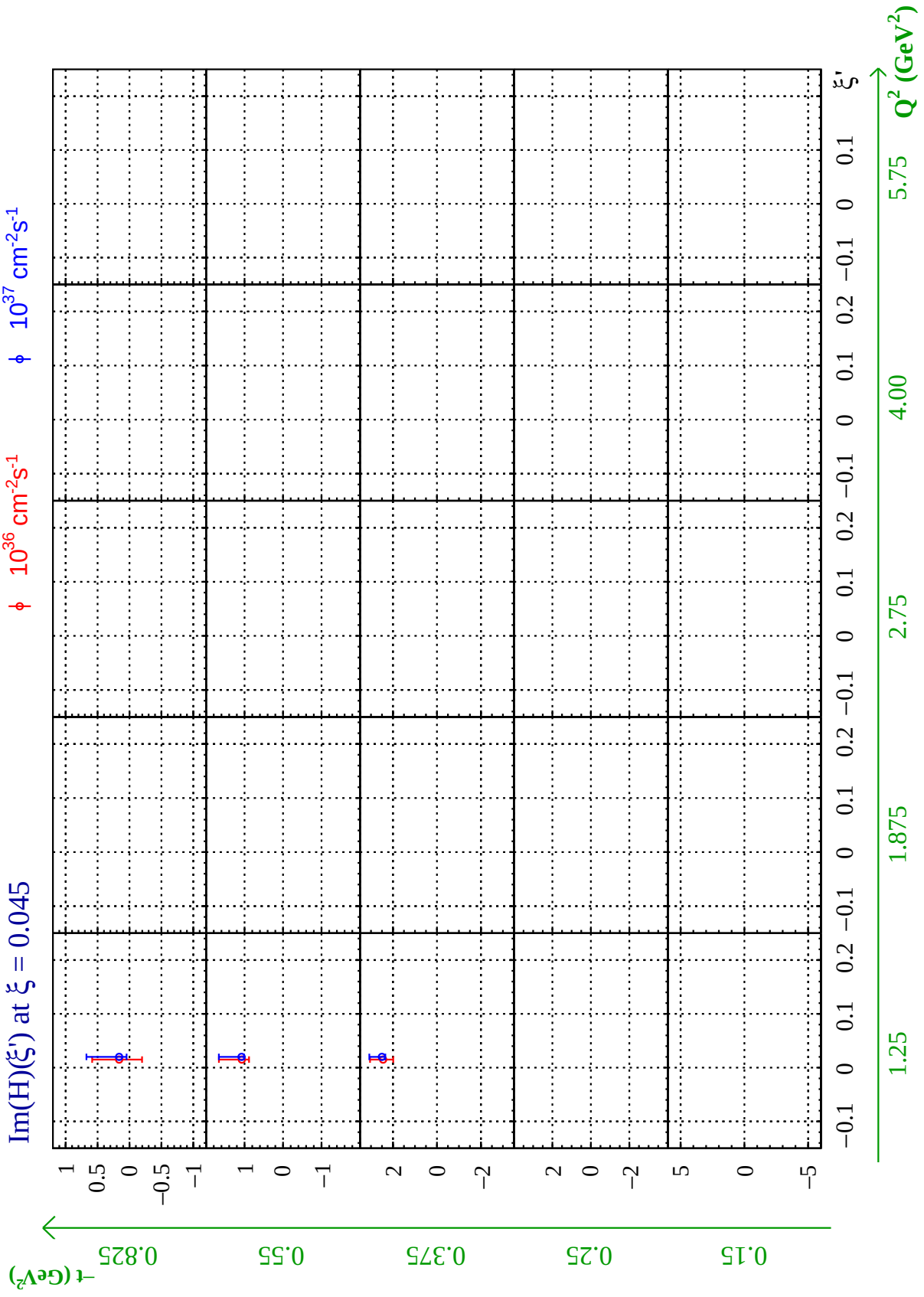

Figure D.2: Im$\mathcal{H}$ at $\xi = 0.045$.

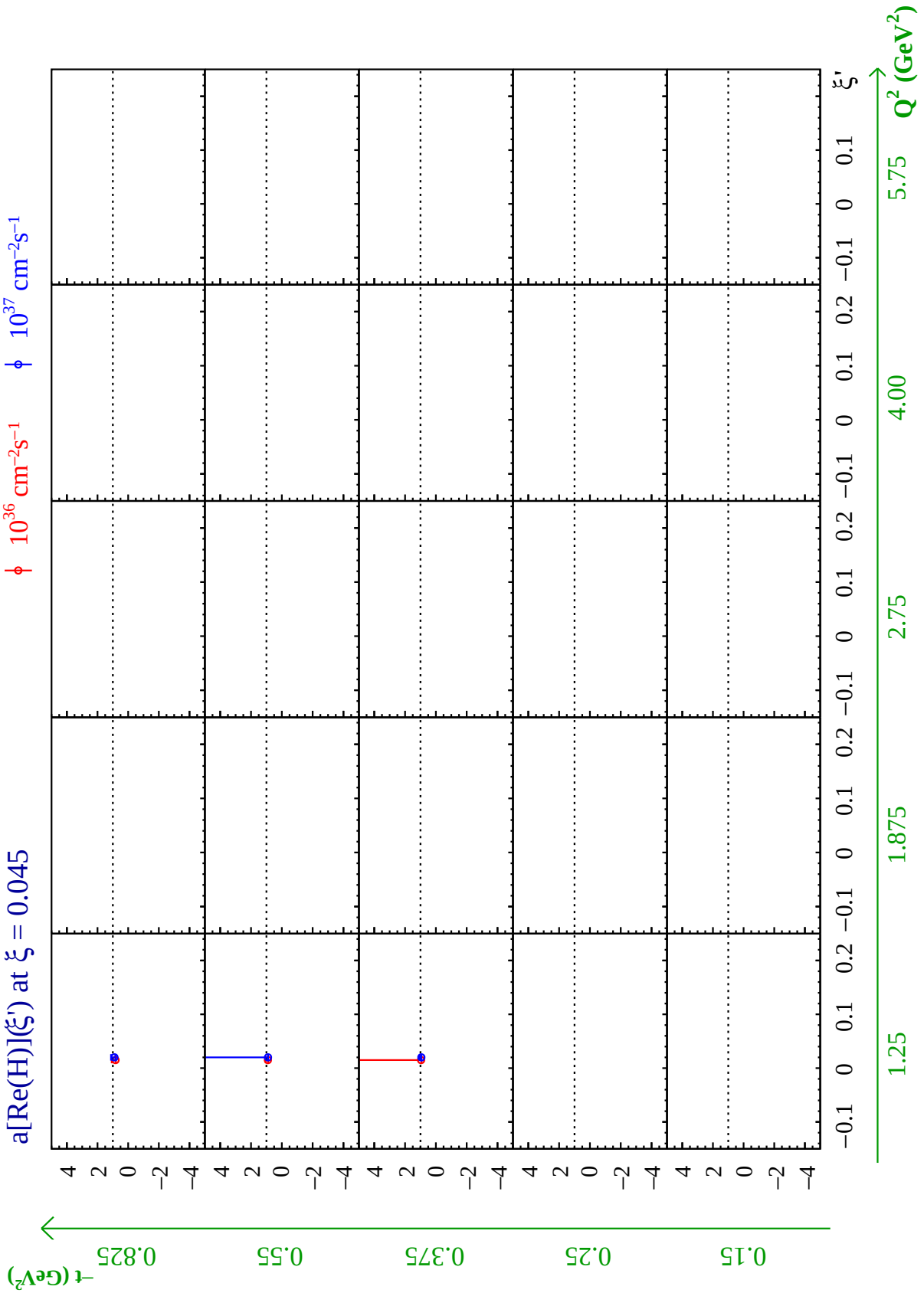

Figure D.3: $a(\mathrm{Re}\mathcal{H})$ at $\xi = 0.045$.

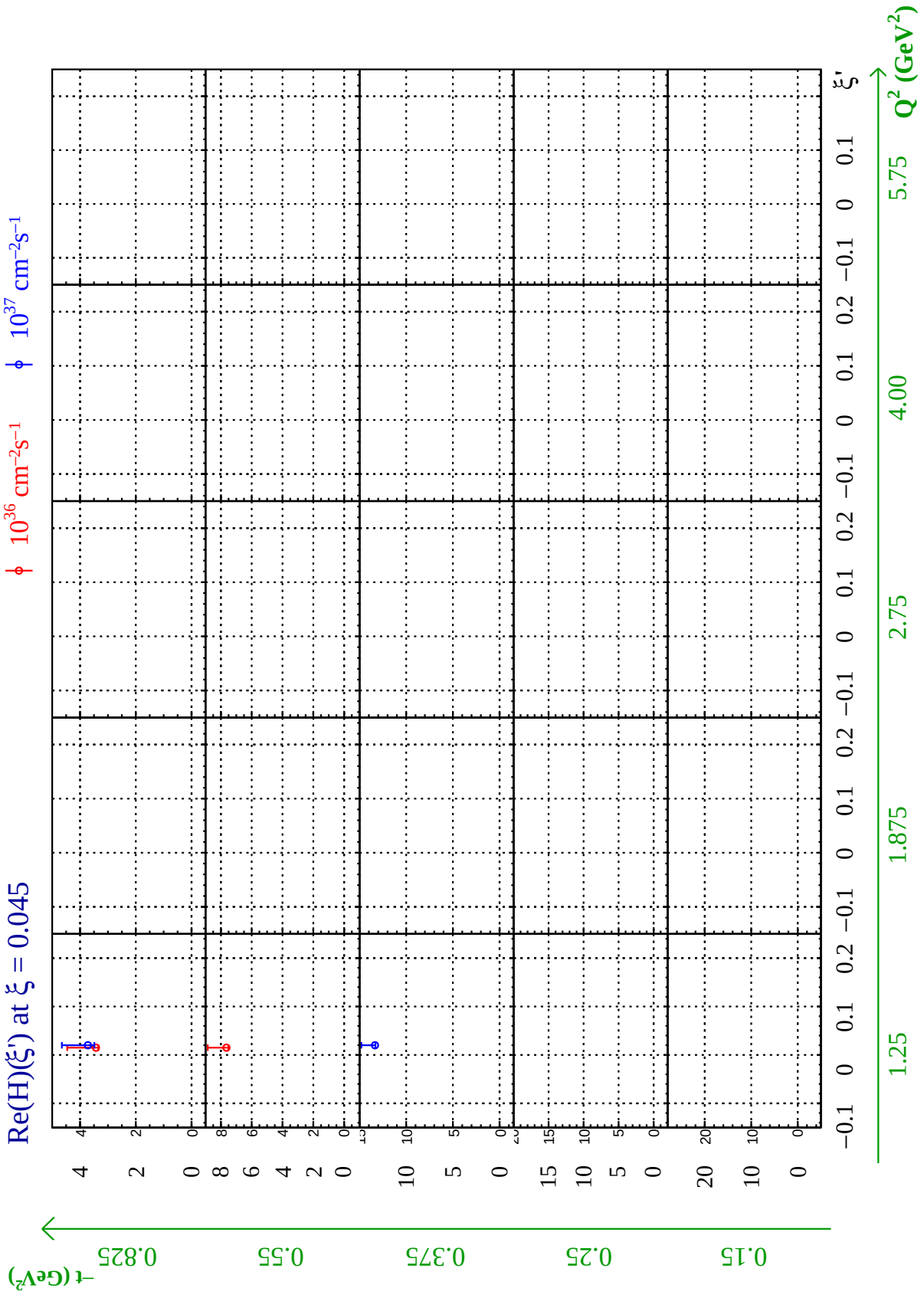

Figure D.4: Re$\mathcal{H}$ at $\xi = 0.045$.

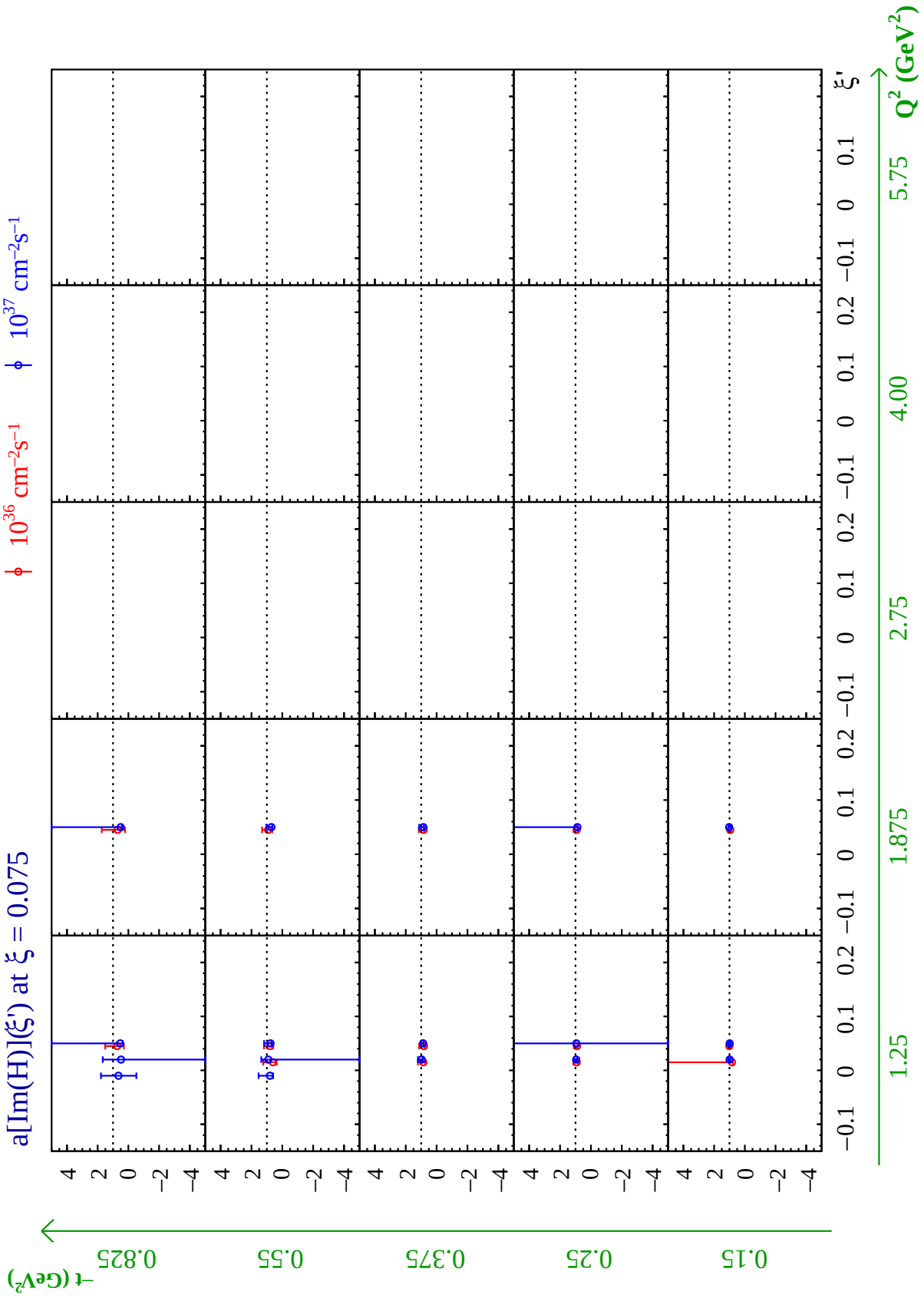

Figure D.5: $a(\mathrm{Im}\mathcal{H})$ at $\xi = 0.075$.

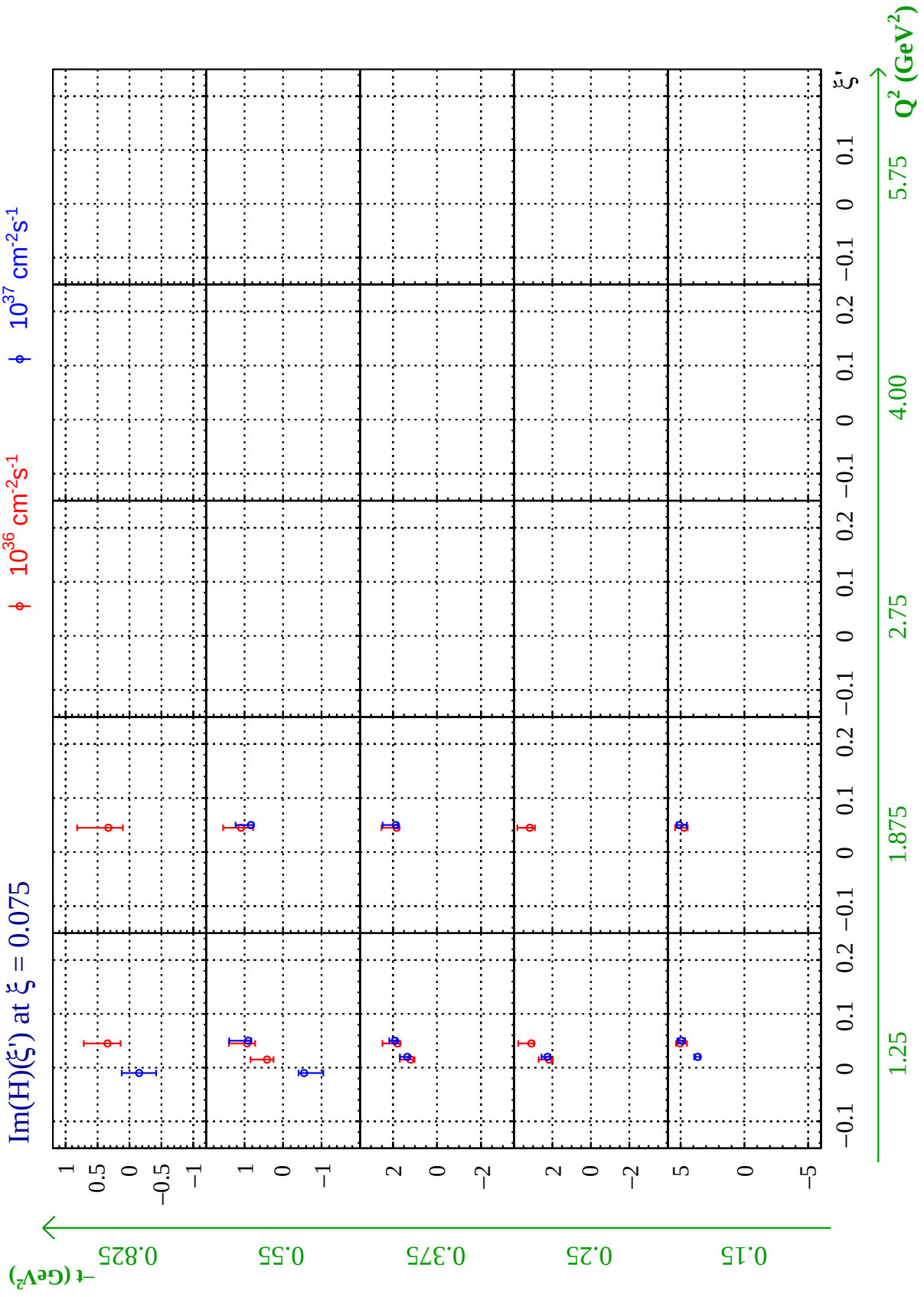

Figure D.6: Im$\mathcal{H}$ at $\xi = 0.075$.

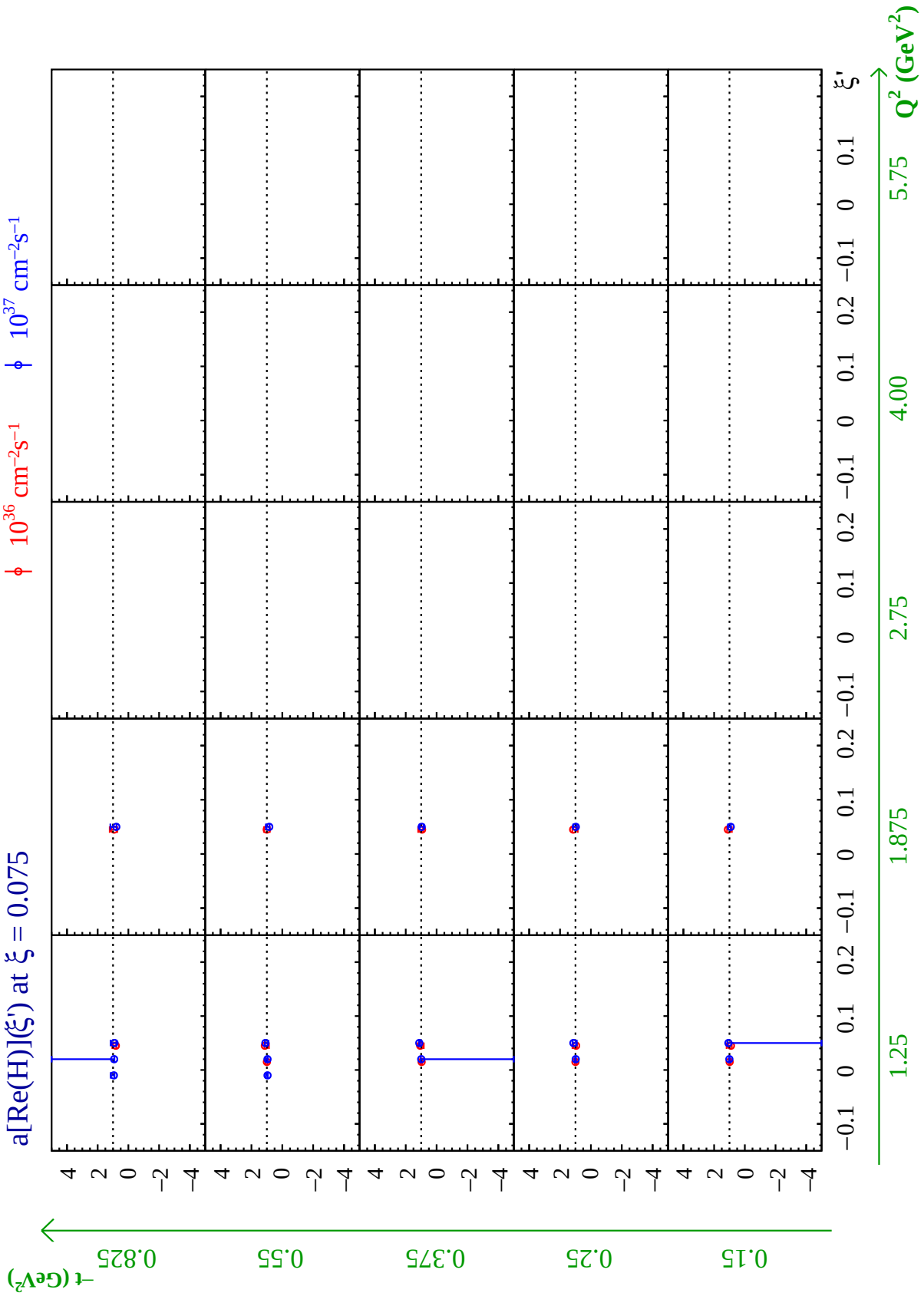

Figure D.7: $a(\mathrm{Re}\mathcal{H})$ at $\xi = 0.075$.

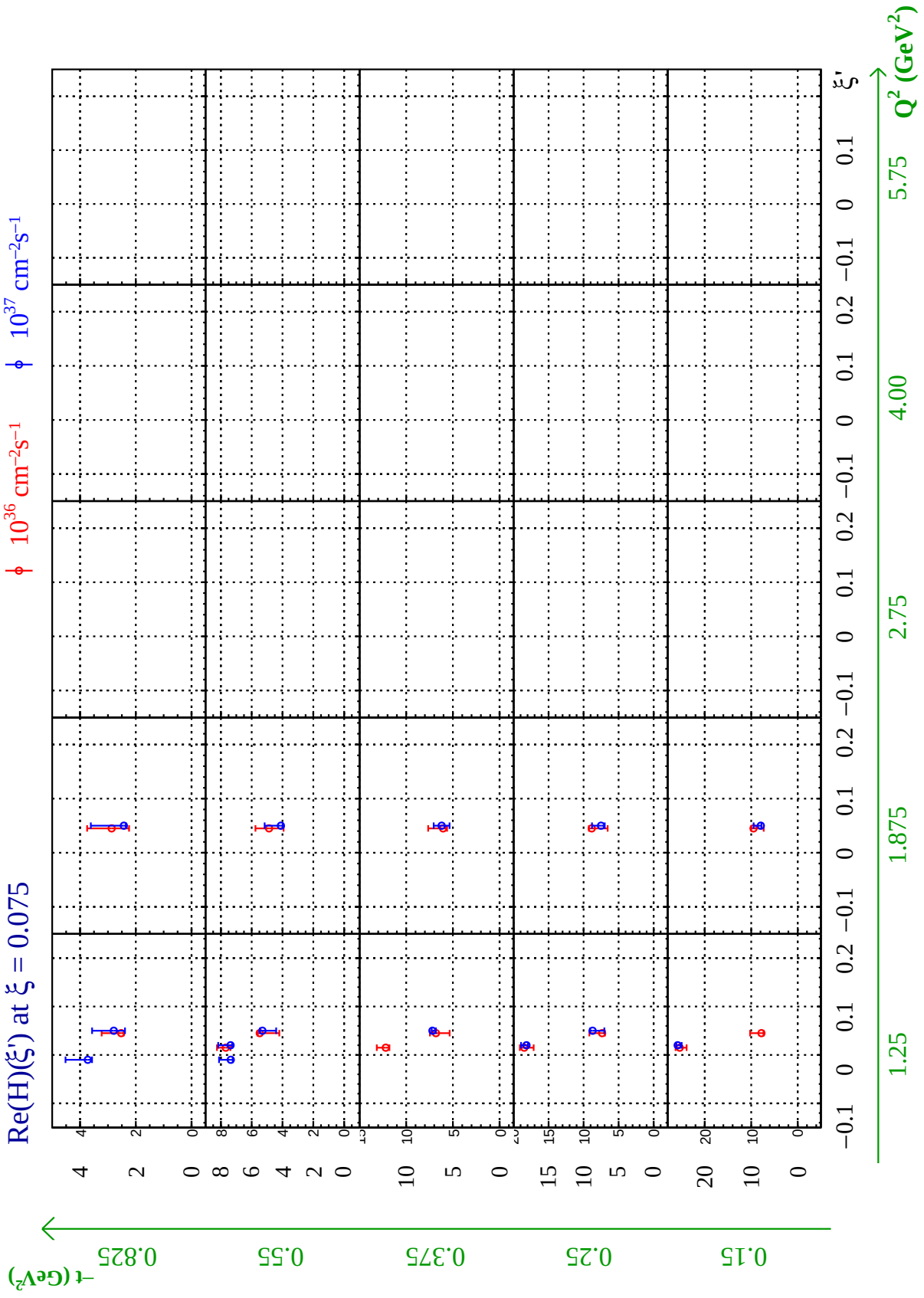

Figure D.8: Re$\mathcal{H}$ at $\xi = 0.075$.

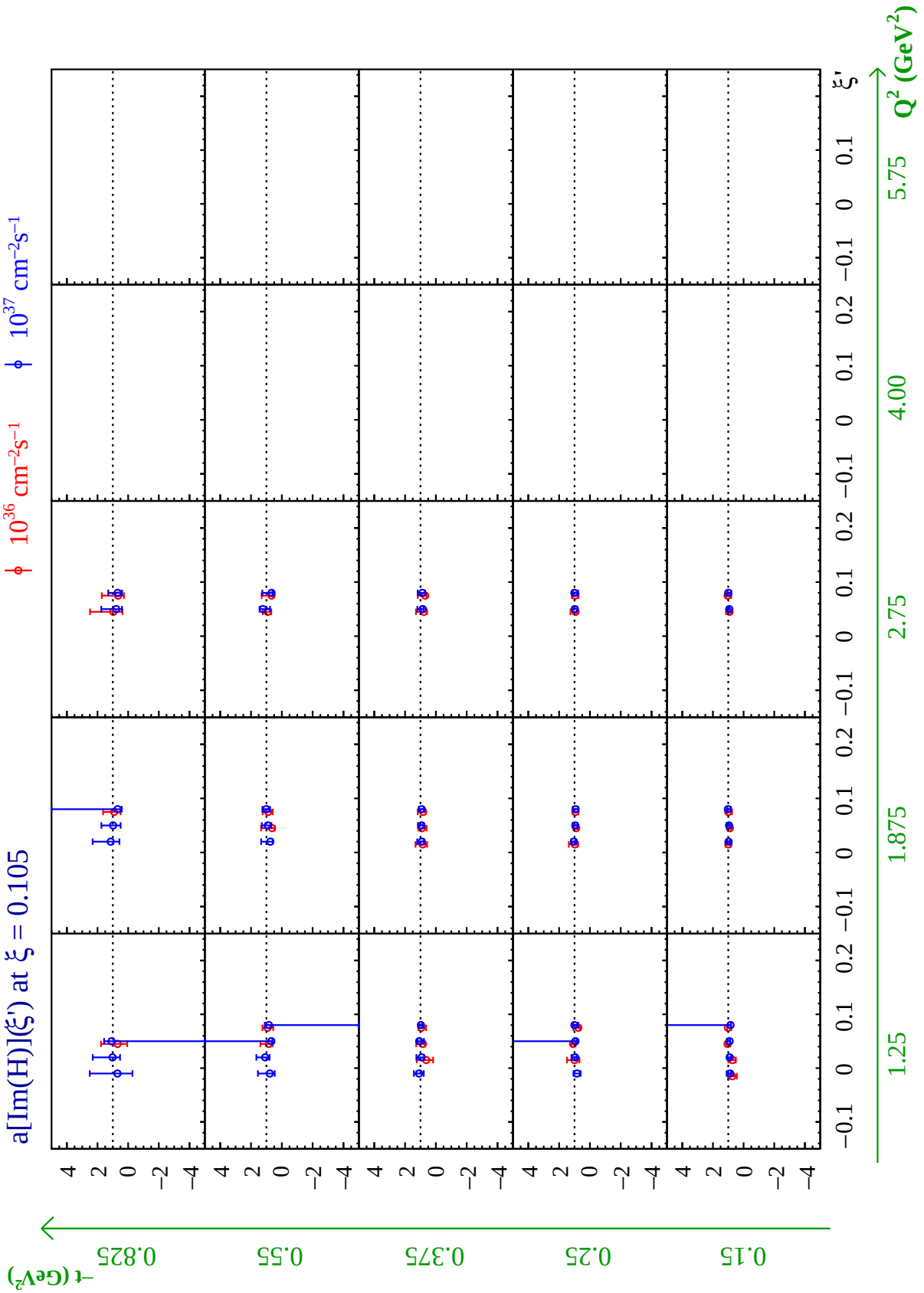

Figure D.9: $a(\mathrm{Im}\mathcal{H})$ at $\xi = 0.105$.

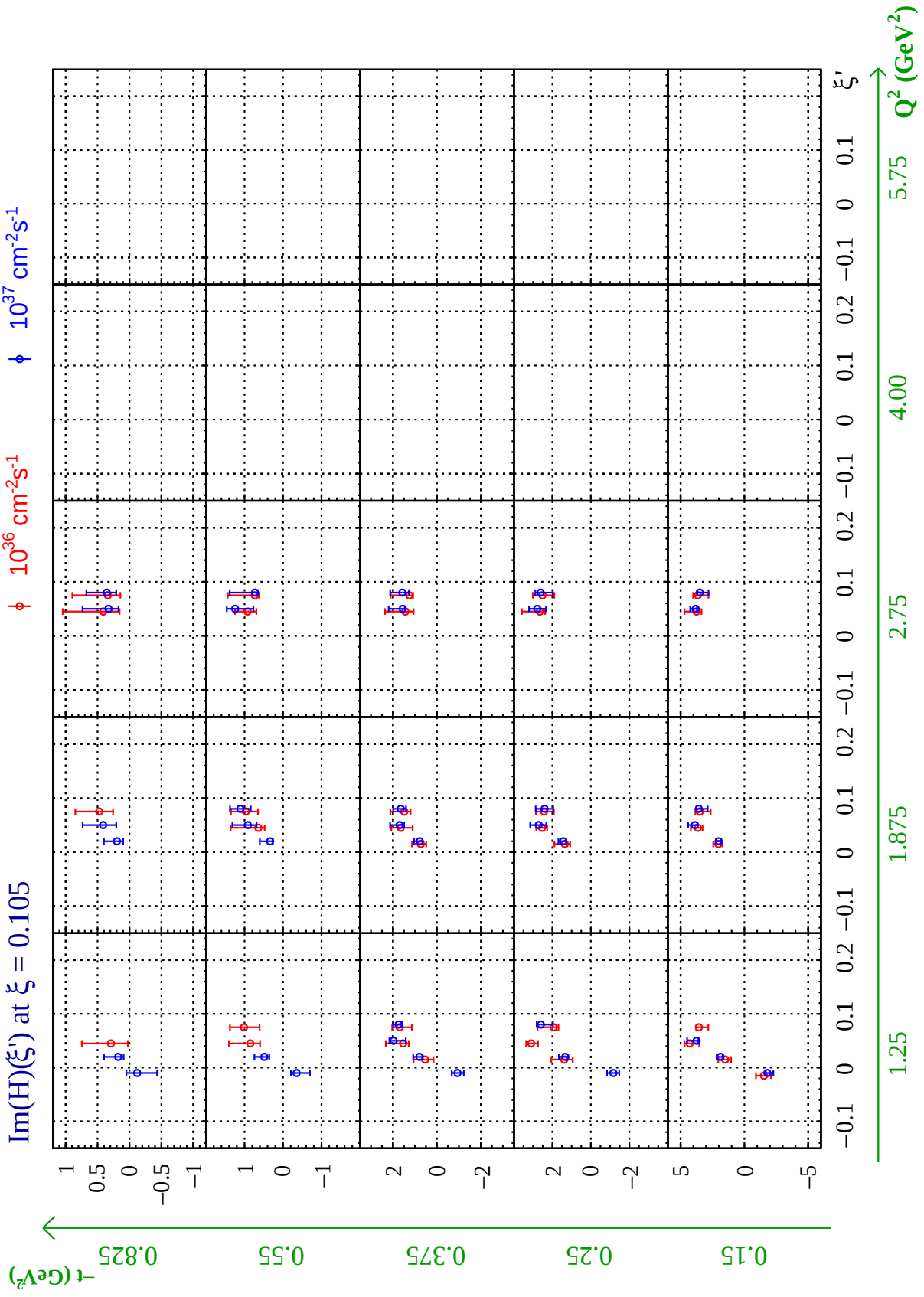

Figure D.10: Im$\mathcal{H}$ at $\xi = 0.105$.

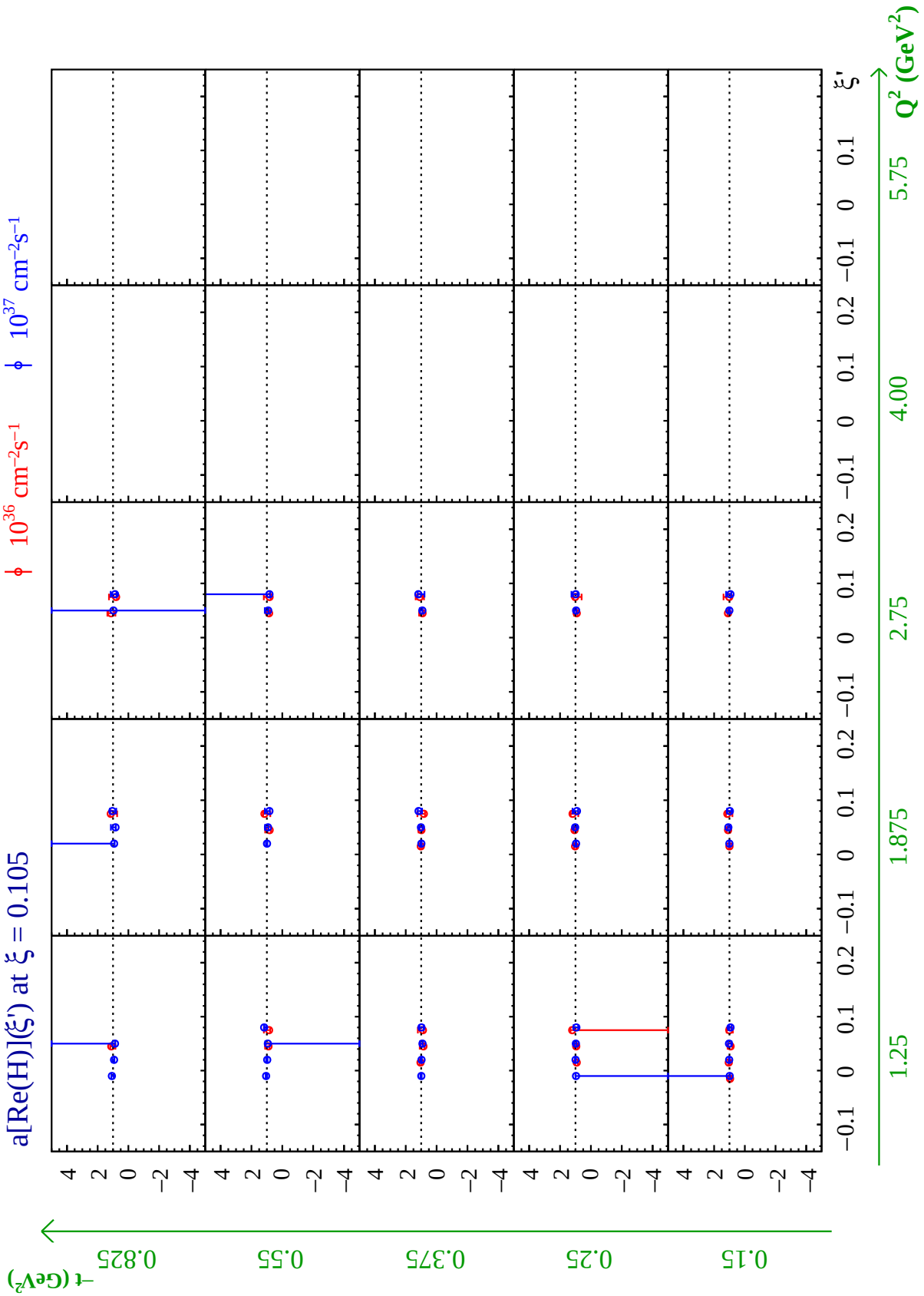

Figure D.11: $a(\mathrm{Re}\mathcal{H})$ at $\xi = 0.105$.

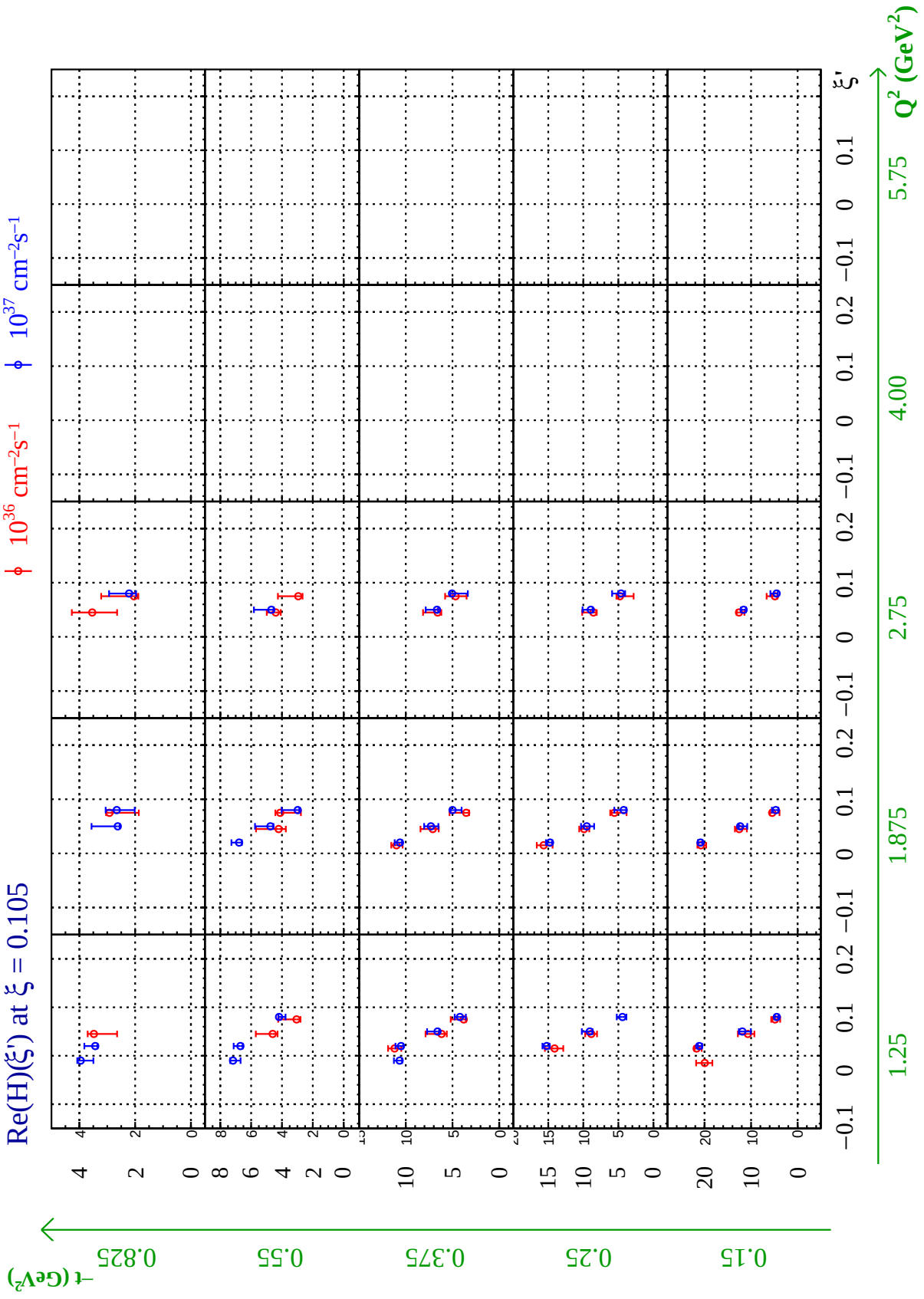

Figure D.12: Re$\mathcal{H}$ at $\xi = 0.105$.

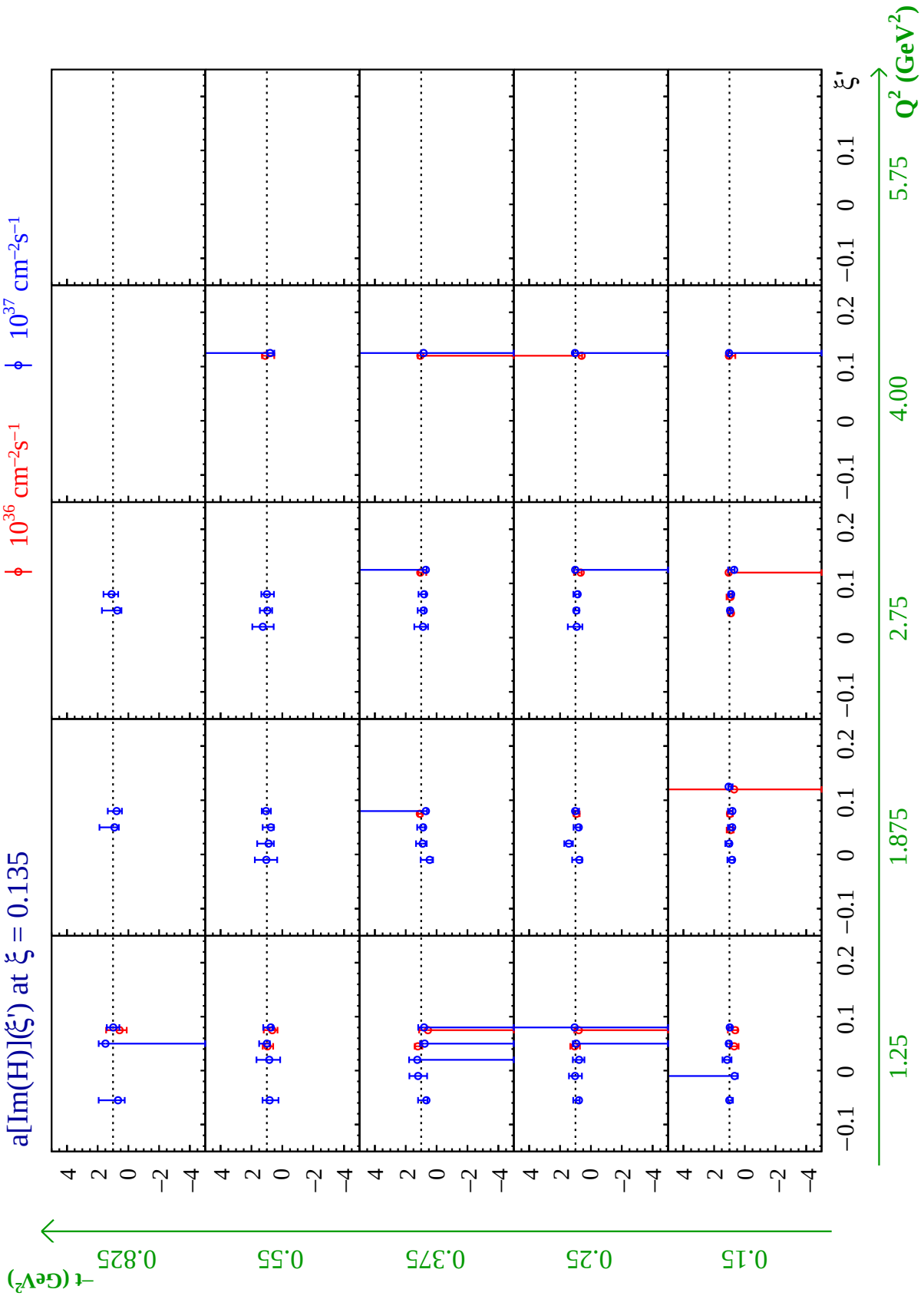

Figure D.13: $a(\mathrm{Im}\mathcal{H})$ at $\xi = 0.135$.

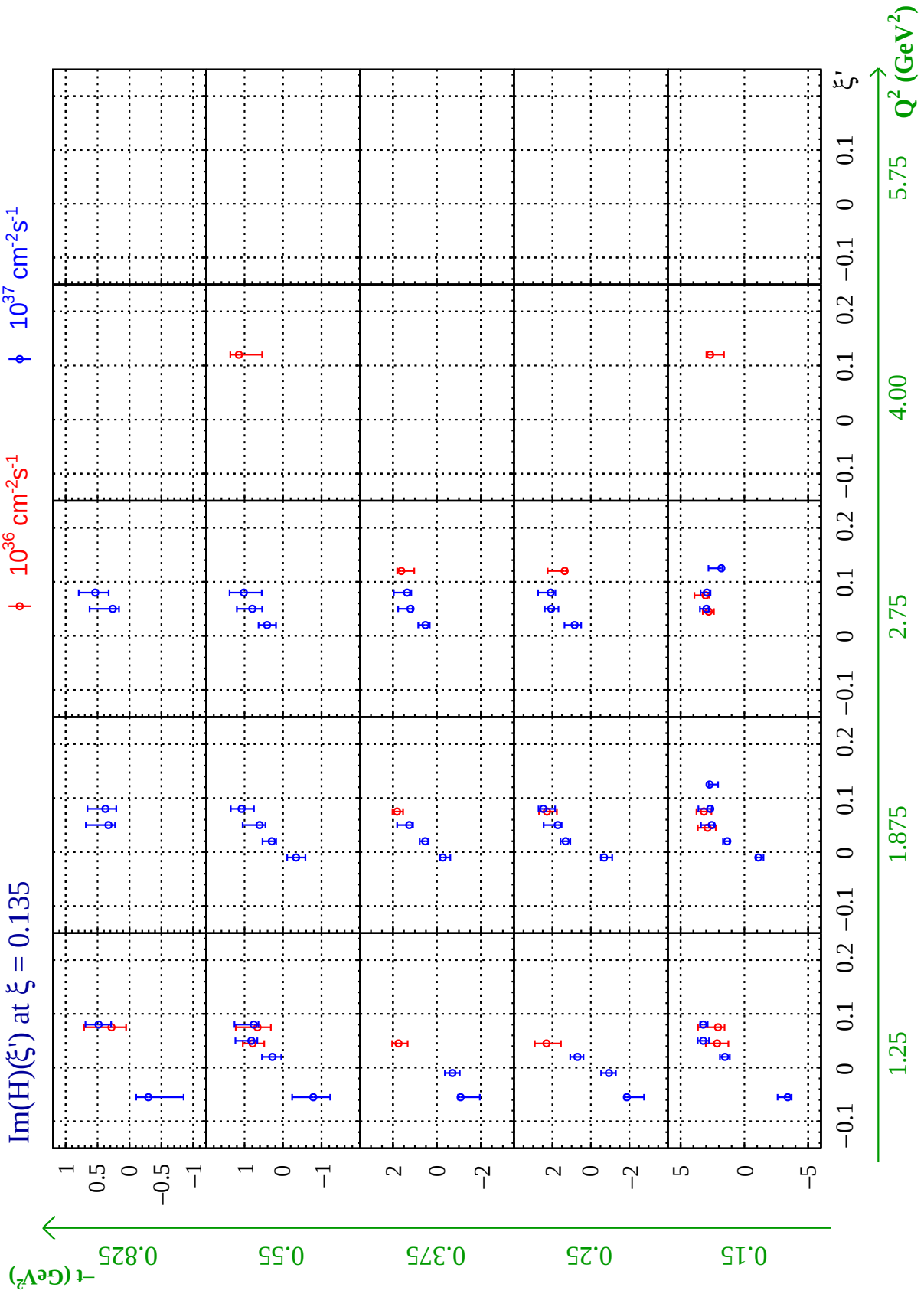

Figure D.14: Im$\mathcal{H}$ at $\xi = 0.135$.

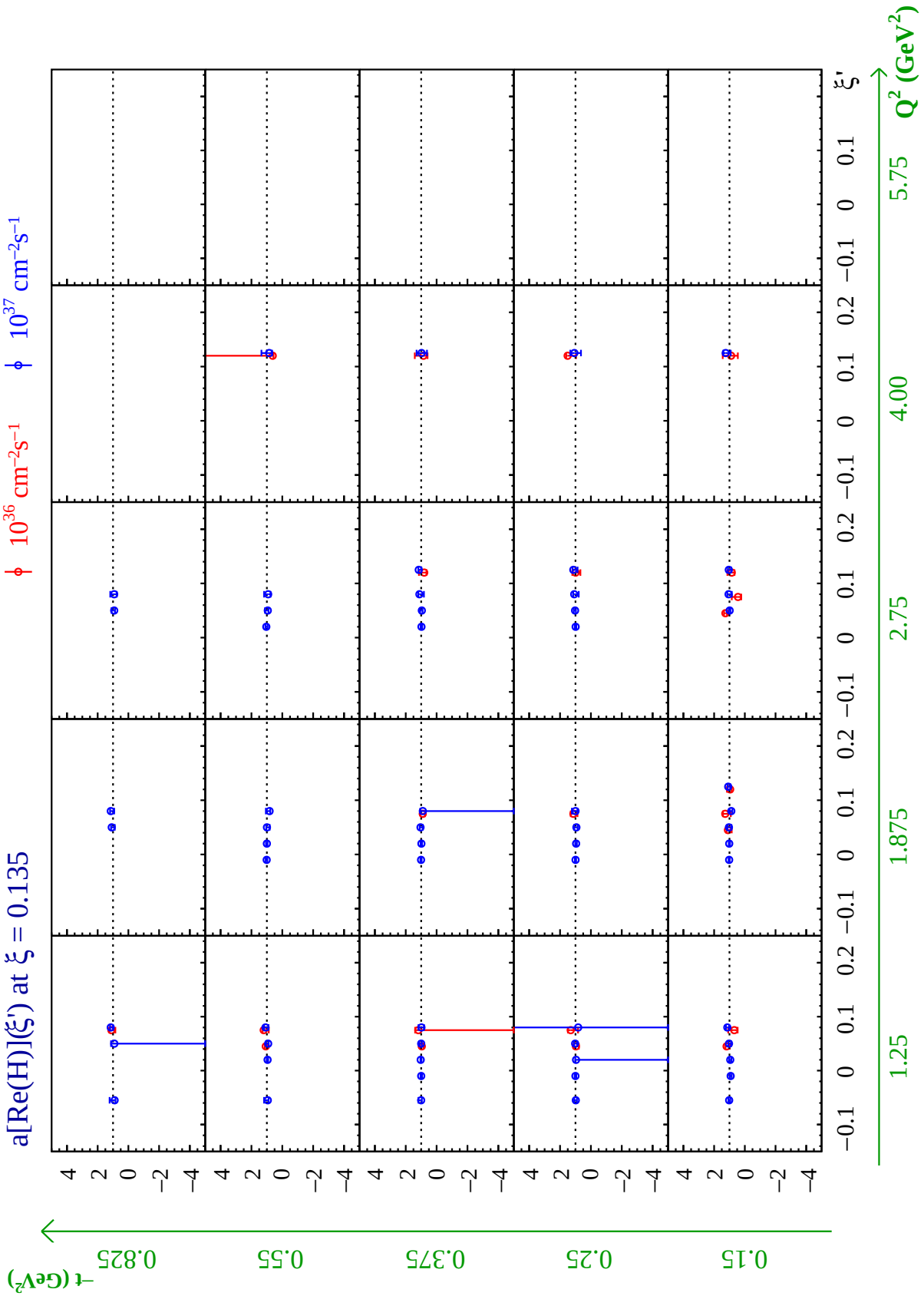

Figure D.15: $a(\mathrm{Re}\mathcal{H})$ at $\xi = 0.135$.

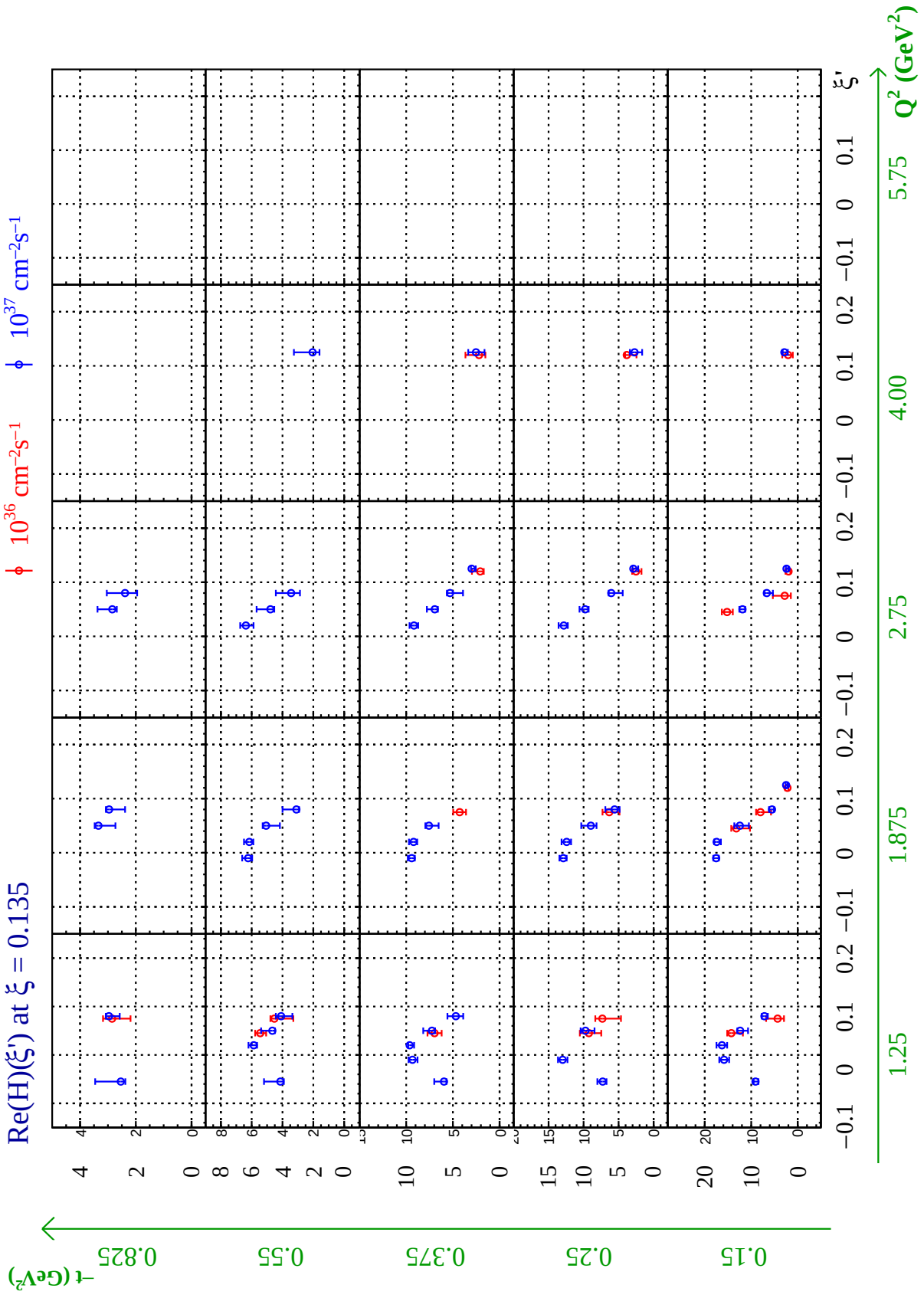

Figure D.16: Re$\mathcal{H}$ at $\xi = 0.135$.

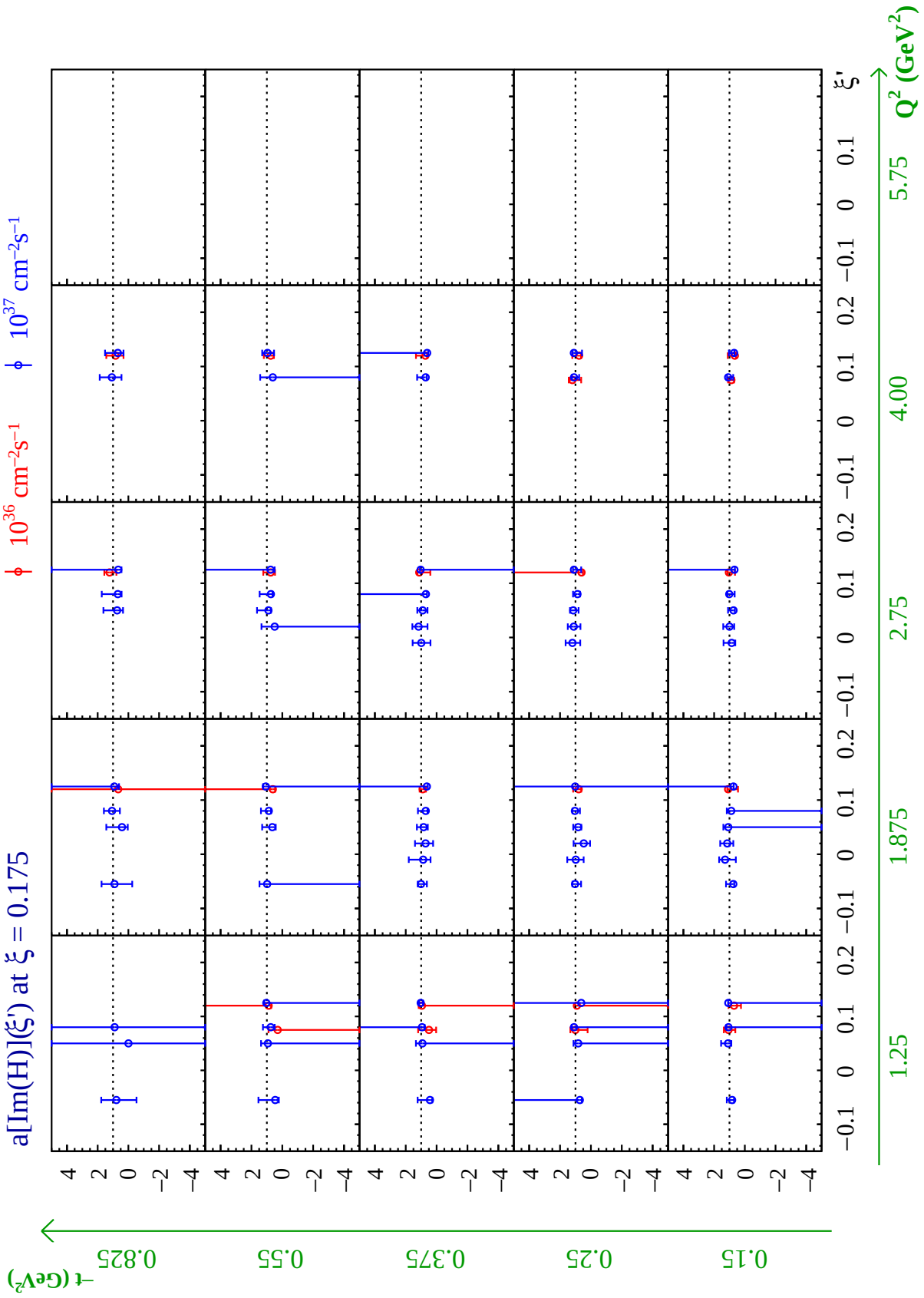

Figure D.17: $a(\mathrm{Im}\mathcal{H})$ at $\xi = 0.175$.

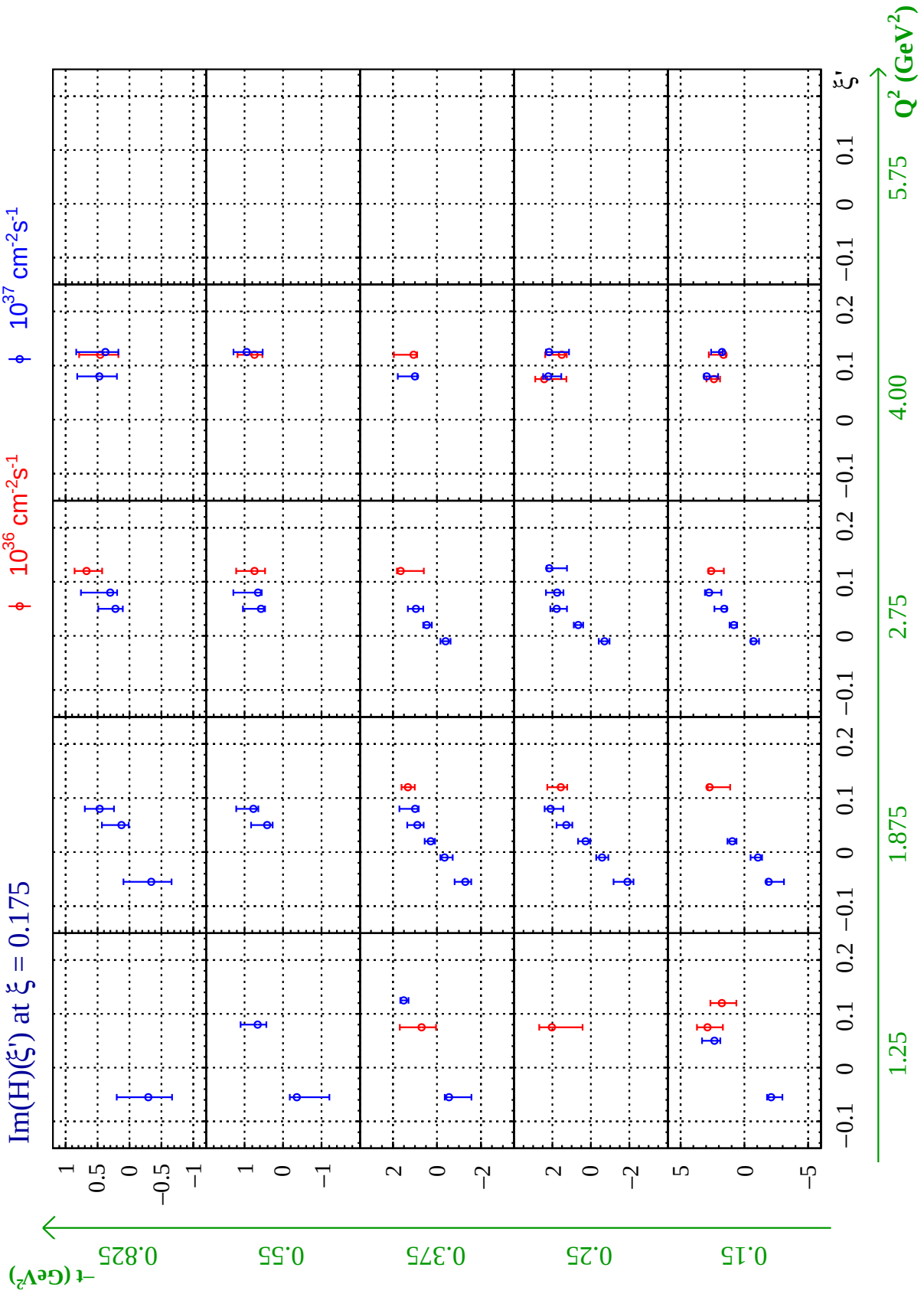

Figure D.18: Im$\mathcal{H}$ at $\xi = 0.175$.

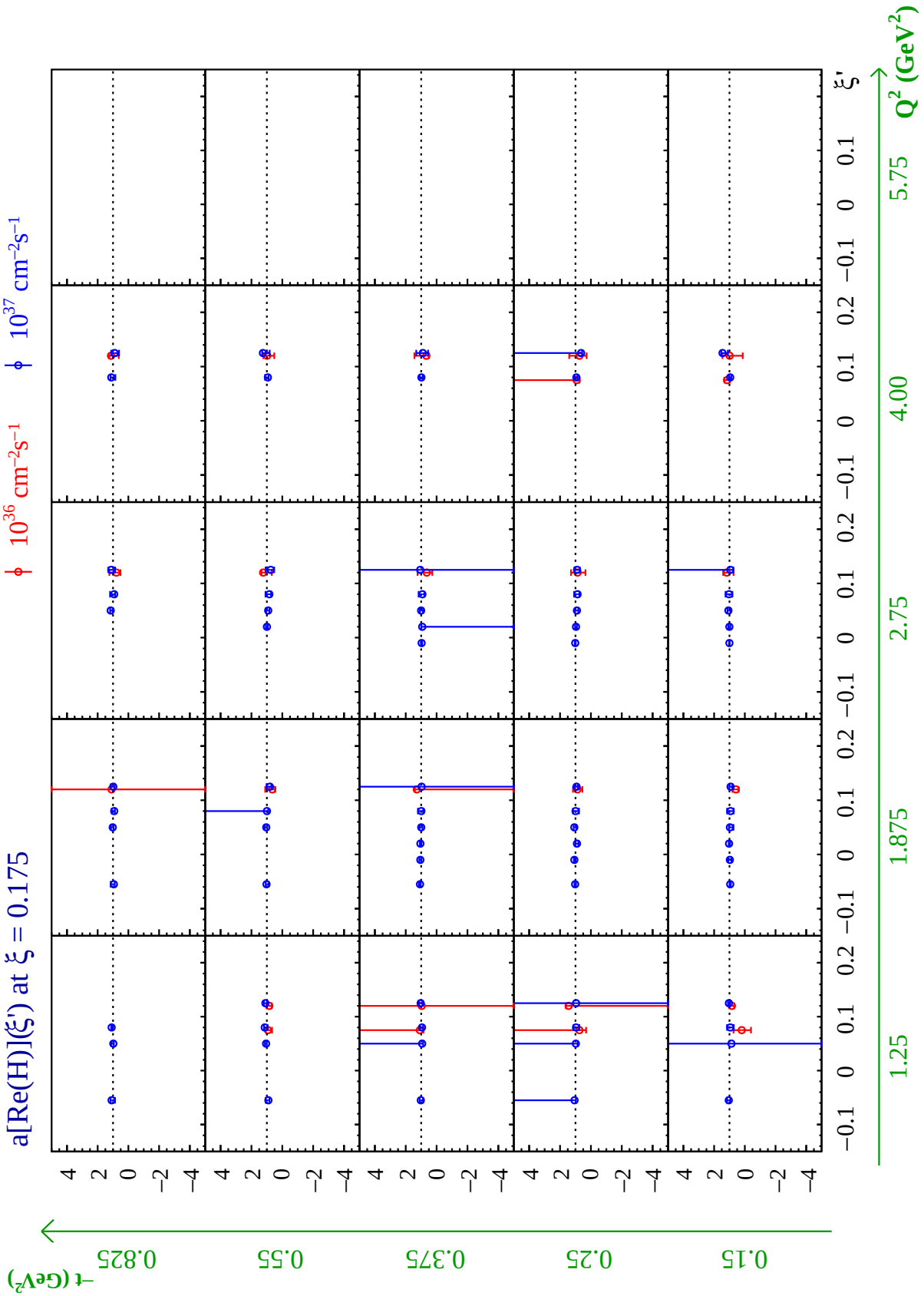

Figure D.19: $a(\mathrm{Re}\mathcal{H})$ at $\xi = 0.175$.

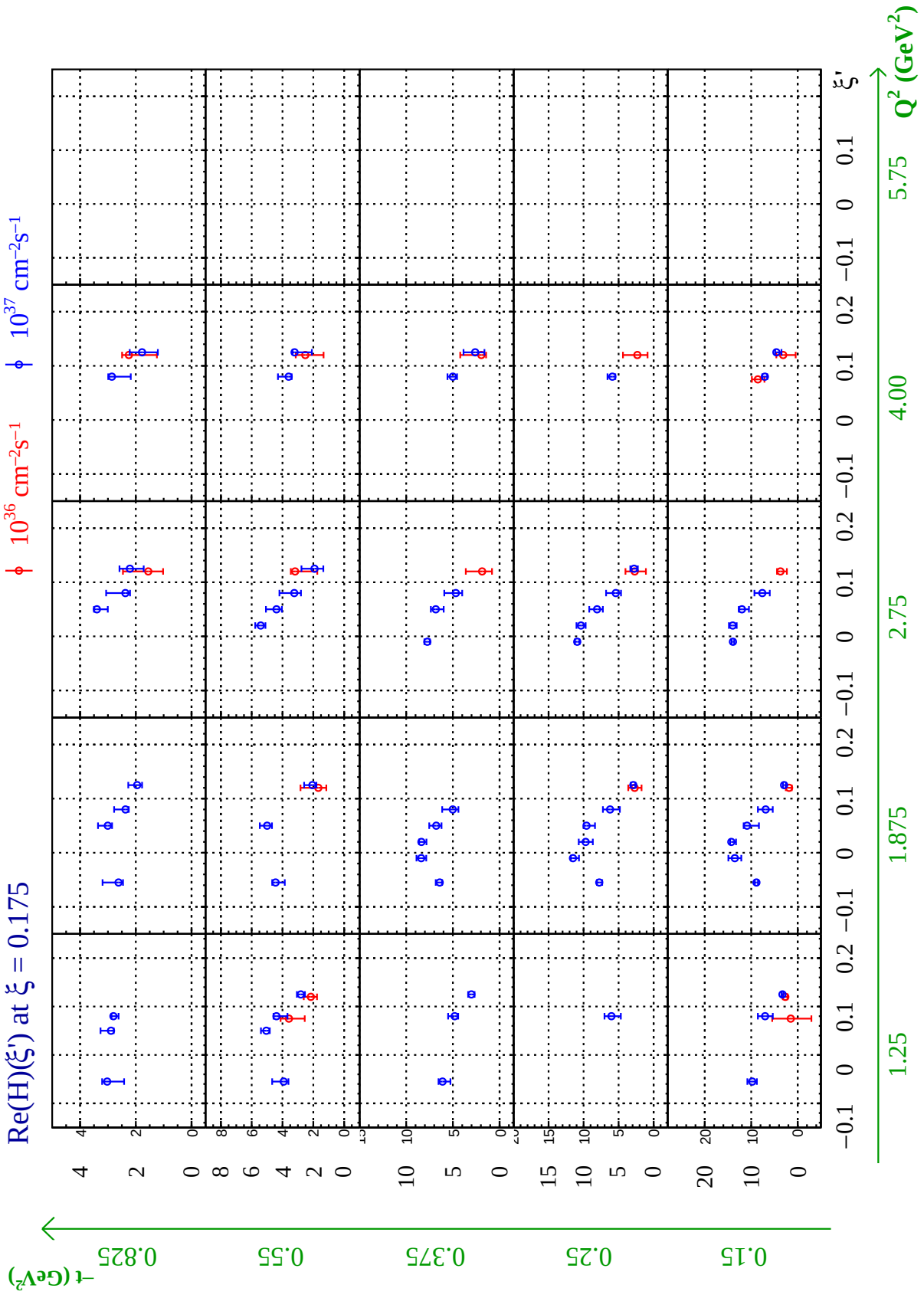

Figure D.20: Re$\mathcal{H}$ at $\xi = 0.175$.

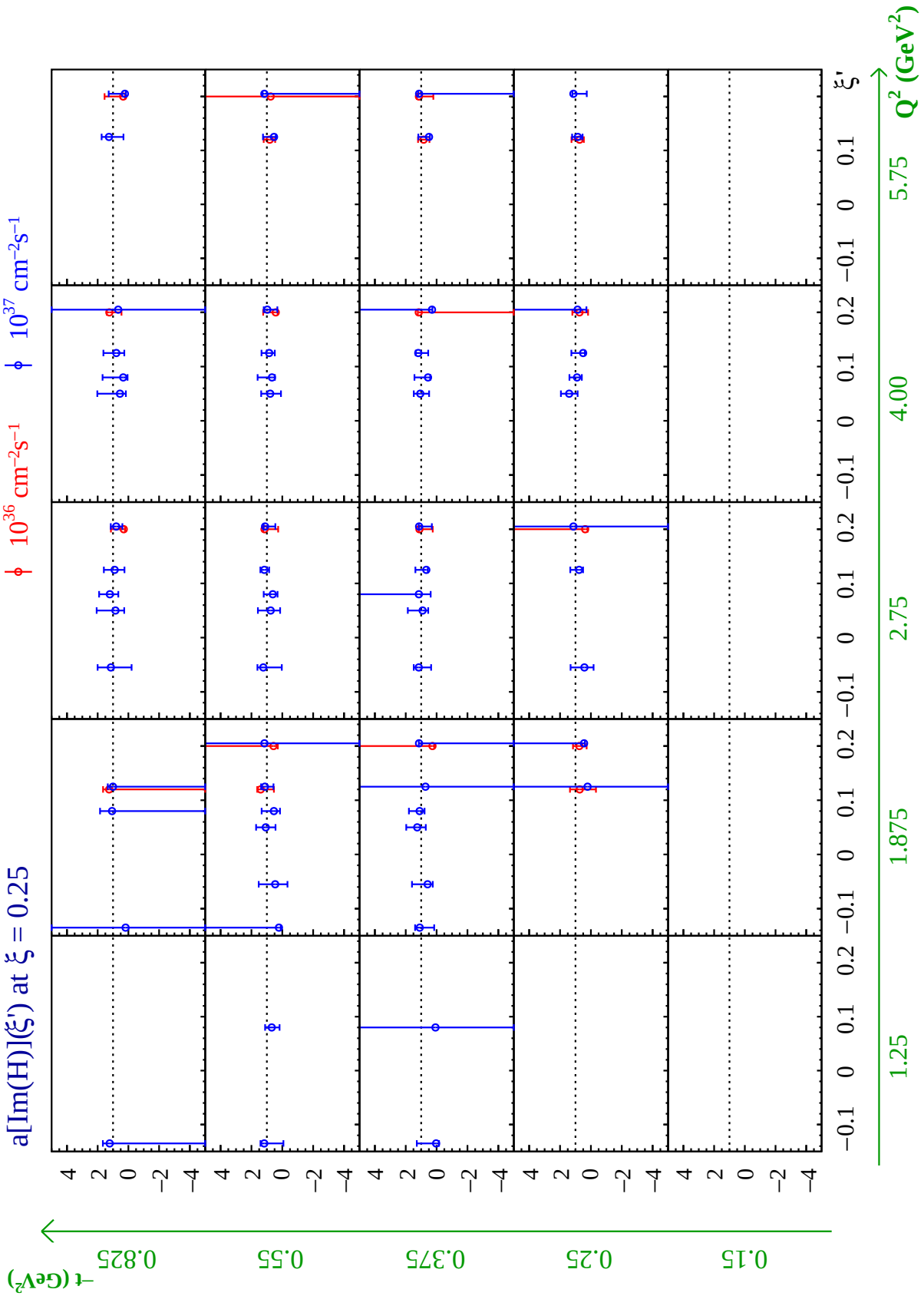

Figure D.21: $a(\mathrm{Im}\mathcal{H})$ at $\xi = 0.25$.

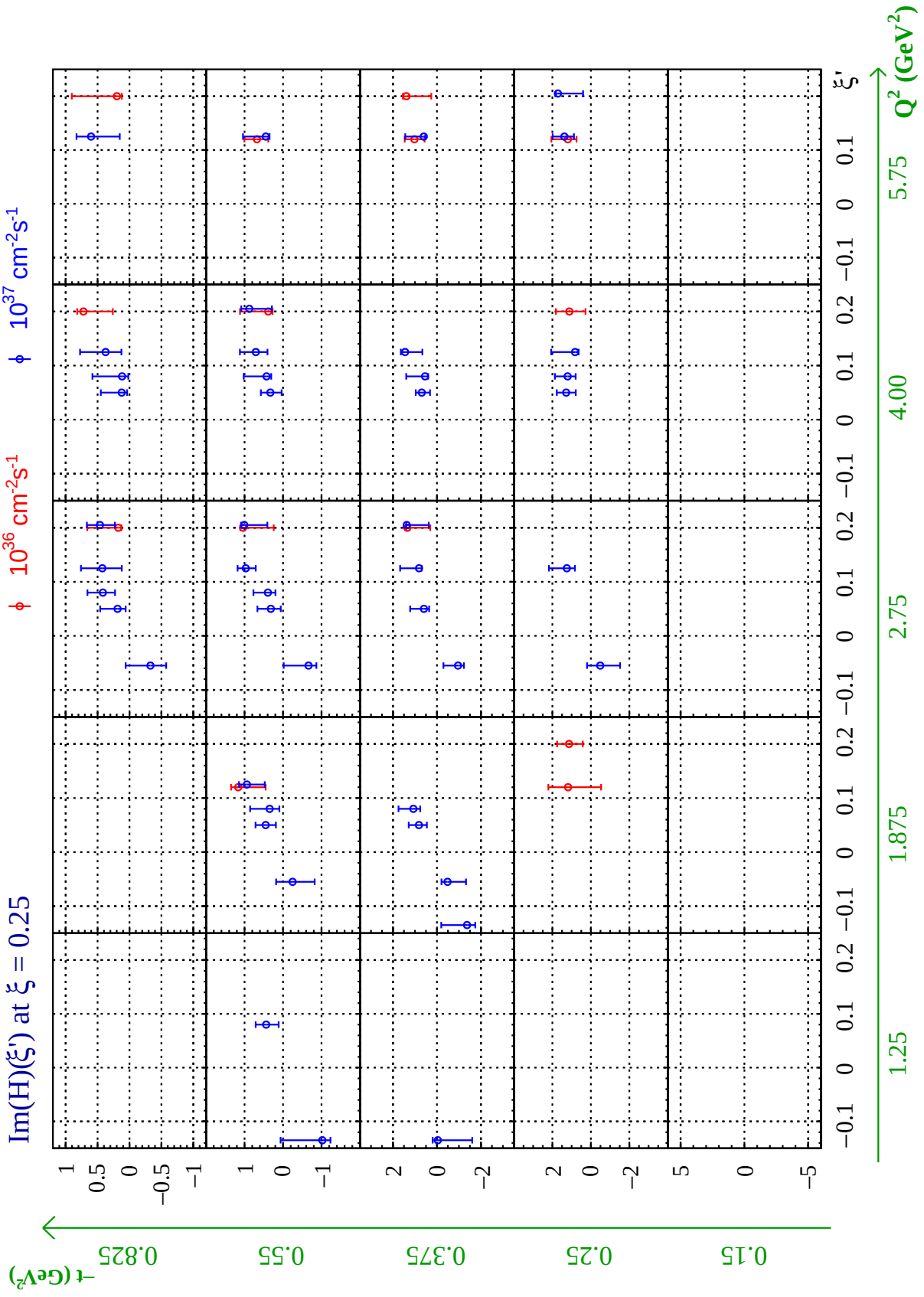

Figure D.22: Im$\mathcal{H}$ at $\xi = 0.25$.

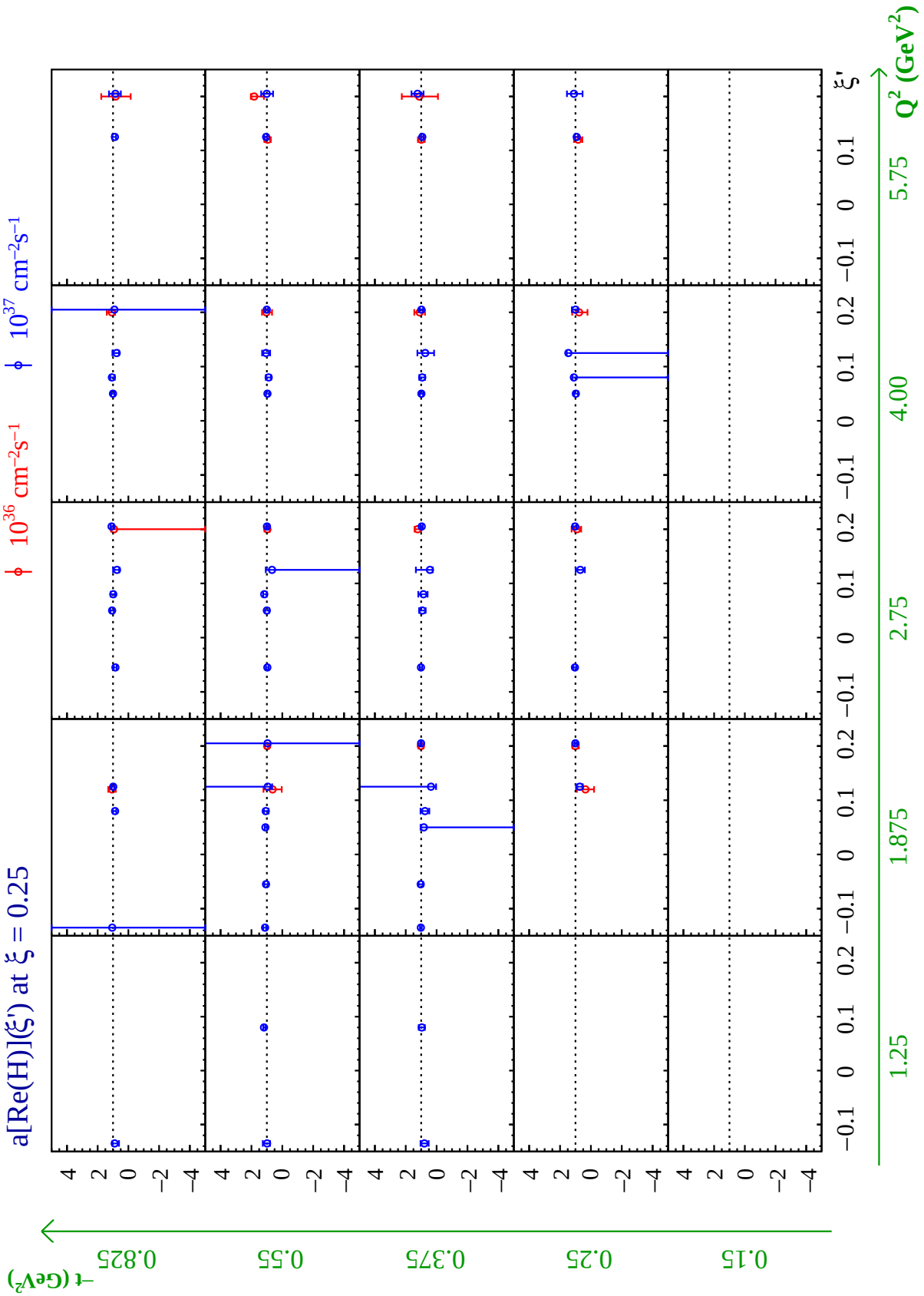

Figure D.23: $a(\mathrm{Re}\mathcal{H})$ at $\xi = 0.25$.

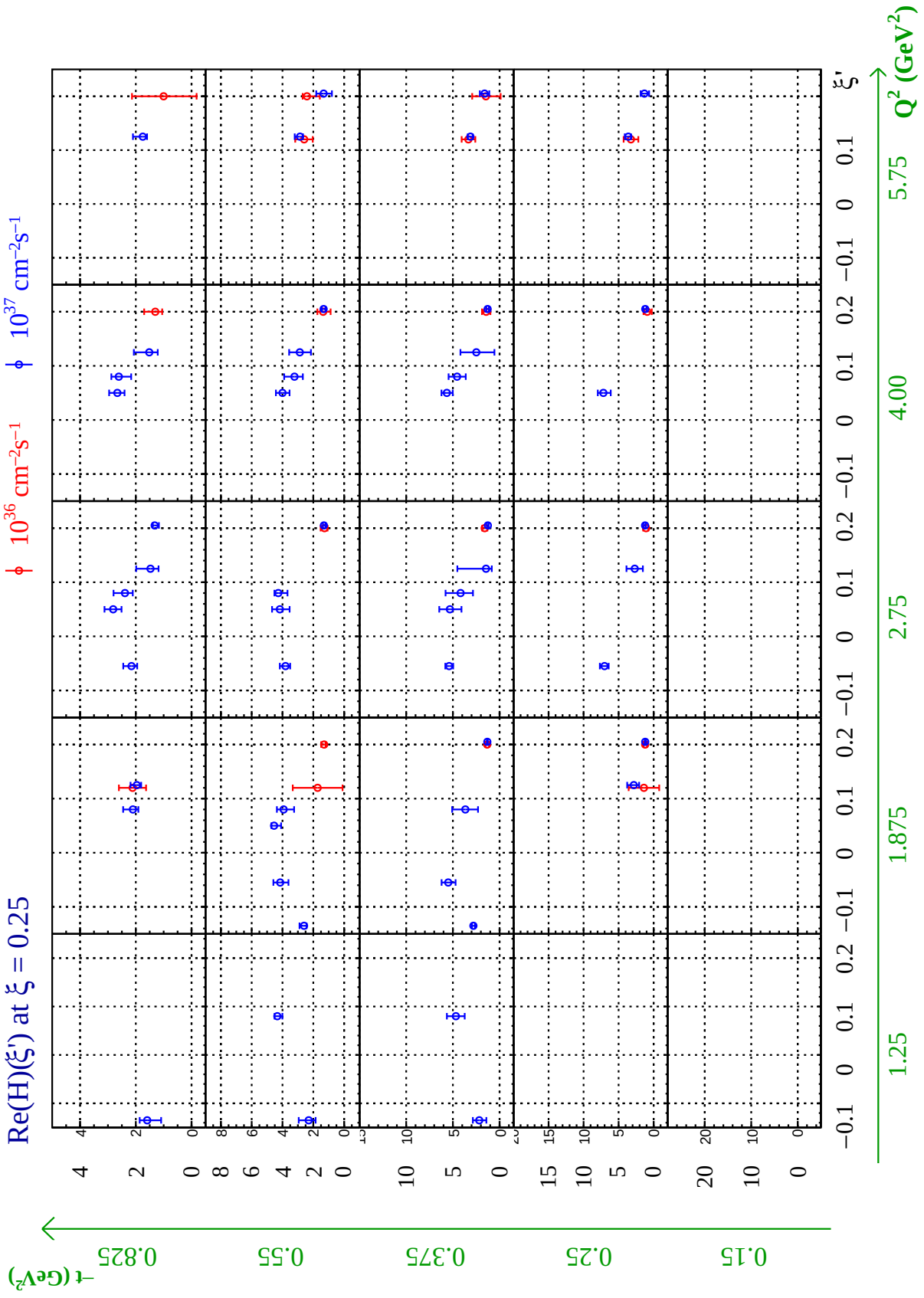

Figure D.24: Re$\mathcal{H}$ at $\xi = 0.25$.

Bibliography

[1] R. Hofstadter and R. W. McAllister, Phys. Rev. **98**, 217 (1955).

[2] M. Breidenbach *et al.*, Phys. Rev. Lett. **23**, 935 (1969).

[3] D. Müller *et al.*, Fortschr. Phys. **42**, 101 (1994).

[4] X. Ji, Phys. Rev. Lett. **78**, 610 (1997).

[5] X. Ji, Phys. Rev. D **55**, 7114 (1997).

[6] A. V. Radyushkin, Phys. Lett. B **380**, 417 (1996).

[7] A. V. Radyushkin, Phys. Rev. D **56**, 5524 (1997).

[8] M. V. Polyakov, Phys. Lett. B **555**, 57 (2003).

[9] K. Kumerički and D. Müller, Nucl. Phys. B **841**, 1 (2010).

[10] V. D. Burkert, L. Elouadrhiri, and F. X. Girod, Nature **557**, 396 (2018).

[11] E. L. Lomon, Phys. Rev. C **66**, 045501 (2002).

[12] S. Galster *et al.*, Nucl. Phys. B **32**, 221 (1971).

[13] V. Punjabi *et al.*, Eur. Phys. J. A **51**, 79 (2015).

[14] R. Pohl *et al.*, Nature **466**, 213 (2010).

[15] P. J. Mohr, B. N. Taylor, and D. B. Newell, Rev. Mod. Phys. **80**, 633 (2008).

[16] W. Xiong *et al.*, Nature **575**, 147 (2019).

[17] J. D. Bjorken, Phys. Rev. **179**, 1547 (1969).

[18] R. P. Feynman, Phys. Rev. Lett. **23**, 1415 (1969).

[19] D. J. Gross and F. Wilczek, Phys. Rev. Lett. **30**, 1343 (1973).

[20] H. D. Politzer, Phys. Rev. Lett. **30**, 1346 (1973).

[21] M. Tanabashi *et al.* (Particle Data Group), Phys. Rev. D **98**, 030001 (2018).

[22] A. V. Belitsky and A. V. Radyushkin, Phys. Rep. **418**, 1 (2005).

[23] H. Moutarde *et al.*, Phys. Rev. D **87**, 054029 (2013).

[24] M. Defurne *et al.*, Nat. Commun. **8**, 1408 (2017).

[25] M. Guidal, H. Moutarde, and M. Vanderhaeghen, Rep. Prog. Phys. **76**, 066202 (2013).

[26] A. Accardi *et al.*, Eur. Phys. J. A **52**, 268 (2016).

[27] M. Burkardt, Int. J. Mod. Phys. A **18**, 173 (2003).

[28] J. Ashman *et al.*, Phys. Lett. B **206**, 364 (1988).

[29] M. Vanderhaeghen, P. A. M. Guichon, and M. Guidal, Phys. Rev. Lett. **80**, 5064 (1998).

[30] M. Vanderhaeghen, P. A. M. Guichon, and M. Guidal, Phys. Rev. D **60**, 094017 (1999).

[31] K. Goeke, M. V. Polyakov, and M. Vanderhaeghen, Prog. Part. Nucl. Phys. **47**, 401 (2001).

[32] N. Kivel, M. V. Polyakov, and M. Vanderhaeghen, Phys. Rev. D **63**, 114014 (2001).

[33] M. Guidal *et al.*, Phys. Rev. D **72**, 054013 (2005).

[34] A. V. Radyushkin, Phys. Rev. D **59**, 014030 (1998).

[35] A. V. Radyushkin, Phys. Lett. B **449**, 81 (1999).

[36] M. V. Polyakov and C. Weiss, Phys. Rev. D **60**, 114017 (1999).

[37] A. Airapetian (HERMES Collaboration), Nucl. Phys. B (Proc. Suppl.) **126**, 232 (2004).

[38] R. Dupré, M. Guidal, and M. Vanderhaeghen, Phys. Rev. D **95**, 011501 (2017).

[39] M. Mazouz *et al.*, Phys. Rev. Lett. **99**, 242501 (2007).

[40] A. Bacchetta *et al.*, Phys. Rev. D **70**, 117504 (2004).

[41] C. Muñoz Camacho *et al.*, Phys. Rev. Lett. **97**, 262002 (2006).

[42] S. Stepanyan *et al.*, Phys. Rev. Lett. **87**, 182002 (2001).

[43] C. Muñoz Camacho, Ph.D. thesis, Université Paris VI (2005).

[44] H. A. Bethe and W. Heitler, Proc. R. Soc. Lond. A **146**, 83 (1934).

[45] A. V. Belitsky, D. Müller, and A. Kirchner, Nucl. Phys. B **629**, 323 (2002).

[46] N. d'Hose, S. Niccolai, and A. Rostomyan, Eur. Phys. J. A **52**, 151 (2016).

[47] A. V. Belitsky and D. Müller, Phys. Rev. D **82**, 074010 (2010).

[48] V. M. Braun *et al.*, Phys. Rev. D **89**, 074022 (2014).

[49] M. Benali *et al.*, Nat. Phys. **16**, 191 (2020).

[50] J. Grames, E. Voutier, *et al.*, JLab Experiment E12-11-105 (2011).

[51] D. Abbott *et al.* (PEPPo Collaboration), Phys. Rev. Lett. **116**, 214801 (2016).

[52] A. Airapetian *et al.*, Phys. Rev. Lett. **87**, 182001 (2001).

[53] F. X. Girod *et al.*, Phys. Rev. Lett. **100**, 162002 (2008).

[54] F. Georges, Ph.D. thesis, Université Paris-Saclay (2018).

[55] M. Guidal and M. Vanderhaeghen, Phys. Rev. Lett. **90**, 012001 (2003).

[56] A. V. Belitsky and D. Müller, Phys. Rev. Lett. **90**, 022001 (2003).

[57] A. V. Belitsky and D. Müller, Phys. Rev. D **68**, 116005 (2003).

[58] E. Berger, M. Diehl, and B. Pire, Eur. Phys. J. C **23**, 675 (2002).

[59] M. Boër, M. Guidal, and M. Vanderhaeghen, Eur. Phys. J. A **51**, 103 (2015).

[60] I. V. Anikin *et al.*, Acta Phys. Pol. B **49**, 741 (2018).

[61] P. Abbon *et al.*, Nucl. Instr. and Meth. A **577**, 455 (2007).

[62] S. Stepanyan *et al.*, JLab Experiment LOI12–16–004 (2016).

[63] M. Boer, A. Camsonne, K. Gnanvo, E. Voutier, Z. Zhao, *et al.*, JLab Experiment LOI12-15-005 (2015).

[64] A. D. Martin, R. G. Roberts, W. J. Stirling, and R. S. Thorne, Phys. Lett. B **531**, 216 (2002).

[65] J. R. Arrington *et al.* (Hall C Collaboration), *Hall C 12 GeV Upgrade Conceptual Design Report* (2002), https://www.jlab.org/Hall-C/upgrade/cdr.pdf.

[66] Y. Kubota *et al.*, Nucl. Inst. Meth. A **320**, 66 (1992).

[67] K. Gnanvo *et al.*, Nucl. Inst. Meth. A **782**, 77 (2015).

[68] Z. Zhao, Private Communication (2020).

[69] H. Moutarde, P. Sznajder, and J. Wagner, Eur. Phys. J. C **78**, 890 (2018).

[70] H. Moutarde, P. Sznajder, and J. Wagner, Eur. Phys. J. C **79**, 614 (2019).

[71] B. Berthou *et al.*, Eur. Phys. J. C **78**, 478 (2018).

[72] M. Guidal, Eur. Phys. J. A **37**, 319 (2008).

[73] M. Guidal, Eur. Phys. J. A **40**, 119 (2009).

[74] M. Guidal and H. Moutarde, Eur. Phys. J. A **42**, 71 (2009).

[75] M. Guidal, Phys. Lett. B **689**, 156 (2010).

[76] M. Guidal, Phys. Lett. B **693**, 17 (2010).

[77] M. Boër and M. Guidal, J. Phys. G: Nucl. Part. Phys. **42**, 034023 (2015).

[78] R. Dupré *et al.*, Eur. Phys. J. A **53**, 171 (2017).

[79] F. James, MINUIT, D507, CERN (1978).

Résumé en Français

Les Distributions Généralisées de Partons (GPD) constituent une source d'information sans précédent et sont devenues un puissant paradigme pour l'étude de la structure et la dynamique du nucléon. Codant les corrélations entre les partons (les quarks et les gluons) du nucléon, les GPD permettent une représentation tridimensionnelle du nucléon à partir du lien dynamique entre la position transverse et l'impulsion longitudinale des partons. En raison de ces corrélations position-impulsion, les GPD fournissent un moyen de mesurer la contribution inconnue du moment orbital des partons au spin total du nucléon.

Le processus de Diffusion Compton Profonde Doublement Virtuelle (DDVCS) est une réaction privilégiée pour accéder les GPD. L'électroproduction d'une paire de leptons $eN \rightarrow eNl^-l^+$, qui implique le processus DDVCS, fournit le seul cadre expérimental permettant une mesure découplée des GPD(x, ξ, t) en fonction de la fraction d'impulsion moyenne x et de celle transférée ξ. Cette caractéristique unique du DDVCS est d'importance, entre autres, pour la détermination des densités de partons transverses et la distribution des forces nucléaires.

En raison de complexes problémes d'antisymmétrisation, la production de paires de muons apparaît comme le seul canal réalisable et prometteur pour la mesure du DDVCS avec des faisceaux d'électrons et de positrons au Jefferson Lab (JLab), et demandent en conséquence le développement d'un détecteur de muons. Le processus DDVCS est très difficile du point de vue expérimental en raison de la très faible grandeur de la section efficace. Les mesures des observables DDVCS nécessitent une luminosité élevée et des détecteurs de grande acceptance pour l'obtention d'une statistique significative sur une durée raisonnable des prises de données. Ainsi, la mesure des observables en terme de section efficace 5 fois différentielle est plus réaliste que celle d'une section efficace complètement (7 fois) différentielle. Les expressions des sections efficaces intégrées d'une part sur l'angle solide des muons, et d'autre part sur l'angle polaire des muons et l'angle azimutal du nucléon, ont été déterminées pour obtenir le fondement théorique des études phénoménologiques du processus DDVCS discutées dans le présent travail.

Dans le domaine cinématique accessible à JLab 12 GeV, les observables DDVCS avec des cibles non polarisées ont été évaluées en utilisant le modèle VGG et sont dominées par le Facteur de Forme Compton (CFF) $\mathcal{H}$. La projection des observables prédites selon le modèle VGG, indique un degré élevé de faisabilité d'une exprérience DDVCS à une luminosité de $10^{37}\mathrm{cm}^{-2}\cdot\mathrm{s}^{-1}$, avec un état final complètement détecté. Une étude plus réaliste soutient la faisabilité expérimentale d'une configuration couplant luminosité raisonnable et grande acceptance par opposition á une configuration de luminosité élevée de faible acceptance. Une étude plus détaillée avec le spectromètre SoLID montre une possibilité concrète de mesure du DDVCS dans la configuration J/Ψ de SoLID complètée d'un détecteur de muons.

Des méthodes numériques ont été spécifiquement développées pour extraire les CFF

des observables. En considérant des faisceaux polarisés d'électrons et de positrons, deux combinaisons linéaires spécifiques de CFF ont été extraites avec une bonne précision à partir de pseudo-données expérimentales simulées à la luminosité de $10^{37}\mathrm{cm}^{-2}\cdot\mathrm{s}^{-1}$. Couvrant un large espace de phase cinématique, il est alors possible d'obtenir, à l'aide d'un algorithme d'ajustement local, la dépendance du CFF $\mathcal{H}$ sur ses trois arguments de manière indépendante, la GPD H singulet étant directement donnée par la partie imaginaire extraite du CFF $\mathcal{H}$.

Le projet SoLID progresse et la conception des divers détecteurs du spectromètre est en cours d'optimisation. La mesure du DDVCS avec SoLID est considérée comme la solution la plus prometteuse pour une future expérience.

Afin de résoudre le puzzle du spin du nucléon, la connaissance de la GPD E est également nécessaire. Les mesures sur une cible de neutrons offrent la sensibilité recherché à la GPD E et deviennent alors particulièrement pertinentes pour la détermination du moment angulaire des partons. Pour accéder aux autres GPD, la mesure d'observables sur cible polarisée est nécessaire. Dans l'état actuel de la technologie des cibles polarisées, une expérience DDVCS sur cible fixe polarisée n'est pas envisageable. Cependant, elle pourrait être réalisée dans un futur proche auprès du prochain Collisonneur Electron-Ion (EIC). Les observables liées à la polarisation des nucléons mesurent d'autres combinaisons de CFF et fournissent des contraintes supplémentaires sur les CFF autres que $\mathcal{H}$, ce qui profite également à l'extraction de $\mathcal{H}$ dans la procédure d'ajustement local.

université PARIS-SACLAY

ÉCOLE DOCTORALE
Particules, hadrons, énergie et noyau : instrumentation, imagerie, cosmos et simulation (PHENIICS)

Titre : Étude la structure du nucléon via la Diffusion Compton Profonde Doublement Virtuelle au Jefferson Laboratory

Mots clés : Structure du nucléon ; Distributions Généralisées de Partons (GPD) ; Diffusion Compton Profonde Doublement Virtuelle (DDVCS) ; Facteurs de Forme Compton (CFF) ; Continuous Electron Beam Accelerator Facility (CEBAF).

Résumé : Les Distributions Généralisées de Partons (GPD) ont émergé au cours des années 1990 comme un paradigme puissant pour l'étude de la structure et de la dynamique du nucléon. Codant les corrélations entre les constituants élémentaires du nucléon (les partons), les GPD procurent une imagerie tridimensionnelle du nucléon à partir du lien dynamique entre la position transverse et l'impulsion longitudinale des partons. Le processus de Diffusion Compton Profonde Doublement Virtuelle (DDVCS) consiste en la diffusion d'un photon virtuel par un nucléon, le photon virtuel de l'état final produisant finalement une paire de leptons, qui peut être une paire électron-positron ou une paire muon-antimuon. Les virtualités du photon initial de type espace et du photon final de type temps peuvent être mesurées et modifiées indépendamment, permettant de cartographier la dépendance des GPD en fonction du moment initial des partons de manière indépendante de leur dépendance en fonction du moment transféré. Cette caractéristique unique du DDVCS est d'importance pour, entre autres, la détermination des densités transverses de partons et la distribution des forces nucléaires.

Ce document présente une étude du processus DDVCS dans le cadre du Continuous Electron Beam Accelerator Facility (CEBAF) au Jefferson Laboratory (JLab, Newport News, VA, États-Unis). Le bénéfice du DDVCS pour l'extraction des GPD est démontré à partir de pseudo-données prédites à l'aide d'un modèle. Cela comprend une étude de la phénoménologie du processus DDVCS et le développement d'outils de simulations, tels qu'un générateur d'événements et un algorithme d'ajustement des données, pour l'évaluation des performances d'une expérience DDVCS. La faisabilité de projets expérimentaux possibles est discutée, y compris une configuration idéale et le détecteur de grande acceptance SoLID (Solenoidal Large Intensity Device). Considérant des faisceaux polarisés d'électrons et de positrons, les combinaisons linéaires de (Facteur de Forme Compton) CFF sont extraites à partir des pseudo-données expérimentales simulées. Les GPD sont ensuite déduites des CFF au moyen d'un algorithme d'ajustement spécifiquement développé.

Title : Studying the nucleon structure via Double Deeply Virtual Compton Scattering at the Jefferson Laboratory

Keywords : Nucleon structure ; Generalized Parton Distributions (GPDs) ; Double Deeply Virtual Compton Scattering (DDVCS) ; Compton Form Factors (CFFs) ; Continuous Electron Beam Accelerator Facility (CEBAF).

Abstract : Generalized Parton Distributions (GPDs) have emerged over the 1990s as a powerful paradigm to study the structure and dynamics of the nucleon. Encoding the correlations between the elementary constituents of the nucleon (the partons), GPDs allows 3-dimensional imaging of the nucleon from the dynamical link between the transverse position and the longitudinal momentum of partons. The Double Deeply Virtual Compton Scattering (DDVCS) process consists of the scattering of a virtual photon off the nucleon, the virtual photon in the final state eventually generating a lepton pair, which can be either an electron-positron or a muon-antimuon pair. The virtualities of the initial space-like photon and the final time-like photon can be measured and varied independently, allowing one to map out the initial parton momentum dependency of GPDs independently of their transferred momentum dependency. This unique feature of DDVCS is of relevance, among others, for the determination of the transverse parton densities and the distribution of nuclear forces.

This document presents a study of the DDVCS process in the context of the Continuous Electron Beam Accelerator Facility (CEBAF) at the Jefferson Laboratory (JLab, Newport News, VA, USA). The benefit of DDVCS for the extraction of GPDs is demonstrated from model-predicted pseudo-data. This involves phenomenological studies of the DDVCS process and the development of simulation tools, such as an event generator and a fitter algorithm, for the evaluation of the performances of a DDVCS experiment. The feasibility of possible experimental projects is discussed, including an ideal configuration and the large acceptance detector SoLID (Solenoidal Large Intensity Device). Considering polarized electron and positron beams, linear combinations of the Compton Form Factors (CFFs) are extracted from simulated experimental pseudo-data. GPDs are further deduced from CFFs using the fitter algorithm specifically developed.

Université Paris-Saclay
Espace Technologique / Immeuble Discovery
Route de l'Orme aux Merisiers RD 128 / 91190 Saint-Aubin, France